A Search for Massive Resonances in Final States with Boosted Top-Antitop Pairs Decaying into a Lepton and Jets with the ATLAS Detector at the Large Hadron Collider

Janna Katharina Behr

Merton College
University of Oxford

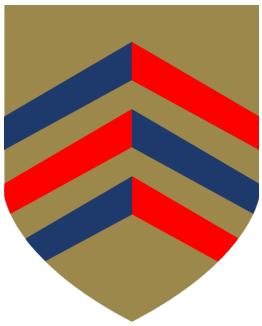

Thesis submitted in partial fulfilment of the requirements
for the degree of Doctor of Philosophy

Trinity Term 2015

A Search for Massive Resonances in Final States with Boosted Top-Antitop Pairs Decaying into a Lepton and Jets with the ATLAS Detector at the Large Hadron Collider

Janna Katharina Behr, Merton College, University of Oxford

Thesis submitted in partial fulfilment of the requirements
for the degree of Doctor of Philosophy. Trinity Term 2015.

Abstract

In this thesis, a search for new elementary particles decaying to a top-antitop pair ($t\bar{t}$) is presented. Massive new particles that preferentially decay to top quarks are predicted by a number of theoretical models that have been proposed to address various open questions in the currently established Standard Model of Particle Physics, in particular those related to the Higgs mechanism through which elementary particles acquire mass.

The search is conducted in proton-proton collision data collected by the ATLAS experiment at the Large Hadron Collider, located at CERN, the European Laboratory for Particle Physics. The integrated luminosity of the dataset, which was collected in 2012, is 20.3 fb^{-1}. This is the first and only search for new particles in $t\bar{t}$ final states that uses the full ATLAS dataset collected in collisions at the centre-of-mass energy $\sqrt{s} = 8$ TeV.

The search focuses on $t\bar{t} \to (W^+b)(W^-\bar{b})$ final states in which one W boson decays into an electron or muon and the corresponding (anti)neutrino and the other W boson decays into a quark and an antiquark. The detector signature of these events is characterised by the presence of an electron or muon, a certain number of hadronic jets and large missing transverse energy.

Two independent reconstruction strategies for top quarks with small and large transverse momenta, respectively, are combined to optimise the sensitivity of the search over the mass range between 0.4 TeV and 3.0 TeV. In particular, jet substructure techniques as well as a transverse-momentum dependent treatment of lepton isolation and lepton-jet overlap are used to account for the collimation of the decay products of highly energetic (*boosted*) top quarks.

The distributions of the reconstructed $t\bar{t}$ invariant mass in data are analysed for local excesses or deficits with respect to the Standard Model prediction. No evidence for the existence of new particles is found in the analysed mass range. Upper limits on the cross-section times branching ratio to $t\bar{t}$, at the 95% confidence level, are derived for four benchmark models. For a narrow Z' resonance, these limits range from 4.2 pb for a resonance mass of 0.4 TeV to 0.03 pb for a mass of 3.0 TeV. A topcolor-assisted technicolor Z'_{TC2} boson with a relative width of 1.2% is excluded for masses between 0.4 TeV and 1.8 TeV. Upper limits on the cross-section times branching ratio of 4.8 pb (0.09 pb) at 0.4 TeV (3.0 TeV) are also derived for a broad colour-octet state with a width of 15.3%. A Bulk RS Kaluza-Klein gluon with the above width is excluded in the mass range between 0.4 TeV and 2.2 TeV. For the first time in ATLAS, the results of a resonance search in $t\bar{t}$ final states are also interpreted in the context of models with a narrow Bulk RS Kaluza-Klein graviton and a generic scalar resonance, respectively. The upper limits on the cross-section times branching ratio for the Bulk RS Kaluza-Klein graviton (scalar resonance) range from 2.5 pb (3.0 pb) at 0.4 TeV to 0.03 pb at 2.5 TeV (3.0 TeV).

To my family

Acknowledgements

This work would not have been possible without the financial support from the Rhodes Trust. The Rhodes Scholarship provided me with the means to conduct the research towards my DPhil degree at Oxford but it also gave me the chance become part of a diverse community of scholars that has shaped and inspired me through numerous discussions and encounters. I am deeply grateful for these experiences, which truly enriched my life at Oxford.

I would also like to extend my gratitude to the Subdepartment of Particle Physics, the Oxford ATLAS Group, and Merton College for supporting my participation in various workshops and meetings at CERN and for their friendly and welcoming communities.

I gratefully acknowledge support through a Charterhouse European Bursary and a scholarship of the German Academic Exchange Service (DAAD) that provided the financial means for a 15 months research stay at CERN. Furthermore, I am indebted to the C R Barber Trust Fund, the Wilhelm & Else Heraeus Stiftung and MCNet for supporting my participation in various schools and conferences.

There are many people whom I would like to thank in particular:

First of all, I am grateful to my supervisor, Çiğdem İşsever, for giving me the opportunity to work in the exciting new field of searches with boosted objects, and on Variable-R jets in particular, and for granting me a great amount of freedom in choosing and pursuing my research projects. Many thanks in particular for some very valuable advice that will undoubtedly also be helpful with regard to future projects.

Thank you to Alfons Weber and Joel Goldstein for agreeing to act as examiners for this dissertation.

I would also like to thank Jeff Tseng for enjoyable discussions about various topics, especially alternative jet algorithms; for his feedback on the statistics chapter; for his support in making a couple of trips to CERN possible; and for giving me the opportunity to give tutorials at St. Edmund's Hall. I am further indebted to Alan Barr for supporting my application for a Rhodes scholarship with his reference letter and for his support, especially in my first weeks at Oxford. Many thanks also go to Daniela Bortoletto for her encouragement and useful advice.

Special thanks go to Jiahang Zhong for sharing his extensive knowledge and experience from past $t\bar{t}$ resonance searches, for useful software tips, and for providing the initial idea of applying Variable-R jets in the context of b-tagging. He and James Ferrando were always there to discuss even the most tricky analysis questions. I am grateful for everything I learned from them. I am also indebted to Samuel Calvet for answering all my questions about `BumpHunter` and for his feedback on the corresponding chapter in my thesis draft. I owe special thanks to Danilo Ferreira de Lima for his invaluable software support in implementing Variable-R jets in the derivation framework for Run 2 and for his enthusiasm and support regarding the application of this algorithm in future $t\bar{t}$ resonance searches.

Many thanks go to Juan Rojo and Nathan Hartland from the Oxford Particle Theory Group, as well as James Frost, for the fruitful and enjoyable collaboration on the feasibility study on the observation of Higgs-boson pair production in $b\bar{b}b\bar{b}$ final states at the High-Luminosity LHC.

I am indebted to Monika Wielers for introducing me into the E/Gamma Trigger Signature Group for what was going to be a very interesting and worthwhile qualification task and to Alessandro Tricoli and Paul Bell, the group conveners at the time, for the excellent supervision. I am especially indebted to Alessandro for supporting my application for a DESY postdoctoral fellowship.

Many thanks also go to Gabriella Pasztor and Denis Damazio, who succeeded Alessandro and Paul as group conveners, and to Jiri Masik for sharing his extensive knowledge of trigger-level tracking algorithms.

Many thanks to everyone in the Oxford ATLAS Group and at CERN who contributed to the enjoyable work environment in both places over the past years: Lucy Kogan and Sarah Livermore for welcoming me into the Oxford Exotics team; Will Kalderon, Mark Pickering, Faye Cheung and Olli Lupton for keeping me company at CERN and for suprising me with the most chocolatey birthday cake I ever received. There are many others whom I cannot all list here but who are not forgotten.

There are also many people in Oxford who work behind the scenes to ensure that things are running smoothly: Many thanks to Sue Geddes, Kim Proudfoot and Francesca Oliver for their support in dealing with exam forms, travel plans and other administrative issues, and to the computing team for their invaluable technical support, with special thanks to Ewan MacMahon and Kashif Mohammad for the emergency laptop repair just a month before the submission deadline.

I took my first steps in experimental particle physics as a diploma student working on the measurement of the top-quark mass with Otmar Biebel at the LMU Munich. I owe a great deal of gratitude to Otmar for everything I learned during that year, for his advice and continued support, and for many long, inspiring discussions on some of the most mind-blowing questions in science. Many thanks to him and Dorothee Schaile, the head of institute, for always keeping an open door for me when I happened to visit Munich.

There are many people outside of physics who have been an important part of my life, not only in the last three-and-a-half years, and it is simply impossible to name them all. Therefore the following list is by no means complete: Thank you to Alma and Verena, whom I was lucky enough to have around me during my time in Oxford after many years together in Munich. I am grateful not only for their helpful feedback on various parts of the thesis draft but also for their advice and support at all times. Thank you to Robert and Isi for all the wonderful time we spent together in Oxford and Munich; to Regina, whose packages and fun cards from Japan brightened up many of my days; to Karo, my oldest friend, who came all the way to Geneva with her family to visit me; to Leo for many great conversations about literature and some excellent book recommendations.

Thank you especially to Carsten, for his love, encouragement and understanding, for being an amazing listener, and for always being there for me. I am glad to have you in my life.

Last but certainly not least I am deeply grateful to my family - my parents, Heike and Bernhard, and my brother Beve - for all their love and their unwavering support. Throughout my life, my parents, by their own example, have shown me the joy of learning and exploring; taught me to never give up easily; reminded me to always keep an open mind and to never stop questioning. This thesis is dedicated to them.

Preface

Research in experimental high-energy physics today is often conducted in large, international collaborations. The analysis presented in this thesis has been performed on data from the ATLAS experiment, which has been designed, built and maintained by a collaboration with currently around 3,000 active members. Many tasks, like the maintenance of hardware systems and the development of common particle reconstruction and calibration tools, are carried out centrally in dedicated working groups. Therefore the search presented in this thesis builds upon the work of past and present members of the ATLAS collaboration, whose contributions are referenced throughout the text.

Figures with the label "ATLAS" or "ATLAS preliminary" have featured in ATLAS publications or conference/public notes, respectively. Figures without the "ATLAS" label have either been taken from non-ATLAS publications or have been included in the ATLAS-internal supporting documentation for an ATLAS publication and circulated internally. All figures and tables without a reference in the caption have been produced by the author of this thesis; for some figures, further details are given below.

The search presented in this thesis has been published in the Journal of High-Energy Physics [1]. Further analysis details are summarised in an ATLAS collaboration internal document [2], which has been reviewed in an internal, multi-stage peer-review process, prior to the release of the paper. The author's contributions to this analysis are detailed in the following:

- The author wrote her own analysis framework for the production of the nominal $m_{t\bar{t}}$ spectra. This involved the implementation of the event selection criteria for all twelve search channels, including all corrections to be applied to simulated events.
- The full set of (nominal and systematic variation) $m_{t\bar{t}}$ spectra, upon which the final search results are based, was produced using a different analysis code, based on software that was originally written by another member of the analysis team and has been extended by this member together with the author to include the full set of systematic variations. The nominal event yields obtained with this code have been cross-checked against those produced with the author's code to ensure the reliability of the final results. The decision to move to a joint analysis code was motivated by the large number of systematic uncertainties that had to be taken into account in the derivation of the final results.
- The author's contributions to the main analysis code include the estimation of the impact of all uncertainties related to large-R jets, the shape of the W+jets background, the electroweak corrections on the $t\bar{t}$ background and the jet vertex fraction of small-R jets.
- The author also determined the impact of the PDF uncertainty on the final result, which required the combination of information from 195 PDF sets from the LHAPDF6 library according to the PDF4LHC recommendations (Section 5.6.4).
- Figures 5.6, 5.7 and 5.8 have been produced by the author using the common analysis code. They are equivalent to Figures 1–3 in [1].
- Figures 6.2–6.4 and the results in Tables 6.1 and 6.2, which have been published in [1], have been derived using the common analysis code, which the author co-developed.
- The author was responsible for the derivation of the exclusion limits on the benchmark models for this search and carried out all studies on the profiling procedure. All results in Section 7.2 have been produced by the author, unless otherwise stated. This includes the limit plots in Figures 7.9 and 7.10, which have been published in [1].

- The author derived the post-fit $m_{t\bar{t}}$ distributions in Figure 6.8. This is the first time that such distributions have been used in an ATLAS search for resonant $t\bar{t}$ production (Section 7.2.4). Figures 6.5–6.8, which have all been produced by the author, have been published in [1].
- The author carried out studies to understand and reduce the inefficiencies of the single-electron triggers that are used in this search. The results of these studies, which are not included in this thesis, will be published as part of a summary paper on the performance of the ATLAS electron and photon triggers in Run 1, which is currently under review by the ATLAS collaboration [3]. The author has also developed a software tool for the monitoring of the electron trigger inefficiencies in Run 1 of the LHC, which has been adapted by the ATLAS E/Gamma Trigger Signature Group to become a standard tool in Run 2.

In addition to the analysis presented in this thesis, the author has worked on the following projects during her time as a DPhil candidate at the University of Oxford:

- The author is one of the main analysers of a feasibility study on the observation of Higgs-boson pair production in $b\bar{b}b\bar{b}$ final states at the High-Luminosity LHC, which is currently being prepared for submission to JHEP [4].
- The author has pioneered the use of (large) Variable-R jets [5] for the reconstruction of highly-energetic top quarks, as an alternative to conventional jet algorithms with fixed R-parameter. These studies, which are briefly described in the outlook (Chapter 9), are summarised in an ATLAS collaboration internal document [6] and are being prepared for release as an ATLAS Public Note.
- The author has carried out the first studies into the use of Variable-R jets in track-based b-tagging algorithms for dense event topologies. Some of these studies have been presented at the DPG 2015 spring conference [7]. A brief summary is given in the outlook (Chapter 9).
- The author provided an estimate of the background from $pp \to hb\bar{b} \to b\bar{b}b\bar{b}$ production for the ATLAS search for Higgs boson pair production in the $b\bar{b}b\bar{b}$ final state at $\sqrt{s} = 8$ TeV, which has been accepted for publication in the European Journal of Physics C [8].

Conventions and units in this thesis:
Throughout this thesis, natural units ($\hbar \equiv c \equiv k_B \equiv 1$) are used. Energy, momentum and mass values are quoted in electron-volts (eV), where 1 eV = $1.602176565(35) \cdot 10^{-19}$ J.

Contents

List of Figures

List of Tables

"Our aim as scientists is objective truth; more truth,
more interesting truth, more intelligible truth.
We cannot reasonably aim at certainty."

– Karl R. Popper, *In Search of a Better World*

1. Introduction

The quest for an understanding of the fundamental constituents of matter and their interactions has been marked by a constant and vital interplay between theory and experiment. Unexpected discoveries as well as precision measurements have challenged theoretical models; theoretical predictions have prompted the construction of small- and large-scale experiments that have explored particle interactions at increasingly high energies and small scales, and measured fundamental parameters of nature with increasing precision.

Over the past eighty years, advancements in both theory and experiment have led to the emergence of an extremely successful set of theories, collectively referred to as the Standard Model (SM) of Particle Physics [9, 10, 11, 12]. It describes all elementary constituents of matter known to date and their interactions via three out of the four known fundamental forces of nature, namely the strong, weak and electromagnetic interactions. The SM has withstood rigorous experimental tests and even predicted the existence of new elementary particles such as the $W^{\pm}$ and Z^0 bosons, discovered at the Super Proton Synchrotron (SPS) at CERN in 1983 [13, 14], and the top quark, discovered at the Tevatron collider at Fermilab in 1995 [15, 16].

The observation of a new scalar particle by the ATLAS and CMS collaborations at the Large Hadron Collider (LHC) at CERN in 2012 [17, 18] marked yet another milestone in the history of particle physics. The properties of this particle have been found to be consistent with those of the long sought-after Higgs boson in subsequent and increasingly precise measurements [19, 20]. The existence of the Higgs boson was predicted by the mechanism of electroweak symmetry breaking (EWSB), put forward in 1964 by F. Englert and R. Brout [21], P. Higgs [22, 23, 24], and G. Guralnik, C. Hagen, T. Kibble [25, 26]. This mechanism, which describes how the weak gauge bosons and the SM fermions acquire mass, is a key element of the SM. Hence, dedicated searches for this particle had previously been performed at the Large Electron Positron (LEP) collider at CERN [27] and the Tevatron [28, 29, 30].

The anticipation that preceded both the discovery of the Higgs boson and that of the top quark is in stark contrast to the reactions following the discovery of the muon [31], almost 80 years earlier - a discovery that, in many ways, can be seen as the beginning of modern particle physics. At the time, the structure of matter seemed well understood and simple: Electrons, protons and neutrons had been established as the building blocks of atoms, and the search was on to discover the carrier of the nuclear force between protons and neutrons in the atomic nucleus, postulated by H. Yukawa in 1935 [32], - a particle that many scientists thought to be the last missing ingredient in the description of the fundamental constituents of matter. The realisation that the muon was not the carrier of the nuclear force but a 200 times heavier copy of the electron came as a complete surprise in 1947. The existence of this seemingly superfluous particle is said to have prompted Nobel laureate I.I.Rabi to exclaim: "Who ordered *that*?"[1]

Despite the great successes of the SM, Rabi's question remains unanswered to this day: The SM describes three generations of quarks and leptons but provides no explanation why heavier copies of the first-generation particles, which make up atoms and molecules of everyday matter, exist. It also fails to explain why the masses of elementary particles differ by several orders of magnitude, or why the scale of the EW interactions is by roughly a factor of 10^{17} smaller than the scale of the gravitational interaction, a question known as the hierarchy problem. These are only a few of a number of reasons why the SM is widely considered an incomplete theory, embedded in a more fundamental theoretical framework that is yet to be formulated. Further shortcomings of the SM will be discussed in Section 2.3.

Various extensions of the SM, so-called **beyond SM (BSM)** theories, have therefore been proposed. The top quark plays a special role in many of these models: Its large mass, $m_{\text{top}} = 173$ GeV [34], which is more than five orders of magnitude larger than that of the electron, is close to the Higgs boson mass, $m_h = 126$ GeV [35], and to the scale of EWSB, $v \approx 246$ GeV. These findings suggest that BSM processes at the TeV scale, especially those related to EWSB and the hierarchy problem, may manifest themselves either through modifications of top quark properties compared to the SM predictions, and/or through decays of new elementary particles into top quarks. Evidence for BSM physics at the TeV scale may therefore be sought through precision measurements of top-quark properties (*indirect searches*) or through **direct searches** for new particles in high-energy particle collisions.

In this thesis, a direct search for BSM particles decaying to a top and an antitop quark ($t\bar{t}$) is

[1] The citation history of this quote appears to be unclear, but it can be found in many textbooks, for example [33].

presented. The search focuses on the $t\bar{t}$ invariant mass spectrum in events that are specifically selected to enhance the fraction of predicted signal events in the sample. The presence of a BSM state would manifest itself as a deviation in the observed mass spectrum from the smoothly falling distribution expected for $t\bar{t}$ production through SM processes. The search presented in this thesis is targeted specifically at *local* enhancements ("bumps") in the spectrum, caused by the **resonant production of massive particles** and their subsequent decay to $t\bar{t}$ pairs.

The prime objectives of this and other direct searches for BSM physics are, firstly, to optimise the sensitivity of the search over a large kinematic regime, in this case the $t\bar{t}$ invariant mass range, and, secondly, to keep the search as general as possible by minimising possible biases towards particular BSM models. The goal of such a **model-independent** search is to find and quantify *any* local deviation of the observed spectrum from the SM prediction. Nevertheless, a number of **benchmark models** are used to gauge the sensitivity of the search to BSM resonances, and to derive exclusion limits on existing models, if no evidence for a BSM resonance is found. It is desirable to choose a number of representative BSM models with different properties to allow the results to be interpreted in the context of a wide range of other BSM models.

The search presented in this thesis is the first search for resonant $t\bar{t}$ production to consider a spin-2 resonance model, in addition to models with spin-1 and spin-0 resonances, and the first to include a systematic study of the dependence of the exclusion limits on the resonance width. It relies on data collected at the ATLAS experiment in proton-proton (pp) collisions at a centre-of-mass energy $\sqrt{s} = 8$ TeV at the LHC in 2012. As a hadron collider, the LHC is ideally suited for searches over a large mass range as it possible to probe a wide range of effective collision energies at a given beam energy (Chapter 3). Importantly, it is only the second particle accelerator in the world, after the Tevatron, capable of producing top quarks, thus allowing for searches for resonant $t\bar{t}$ production. Its collision energy of $\sqrt{s} = 8$ TeV in 2012 was already around four times higher than that at which the Tevatron had previously been operating; the increase of the LHC collision energy to $\sqrt{s} = 13$ TeV in 2015 allows for another significant extension of the kinematic regime accessible to direct searches.

Searches for the resonant production of $t\bar{t}$ pairs via BSM processes have been carried out by the CDF [36, 37] and DØ [38] collaborations in $p\bar{p}$ collisions the Tevatron at the centre-of-mass energy $\sqrt{s} = 1.96$ TeV, probing a mass range up to around 900 GeV. The ATLAS [39, 40, 41] and CMS [42, 43, 44] collaborations have conducted similar searches using pp collision data from the LHC at $\sqrt{s} = 7$ TeV, probing a mass range up to 3 TeV; the CMS collaboration has

also presented a search in LHC collision data at $\sqrt{s} = 8$ TeV in the same mass range [45]. To date, no evidence for resonant $t\bar{t}$ pair production has been found. Instead, upper limits on the production cross-section times branching ratio for BSM resonances decaying to $t\bar{t}$ have been set. Further details on current limits for various benchmark models are given in Section 2.5.

The significant extension of the kinematic regime accessible to BSM searches in the LHC era has triggered the development of a new generation of techniques for the reconstruction and identification of highly energetic (**boosted**) top quarks: With increasing transverse momentum, the top-quark decay products appear increasingly collimated in the detector frame and can no longer be resolved by traditional reconstruction techniques. Searches for resonant $t\bar{t}$ production have traditionally been a testing ground for novel reconstruction techniques for boosted particle decays that have later been applied in other searches and even measurements, involving not only top quarks but also boosted $W^{\pm}$, Z^0 and Higgs bosons. For a recent overview see [46].

The search presented in this thesis relies on two different reconstruction strategies to optimise its sensitivity over a large mass regime between 0.4 and 3.0 TeV, one targeted at low-energetic top quarks, for which the decay products are well separated in the detector (**resolved topology**), the other targeted at highly energetic top quarks (**boosted topology**). In particular, an improved reconstruction strategy for semileptonically decaying boosted top quarks is used, which has been developed specifically for this search (Section 5.2.3).

Further improvements will be necessary with regard to the recent increase in the LHC collision energy. The limitations of current techniques with regard to future searches at the higher LHC collision energy, $\sqrt{s} = 13$ TeV, are discussed in Chapter 9, together with an outlook on on-going and recommended improvements that will be required to fully explore the unprecedented mass range that is now accessible at the LHC.

This thesis is structured as follows: An **overview of the SM, its shortcomings and the benchmark models** considered in this thesis is given in Chapter 2. The **experimental setup** is described in Chapter 3, followed by an overview of the **reconstruction, identification and calibration strategies for physics objects** in the ATLAS experiment (Chapter 4). A detailed account of the **search strategy**, including the definition of the signal regions, the estimation of background processes and systematic uncertainties, is given in Chapter 5. The **results of the search** are presented in Chapter 6; their **statistical interpretation** is discussed in Chapter 7.

2. Theoretical Foundations and Motivation for the Search for Resonant $t\bar{t}$ Production

In this chapter, the theoretical foundations and motivation for the search for resonant $t\bar{t}$ production are introduced. First, an overview of the Standard Model of Particle Physics is given (Section 2.1), followed by a discussion of $t\bar{t}$ pair production and top-quark decays in the Standard Model (Section 2.2). The limitations of the Standard Model and the role of the top quark with regard to theories beyond the Standard Model are discussed in Sections 2.3 and 2.4. The benchmark models used in this search for resonant $t\bar{t}$ production are detailed in Section 2.5.

2.1. The Standard Model of Particle Physics

The Standard Model of Particle Physics (SM) is the theoretical framework that describes all elementary constituents of matter known to date and the interactions between them via the strong, weak and electromagnetic forces. In the following, an overview of the particles and interactions of the SM is given. The information summarised here can be found in a number of textbooks, which are also recommended for more extensive reviews [33, 47, 48, 49].

The SM is a gauge field theory that is characterised by the following product of gauge groups

$$SU(3)_C \times SU(2)_L \times U(1)_Y. \tag{2.1}$$

The non-Abelian group $SU(3)_C$ describes the **strong interaction**, which conserves the **colour charge** C and is mediated by an octet of **vector boson** (gauge) fields in the (eight-dimensional) adjoint representation of the group, the gluon fields. The product group $SU(2)_L \times U(1)_Y$ corresponds to the electroweak (EW) interactions, which are mediated by an $SU(2)_L$ triplet of gauge fields, W^i_μ ($i \in 1, 2, 3$), which couple only to left-handed[1] ("L") **fermion** fields, and a $U(1)_Y$ singlet gauge field, B_μ, which conserves the weak hypercharge Y.

[1] A fermion (spinor) field Ψ is defined as left-(right-)handed if it is an eigenstate of the chirality operator $P_{L/R} = \frac{1}{2}(1 \mp \gamma^5)$, where $\gamma^5 \equiv i\gamma^0\gamma^1\gamma^2\gamma^3$ is the product of the four Dirac matrices, see for example [33, 47].

The matter particles in the SM are represented by **fermion** fields with spin $\frac{1}{2}$, also referred to as *spinor* fields. They fall into two groups: **Quark** fields carry colour charge (in addition to a fractional electric charge) and therefore couple to the gluon fields of the strong interaction. **Lepton** fields, on the other hand, are colour-neutral and are further distinguished based on their electric charges: charged leptons (antileptons) carry negative (positive) unit charge, while **neutrinos** are uncharged. There are six **lepton flavours**, namely **electrons**, **muons** and τ-**leptons**, and the corresponding electron-, muon- and τ-neutrinos. Analogously, six different **quark flavours** are described in the SM: the *up-type* quarks are referred to as **up**, **charm** and **top**, while the *down-type* quarks have flavours **down**, **strange** and **bottom**. The different quark (lepton) types and their properties are summarised in the upper (lower) part of Table 2.1 at the end of this section.

Under the EW interactions, all SM fermion fields are grouped into doublets and singlets based on their **weak isospin**, I, a quantum number related to the chirality of spinor fields: left-handed fermions form isospin doublets with $I = \frac{1}{2}$ and isospin component $I_3 = \pm\frac{1}{2}$, while right-handed fermions are isospin singlets ($I = 0$). In the quark sector, an isospin doublet consists of a down-type ($I_3 = -\frac{1}{2}$) and an up-type quark ($I_3 = +\frac{1}{2}$); in the lepton sector, a doublet comprises a charged lepton ($I_3 = -\frac{1}{2}$) and its corresponding neutrino ($I_3 = +\frac{1}{2}$). The $SU(2)_L$ gauge fields, which themselves form an isospin triplet, couple only to the left-handed isospin doublet fields, implying that **parity** is maximally violated in their interactions.

The gauge fields of the *observed* EW vector bosons, the $W^{\pm}$ bosons, the Z^0 boson and the photon, are linear superpositions of the above fields, parameterised by the **weak mixing angle**[2] θ_W:

$$W_\mu^{\pm} = \frac{1}{2}(W_\mu^1 \mp iW_\mu^2), \tag{2.2}$$

$$Z_\mu^0 = -B_\mu \ \sin\theta_W + W_\mu^3 \ \cos\theta_W, \tag{2.3}$$

$$\mathcal{A}_\mu = B_\mu \ \cos\theta_W + W_\mu^3 \ \sin\theta_W. \tag{2.4}$$

The $W^{\pm}$ boson fields act on the weak isospin doublets by turning one isospin partner into the other. The interactions mediated by the charged EW bosons are therefore **flavour changing** interactions. It must be noted that the fields in the isospin doublets, to which the $W^{\pm}$ boson fields couple, are eigenstates of the *weak isospin* rather than the *mass* operator. In the quark sector, the relation between the two sets of states is described by the **Cabibbo-Kobayashi-**

[2] The weak mixing angle can be expressed in terms of the masses of the W and Z bosons: $\cos\theta_W = m_W/m_Z$.

Maskawa (CKM) matrix [50, 51, 52], a 3×3 unitary matrix that is parameterised by three angles $(\theta_{12}, \theta_{23}, \theta_{13})$ and a CP violating[3] phase (δ_{13}), the values of which have been determined experimentally [52]. The fact that this matrix has non-zero off-diagonal elements allows for the possibility of quark-flavour changes between different generations, mediated by the $W^{\pm}$ bosons. The corresponding transition rates are proportional to the square values of the magnitudes of the CKM matrix elements, $|V_{ij}|$. These magnitudes, which are determined experimentally, are summarised in the following matrix [52]:

$$\begin{pmatrix} |V_{ud}| = 0.97425 \pm 00022 & |V_{us}| = 0.2253 \pm 0.0008 & |V_{ub}| = (4.13 \pm 0.49) \cdot 10^{-3} \\ |V_{cd}| = 0.225 \pm 0.008 & |V_{cs}| = 0.986 \pm 0.016 & |V_{cb}| = (41.1 \pm 1.3) \cdot 10^{-3} \\ |V_{td}| = (8.4 \pm 0.6) \cdot 10^{-3} & |V_{ts}| = (40.0 \pm 2.7) \cdot 10^{-3} & |V_{tb}| = 1.021 \pm 0.032 \end{pmatrix}. \quad (2.5)$$

An equivalent matrix, the Pontecorvo-Maki-Nakagawa-Sakata (PMNS) matrix [53, 54, 52], has been introduced in the neutrino sector to explain neutrino oscillations. The observation of neutrino oscillations not only indicates that neutrino flavour and mass eigenstates are not identical but that neutrinos must have non-zero mass.

The $SU(2)_L \times U(1)_Y$ symmetry is **spontaneously broken** by the **Higgs mechanism**, which postulates the existence of a complex, scalar $SU(2)_L$ doublet field with weak hypercharge $Y = 1$ and a ground state that is characterised by a non-zero vacuum expectation value v. This field possesses four real, scalar degrees of freedom, three of which are "absorbed" by the $W^{\pm}$ and Z^0 vector boson fields, which thereby acquire mass. The photon field remains massless in the SM. The remaining degree of freedom corresponds to the scalar Higgs field, the quanta of which, the Higgs bosons, have been observed at the LHC. This mechanism of EW symmetry breaking (EWSB) is required to explain the observed masses of the $W^{\pm}$ and Z^0 bosons: The introduction of explicit mass terms for the gauge fields in the EW Lagrangian would violate local gauge invariance. The gauge boson masses must therefore be generated *dynamically*.

The Higgs mechanism also describes the masses m_f of the fermion fields via their Yukawa couplings to the Higgs field with coupling strength

$$\zeta_f = \frac{\sqrt{2}\, m_f}{v}. \quad (2.6)$$

The vacuum expectation value, $v \approx 246$ GeV, is determined through precision measurements of

[3] Here, "C" stands for charge conjugation and "P" for parity.

EW observables [52]. In group theoretical terms, the EWSB can be expressed as

$$SU(2)_L \times U(1)_Y \rightarrow U(1)_{em}, \tag{2.7}$$

where $U(1)_{em}$ is the gauge group of **Quantum Electrodynamics (QED)**, the theory that describes the electromagnetic interaction between electrically charged particles. The relation between the electric charge Q_{em}, the weak hypercharge Y, and the weak isospin component I_3 is given by the *Gell-Mann-Nishijima* formula, which can be found in many textbooks:

$$Q_{em} = I_3 + \frac{1}{2}\, Y. \tag{2.8}$$

The quanta of the $U(1)_{em}$ gauge field are the photons, which couple to all electrically charged fermions with a coupling strength determined by the coupling parameter α_{em}. The value of α_{em} depends on the momentum scale Q of the interaction,[4] a consequence of *vacuum fluctuations* involving virtual pairs of charged leptons and antileptons, which *screen* the bare electric charge at large distances. This leads to a decrease of α_{em} at larger distances or, equivalently, smaller values of Q.

The strong interaction, in contrast, which is described by the theory of **Quantum Chromodynamics (QCD)**, acts on colour-charged particles with a coupling strength determined by a parameter α_s that *increases* with decreasing momentum scale Q: unlike the photon field, which is uncharged, the gluon fields carry colour charge, more specifically a combination of colour and anticolour, and therefore interact not only with the quark fields but also with each other. This **gluon self-interaction**, which is a direct consequence of the non-Abelian nature of the QCD gauge group, results in gluon loop contributions to the QCD vacuum, which lead to an *antiscreening* of colour charges at large distances. This has profound phenomenological consequences, especially for reactions at hadron colliders: At large momentum scales, for example in hard scattering processes between the initial-state partons in pp collisions, α_s is small. Quarks and gluons behave approximately like free particles (**asymptotic freedom**) and their interactions can be calculated perturbatively. With increasing separation between them, however, α_s becomes large enough to allow for the creation of a whole cascade of additional quark-antiquark pairs from the energy stored in the colour field, which then form colourless bound states (**hadrons**), in which the quarks are **confined**. Quark-antiquark bound states

[4] For $Q^2 = 0$, $\alpha_{em} \approx 1/137$, while for $Q^2 = m_W^2$, $\alpha_{em} \approx 1/128$ [52].

are referred to as **mesons**; bound states of three quarks are named **baryons**.[5] Thus, a highly energetic quark or gluon from a hard scattering process gives rise to a whole cascade of hadrons, a **hadronic jet** (Section 4.3). This **hadronisation** process cannot be calculated perturbatively (Section 3.4).

The elementary particles of the SM and some of their properties are summarised in Table 2.1. In total, the SM contains twelve types of fermions (in addition to the corresponding antifermions, which are not listed in the table), arranged in three *generations*. Corresponding particles in different generations, for example all up-type quarks, have different masses but carry the same spin and charge quantum numbers. In addition, there are five vector bosons, the quanta of the gauge fields that mediate the weak, electromagnetic and strong forces: the $W^{\pm}$ and Z^0 bosons, the photon, and the gluon. The SM also contains a single scalar particle, the Higgs boson.

	I		II		III			
	u	d	c	s	t	b	g	γ
Mass [MeV]	2.3	4.8	$1.3 \cdot 10^3$	95	$173 \cdot 10^3$	$4.18 \cdot 10^3$	0	$< 10^{-24}$
Charge [e]	+2/3	-1/3	+2/3	-1/3	+2/3	-1/3	0	0
Spin	1/2	1/2	1/2	1/2	1/2	1/2	1	1
	ν_e	e	ν_μ	μ	ν_τ	τ	$W^{\pm}$	Z^0
Mass [MeV]	$< 0.225 \cdot 10^{-3}$	0.511	< 0.19	106	< 18.2	$1.78 \cdot 10^3$	$80.4 \cdot 10^3$	$91.2 \cdot 10^3$
Charge [e]	0	-1	0	-1	0	-1	± 1	0
Spin	1/2	1/2	1/2	1/2	1/2	1/2	1	1

Table 2.1.: Overview of the elementary fermions and vector bosons of the SM and their properties. First line: up (u), down (d), charm (c), strange (s), top (t) and bottom (b) quark, gluon and photon. Second line: electron neutrino, electron, muon neutrino, muon, τ-neutrino, τ-lepton, W bosons, Z boson. The Higgs boson (h), which has a mass of 126.09 GeV and zero charge and spin, is not listed in the table. Numbers taken from [52, 34, 35]. The references also include the uncertainties on the quoted values and details on the definition of quark and neutrino masses. Note that the neutrino mass values refer to the mass rather than the flavour eigenstates.

2.2. Production and Decay of Top Quarks in the Standard Model

In the SM, top quarks can be produced both via the strong and the EW interaction; their decay into lighter particles is governed by the weak interaction. A comprehensive summary of the phenomenology of the top quark, which goes beyond the aspects discussed in this section can be found in [52].

[5] Recently, the LHCb collaboration at the LHC reported the observation of resonances consistent with *pentaquark* states [55]. A pentaquark is a quark bound state consisting of four quarks and one antiquark.

2.2.1. Pair Production of Top Quarks

Production via the strong interaction is the dominant SM production mechanism for top quarks at hadron colliders like the LHC. The strong interaction conserves quark flavour, hence a top quark can only be produced together with its antiquark. The production of top-antitop ($t\bar{t}$) pairs constitutes the main background process in the search for BSM resonances decaying to $t\bar{t}$ that is presented in this thesis. As discussed in Chapter 5, it constitutes an *irreducible* background, implying that a data-driven estimation of this background process from signal-depleted control regions enriched in SM $t\bar{t}$ events is not possible. The estimation of this background process in the signal regions therefore relies entirely on Monte Carlo simulations (Section 3.4.2). A precise understanding, calculation and modelling of this process is therefore of the utmost importance.

The process of top-quark pair production from a proton-proton (pp) initial state is determined by two components: the **hard-scattering process** between two partons i and j, one from each proton, which is characterised by the momentum transfer scale Q that is large enough for the process to be described by perturbative QCD; and the **parton distribution functions (PDFs)** of the proton, $f_i(x, Q^2)$, which quantify the probability of finding a parton of type i carrying a fraction x of the longitudinal momentum of a proton that is probed at a momentum scale Q. In the calculation of quantities such as the production cross-section these components can be treated separately. The separation or *factorisation* of processes mediated by the strong interaction into a *process dependent*, short-distance component and a *universal, process independent* component, that is determined by long-distance behaviour, is a fundamental property of QCD.[6] The former component can be calculated perturbatively while the latter is not computable in perturbative QCD and needs to be determined in separate measurements (see below).

The cross-section for top-quark pair production is then derived as the convolution of the partonic cross-sections $\hat{\sigma}_{i,j}$ of the hard-scattering process with the corresponding parton luminosities $\mathcal{L}_{i,j}$:

$$\sigma_{pp\to t\bar{t}X}(s, m_{\text{top}}) = \sum_{i,j} \int_{(2m_{\text{top}})^2}^{s} d\tilde{s}\ \ \mathcal{L}_{i,j}(\tilde{s}, s, \mu_f)\ \hat{\sigma}_{i,j}(\tilde{s}, m_{\text{top}}, \alpha_s(\mu_r), \mu_f), \tag{2.9}$$

where the parton luminosities are determined by the PDFs as follows:

$$\mathcal{L}_{i,j}(\tilde{s}, s, \mu_f) = \frac{1}{s} \int_{\tilde{s}}^{s} \frac{d\hat{s}}{\hat{s}} f_{i,p}(\frac{\hat{s}}{s}, \mu_f) f_{j,p}(\frac{\tilde{s}}{\hat{s}}, \mu_f). \tag{2.10}$$

[6] An overview of QCD factorisation theorems and discussion of their relevance for perturbative QCD can be found in [56].

In these equations, taken from [57],[7] m_{top} is the top-quark mass evaluated in the pole-mass scheme,[8] $s = E_{cm}^2$ is the centre-of-mass energy squared of the two protons, $\hat{s} = x_i x_j s$ is the centre-of-mass energy squared of the two initial-state partons (with momentum fractions x_i and x_j, respectively) of the hard-scattering process that leads to the $t\bar{t}X$ final state. Finally, μ_r and μ_f are the renormalisation[9] and factorisation[10] scales, respectively. While the choice of the values of these (unphysical) QCD scales is, in principle, arbitrary and can be made independently for the two scales, it is convenient to choose the values such that they are close to the typical momentum and mass scale(s) of the process of interest in order to minimise the impact of terms in the perturbative calculations of the cross-section that scale logarithmically with Q/μ_r or μ_r/μ_f. Hence $\mu_r = \mu_f = Q$ is a common choice. Furthermore, in calculations of the $t\bar{t}$ production cross-section, a natural choice of the momentum transfer scale is $Q = m_{\text{top}}$ where the top-quark mass is set to 172.5 GeV, such that $\mu_r = \mu_f = 172.5$ GeV [59]. The arbitrariness of this choice is taken into account as a systematic uncertainty on the cross-section by varying the two scales independently by factors of 0.5 and 2 from their default value. Details are given in Section 5.6.3.

The partonic cross-section can be expanded perturbatively in powers of α_s [57]:

$$\hat{\sigma}_{i,j} = a_s^2\, \hat{\sigma}_{i,j}^{(0)}(s, m_{\text{top}}) + a_s^3\, \hat{\sigma}_{i,j}^{(1)}(s, m_{\text{top}}, \mu_r, \mu_f) + a_s^4\, \hat{\sigma}_{i,j}^{(2)}(s, m_{\text{top}}, \mu_r, \mu_f) + \mathcal{O}(a_s^5), \qquad (2.11)$$

where $a_s = \alpha_s/\pi$. The Feynman diagrams for top-quark pair production at **leading order (LO)** in α_s, that is for processes whose cross-section is proportional to α_s^2 (first term in Equation 2.11), are shown in Figure 2.1. At this order, only the gg and $q\bar{q}$ parton initial states contribute and all diagrams represent $2 \to 2$ processes with two partons in the initial and two in the final state. Starting from **next-to-leading order (NLO)**, there are also contributions from $2 \to 3$ processes and from gq and $g\bar{q}$ initial states.

The total cross-section $\sigma_{pp\to t\bar{t}X}(s, m_{\text{top}})$ can then be calculated (perturbatively) at a fixed order in α_s if the PDFs are known. The universality of these long-distance functions allows for them to

[7] Some variable names in these and the following equations have been changed to match the variable naming conventions in this thesis.

[8] The pole mass of the top quark is defined as the real part of the pole in the propagator of the top quark. The concept of the top-quark pole mass is discussed in detail in [58].

[9] The renormalisation scale is the scale introduced in renormalisable quantum field theories such as QCD to separate ultra-violet divergent from finite terms in the calculation of physical quantities, a process referred to as *regularisation*. For details see, for example, [47].

[10] The factorisation scale determines the separation between long-distance and short-distance processes in the factorisation of the cross-section.

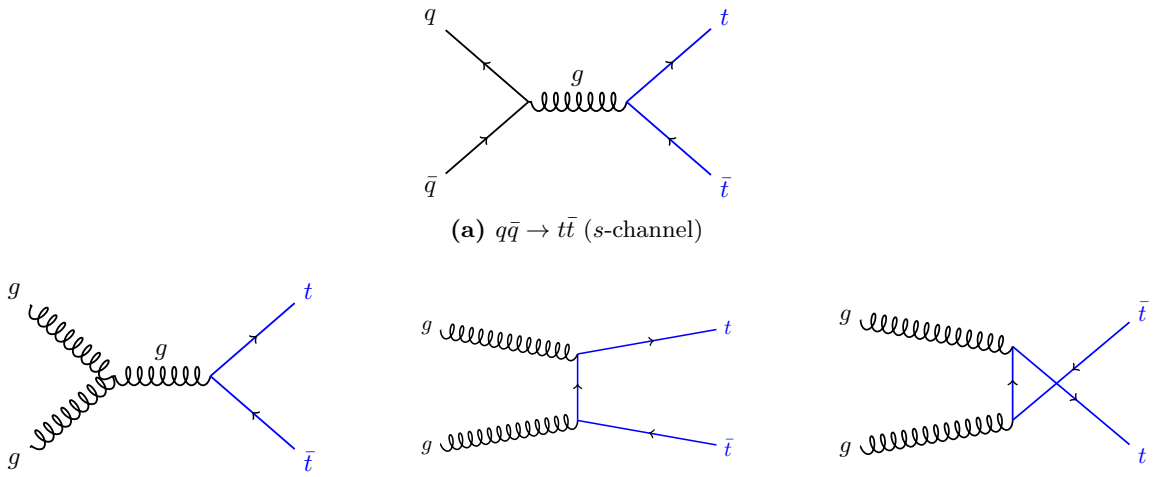

(a) $q\bar{q} \to t\bar{t}$ (s-channel)

(b) $gg \to t\bar{t}$ (s-channel)

(c) $gg \to t\bar{t}$ (t-channel)

(d) $gg \to t\bar{t}$ (u-channel)

Figure 2.1.: Representative Feynman diagrams for the production of $t\bar{t}$ pairs at LO in α_s ($2 \to 2$ processes).[11]

be determined in separate measurements and used in the calculation of a multitude of hadronic processes. A precise knowledge of the proton PDFs is essential for precision measurements in pp collisions. It also plays an important role in many BSM physics searches, including the one presented in this thesis, which rely on an accurate knowledge of the cross-section of the dominant background process(es).

PDFs are obtained by first choosing a parameterisation at a low momentum scale Q_0^2. The parameters are then determined by fitting a number of observables to a given experimental dataset, which covers a certain kinematic range in x and Q^2. Finally, the PDFs are evolved from the initial scale Q_0^2 to higher values of Q^2 using the (perturbative) DGLAP evolution equations [61, 62, 63]. For further details on this procedure see [64]. Typical input datasets include Deep Inelastic Scattering (DIS) data from the HERA ep-collider at DESY, Germany, and from fixed-target experiments. Additional measurements from the Tevatron and, more recently, the LHC experiments have extended the kinematic reach of the PDF fits to higher values of x and constraints on the PDFs are expected to improve further as more LHC data becomes available.[12]

A number of different collaborations derive PDF sets which differ in various aspects such as the choice of input datasets, the assumptions made in the parameterisation of the PDFs, the treatment of heavy quark flavours or their associated uncertainties. An overview of the different

[11] All Feynman diagrams in this and the following sections have been produced by the author and were first published in [60].

[12] For a recent review of the status and prospects of PDFs at the beginning of Run 2 of the LHC see [65].

collaborations and their approaches can be found in [66]. A possible bias from the choice of the PDF set used in the calculation of the $t\bar{t}$ cross-section is taken into account as a systematic uncertainty on the cross-section, together with the uncertainties associated with a specific PDF set. Details are given in Section 5.6.4.

The PDFs of the proton and the corresponding parton luminosities for the gg and $q\bar{q}$ initial states at $\sqrt{s} = 8$ TeV are shown in Figure 2.2 for the MSTW2008NLO [67] PDF set, which is one of the PDF sets used in this thesis. A comparison of the PDFs of the different quark flavours in Figure 2.2a shows that the probability of finding a u- or a d-quark is significantly higher than that of finding the corresponding antiquark, especially for $x > 0.1$. This is a consequence of the u- and d-valence quark contributions and the fact that the respective antiquarks only contribute as "sea" quarks. For $x < 0.1$, the PDF of the gluon dominates over those of the individual quarks. This has significant consequences for the production of $t\bar{t}$ pairs in pp collisions as can be seen from the following consideration: The threshold condition for the partonic centre-of-mass energy that is required for the production of a $t\bar{t}$ pair is

$$(2m_{\text{top}})^2 \leq \hat{s}. \tag{2.12}$$

For central production, $x_i = x_j \equiv x$, this yields a momentum fraction $x \geq 2m_{\text{top}}/\sqrt{s} \approx 0.043$ for the initial-state partons at $\sqrt{s} = 8$ TeV. For x-values in this regime, the PDF of the gluon is more than a factor of ten larger than the PDFs of the $\bar{u}$- and $\bar{d}$-quarks, respectively, implying that a gg initial state is significantly more likely than a $q\bar{q}$ initial state. This is also reflected in the corresponding parton-luminosity distributions in Figure 2.2b which differ by a factor of 10 around $M_X = 2m_{\text{top}}$.

The search presented in this thesis relies on the most precise calculation of the $t\bar{t}$ production cross-section available to date. It has been performed with the Top++ 2.0 [70] software following the recommendations described in [59]. The cross-section has been calculated at exact NNLO accuracy in the strong coupling constant α_s, including the resummation of next-to-next-to-leading logarithmic (NNLL) soft gluon terms[13] as derived in [72, 73] and references therein.

[13] The emission of soft gluons with momenta above some cut-off scale μ_{cut}, which is considerably smaller than the momentum scale Q of the hard process, leads to non-negligible corrections to the perturbative cross-section which scale like $\ln(\mu_{\text{cut}}/Q)$. These corrections are determined by a resummation procedure. An introduction to the principle of soft gluon resummation can, for example, be found in [71].

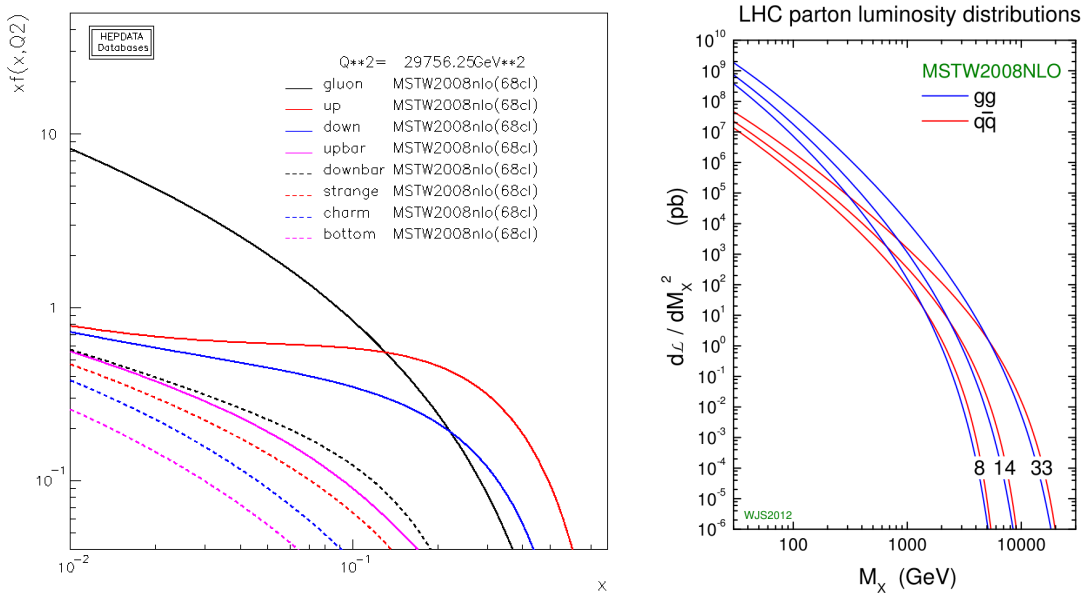

(a) Proton PDFs **(b)** Parton luminosities

Figure 2.2.: (a) Parton distribution functions of the proton at momentum scale $Q^2 = m_{\text{top}}^2$ as used in the calculation of the $t\bar{t}$ production cross-section. The quantity $xf^{\alpha}(x, Q^2)$ is plotted as a function of the parton momentum fraction x for $\alpha \in \{g, u, d, \bar{u}, \bar{d}, s, c\}$. Produced courtesy of [68]. (b) Parton luminosity distributions of the proton for the gg and $q\bar{q}$ initial states as a function of the mass M_X of the intermediate state at $\sqrt{s} = 8$ TeV, $\sqrt{s} = 14$ TeV and $\sqrt{s} = 33$ TeV [69]. The MSTW2008NLO PDF set is used in both cases.

The resulting value for the SM $t\bar{t}$ cross-section is [59]:

$$\sigma_{pp\to t\bar{t}X}(s, m_{\text{top}}) = 252.89\ {}^{+6.39}_{-8.64}(\text{scale})\ {}^{+7.58}_{-7.33}(m_{\text{top}})\ {}^{+11.67}_{-11.67}(\text{PDF} + \alpha_s)\ \text{pb}, \tag{2.13}$$

where $\sqrt{s} = 8$ TeV and $m_{\text{top}} = 172.5$ GeV, which is the value that is used in the generation of the nominal MC sample for SM $t\bar{t}$ production (Section 3.4.2). The derivation of the uncertainties is described in Section 5.6.3. The calculated value in Equation 2.13 is consistent with recent measurements of the inclusive $t\bar{t}$ production cross-section by the ATLAS [74, 75] and CMS [76, 77] experiments at $\sqrt{s} = 8$ TeV.

2.2.2. Production of Single Top Quarks

The production of single top quarks is possible only via the weak interaction. At leading order, three production modes exist: s- and t-channel production and production in association with a W-boson (Wt-channel). The corresponding Feynman diagrams are shown in Figure 2.3. The dominant production mode at the LHC is t-channel production, followed by associated production with a W-boson [52]. The cross-sections for these processes, which are summarised in

Table 3.5 in Section 3.4.2, are one to two orders of magnitude smaller than that for top pair production and the contribution of single top-quark production to the SM background in the signal regions[14] of the search presented in this thesis is small, but not negligible.

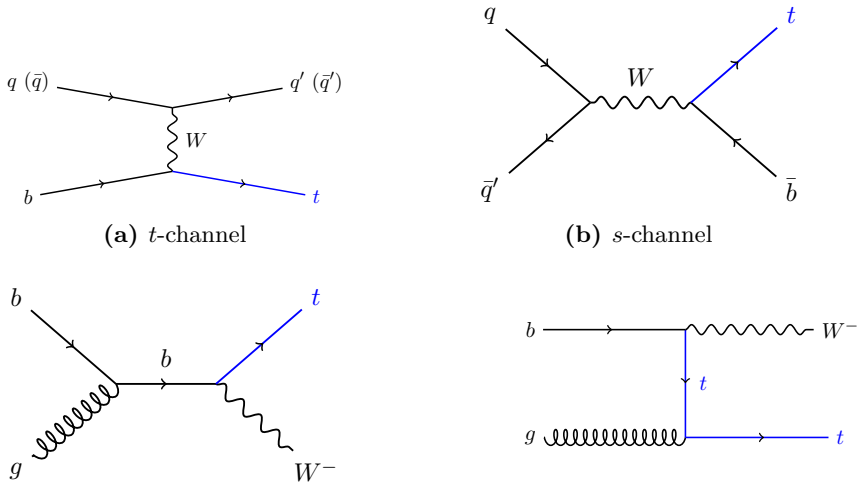

Figure 2.3.: Representative Feynman diagrams for single-top production at LO. (a) s-channel, (b) t-channel, (c) associated production with a W-boson (Wt-channel).

2.2.3. Top-Quark Decay

Top quarks decay via the weak interaction only. Their large mass[15] of $173.34 \pm 0.27(\text{stat}) \pm 0.71(\text{syst})$ GeV allows for them to decay into a real W-boson and any of the three known down-type quarks. The branching ratios for these three possible two-body decays, $t \to Wb$, $t \to Ws$ and $t \to Wd$,[16] depend on the CKM-matrix elements V_{tb}, V_{ts} and V_{td}, respectively. Given that $|V_{tb}| \gg |V_{ts}|, |V_{td}|$ with $|V_{tb}|$ close to unity [52], the decay mode $t \to Wb$ dominates.

The decay width of the top quark at NLO for the decay $t \to Wb$ as predicted in the SM is [52]

$$\Gamma_{\text{top}} = \frac{G_F m_{\text{top}}^3}{8\pi\sqrt{2}} |V_{tb}|^2 \left(1 - \frac{m_W^2}{m_{\text{top}}^2}\right) \left(1 + 2\frac{m_W^2}{m_{\text{top}}^2}\right) \left[1 - \frac{2\alpha_s}{3\pi}\left(\frac{2\pi^2}{3} - \frac{5}{2}\right)\right], \tag{2.14}$$

where terms of order m_b^2/m_{top}^2, α_s^2 and $(\alpha_s/\pi)m_W^2/m_{\text{top}}^2$ are neglected; m_{top} is the pole mass of the top quark; m_W denotes the W-boson mass; α_s is the strong coupling constant; and $G_F = 1.1663787(6) \cdot 10^5$ GeV^{-2} denotes the Fermi constant of the weak interaction [52]. The decay width is proportional to the third power of the top-quark mass, implying that the large

[14] This term is introduced at the beginning of Chapter 5.
[15] The mass value quoted here is obtained from the first combination of measurements conducted by the CDF and DØ experiments at the Tevatron collider and the ATLAS and CMS experiments at the LHC [34].
[16] This notation refers to the process $t \to W^+b$ as well as its charge-conjugated counterpart $\bar{t} \to W^-\bar{b}$.

value of m_{top} results in a correspondingly large decay width: For $m_{\text{top}} = 173.34$ GeV and $\alpha_s(m_Z) = 0.118$, Equation 2.14 yields $\Gamma_{\text{top}} = 1.35$ GeV, which corresponds to a lifetime $\tau_{\text{top}} = 1/\Gamma_{\text{top}} \simeq 0.5 \cdot 10^{-24}$ s. This decay width is significantly larger than the QCD scale $\Lambda_{\text{QCD}} \approx 200$ MeV, which can be interpreted as the scale at which the (perturbatively defined) coupling $\alpha_s(Q)$ becomes large and below which hadronisation occurs. For a more detailed discussion of the definition and determination of Λ_{QCD} see [78] and references therein. The top quark is therefore unique among all quarks in that it decays before top-flavoured bound states, such as $t\bar{t}$ quarkonium, are formed. As a result, properties such as its spin or polarisation are conserved and can be measured in the top-quark decay products. While this fact is not explicitly used in the resonance search presented in this thesis, it is exploited in measurements of the spin correlation of the top quarks in $t\bar{t}$ events [79, 80] as well as measurements of the W-boson helicity in top-quark decays [81, 82], which serve as precision tests of SM predictions and provide constraints on BSM physics scenarios. Importantly, this property could also be exploited, in the case that a new, heavy resonance decaying to $t\bar{t}$ pairs was discovered, to determine the spin and couplings of this resonance, as has been shown in [83].

The W-boson from the top-quark decay can decay either hadronically into a pair of an up-type quark and a down-type antiquark (and vice versa in the charge-conjugated case), $W \to q'\bar{q}$, or leptonically into a charged lepton ℓ and its corresponding neutrino ν_ℓ, $W \to \ell\nu_\ell$, where $\ell = e, \mu$ or τ. The branching ratios for the two decay modes can be estimated from the magnitudes (squared) of the CKM matrix elements (Equation 2.5) for the kinematically allowed hadronic final states, namely $u\bar{d}$, $u\bar{s}$, $u\bar{b}$, $c\bar{u}$, $c\bar{s}$, $c\bar{b}$ in the case of a W^+-boson decay,[17] and the fact that each quark carries one of three colour charges, which results in an enhancement of the branching ratios for hadronic final states by a factor of three compared to that for leptonic final states. Assuming lepton universality[18] and neglecting the masses of the final state particles, which are significantly smaller than m_W (Table 2.1), the branching ratios for the hadronic and leptonic decay modes are predicted to be roughly $2/3 \approx 67\%$ and $1/3 \approx 33\%$, respectively. The probability for a W-boson decay to yield a particular lepton flavour is predicted to be $\approx 11\%$. These numbers agree well with the values measured experimentally [52].

The possible final states of a $t\bar{t}$ decay can be divided into three categories, based on the decay

[17] In the case of W^--bosons these are replaced by the charge-conjugated states.

[18] Lepton universality – the assumption that the couplings between leptons and the weak gauge bosons are independent of the lepton generation – is a key premise in the SM. This assumption has been challenged by recent (as of September 2015) results from the LHCb collaboration at the LHC [84].

modes of the two W-bosons from the top-quark decays:

- **Fully hadronic** (or all-jets) mode: both W-bosons decay hadronically,
- **Lepton+jets** (or ℓ+jets) mode: one W-boson decays hadronically, the other W-boson decays leptonically,
- **Dilepton** mode: both W-bosons decay leptonically.

The branching ratios for the three decay modes, derived from the branching ratios for the W-boson decay modes, are summarised in Table 2.2 along with details on the respective final states. The fully hadronic and lepton+jets modes dominate over the dilepton mode.

Decay mode	Final state	BR
Fully hadronic	$t\bar{t} \to (W^+b)(W^-\bar{b}) \to (q'\bar{q}b)(q'''\bar{q}''\bar{b})$	45.7%
Lepton+jets	$t\bar{t} \to (W^+b)(W^-\bar{b}) \to (\ell^+\nu_\ell b)(q'''\bar{q}''\bar{b})$ or $(q'\bar{q}b)(\ell^-\bar{\nu_\ell}\bar{b})$	43.8%
Dilepton	$t\bar{t} \to (W^+b)(W^-\bar{b}) \to (\ell^+\nu_\ell b)(\ell^-\bar{\nu_\ell}\bar{b})$	10.5%

Table 2.2.: The three $t\bar{t}$ decay modes and their relative contributions. Numbers taken from [52].

The above classification of W-boson decays with a τ-lepton in the final state as leptonic is impractical from the experimental viewpoint: While electrons and muons yield detector signatures that can be comparatively clearly identified, the identification of τ-leptons is more challenging because the large τ-lepton mass of 1.77682 ± 0.00016 GeV and resultingly short decay length $c\tau = 87.11\ \mu m$ [52] prevent τ-leptons from being measured directly in the detector and the reconstruction from their decay products is more complicated due to the complex nature of the τ-lepton decay, $\tau \to W + \nu_\tau$, which results in at least one additional neutrino, and, in roughly two thirds of all cases, in additional hadronic jets. Analyses involving hadronically decaying τ-leptons therefore require special reconstruction and identification algorithms. Events with top quark decays involving hadronically decaying τ-leptons are therefore not considered in the search presented in this thesis. Those involving leptonically decaying τ-leptons, however, are implicitly included in the ℓ+jets final state as their detector signatures are hard to distinguish from top-quark decays in which the W-boson decays directly into an electron or muon. The branching ratios for the lepton+jets and dilepton decay modes with electrons or muons in the final state (including those from leptonically decaying τ-leptons) are $\simeq 34\%$ and $\simeq 7\%$, respectively [52].

2.3. Motivation for Theories Beyond the Standard Model

Despite its undisputable successes in predicting the existence of new elementary particles, like the top quark and the Higgs boson, and describing many particle properties and processes with an accuracy at the sub per mille level, the SM is widely considered an incomplete theory for a number of reasons.

For one, as mentioned above, it does not include the **gravitational force**, which shapes the large structures of the universe. It also fails to explain key cosmological observations, such as the observed imbalance between baryonic matter and antimatter in the universe. Assuming that equal amounts of matter and antimatter were created in the Big Bang, there must be processes capable of generating an excess of baryons over antibaryons. A necessary condition for the occurrence of **baryogenesis** is the existence of CP-violating processes, as pointed out by A. Sakharov in 1967 [85]. While the CKM matrix of the SM model contains a CP violating phase (Section 2.1), its effect is deemed too small to explain the observed imbalance [86]. The PMNS matrix (Section 2.1) also includes a CP violating phase. However, its value is not known to date. The measurement of this phase will be one of the main goals of neutrino experiments over the next years.

Cosmological observations also suggest that ordinary matter, which is made up of the particles described in the SM, accounts for only around 15% of the matter content of the universe, while the remaining 85% of matter, the **Dark Matter** (DM), is of a yet unknown nature [52]. Evidence for DM, which is "non-luminous and non-absorbing" [52] but has observable gravitional effects, comes from a variety of sources, such as observations of galactic rotation curves [87] and gravitational lensing [88], as well as precision measurements of the power spectrum of the cosmic microwave background (CMB) radiation [89]. While the SM neutrinos have long been considered viable candidates for DM, current constraints on the neutrino relic density, derived from the upper limits on the neutrino masses from direct measurements [52] as well as CMB precision measurements [89], and the fact that neutrinos are relativistic particles, disfavour them as DM candidates [90]. It is widely believed that BSM physics is required to explain the nature and origin of DM.

There are also a number of intrinsic reasons, related to the SM itself, that motivate searches for BSM physics. For one, the SM contains a number of **free parameters**, the values of which are not predicted in the SM and can only be determined in measurements. These include the

twelve fermion masses, the parameters of the CKM and PMNS matrices, the electromagnetic, strong and weak coupling constants and the Higgs boson mass. These free parameters suggest that the SM may be embedded in a more fundamental "Theory of Everything", in which the values of these parameters can be derived from first principles. Moreover, a more fundamental theory might also provide an explanation for the existence of three generations of fermions in the SM, as well as the large observed differences in the strength of the Yukawa couplings of the SM fermions to the Higgs field. These differ by several orders of magnitude, as illustrated in Figure 2.4. The SM provides no explanation for these large discrepancies.

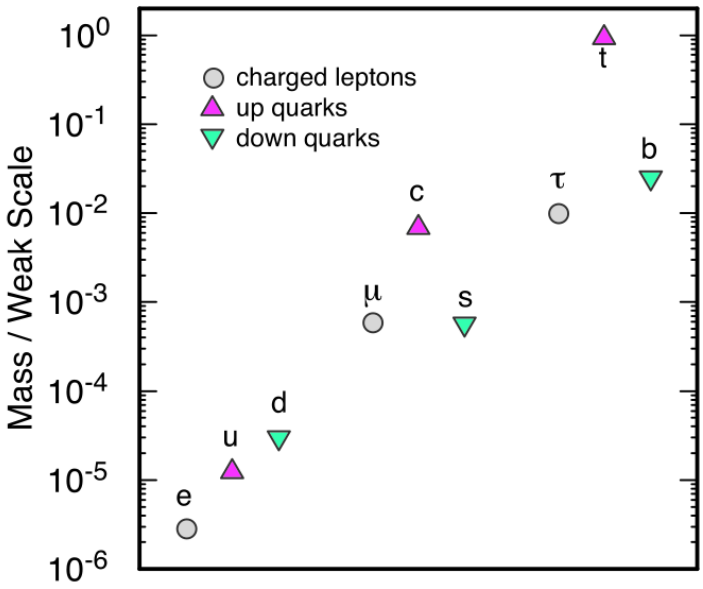

Figure 2.4.: Yukawa couplings $\zeta_f = \frac{\sqrt{2}\, m_f}{v}$ of quarks and charged leptons in the SM. Taken from [91].

Another central problem of the SM with regard to particle masses concerns the mass of the Higgs boson itself. Unlike the masses of the fermions and vector bosons, the physical mass of this elementary scalar is not protected against divergent contributions from virtual particle loops. Assuming the SM is valid up to the Planck scale, $M_{Pl} \sim 10^{19}$ GeV [52], at which quantum effects of gravity are expected to become relevant, the loop corrections to the Higgs boson mass are expected to be comparable to M_{Pl}, and an extreme fine-tuning of the value of the bare Higgs mass is required to obtain the observed, physical Higgs mass, $m_h \approx 126$ GeV. Many BSM theories have been proposed as solutions to this **hierarchy problem**. These theories typically involve modifications to SM processes at the TeV scale to allow for a *natural* explanation of the measured Higgs boson mass, and therefore offer predictions that are testable at the LHC. Notably, many of these theories predict the existence of new particles with masses in the TeV

regime. The top quark may play a key role in both direct and indirect searches for BSM phenomena.

2.4. The Role of the Top Quark in the SM and its Extensions

The top quark stands out among all SM fermions due to its large mass, which is several orders of magnitude greater than that of the lightest quarks, the up and down quarks, which make up the protons and neutrons in atomic nuclei. In particular, its mass is close to the vacuum expectation value v of the Higgs field, resulting in a close to unitary Yukawa coupling strength ζ_{top} (Equation 2.6 and Figure 2.4).

Loop contributions to the Higgs boson propagator involving top quarks therefore represent the largest contribution to the quantum loop corrections to the Higgs boson mass in the SM, implying that the top quark may play a special role with regard to the hierarchy problem and BSM physics. In particular, precision measurements of the masses of the top quark and the W boson allowed experiments to place constraints on the mass of the Higgs boson, even before its discovery [92]. Precision measurements of m_{top} [34], along with precision measurements of m_W [93] and m_h [35], remain key tests of the SM predictions.

The top quark propagator and couplings themselves may be sensitive to the presence of heavier, as yet undiscovered BSM particles. **Precision measurements** of top-quark properties can therefore be regarded as **indirect searches** for BSM physics. To date, the results of almost all precision measurements of top-quark properties have been found to be in agreement with the SM predictions. The only notable exception is the **forward-background asymmetry** (A_{FB}) in the production of $t\bar{t}$ pairs in $p\bar{p}$ collisions at the Tevatron, where the rate of top quarks found in the hemisphere defined by the direction of the proton beam is larger than that of top quarks found in the opposite hemisphere. Such an asymmetry arises within the SM at NLO in QCD, see for example [52] and references therein. Various measurements conducted by the CDF and DØ collaborations have found this asymmetry to be larger than the calculated value, with the discrepancies amounting to 2-3 standard deviations (σ) [94, 95]. These results have fuelled speculations about the existence of BSM processes at the TeV scale that would lead to an enhancement of A_{FB} compared to the SM predictions. An extensive summary of BSM models proposed in response to the Tevatron measurements, and an overview of related asymmetry measurements at the LHC can be found in [96]. However, more recent calculations of A_{FB} that include NNLO corrections in QCD, have found its value to be 27% larger than the value obtained

from previous NLO calculations [97]. The new value agrees with the latest DØ measurement [98] and is within 1.5 σ from the value obtained by CDF [94].

The unprecedent energy range accessible at the LHC may allow for the direct production of BSM particles in the collisions. Many BSM models, in particular those proposed in response to the hierarchy problem, predict massive resonances with large couplings to top quarks that preferentially decay to $t\bar{t}$ pairs. Direct searches for BSM particles in $t\bar{t}$ final states are therefore a key component of the physics programmes of the ATLAS and CMS experiments at the LHC. In the following sections, a number of benchmark models that predict massive resonances decaying to $t\bar{t}$ pairs are described.

2.5. Benchmark Models

Four different benchmark models, which are introduced in the following, are considered in the search presented in this thesis. The types of resonances they predict differ in various properties such as their width and spin. In each case, a number of different resonance mass points in the range 0.4 - 3.0 TeV are studied. Details on the chosen mass points, the corresponding widths and production cross-sections as well as the simulation of the signal processes are given in Section 3.4.1. A comparison of the kinematic properties of the resonances predicted by the different benchmark models is given in Appendix A.

2.5.1. Benchmark Model 1: Spin-1 Colour-Singlet

The first type of resonance under consideration is a spin-1 colour-singlet vector boson, the Z'_{TC2} (referred to as Z' in the following), which is predicted by topcolor-assisted technicolor (TC2) models [99, 100, 101]. The relative width Γ/m of the Z' resonances studied in this thesis is 1.2% for all mass points. This is considerably smaller than the experimental resolution of the (reconstructed) $t\bar{t}$ invariant mass which is found to be 6-8% for the resonance models considered in this search (Section 5.4.4). The Z' boson thus serves as an example of a *narrow* resonance.

Topcolor-assisted technicolor models are extensions of the class of BSM theories collectively referred to as *technicolor*. Originally proposed by S. Weinberg [102] and L. Susskind [103], technicolor introduces new gauge interactions to explain EWSB without postulating elementary scalar particles, thus avoiding the hierarchy problem associated with the Higgs boson. The new gauge interactions, modelled closely on QCD in early models, act on massless "technifermions", exhibiting asymptotic freedom at large energies and confinement close to the EW scale. EWSB

occurs *naturally*, analoguous to the spontaneous breaking of chiral symmetry in QCD [49].

Extensions of technicolor are needed to explain the masses of quarks and leptons which are massless in the original theory. In topcolor-assisted technicolor models, this is achieved through the introduction of a $t\bar{t}$ *condensate* in which the top quark and its antiquark form a bound state, analoguous to Cooper pairs in BCS superconductors [104], that acts effectively like a Higgs boson [105]. The Z' boson constitutes an important component of topcolor models that is required to enhance the formation of the $t\bar{t}$ condensate while suppressing that of a $b\bar{b}$ condensate, thus ensuring that the b-quark is light and the top quark is heavy. In [100] four Z' models consistent with these requirements are defined.

The Z' boson used as a benchmark model in this thesis is a leptophobic boson that couples only to the first and third quark generation of the SM. It is defined by Model IV in Section 3(B) of [100]. This model contains three parameters that control the properties of the Z': f_1 and f_2 define the couplings to up- and down-type quarks, respectively, and $\cot\theta_H$ controls the production cross-section and width. The settings $f_1 = 1$ and $f_2 = 0$ are chosen for all mass points to maximise the branching fraction to $t\bar{t}$, which is 33% for $m_{Z'} > 800$ GeV [2], while $\cot\theta_H$ is tuned for each mass point to achieve a relative width of 1.2% over the whole mass range. The corresponding cross-sections for the different mass points used in this search are derived in [101] and summarised in Table 3.1.

The discovery of a new boson in 2012, with properties that have been found to be consistent with those of the Higgs boson in subsequent measurements, disfavours a wide range of technicolor models as an explanation for EWSB, although it has subsequently been demonstrated that a subset of models of type *walking technicolor*,[19] are able to accommodate a scalar boson with properties consistent with those measured at the LHC, if the new boson is interpreted as a composite particle, see for example [107] and [108]. The use of the TC2-type Z' boson as a benchmark models in this search, however, is motivated by arguments independent of the validity of technicolor models: The fact that the Z' is a narrow resonance with a relative width well below the experimental resolution implies that the derived upper limits on its production cross-section times branching ratio to $t\bar{t}$ are valid for all other models with spin-1 narrow resonances decaying to $t\bar{t}$. Moreover, this particular benchmark model has already been studied in previous ATLAS searches and in searches conducted by other experiments. The choice of this benchmark model thus provides a certain consistency and allows for direct comparisons with previous results.

[19] A pedagogical introduction to the concept of walking technicolor can be found in part II of [106].

Upper limits on the production cross-section times branching ratio of the TC2-type Z' boson have been set by the CDF [36, 37] and DØ [38] collaborations using $\sqrt{s} = 1.96$ TeV data from $p\bar{p}$ collision at the Tevatron. Further constraints have been derived by both the ATLAS [39, 40] and CMS [42, 43, 44] collaborations using a dataset with an integrated luminosity of 4.7 fb^{-1} collected in pp collisions at $\sqrt{s} = 7$ TeV at the LHC. The strongest constraint on the allowed mass range for a TC2-type Z' resonance with a width of 1.2% stems from a search conducted by the CMS collaboration in 19.7 fb^{-1} of $\sqrt{s} = 8$ TeV LHC data [45], combining all three $t\bar{t}$ decay channels, which excludes resonance masses below 2.4 TeV at 95% confidence level.[20]

2.5.2. Benchmark Model 2: Spin-1 Colour-Octet

The second benchmark model that is studied in the search presented in this thesis is the bulk Kaluza-Klein gluon (KK gluon or g_{KK}) predicted by certain Randall-Sundrum (RS) scenarios of warped extra dimensions [109]. It serves as an example of the resonant production of a spin-1 colour-octet vector boson. Unlike the Z' boson, it has a resonance width that is larger than the experimental resolution. It is therefore classified as a *broad resonance*. In the search presented here, a nominal width $\Gamma/m = 15.3\%$ is chosen. In addition, the width is varied between 10% and 40% for the 1.0, 2.0 and 3.0 TeV mass points to study its impact on the upper limits on the production cross-section.

Models predicting additional spacetime dimensions have been proposed to explain the hierarchy between the EW scale, $v \sim 10^2$ GeV, and Planck scale, $M_{Pl} \sim 10^{19}$ GeV. The original idea, also known as the *ADD model*, was formulated in 1998 by N. Arkani-Hamed, S. Dimopoulos and G. Dvali as an alternative to technicolor and supersymmetry [110, 111]. It is based on the fact that M_{Pl} is inferred only through measurements of the gravitational force at distances $\gg M_{Pl}^{-1}$ while the EW interactions have been probed at distances $\mathcal{O}(v^{-1})$ and below. Modifications of the gravitational constant (and hence the Planck scale) at distances smaller than the ones probed by experiments are therefore possible. If there are n compact extra spatial dimensions of toroidal shape defined by radius parameter R, in addition to the four known spacetime dimensions, the (3+1)-dimensional Planck scale, M_{Pl}, measured at distances $r \gg R$ arises as an effective scale from the Planck scale $M_{Pl(4+n)}$ in $n+4$ dimensions:

$$M_{Pl}^2 \sim M_{Pl(4+n)}^{2+n} R^n, \tag{2.15}$$

[20] In the same analysis, upper limits are derived on a TC2-type Z' with a larger width of 10% which is excluded for masses below 2.9 TeV. Note that this alternative model has a width larger than the experimental resolution and hence does not qualify as a narrow resonance.

where $M_{Pl(4+n)} \sim v$. Hence the EW scale becomes the only fundamental short-distance scale of nature. In the ADD model, only the gravitational fields can propagate in the full higher-dimensional volume, the *bulk*, while the SM fields are confined to a (3+1)-dimensional subspace or *brane*. The requirement that the radius R must be smaller than the distances at which the gravitational force has been measured by experiments leads to the exclusion of the case $n = 1$ for which the requirement $M_{Pl(4+n)} \sim v$ yields $R \sim 10^{11}$ m. The case $n \geq 2$ yields values of R as large as ~ 1 mm; however, subsequent experiments, which have probed the gravitational interaction in the submillimetre range, constrain the size of the extra dimensions to $R < 37$ μm for $n = 2$ [52]. Further constraints on the size, shape and number of extra dimensions in the ADD model stem from astrophysical observations and searches at colliders such as the Tevatron and the LHC [52].

The Randall-Sundrum scenario of *warped* extra dimensions was proposed by L. Randall and R. Sundrum in 1999 [112, 113] in response to a problem of the ADD model: the hierarchy between v and the Planck scale is eliminated at the cost of introducing a new hierarchy, namely that between v and the significantly smaller compactification scale $\mu_c = 1/R$. The RS scenario relies on a single extra dimension of size r_c and curvature k and uses a non-factorisable (4+1)-dimensional spacetime metric:

$$ds^2 = e^{-2kr_c\phi}\eta_{\mu\nu}dx^\mu dx^\nu + r_c^2 d\phi^2, \tag{2.16}$$

where x^μ are the usual (3+1)-dimensional spacetime coordinate and $0 \leq \phi \leq \pi$ is the coordinate of the warped extra dimension.[21] The exponential function in this metric allows for the large observed hierarchy between v and M_{Pl} to be generated from values of r_c that are considerably smaller than those typically assumed for the radius R in the ADD model. This has the dual advantage of avoiding the hierarchy problem of the ADD model while postulating only a single extra dimension of a size compatible with current experimental constraints.

The class of RS models which, along with its extensions, is considered in this thesis, contains two (3+1)-dimensional branes, the *TeV brane* and the *Planck brane*. Gravity originates on the Planck brane and gravitons are allowed to propagate in the bulk. In the original RS model, like in the ADD model, the SM gauge and fermion fields are confined to a single brane, the *TeV brane*.

[21] Note that ϕ can take any value between $-\pi$ and π. However, the boundary conditions imposed on the extra dimension imply that the metric is fully specified by the values of ϕ between 0 and π, as discussed in Section 2 of [112].

Subsequent research [114, 115, 116, 117, 118] has shown that modified versions of this model in which the SM gauge and fermion fields are allowed to propagate in the bulk exhibit a number of desirable features: Their predictions are in better agreement with experimental constraints on flavour-changing neutral currents; the observed differences in fermion masses can be explained with an appropriate localisation of the different fermion fields in the bulk [116, 117]; and it is possible to achieve gauge coupling unification at high energies [119].

The postulation of compact extra spatial dimensions has relevant phenomenological consequences: Particle fields propagating in the higher-dimensional bulk exhibit a discrete spectrum of mass states with identical spin and quantum numbers. These are known as **Kaluza-Klein (KK) excitations**, collectively referred to as the **Kaluza-Klein tower**.[22] The smaller the size of the compact extra dimensions, the larger the mass of the lightest KK excitation of a particle and the larger the separation between KK excitations in the mass spectrum of the KK tower. Thus, the small size of the extra dimension in the RS scenario leads to the prediction of individual resonances with masses in the TeV range, in contrast to the ADD model where the mass spectrum of the KK gravitons, the only particle states in the bulk, is quasi-continuous.

Among the KK excitations of the SM fields in the bulk, the lightest KK excitation of the gluon is the most relevant with regard to resonance searches in $t\bar{t}$ final states: it is predicted to be the most strongly coupled of the new KK states and therefore has the largest production cross-section [109], rendering it the signal process of the RS scenario that is most likely to be observed first.[23] The KK gluon studied in this thesis has a branching ratio of 92.5% for its decay to $t\bar{t}$ [109].

Upper limits on the production cross-section times branching ratio of the KK gluon described in [109] have been set by the ATLAS collaboration using 4.7 fb^{-1} of data from pp collisions at $\sqrt{s} = 7$ TeV [39]. This search excludes g_{KK} masses below 2.1 TeV at 95% confidence level. The CMS collaboration has conducted a search in 19.7 fb^{-1} of $\sqrt{s} = 8$ TeV data [45] in which limits are derived for a KK gluon based on a slightly different benchmark model [123] which predicts a larger natural width of 20% and a larger production cross-section. For this model, the CMS collaboration excludes the mass range below 2.8 TeV at 95% confidence level.

[22] The name refers to a theory developed by T. Kaluza and O. Klein who first proposed the existence of a fifth spacetime dimension in an attempt to develop a unified (quantum) field theory of gravitation and electromagnetism [120, 121, 122].

[23] The $t\bar{t}$ final state also plays a special role as the primary decay channel of the KK excitations of the other SM gauge fields. Like the fermion field of the top quark, these gauge fields are predicted to be localised close to the TeV brane to explain the mass hierarchy of the SM [109], resulting in considerable overlap of the corresponding wave functions and hence a large branching fraction for the decay to $t\bar{t}$ final states.

2.5.3. Benchmark Model 3: Spin-2 Colour-Singlet

The third benchmark model under consideration is a spin-2 colour-singlet, more specifically, a particular type of Kaluza-Klein graviton (KK graviton or G_{KK}) that is predicted by RS models in which the SM gauge and matter fields are located in the bulk [124, 125]. The search presented in this thesis is the first direct search for RS-type KK gravitons in the decay channel $G_{KK} \to t\bar{t}$.

The choice of the KK graviton as a benchmark model is motivated by three considerations. Firstly, from the experimental point of view, it provides the possibility to study the sensitivity of the search with regard to spin-2 resonances. Moreover, the fact that the resonance width is smaller than the experimental resolution allows the results to be interpreted in the context of other models with narrow spin-2 resonances. Finally, with regard to the specific case of RS models, the discovery of a resonance compatible with the properties of the KK graviton would provide strong evidence in favour of these models: While KK gluons are considered to be the KK state that is most likely to be discovered first, as explained above, the discovery of a spin-1 resonance would not conclusively establish the nature of the underlying BSM model. The discovery of a spin-2 resonance, on the other hand, would favour RS scenarios over purely four-dimensional BSM models, although even in this case additional measurements would be required to establish the exact nature of the resonance.

The set of KK gravitons predicted by RS models is characterised by two parameters: the mass of the lightest state in the KK tower, $m_{G_{KK}}$, and the dimensionsless coupling of the KK gravitons to the SM fields, $k/\bar{M}_{Pl}$, where $\bar{M}_{Pl} = M_{Pl}/\sqrt{8\pi}$ is the reduced Planck mass and k is the curvature of the warped extra dimension. Larger values of $k/\bar{M}_{Pl}$ yield a larger production cross-section as well as a larger resonance width. In RS models with SM fields in the bulk, values of $k/\bar{M}_{Pl} \sim 1$ are favoured [124]. In the search presented in this thesis, a KK graviton model with $k/\bar{M}_{Pl} = 1.0$ is used. This choice maximises the production cross-section while keeping the resonance width below the experimental resolution.

The couplings of the KK graviton to the bosons and fermions of the SM are further determined by the localisation of the SM fermion fields in the bulk. The class of KK gravitons considered in this thesis [124, 125] is predicted by a model in which the light fermion fields are localised near the Planck brane while the top-quark field is close to the TeV brane to which the Higgs field is confined, thus generating the known hierarchy of fermion masses [118]. The KK gravitons in

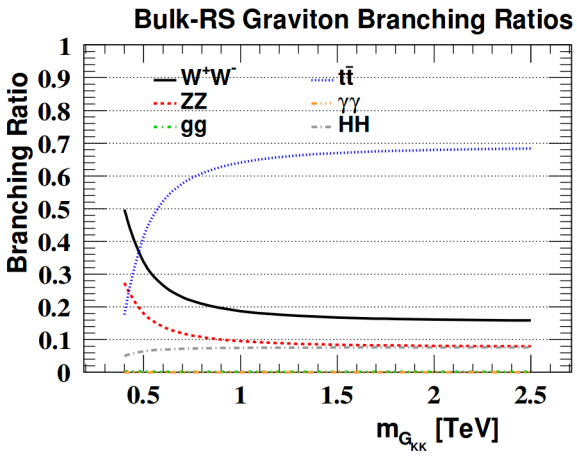

Figure 2.5.: Branching ratios for the decay of a KK graviton with coupling $k/\bar{M}_{Pl} = 1.0$ in RS models with SM gauge and matter fields in the bulk, given as a function of the graviton mass $m_{G_{KK}}$. Taken from [2].

this model are found to couple strongly to the top quark as well as, to a lesser extend, the Higgs and the SM gauge bosons but only very weakly to light quarks and leptons. This has significant consequences for the phenomenology of searches for KK gravitons at hadron colliders: Firstly, the weak coupling of the KK gravitons to light quarks implies that gluon fusion is the primary production mode for this resonance as opposed to $q\bar{q}$ annihilation.[24] Secondly, decays to leptons or photons, which would normally be the favoured search channel due to the large suppression of hadronic background processes achievable in these final states, are suppressed. The branching ratios for the decay of the KK graviton with coupling $k/\bar{M}_{Pl} = 1.0$ is shown in Figure 2.5. For $m_{G_{KK}} > 0.5$ TeV, $G_{KK} \to t\bar{t}$ becomes the primary decay mode.

The same KK graviton model with $k/\bar{M}_{Pl} = 1.0$ has been used by the ATLAS collaboration in searches at $\sqrt{s} = 8$ TeV focusing on the $G_{KK} \to ZZ$ decay channel with one leptonically and one hadronically decaying Z-boson [126], the $G_{KK} \to WW$ decay channel with one leptonically and one hadronically decaying W-boson [127] and the $G_{KK} \to ZZ$ and $G_{KK} \to WW$ decay channels, where both bosons are boosted and decay hadronically, yielding two boson-tagged hadronic jets [128]. In addition, the di-Higgs decay channel $G_{KK} \to hh \to (b\bar{b})(b\bar{b})$ has been studied [8]. The strongest constraints on the allowed mass range stem from the search in the $G_{KK} \to ZZ$ decay channel [126], excluding graviton masses below 740 GeV at 95% confidence level. The CMS collaboration has conducted searches for KK gravitons in the $G_{KK} \to ZZ$ and $G_{KK} \to WW$ decay channels, considering final states in which both vector bosons decay hadronically as well as final states with one hadronic and one leptonic vector-boson decay [129].

[24] The production of KK gravitons via vector-boson fusion (VBF) has also been calculated but found to be negligible compared to gluon fusion [124].

In these searches, however, only KK graviton models with $k/\bar{M}_{Pl} \leq 0.5$ are studied; the case $k/\bar{M}_{Pl} = 1.0$ is not considered.

2.5.4. Benchmark Model 4: Spin-0 Colour-Singlet

The last benchmark model considered in this thesis is a spin-0 colour-singlet. It is a generic model in which a scalar resonance with a branching fraction to $t\bar{t}$ of 100% is produced via gluon fusion. The resonance width is set to a negligible 0.66% to obtain another narrow resonance. Any interference with SM $t\bar{t}$ production is neglected. While such a resonance without interference is not predicted by any particular BSM model, it can be used to gauge the sensitivity of the search to scalar colour-singlets.

The CMS collaboration has studied the same benchmark model in its search for resonances decaying to $t\bar{t}$ pairs in 19.7 fb^{-1} of $\sqrt{s} = 8$ TeV data, combining the ℓ+jets and fully hadronic $t\bar{t}$ final states [130]. The upper limits on the production cross-section derived from this search are 0.8 pb and 0.3 pb for a resonance mass of 500 GeV and 750 GeV, respectively.

2.6. Summary

The SM describes all fundamental constituents of matter known to date and their interactions via the electromagnetic, strong and weak forces. The masses of the weak gauge bosons are generated dynamically through spontaneous EWSB via the Higgs mechanism. Fermions acquire mass via their Yukawa couplings to the Higgs field. While the SM has withstood increasingly rigorous tests and successfully predicted the existence of new particles, there are various reasons to believe that it is not a complete theory. The top quark is expected to play a special role in both direct and indirect searches for physics beyond the SM due to its large Yukawa coupling. Four benchmark models that predict the existence of new resonances decaying to $t\bar{t}$ are described.

3. Experimental Setup

Direct searches for evidence of new physics beyond the SM rely on particle colliders where the kinetic energy of accelerated particle beams is used to create new, potentially unknown, particles according to Einstein's energy-mass relation (in natural units): $E = m$. While the theoretical extensions of the SM described in Section 2.5 define the type and interactions of the new states they involve, they make no exact predictions with regard to their masses.

It is therefore important that direct experimental searches are sensitive to new physics across a large mass range. Here lies a clear advantage of hadron colliders over, for example, electron-positron colliders. In the latter case, the centre-of-mass energy of the colliding beams directly determines the energy available for the resonant (s-channel) production of new particles and hence the range of resonance masses that can be probed. At a hadron collider, in contrast, the effective center-of-mass energy of an interaction, $\hat{s} = x_a \cdot x_b \cdot s$, also depends on the momentum fractions x_a and x_b of the initial-state partons in each hadron, which take values between zero and one with probabilities determined by the parton distribution functions (PDFs) of the respective hadron. Hadron colliders therefore probe a wide range of effective resonance masses at a given beam energy. This makes them well suited for model-independent searches for new physics over a large mass range.

3.1. The Large Hadron Collider

The Large Hadron Collider (LHC) [131, 132] is the most powerful particle accelerator that has been built to date. It is a circular hadron collider with a circumference of roughly 27 km, located at CERN, the European Organisation for Nuclear Research near Geneva, Switzerland, where it has been built into a tunnel below the Franco-Swiss boarder at a depth between 50 and 175 m. It is designed to accelerate and collide two counter rotating beams of either protons or other nuclei. The results presented in this thesis are based on data from proton-proton (pp) collisions, hence the focus of this section will be on proton beams.

The protons are obtained from the ionisation of hydrogen gas and accelerated in several stages using a number of pre-accelerators.[1] They are then injected into the LHC with an initial energy of 450 GeV and accelerated to their peak energy. The protons of each such *fill* are kept in the storage ring at this energy for several hours. Each proton beam consists of a number of discrete bunches of $\mathcal{O}(10^{11})$ protons, a result of the use of radiofrequency (RF) cavities for the acceleration.

As a *pp* collider, the LHC is designed to reach a maximum beam energy of 7 TeV,[2] corresponding to an unprecedented centre-of-mass energy of $\sqrt{s} = 14$ TeV.[3] During its first run between 2010 and 2012 (**Run 1**), it operated at lower energies of $\sqrt{s} = 7$ TeV (30 March 2010 - 30 October 2011) and $\sqrt{s} = 8$ TeV (5 April 2012 - 17 December 2012) due to technical constraints imposed by its magnetic system. Following a two year long shut-down period during which both the collider and its experiments have undergone a number of technical upgrades, the LHC has resumed operation in spring 2015 at $\sqrt{s}$ =13 TeV (**Run 2**).

The LHC also holds a record with regard to the second key design parameter of particle colliders: the **(instantaneous) luminosity** $\mathcal{L}$, which determines the rate $\dot{N}$ of a reaction with cross-section σ via the relation $\dot{N} = \mathcal{L}\ \sigma$. It plays a major role in searches for new physics as the observation of rare processes requires large amounts of collision data and these have to be collected in a limited amount of time due to financial and technical constraints, such as the lifetime of machine components. The value of $\mathcal{L}$ is determined by a number of beam parameters: its transverse profile, the number of protons in two colliding bunches as well as the frequency at which the bunches collide. During Run 1, the bunches had a temporal separation (*bunch spacing*) of 50 ns, yielding a peak collision rate of 20 MHz.[4]

The data analysed in this thesis was taken in 2012 when the LHC was operating at a luminosity still below its design value of $\mathcal{L} = 10^{34}$ cm^{-2} s^{-1}, although this number steadily increased over the year, reaching a peak value of $\mathcal{L} = 7.73 \cdot 10^{33}$ cm^{-2} s^{-1} in August 2012. The peak luminosity per fill delivered to the ATLAS experiment (see below) by day in 2012 is shown in Figure 3.1a. The corresponding cumulative or **integrated luminosity** $\int \mathcal{L} \mathrm{d}t$, a measure for the total amount of data collected, is shown in Figure 3.1b.

[1] For details on the LHC injector chain see Volume III of [132].
[2] The maximum beam energy is limited by the bending power of the dipole magnets used to guide the beam around the storage ring. These are designed to reach a maximum field strength of 8.33 T
[3] This value is around seven times higher than the maximum centre-of-mass energy of $\sqrt{s} = 1.96$ TeV reached by the Tevatron at Fermilab, which held the record as the world's most powerful particle collider until the LHC surpassed this energy in 2009.
[4] In practice, this rate is lower as it is not possible to collide all bunches in a fill due to technical constraints.

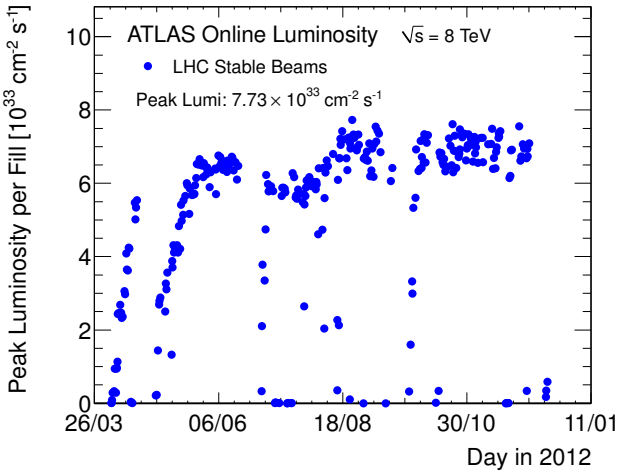

(a) Peak luminosity per fill in 2012

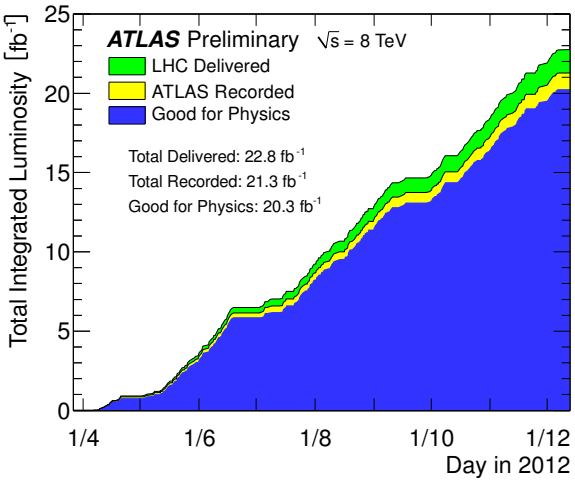

(b) Total integrated luminosity

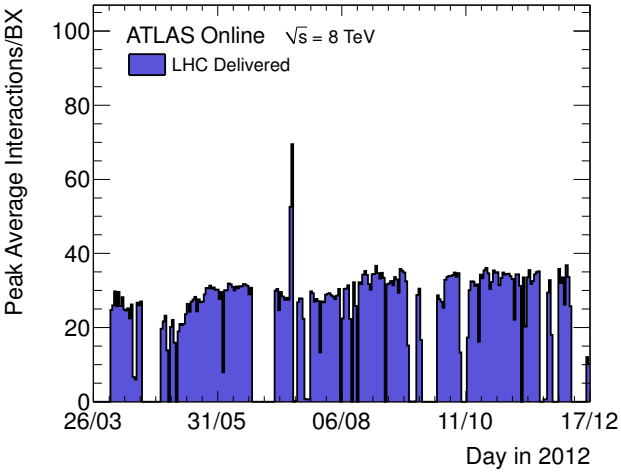

(c) Peak average number of interactions per bunch crossing

Figure 3.1.: (a) Peak (instantaneous) luminosity per fill delivered to the ATLAS experiment during the LHC operation at $\sqrt{s} = 8$ TeV in 2012. (b) The corresponding integrated luminosity, differentiated by the amount delivered by the LHC during stable beam conditions, the amount recorded by the ATLAS experiment and the subset identified to be of sufficient quality for physics analyses. (c) Peak average number of bunch crossings per day for the same operation period. All taken from [133].

The high instantaneous luminosity of the LHC leads to a phenomenon known as **pile-up** which refers to the overlap of several *pp* interactions in a single collision event or between consecutive collision events. There are two main types of pile-up: the occurence of addititional *pp* interactions in the *same* bunch crossing as the interaction of interest is known as **in-time pile-up**. **Out-of-time pile-up** refers to the overlap of detector signatures from interactions in bunch crossings just before or after the one of interest and is related to the finite read-out time of the detector systems. A common measure for the amount of pile-up in a collision event is the number of interactions per bunch crossing which is averaged over all bunch crossings in a fixed time interval[5] and denoted as $< \mu >$. The peak values of $< \mu >$ by day in 2012 are shown in Figure 3.1c. The average number of interactions per crossing was found to be around 20 in 2012. The mitigation of pile-up effects to better isolate the interactions of interest is a major challenge for physics analyses at the LHC. Various techniques will be discussed throughout this thesis.

The two proton beams are brought to collision at four points around the LHC accelerator ring where its four main experiments ALICE[6] [134], ATLAS[7] [135], CMS[8] [136] and LHCb[9] [137] are located. ALICE and LHCb are experiments specialised to heavy ion and *b*-physics, respectively. ATLAS and CMS, in contrast, are multi-purpose experiments dedicated to a wide range of precision measurements and new physics searches. The existence of two such experiments with different detector design is crucial as it allows for independent cross-checks, especially with regard to potential discoveries.

3.2. The ATLAS Detector

The ATLAS detector was designed as a multi-purpose detector suitable for a wide range of new physics searches and precision measurements. As such it needs to meet a number of key design requirements: First and foremost, it must provide a full 4π solid angle coverage around the interaction point to ensure that all particles produced in the collision pass through the detector. This is particularly important for the calculation of the missing transverse energy of a collision event (Section 3.2.1). In practice, a perfect 4π-coverage is not feasible because the beam pipe traverses the detector. Particles emitted at very small angles to the beam line are therefore hard to impossible to detect.

[5] The time interval commonly chosen is the *luminosity block* defined in Section 3.2.6.
[6] **A L**arge **I**on **C**ollider **E**xperiment.
[7] **A T**oroidal **L**HC **A**pparatu**S**.
[8] **C**ompact **M**uon **S**olenoid.
[9] **LHC b**eauty.

Secondly, the sensitivity of searches as well as the precision of measurements depends crucially on the ability to accurately reconstruct the full four momentum of each particle from its energy deposits in the detector. The detector must therefore be designed to provide a high energy, momentum and angular resolution. The latter is also important to distinguish close-by particles in the dense event topologies that result from the decays of highly-energetic massive particles, such as top quarks (Sections 5.1).

Furthermore, the detector must be designed in a way to allow the identification of different particle types such as electrons, muons and hadrons. Given the large cross-sections and the diversity of processes with purely hadronic final states typical for a hadron collider like the LHC, the ability to distinguish different types of hadrons such as pions, kaons and heavy-flavour states is also desirable.

Finally, the high bunch crossing rates of the LHC require fast read-out electronics to provide a high temporal resolution and reduce the effects of out-of-time pile-up. Morover, a fast and efficient trigger system is needed to filter out the events of interest to be stored permanently for future analyses.

Based on these considerations, a multi-layer detector design with rotational symmetry around the beam axis and forward-backward symmetry has been chosen. Each layer can be divided into a cylindrical **barrel** and a wheel-shaped **end-cap region**. A schematic representation of the ATLAS detector and its various subsystems is given in Figure 3.2. With a length of 44 metres and a diameter of 25 metres, ATLAS is the largest of the four main detectors at the LHC.

Each subsystem is specifically designed to be sensitive to different types of particles and to measure a different set of quantities. The combination of the information from all detector components yields the **detector signature**, which fully characterises a particular event and can be used to reconstruct and identify the individual particles produced in the collision, as described in Chapter 4. In the following sections, the ATLAS coordinate system and its various subdetectors will be discussed. All numbers and further technical details can be found in [135, 139], unless otherwise stated.

3.2.1. The ATLAS Coordinate System

ATLAS uses a right-handed coordinate system with its origin at the nominal interaction point of the two beams in the centre of the detector and the z-axis along the beam axis. The x-axis is chosen to point from the interaction point to the centre of the LHC ring and the y-axis is

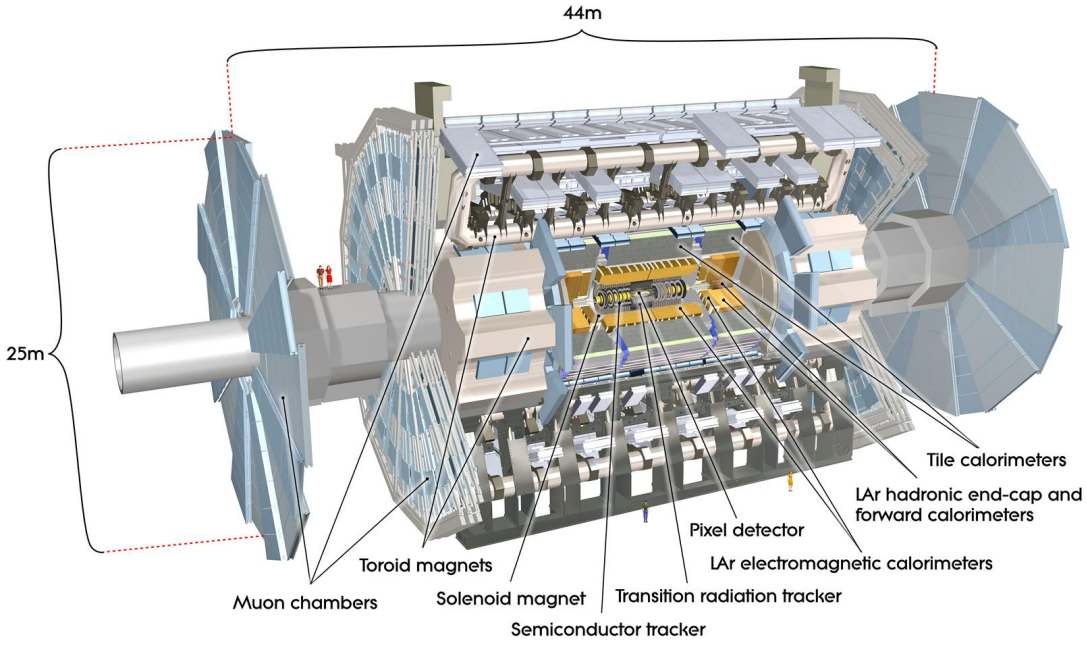

Figure 3.2.: Schematic representation of the ATLAS detector and its subsystems. Taken from [138].

perpendicular to the LHC plane and points upwards. The rotational symmetry of the detector around the beam axis suggests the use of cylindrical coordinates (r, θ, ϕ) where θ is the polar angle with respect to the beam axis and ϕ denotes the azimuthal angle in the transverse $(x-y)$ plane. The angle θ is commonly replaced by the **pseudorapidity** η which is defined as

$$\eta = -\ln[\tan\left(\frac{\theta}{2}\right)]. \tag{3.1}$$

The pseudorapidity is zero in the transverse plane ($\theta = \pi/2$) and increases in magnitude rapidly in the proximity of the beam axis with $|\eta| \to \infty$ for $\theta \to 0$ and $\theta \to \pi$. For massless particles, the pseudorapidity equals the **rapidity** y which is defined as

$$y = \frac{1}{2} \ln\left(\frac{E + p_z}{E - p_z}\right). \tag{3.2}$$

E stands for the total energy of the particle and p_z denotes the z-component of its momentum.

The reason for using the pseudorapidity instead of the angle θ is that differences in pseudorapidity $\Delta\eta = \eta_1 - \eta_2$ are invariant under Lorentz boosts along the beam axis: At hadron colliders like the LHC, the center-of-mass frame of a process does not necessarily coincide with the laboratory frame because the momentum fractions x_1 and x_2 of the initial-state partons, and hence their

longitudinal momenta along the beam axis, cannot be predicted for a particular event; only their probabilities are given by the PDFs of the respective hadrons.

On the other hand, the transverse momentum components of the initial-state partons are known to be zero to a good approximation. Momentum conservation dictates that the vector sum of the transverse momenta of all final-state particles must also be zero. By measuring the transverse momenta of all particles that interact in the detector and taking the vectorial sum of their transverse momenta, one can determine the **missing transverse momentum** or **missing transverse energy** E_T^{miss}. For details on the measurement of E_T^{miss} see Section 4.4.

Based on these considerations, it is common practice at hadron colliders to characterise the four-momentum p of a particle not by its cartesian components (p_x, p_y, p_z, E) but in the form (p_T, η, ϕ, E). Here, the transverse momentum p_T is related to the absolute momentum $|\vec{p}|$ of the particle via the relations $|\vec{p}| = p_T \cdot \sin\theta = p_T \cdot \cosh\eta$. Moreover, the angular separation between two particles i and j is defined by the distance parameter

$$\Delta R_{i,j} = \sqrt{(\eta_i - \eta_j)^2 + (\phi_i - \phi_j)^2}. \tag{3.3}$$

For charged particles, the transverse momentum can be measured directly from the curvature of their tracks in the magnetic field of the inner detector and/or the muon system, as described below. For all other interacting particles, it is calculated from the associated energy deposits in the calorimeter by measuring their energies and angular positions and using these to calculate the **transverse energies** $E_T = E \cdot \sin\theta$. For further details, see in particular Section 4.3.

3.2.2. The Inner Detector

The inner detector (ID) is a high-resolution detector which is located directly around the beam pipe and records the trajectories of charged particles. It has a length of 6.2 m, a diameter of 2.1 m and covers a pseudorapidity range of $|\eta| < 2.5$. The ID is contained within the 2 T field of a surrounding solenoid which bends the tracks of charged particles, thus allowing the particle momentum to be measured from the track curvature.

The information about the tracks and vertices that are reconstructed from the energy deposits in the ID is of key importance for both event reconstruction and particle identication. Firstly, it allows the determination of the **primary vertex**, which is defined as the vertex with the largest sum of scalar momenta of its associated tracks and corresponds to the hardest interaction in

the event, usually the interaction of interest. Vertices associated with other, softer interactions in the same bunch crossing can be used to identify and reject pile-up jets. Secondly, displaced **secondary** (and to some extend tertiary) **vertices** corresponding to the decays of short-lived particles, such as B- and D-hadrons, are important discriminants in flavour tagging algorithms (Section 4.3.5), which play a key role in many physics analyses.

The large track density resulting from the high luminosity of the LHC requires high-precision, high-granularity detectors to resolve the individual tracks and vertices and yield precise momentum and position measurements. At the same time, the material density must be kept to a minimum to reduce energy losses in the ID. The choice of the material itself is further dictated by the requirements of radiation tolerance and cost efficiency.

The ID is designed based on these considerations. It consists of three independent, but complementary subsystems: the **pixel detector**, the **semiconductor tracker (SCT)** and the **transition-radiation tracker (TRT)**, as illustrated in Figure 3.3.

The **pixel detector**, closest to the interaction point, is a silicon-based semiconductor tracker consisting of three pixel layers in the barrel and three disks in each end-cap. It has about 80 million read-out channels and provides a spatial resolution of around 10 μm in the transverse ($R-\phi$) plane and around 115 μm in the z direction. Its innermost layer in the barrel region, referred to as the **B-layer**, is installed at a distance of 50.5 mm from the beam line and significantly contributes to the high precision of the vertex position measurements.

The pixel detector is surrounded by the **SCT**, a silicon-microstrip detector with around 6.3 million read-out channels. It is arranged in four cylindrical layers in the barrel and eight disks in each end-cap. Its intrinsic accuracy is lower than that of the pixel detector with around 17μm in the transverse ($R-\phi$) plane and around 580μm in the z direction.

The TRT constitutes the outermost subsystem of the ID. It consists of straw tubes with a diameter of 4 mm, filled with a xenon-based gas mixture. The straw tubes are oriented parallel to the beam axis in the barrel region and arranged radially in wheels in the end-caps. Position measurements are possible in the $R-\phi$ plane only, with an average precision of 130 μm per straw tube. Typically, 36 hits are recorded for a track passing throught the TRT. Despite its lower resolution per space point compared to the silicon detectors, the TRT contributes significantly to the precision of the momentum measurement as its larger radius and higher number of hits increase the accuracy with which the track curvature can be measured. Moreover, it can be used

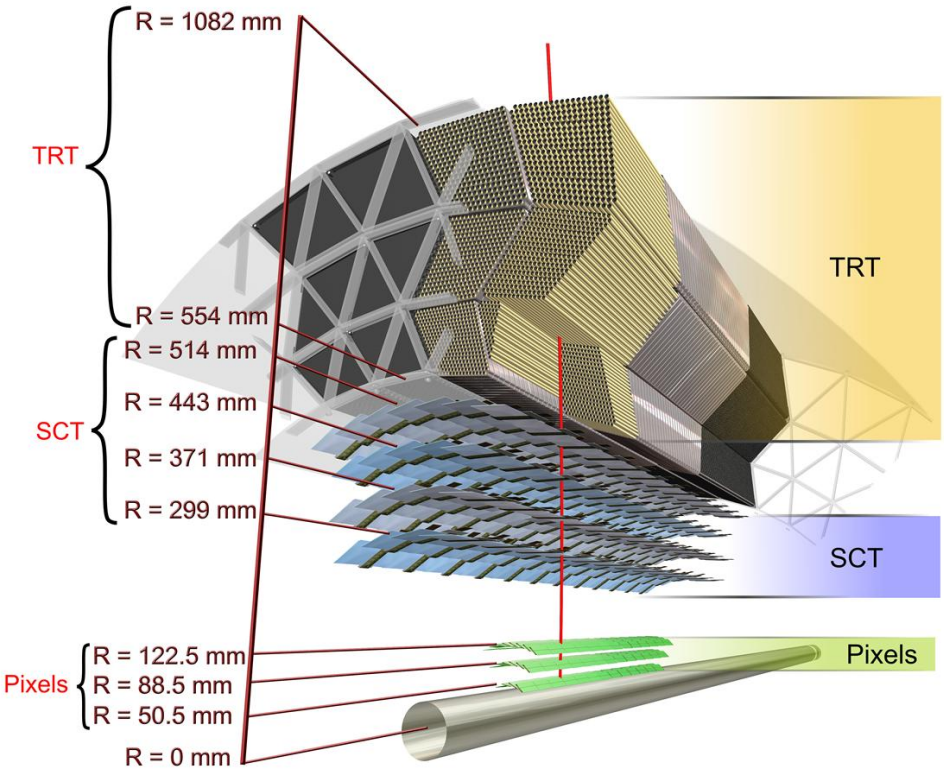

Figure 3.3.: Section of the ATLAS inner detector (ID) in the barrel region showing the arrangement of its three subsystems: the pixel detector, the semiconductor tracker (SCT) and the transition-radiation tracker (TRT). The numbers mark the radial distance of the different layers from the beam line at R = 0 mm. The beryllium beam pipe is shown in grey. The red vertical line in the centre marks the trajectory of a charged particle through the ID [138].

to distinguish between electrons and pions via the detection of transition radiation.

3.2.3. The Electromagnetic and Hadronic Calorimeter System

The calorimeter system surrounds the inner detector and the solenoid. It has a length of 12.20 m, an outer radius of 4.25 m and consists of an electromagnetic (EM) and a hadronic calorimeter system, as shown in Figure 3.4. Its purpose is to measure the energy of electrons, photons and hadronic particle jets. It also contributes significantly to the measurement of E_T^{miss}.

The basic principle of the calorimetric energy measurement is the total absorption of all particles that interact via the electromagnetic and/or the strong force, with the exception of muons. In the *sensitive material* of the calorimeter, a fraction of the absorbed energy is turned into measurable quantities such as electric charges or, in the case of the ATLAS detector, photons which are read

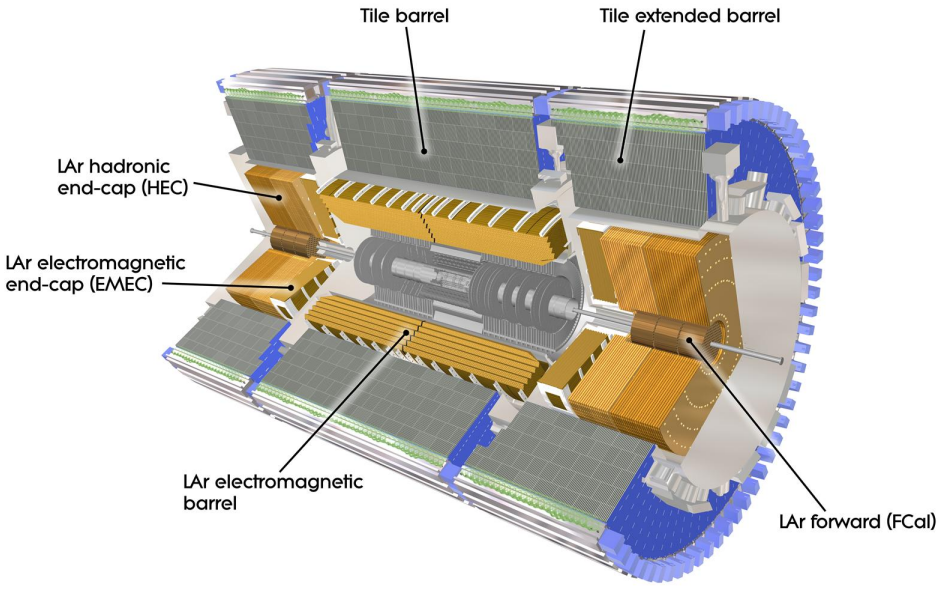

Figure 3.4.: Schematic representation of the calorimeter system, comprising the EM and hadronic calorimeters [138].

out by dedicated sensors, for example, photomultiplier tubes. A *calibration* procedure is then applied to derive the total absorbed energy from that measured in the sensitive layers of the calorimeter.

Incident particles initiate cascades of secondary particles in the detector material: Electrons and photons give rise to pure electromagnetic showers, mainly via bremsstrahlung and photon conversion to electron-positron pairs in the electric field of atomic nuclei.

The showers triggered by hadronic particles are more complex. They arise from inelastic strong interactions between the hadrons and atomic nuclei and typically have both a hadronic and an electromagnetic component, the latter resulting from electromagnetic hadron decays, such as $\pi^0 \to \gamma\gamma$.

The overall calorimeter *response* to hadrons is considerably lower than that to electrons or photons, because the hadronic shower involves nuclear reactions, which convert kinetic energy into forms of energy that are hard to detect: Examples of such reactions include processes in which a nucleus is broken up or remains in an excited state or processes resulting in neutrons that undergo only elastic scattering and leave the calorimeter undetected. Moreover, weak hadron decays, for example $\pi \to \mu\nu_\mu$, may produce neutrinos which also escape the calorimeter. The energy calibration of hadronic jets is therefore more complex and associated with considerably larger uncertainties than that of electrons or photons. An overview of the calibration procedure

for hadronic jets can be found in Section 4.3.

The large energies of the particles produced in the collisions at the LHC make it necessary to introduce extra layers of purely absorbing material in addition to the sensitive layers. This is necessary in order to reduce the absorption length and hence the calorimeter volume and material costs to a manageable size. The absorbing layers typically consist of dense materials with large atomic numbers, such as iron or lead. Calorimeters with alternating layers of sensitive and absorbing material are referred to as *sampling* calorimeters. Both calorimeter systems of the ATLAS detector are based on this principle.

The design parameters are chosen such that the leakage of electromagnetic showers from electrons and photons into the hadronic calorimeter and of hadronic showers into the muon system are reduced as much as possible. The latter effect is known as *punch-through* and needs to be taken into account in the calibration of the jet energies (Section 4.3). In the following two subsections the properties of the EM and hadronic calorimeters will be described in further detail.

The EM Calorimeter

The EM calorimeter covers the pseudorapidity range $|\eta| < 3.2$, with its barrel part extending over the range $|\eta| < 1.475$ and the end-caps covering $1.375 < |\eta| < 3.2$. It is a sampling calorimeter which combines sensitive layers of liquid argon (LAr), chosen due to its good radiation hardness, with lead absorbers in both the barrel and the end-cap regions. Its accordion-shape geometry in the radial direction, illustrated in Figure 3.5. has been specifically designed to avoid azimuthal cracks because these would have an adverse impact on the energy resolution.

Over the central region $|\eta| < 2.5$, which is the detector region used by most analyses, including the ones presented in this thesis, the EM calorimeter is segmented radially into three longitudial layers with different granularities, see again Figure 3.5: The innermost layer consists of narrow strips with a granularity of $\Delta\eta \times \Delta\phi = 0.003 \times 0.1$ which allows for a precise measurement of the electromagnetic shower profile in η. This information plays an important role in the identification of particle types. For example, it can be used to distinguish single photons, γ, from the decays of neutral pions, $\pi^0 \to \gamma\gamma$, where the two photons tend to have a small angular separation in the laboratory frame. The middle layer is segmented into radial towers with a cross-section of $\Delta\eta \times \Delta\phi = 0.025 \times 0.0245$. The cells in the outer layer have a granularity of $\Delta\eta \times \Delta\phi = 0.05 \times 0.0245$.

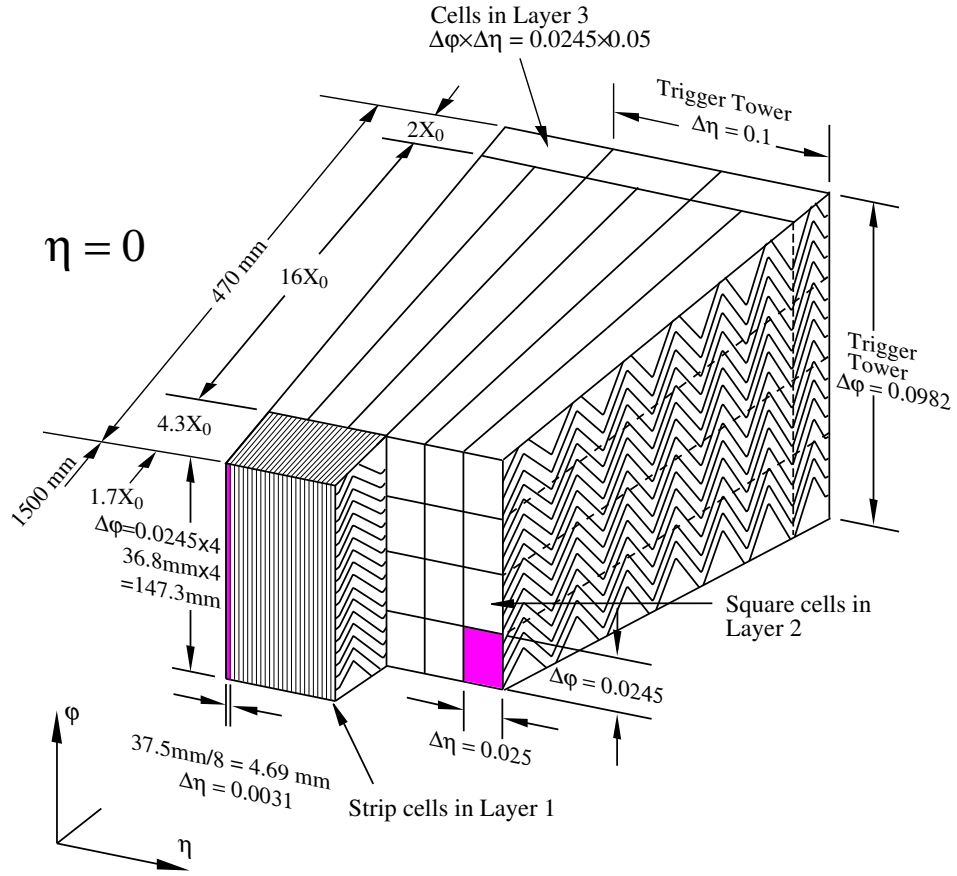

Figure 3.5.: Schematic representation of the three layers of the EM calorimeter for $|\eta| < 2.5$. The accordion-shape structure is clearly visible in all three layers. The radial thickness of each layer is given both in mm and in units of the radiation length X_0 [140]

.

The Hadronic Calorimeter

The hadronic calorimeter surrounds the EM calorimeter. It consists of three subsystems covering a total pseudorapidity range of $|\eta| < 4.9$. The **tile calorimeter** is a sampling calorimeter which combines iron absorber plates with radially-oriented scintillating tiles as an active material. As illustrated in Figure 3.4, it falls into three cylinders: the central barrel, covering a range of $|\eta| < 1.0$ and two extended barrels, covering the region $0.8 < |\eta| < 1.7$. The two 68 cm wide gaps dividing these three parts provide space for services to the ID, EM calorimeter and cooling systems. Like the EM calorimeter, the tile calorimeter is segmented into three longitudial layers or *samplings* in the radial direction, as shown in Figure 3.6 for a module in the central region.

The **hadronic end-cap calorimeter (HEC)** covers the range $1.5 < |\eta| < 3.2$. The larger radiation doses in this region have motivated the choice of LAr as the sensitive medium. Copper plates are used as the absorbing material. Finally, the **Forward Calorimeter (FCal)** extends

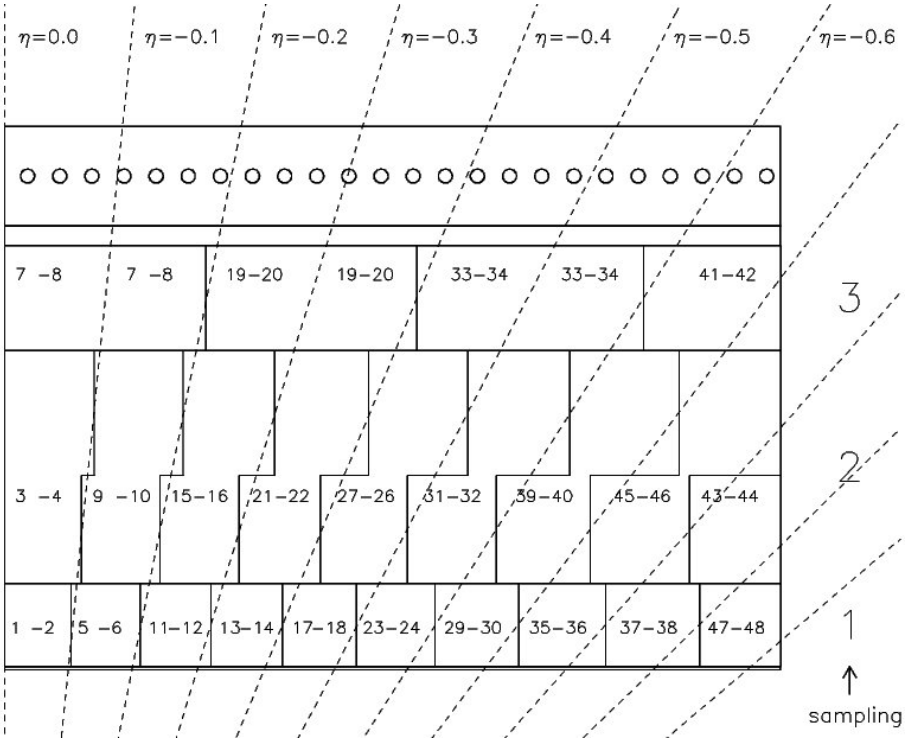

Figure 3.6.: Schematic representation of the three layers or *samplings* in the $R - z$ plane of a module from the central barrel region of the tile calorimeter. The numbers in the blocks denote the pair of photomultiplier tubes connected to each cell for read-out [141].

the coverage of the hadronic calorimeter across the range $3.1 < |\eta| < 4.9$. It consists of three sections, the first one using copper as an absorber, the other two using tungsten. Again, LAr is chosen as the sensitive medium in this high-radiation region.

The overall granularity of the hadronic calorimeter system is coarser than that of the EM calorimeter: For the pseudorapidity range relevant to the analysis and the studies presented in this thesis, $|\eta| < 2.5$, the typical granularity is $\Delta\eta \times \Delta\phi = 0.1 \times 0.1$ with the exception of the third sampling in the central barrel, which has a coarser granularity of $\Delta\eta \times \Delta\phi = 0.2 \times 0.1$, as shown in Figure 3.6.

Despite the fact that many physics analyses in ATLAS consider only hadronic jets reconstructed with $|\eta| < 2.5$ to allow for the use of tracking information in the jet energy and mass calibration and in jet energy and mass resolution measurements (Section 4.3.4), the coverage of large pseudorapidity ranges provided in particular by the FCal is important in order to guarantee a reliable measurement of E_T^{miss}, a quantity that plays a key role in many searches for BSM physics, such as searches for Dark Matter candidates.

3.2.4. The Muon Spectrometer

The Muon Spectrometer (MS) is the outermost subsystem of the ATLAS detector and has been designed for stand-alone muon reconstruction. The muon momentum is measured from the curvature of the muon tracks in the magnetic field of three air-core superconducting toroids covering a pseudorapidity range of $|\eta| < 2.7$. The magnetic field has an average strength of 0.5 T and a typical bending power $\int Bdl$ of 3 Tm in the barrel and 6 Tm in the end-cap regions [142].

The muon tracks are reconstructed from energy deposits in dedicated muon chambers: In the barrel region ($|\eta| < 1.0$), three cylindrical layers of **Monitored Drift Tubes (MDTs)** are used. The MDTs consist of aluminium tubes with a central W-Re wire and are filled with a gas mixture of 93% argon and 7% CO_2. In the end-cap region ($1.0 < |\eta| < 2.7$), **Cathode Strip Chambers (CSCs)** are installed, arranged in four concentrical disks around the beam axis. A schematic overview of the MS is given in Figure 3.7.

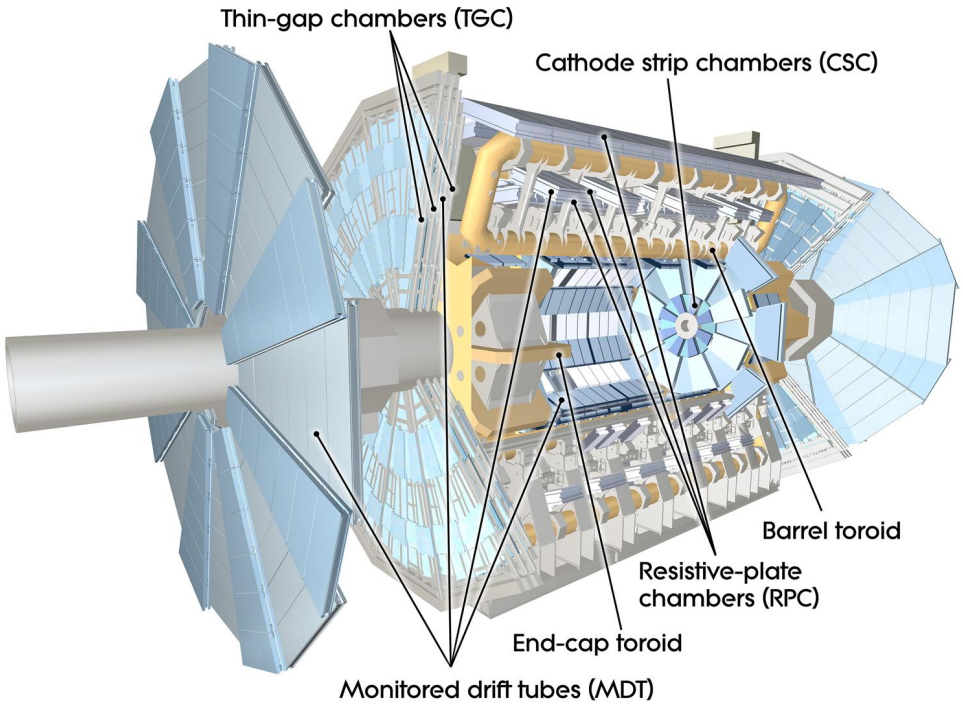

Figure 3.7.: Schematic representation of the ATLAS Muon System [138].

The transverse momentum resolution $\Delta p_T^\mu / p_T^\mu$ for an MS stand-alone measurement is around 2.5% for $p_T^\mu = 20$ GeV and around 11% for $p_T^\mu = 1000$ GeV. The resolution can be further improved by using additional tracking information from the ID, in particular for low values of p_T^μ for which the curvature of the muon tracks within the volume of the ID is sufficiently large. For $p_T^\mu = 20$ GeV, for example, the resolution is improved to 1.6% [142].

In addition, a fast muon system for triggering with a pseudorapidity coverage of $|\eta| < 2.4$ is installed. It consists of three layers of **Resistive Plate Chambers (RPCs)** in the barrel ($|\eta| < 1.05$) and three layers of **Thin Gap Chambers (TGCs)** in the end-cap regions ($1.05 < |\eta| < 2.4$). Both types of chambers provide a high time resolution which is exploited to resolve and uniquely identify the individual bunch crossings. The overall geometric coverage of the trigger system in the end-cap regions is around 99% while only 80% is reached in the barrel region [143]. This is due to a gap at $\eta = 0$, which is needed to provide services, such as cables and cooling tubes, to the ID and the calorimeter system, as well as further uncovered space due to the support structure of the ATLAS detector and two elevators in the lower part of the spectrometer.

3.2.5. The Trigger and Data Acquisition (TDAQ) System

The high collision rates at the LHC and the large number of $\mathcal{O}(10^7)$ read-out channels for the different detector components render it impossible to store the detector information of each single collision event, even temporarily. A multi-level trigger system has therefore been installed to select events of interest for permanent storage. It has been optimised for the dual challenge of providing a high selection efficiency for events of interest while reducing the fraction of background events as far as possible to save storage space, and of making this selection fast enough to cope with the high incoming event rates. During the 2012 data-taking period, the trigger system reduced the incoming rate of 20 MHz to an output event rate of around 400 Hz that was written to permanent storage. The average processing time at the last, and longest, trigger stage was 1 s. [144]

The ATLAS trigger system consists of three consecutive stages, which successively reduce the incoming event rate by applying more and more refined selection criteria and by using additional detector information: The hardware based **level-1 (L1) trigger** and the mostly software-based **high-level trigger (HLT)**, which consists of two stages, the **level-2 (L2) trigger** and the **Event Filter (EF)**. The operating parameters quoted in the following are based on the trigger setup during the 2012 data-taking period, described in [139] and [144].

The **L1 trigger** constitutes the first stage of the ATLAS trigger system. It is entirely hardware based and uses fast, custom-made electronics to process reduced-granularity information from a number of detector subsystems, namely the calorimeter and the RPCs and TGCs in the muon system. No tracking information is available at this stage. The L1 trigger uses this information

to search for signatures of high transverse-momentum muons, electrons, photons and jets as well as hadronically decaying τ-leptons and to identify events with large missing transverse energy or large total transverse energy. It also defines *Regions of Interest (ROIs)* around notable signatures in the detector. If an event is accepted by the L1 trigger, its data is read out and stored in the read-out buffers (ROBs) for further use by the following trigger stages. The processing time of the L1 trigger is around 2.5 μs and its maximum output rate is 75 kHz.

The mostly software-based **L2 trigger** is seeded by the ROIs defined at L1. It has access to the full-resolution information from all detector subsystems, including the tracking information from the ID, but it performs only a partial event reconstruction limited to the ROIs and/or one or more detector subsystems. Moreover, it uses simplified, fast reconstruction algorithms to achieve an average processing time of 90 ms. If an event is accepted by the L2 trigger, its full detector information is read out of the ROBs and stored in memory accessible to the EF processors. This process is referred to as *event building (EB)*. The average EB rate was 6.5 kHz during the 2012 data-taking period.

The **EF** has access to the full event information provided by the EB. It relies on reconstruction algorithms and identification criteria very similar to those used in the offline reconstruction of events that pass the complete trigger chain, but with small adjustments due to constraints on the processing time, which is 1 s on average. The EF selection reduces the event rate to around 400 Hz. Events accepted at this final trigger stage are written to permanent storage.

At each trigger level, the decision to keep or reject an event is based on the presence of one or more physics objects such as electrons or muons which are required to pass certain selection criteria or *trigger thresholds* imposed on properties such as their transverse momentum or isolation. The sequence of selection and reconstruction algorithms that is used to select events with a specific detector signature, for example events with a single high-p_T electron, is referred to as a *trigger chain*. Details of the trigger selection used in this thesis will be given in Chapter 4 and Section 5.3.2.

3.2.6. Data Streams, Runs and Luminosity Blocks

The events that have passed the trigger system are assigned to *data streams* based on the trigger chain(s) by which they were selected. These data streams are written to separate files to allow for selective offline (re-)processing based on the event type. The categorisation is inclusive, meaning that an event may belong to more than one stream. There are three streams commonly used in

physics analyses: the `EGamma` stream for electron and photon trigger output, the `Muon` stream and the `JetTauETMiss` stream which corresponds to various hadronic trigger signatures. The use of single electron and muon triggers in the analysis presented in this thesis implies the use of data from the `EGamma` and the `Muon` stream.

The data streams described above are referred to as **prompt data streams** because the reconstruction of the corresponding raw data starts almost immediately after it is written to storage. In 2012, additional **delayed data streams** with associated delayed-stream triggers were introduced in ATLAS. Their introduction was motivated by the fact that the main computing challenge for the LHC experiments is not data storage but data processing. While it is not possible to process data at a rate of more than 400 Hz, the storage capacities allow for an extra 200 Hz of data to be procured. The reconstruction of this extra data was *delayed* until the shutdown of the LHC in 2013 when the experiments stopped taking new data, thus freeing computing resources for delayed data processing.[10] The analysis presented in this thesis uses a delayed stream trigger to increase the overall efficiency times acceptance of the event selection (Section 5.3.2).

The data recorded by the ATLAS detector is further organised into **runs**, each run usually corresponding to a fill of the LHC (Section 3.1).[11] The runs are subdivided into time intervals of one minute length, referred to as **luminosity blocks**. The beam and detector conditions can be assumed to be approximately constant over each luminosity block. This allows the calculation of quantities such as the number of interactions per bunch crossing, $< \mu >$, averaged over a luminosity block. Luminosity blocks also play a central role in the evaluation of data quality criteria.

3.2.7. Data Quality

A number of quality requirements is imposed on data used in physics analyses. These are defined by the ATLAS Data Quality Group and include global requirements, such as stable beam conditions at the LHC during the time when the data was recorded, as well as requirements related to the individual subsystems. More than a 100 data quality flags are used to indicate possible hardware or read-out problems in the different subsystems. They are used to create **Good Runs Lists**, which contain information about the runs and luminosity blocks deemed of

[10] This concept was also used by CMS where it is referred to as *Data Parking*.

[11] Detector problems or other considerations may lead to a run being ended and another one started later during the same fill.

sufficient quality with regard to the requirements of different physics analyses and performance studies.

3.2.8. The Dataset analysed in this Thesis

The dataset analysed in this thesis corresponds to the complete dataset recorded at the ATLAS experiment during the data-taking period in 2012 under the run conditions described in Section 3.1. The final recommendations by the ATLAS Data Quality Group have been followed in selecting only luminosity blocks of sufficient quality. The resulting integrated luminosity of the total selected dataset is $\int \mathcal{L} dt = 20.3$ fb^{-1}.

3.3. The ATLAS Analysis Model

With a nominal trigger output rate of around 400 Hz and an average event size of 1.5 MB during Run 1 of the LHC [144], the ATLAS detector produces unprecedented amounts of data that need to be stored and processed. The necessary resources are provided by the **Worldwide LHC Computing Grid (WLCG)** [145], a network of more than 160 interconnected computing centres from more than 40 countries organised hierarchically in a network of different layers or **tiers**. The decentralised computing strategy and the large number of analysis groups involved in the ATLAS experiment require a common software framework and a data management model that allows the sharing of common tasks that are to be carried out centrally by dedicated Combined Performance Groups, while providing sufficient flexibility for individual analysis teams to maintain their own specialised analysis codes and process only the subset of event information relevant for their analysis. A common C++ based software framework, **Athena** [146], based on the GAUDI framework developed by the LHCb collaboration [147], has been developed to meet these requirements. The specific set of event selection and reconstruction criteria for the search presented in this thesis (Section 5.3) was implemented as C++ code relying on the ROOT [148] software framework. This analysis code, which has access to calibration and performance results provided centrally by the Combined Performance Groups, was used to derive all results presented in Chapter 6, unless otherwise stated. A detailed description of the ATLAS analysis model can be found in [146].

3.4. Simulation of Collision Events

The simulation of particle interactions, such as those occurring in pp collisions, is a key aspect of particle physics analyses. First and foremost, simulations provide predictions about the outcome of an experiment based on commonly accepted theoretical models, such as the SM. Searches for new physics compare these *expectations* to the *observations* made in data to identify potential deviations and to test the SM hypothesis (see Section 7.1 on hypothesis testing). In this context, simulations are also used to study the properties of new signal processes and to test these *alternative* hypotheses against the observed data. Finally, simulated data is often used in the calibration of reconstructed objects as shown in Section 4. It is therefore crucial that the simulations are reliable and thoroughly tested against well-understood processes measured in data.

All simulated collision events used in this thesis have been modelled with event generators using the Monte Carlo (MC) method described in chapters 39 and 40 of [52]. Each pp collision event is generated in several stages: The simulation of the **hard interaction** of the initial-state partons is at the core of the MC event generation. Its large momentum transfer and correspondingly small distance scale allows for the use of perturbative QCD (pQCD) in the calculation of the **matrix element (ME)** at a fixed order in α_s. Generators with leading-order (LO) and next-to-leading order (NLO) accuracy are used in this thesis.

The **parton shower (PS)** evolving from the final-state partons of the hard process via gluon radiation and gluons splitting into $q\bar{q}$ pairs represents higher-order corrections to the hard process that can only be calculated approximately. Different MC generators using different PS models are available [149], the two most common ones at the LHC experiments being the general-purpose generators Pythia [150, 151] and Herwig [152, 153]. They can either be used to generate both the ME and the PS or they can be combined with dedicated (NLO) ME generators. In both cases, it is essential to match the ME and the PS in a way that avoids double-counting or gaps in the phase-space coverage of these two complementary processes. Different **ME/PS matching** schemes are used in different generators [149].

The hard-scattering process is accompanied by a number of softer interactions, collectively referred to as the **underlying event (UE)**. These processes are related to the *beam remnants*, which consist of partons that do not directly participate in the hard interaction but are colour connected to the partons that do, as well as interactions between other partons in the same pp

pair, referred to as *multiple-parton interactions*. MC generators use phenomenological models with parameters adjusted by comparison to data to simulate these soft interactions. A set of parameters chosen based on certain aspects of one or more datasets is referred to as a **tune**.

The PS related to both the hard interaction and the UE evolves towards lower energy scales where α_s becomes large and the partons form colourless bound-states. This **hadronisation** process is governed by non-perturbative effects and can only be described phenomenologically. Two main classes of models exist: string models, such as the one used by Pythia, and cluster models, used for example in Herwig [149].

The final stage of the MC event generation is the decay of any unstable hadrons (and τ-leptons) produced during hadronisation. In this context, a particle is considered unstable if it has a lifetime smaller than approximately 10 ps which means that it will decay before it reaches the first layer of the detector. All "stable" particles are then passed through a full simulation[12] of the ATLAS detector [155] based on the GEANT4 toolkit [156] to model their interaction with the detector material. The effects of pile-up are simulated by overlaying the detector signatures of additional proton-proton interactions generated with Pythia v8.1 [151]. The simulated energy deposits are then digitised into voltages and currents to produce output equivalent to the real data obtained from the DAQ. This way, both simulated and real data can be processed with the same reconstruction software.

As explained above, a given process can be modelled using a number of different MC generators which rely on different modelling assumptions. The choice of generator depends on the process of interest as well as the kinematic regions probed by an analysis. It is important to test the impact of different modelling choices on the final result of an analysis and take any discrepancies into account as systematic uncertainties (Section 5.6.3).

3.4.1. Simulation of Signal Processes

The resonant production of $t\bar{t}$ pairs, $pp \to X \to t\bar{t}$, via a BSM resonance X - the *signal process* - is modelled based on the theoretical assumptions made in the benchmark models discussed in Section 2.5. The technical details of the signal samples used in this thesis are discussed in the following sections.

[12] Alternatively, a fast simulation relying on parameterised showers in the calorimeters is available [154]. While it greatly reduces the CPU time required for the event generation, its description of jet substructure variables (Section 4.3.2) is known to be less accurate than that samples using a full detector simulation. Therefore, fast-simulation samples are used only in the generation of alternative $t\bar{t}$ samples for the estimation of modelling uncertainties in Section 5.6.3.

$Z' \to t\bar{t}$ Signal

The production and decay of the leptophobic topcolour Z' boson introduced in Section 2.5.1 is modelled using Pythia v8.1 with the MSTW2008LO [67] PDF set for both the hard-scattering process and the PS. The samples are generated with the Pythia default settings for the production and decay of a Z' boson in the so-called sequential SM (SSM). This particular Z' resonance, referred to as Z'_{SSM} in the following, has the same couplings as the Z boson of the SM. The values for the cross-section times branching ratio and the relative width of the Z'_{SSM} resonance generated with this simple Pythia default model differ from those of the Z'_{TC2} resonance model described in Section 2.5.1. Nevertheless, it serves as a valid simulation of a Z'_{TC2} resonance as it has the same charge and spin, thus producing $t\bar{t}$ pairs with kinematic properties that are equivalent to those expected for the decay of a Z'_{TC2}. To allow for an interpretation of the analysis in the context of the Z'_{TC2} model, the generated values of the cross-section times branching ratio to $t\bar{t}$ are re-scaled to those for the TC2 model which are given in [101]. A k-factor of 1.3 is applied to correct the cross-section to NLO in α_s based on calculations in [157, 158]. The values for the cross-section times branching ratio for the different resonance masses are summarised in Table 3.1, along with the corresponding relative widths obtained for the generation of the Z'_{SSM}. With values around 3% these generated resonance widths are well below the experimental resolution and the results therefore equivalent to those that would have been obtained using the nominal resonance width of 1.2% that is used in the derivation of the cross-sections for the TC2 model.

Z' Mass [GeV]	Z'_{SSM} Width [%]	$\sigma(Z') \times BR \times 1.3$ [pb]
400	2.86	45.66
500	2.94	24.63
750	3.05	5.65
1000	3.10	1.66
1250	3.12	0.566
1500	3.14	0.213
1750	3.15	0.0853
2000	3.16	0.0357
2500	3.17	0.00687
3000	3.17	0.00147

Table 3.1.: Production cross-section times branching ratio and relative widths for Z' signal samples with different Z' masses. Sample information provided by the ATLAS Top Working Group [159].

$g_{KK} \to t\bar{t}$ Signal

The KK gluon (g_{KK}) samples are generated using MADGRAPH5 [160] for the ME process which is interfaced with PYTHIA v8.1 for the PS. Like in the case of the Z' resonance samples, the MSTW2008LO PDF set is used. All couplings and other parameters are chosen according to Section 2 of [109]. This leads to a relative width of 15.3% for all generated mass points. In order to study the dependence of the sensitivity of the analysis on the resonance width, additional samples are generated. For KK gluon masses of 1.0, 2.0 and 3.0 TeV, the width is varied between 10% and 40% in steps of 5%. The available mass points, their widths and values for the cross-section times branching ratio to $t\bar{t}$ are listed in Table 3.2. No LO→NLO k-factor is applied to the cross-section values as there is currently no consensus in the literature regarding the validity of proposed calculations [2].

$G_{KK} \to t\bar{t}$ Signal

The KK graviton (G_{KK}) samples are generated using MADGRAPH5 interfaced with PYTHIA v8.1, as in the case of the KK gluon. In this case, the CTEQ6L1 [161] PDF set is used to be consistent with other KK graviton searches in ATLAS like, for example, the search for resonant diboson production published in [126]. The parameters of the simulation are chosen according to the model in [124]. The resulting widths vary between 3% and 6% for the different mass points, see Table 3.3 for details.

Scalar Resonance Signal

The generic spin-0 resonance is modelled using MADGRAPH5_aMC@NLO [162] with LO matrix elements. It is interfaced with PYTHIA v8.1 and the CTEQ6L1 PDF set is used. As discussed in Section 2.5, the branching ratio to $t\bar{t}$ final states is taken to be 100%. The width is set to a negligible 0.67%. The generated resonance masses and the corresponding production cross-sections are summarised in Table 3.4.

3.4.2. Simulation of Background Processes

The majority of background processes considered in this thesis are estimated using MC simulations. Two exceptions where fully or partially data-driven methods are used are discussed in Section 5.5.

g_{KK} Mass [GeV]	g_{KK} Width [%]	$\sigma(g_{\mathrm{KK}}) \times BR$ [pb]
400	15.3	112.2
500	15.3	81.9
600	15.3	45.0
700	15.3	25.2
800	15.3	14.6
900	15.3	8.81
1000	10	3.61
	15	5.37
	15.3	5.47
	20	7.08
	25	8.72
	30	10.3
	35	11.7
	40	13.1
1150	15.3	2.82
1300	15.3	1.52
1600	15.3	0.500
1800	15.3	0.255
2000	10	0.080
	15	0.133
	15.3	0.137
	20	0.193
	25	0.257
	30	0.324
	35	0.393
	40	0.461
2250	15.3	0.0670
2500	15.3	0.0351
2750	15.3	0.0196
3000	10	0.0057
	15	0.0113
	15.3	0.0120
	20	0.0184
	25	0.0268
	30	0.0361
	35	0.0462
	40	0.0568

Table 3.2.: Production cross-section times branching ratio and relative widths for Kaluza–Klein gluon g_{KK} signal samples with different g_{KK} masses. Sample information provided by the ATLAS Top Working Group [159].

Background from SM $t\bar{t}$ Production

The pair production of top quarks in the SM is by far the dominant background in the search presented in this thesis. Hence an accurate modelling of this process that also takes into account higher-order QCD and electroweak corrections is of key importance. The POWHEG-BOX [163,

G_{KK} Mass [GeV]	G_{KK} Width [%]	$\sigma(G_{\mathrm{KK}}) \times BR$ [pb]
400	2.810	1.943
500	3.674	1.342
600	4.337	0.622
700	4.799	0.2859
800	5.125	0.1368
900	5.361	0.06838
1000	5.535	0.03569
1200	5.769	0.01077
1400	5.915	0.003578
1600	6.011	0.001288
1800	6.078	0.0004936
2000	6.125	0.0001978
2500	6.199	0.00002345

Table 3.3.: Production cross-section times branching ratio and relative widths for Kaluza–Klein graviton G_{KK} signal samples with different G_{KK} masses. Sample information provided by the ATLAS Top Working Group [159].

Scalar Resonance Mass [GeV]	$\sigma \times BR$ [pb]
400	0.7775
500	0.9805
750	0.1931
1000	0.03342
1250	0.006745
1500	0.001560
1750	0.00040060
2000	0.00011120
2250	0.000032670
2500	0.0000099920
2750	0.0000031480
3000	0.0000010090

Table 3.4.: Production cross-section times branching ratio for different samples of a scalar resonance decaying to $t\bar{t}$ with a BR of 100%. Sample information provided by the ATLAS Top Working Group [159].

164, 165] generator r2330.3 is used to simulate the hard interaction at NLO in α_s, using the method described in [166]. It is interfaced with Pythia v6.427 [150] to model the parton shower, using the Perugia2011C [167] tune which, unlike previous tunes, takes into account results from early LHC data at $\sqrt{s} = 900$ GeV and $\sqrt{s} = 7000$ GeV. The CT10 [168] NLO PDF set is used and the top-quark mass is set to $m_{top} = 172.5$ GeV.

Moreover, the `hdamp` parameter, a Powheg parameter that controls the ME/PS matching [165] and effectively regulates ("dampens") the amount of high-p_T radiation, is set to `hdamp` $= m_{top}$.

Previously, the default setting for the centrally produced POWHEG+PYTHIA $t\bar{t}$ samples in ATLAS was `hdamp` $= \infty$. During 2014, various studies carried out by analysis teams in the ATLAS Exotics and SUSY WGs, involving the author of this thesis, found that setting `hdamp` $= m_{top}$ yields improvements in the agreement between LHC data and MC predictions for a number of relevant kinematic distributions [169, 170]. It was therefore decided to adopt this value as the new default setting.

The systematic studies of the choice and configuration of different MC generators for SM $t\bar{t}$ production presented in [170] and [171] were partly motivated by a **discrepancy between MC predictions and observed data** in the p_T distribution for the top quarks at high p_T^{top} which has been observed with all generator, parameter and PDF choices studied so far, including the SM $t\bar{t}$ MC sample with `hdamp` $= m_{top}$ used in this thesis: The p_T spectrum of the top quarks in all simulated samples is found to be harder than the one observed in data, the discrepancy increasing with p_T^{top}. For $p_T^{\text{top}} \approx 1$ TeV, the cross-section predicted by simulations is between 30 and 70% larger than the one measured in data, the size of the deviation depending on the choice of MC generator [172]. Investigations into the cause of this discrepancy involving both theorists and experimentalists are in progress, but no conclusive explanation has been found to date. A similar discrepancy is visible in the $m_{t\bar{t}}$ distributions in Sections 6.1.3; its impact on the search results will be discussed in Section 7.

In order to estimate the systematic uncertainties related to the modelling choice described above, additional $t\bar{t}$ samples with alternative generator combinations and parameter settings have been produced and compared to the nominal POWHEG+PYTHIA $t\bar{t}$ sample. Details are given in Section 5.6.3.

The generated NLO cross-section times branching ratio for the nominal $t\bar{t}$ sample, which, like the samples for the derivation of systematic uncertainties, contains only dileptonic and semileptonic $t\bar{t}$ decays, is 114.51 *pb*. All samples are normalised to the NNLO+NNLL cross-section calculated with TOP++ 2.0 (Section 2.2.1). The corresponding k-factor is 1.1992.

Finally, the $t\bar{t}$ events are reweighted to take into account higher-order electroweak corrections to the $t\bar{t}$ kinematics. These corrections are applied for the first time in this iteration of the analysis.[13] They are based on calculations by J. Kühn, A. Scharf and P. Uwer [175] and calculated using an extended version of the HAdronic Top and Heavy quarks crOss section calculatoR

[13] Electroweak virtual corrections based on calculations by A. Manohar and M. Trott [173] were taken into account in the form of a systematic uncertainty in an earlier published version of the search [174].

HATHOR [57] (HATHOR 2.1-alpha). The calculations yield both the differential cross-section of the electroweak correction, σ_W, and the differential cross-section at LO in QCD, σ_{LO}. The scale factor $w = 1 + \frac{\sigma_W}{\sigma_{LO}}$ depends on the parton kinematics of an event as well as the parton types in the initial state. Details on the application of these scale factors to NLO MC samples can be found in Appendix E of [2].

Background from Single-Top Production

The production of single top quarks is simulated with the POWHEG-BOX generator interfaced with PYTHIA v6.426. The same configuration as for the generation of the $t\bar{t}$ samples is used. The overlap between the Wt and $t\bar{t}$ samples is taken into account by applying the diagram removal scheme described in [176]. All samples are normalised to the approximate NNLO cross-sections [177, 178, 179]. The values for the cross-section times branching ratio and the k-factors for the different single-top samples are summarised in Table 3.5. The uncertainty on the cross-section for this background component is given in Section 5.6.3.

Sub-sample	$\sigma \times BR$ [pb]	k-factor
t-channel, top	17.519	1.0501
t-channel, antitop	9.3964	1.0613
s-channel	1.6424	1.106
Wt-channel	20.461	1.0933

Table 3.5.: Cross-section times branching ratio $\sigma \times BR$ and k-factors for the single-top samples. Sample information provided by the ATLAS Top Working Group [159].

Background from Vector-Boson Production in Association with $t\bar{t}$ ($t\bar{t}V$)

Vector-boson production in association with $t\bar{t}$ is modelled with MADGRAPH5 interfaced with PYTHIA v6.426 and using the CTEQ6L1 PDF set. The samples are normalised to NLO in α_s [180] and the values for the k-factors as well as the simulated cross-section times branching ratio are given in Table 3.6. The uncertainty on the cross-section for this background component is given in Section 5.6.3.

Background from W+jets Events

The production of W bosons in association with hadronic jets (W+jets) constitutes another relevant background in the search presented in this thesis. The ALPGEN [181] generator is used to simulate the production of W bosons with up to five extra partons in the ME, using the

Sub-sample	$\sigma \times BR$ [pb]	k-factor
$t\bar{t} + W$	0.10410	1.1700
$t\bar{t} + W + j$	0.0933317	1.1700
$t\bar{t} + Z$	0.067690	1.3500
$t\bar{t} + Z + j$	0.087339	1.3500

Table 3.6.: Cross-section times branching ratio $\sigma \times BR$ and k-factors for the $t\bar{t} + V$ samples. Sample information provided by the ATLAS Top Working Group [159].

CTEQ6L1 PDF set. ALPGEN is interfaced with PYTHIA v6.426 for the PS. Like in the case of the $t\bar{t}$ samples, the Perugia2011C tune is used. For technical reasons, events are generated in mutually exclusive samples according to the number of extra partons (Np) in the ME final state. The MLM matching scheme [182] is applied to combine the ME with the PS and to avoid the double-counting of events which would otherwise occur because $W + n$-jet events may either correspond to a final state with n partons in the ME or from a final state with $n - 1$ partons in the ME and another hard parton arising from the PS.

Two sets of W+jets samples are generated: In W+**light-flavour** (W+LF) samples, the extra final-state partons are gluons or massless down, up, strange or charm quarks. Samples with massive heavy-flavour (c and b) partons in the ME final state are generated separately. These W+**heavy-flavour** (W+HF) samples comprise $W + b\bar{b}$, $W + c\bar{c}$ and $W + c\,(\bar{c})$ events. While the MLM matching scheme accounts for the overlap between subsamples with different parton multiplicities in the ME, as explained above, ALPGEN does not automatically account for the overlap between the W+LF and W+HF samples. This overlap occurs because in W+LF events additional heavy quarks can be produced in the PS, for example by gluons splitting to $b\bar{b}$ pairs. The W+LF samples are complementary to the W+HF samples in that they provide a more accurate description of small opening angles between heavy-flavour jets which are typical for gluon splittings in the PS. The ME production of heavy-flavour jets in the W+HF samples, in contrast, is more appropriate for large angular separations. These differences in phase-space coverage can be exploited to avoid the double-counting of events by vetoing events in different samples based on appropriate kinematic criteria. Details on the approach adopted by ATLAS can be found in Section 4 of [183].

The values of $\sigma \times BR$ for the W+LF and W+HF samples are listed in Tables 3.7 and 3.8, respectively. In order to provide sufficient statistics in the boosted regime of the search presented in this thesis, another set of W+jets samples has been generated with the same settings as

described above, but with the additional requirement that all events contain at least one trimmed AKT10 truth jet (Section 4.3) with $p_T > 250$ GeV. The corresponding values of $\sigma \times BR$ for these *filtered* samples are given in the second column of the tables. A k-factor of 1.133 (1.520 for the $W+c$ (or $\bar{c}$) samples) is applied to correct the cross-sections to NNLO in α_s based on calculations with FEWZ [184], which have been documented in [185]. To improve the MC modelling of the W+jets background, scale factors for the overall normalisation and the individual flavour fractions are derived using data-driven methods. The derivation of the scale factors is described in Section 5.5.1; the systematic uncertainties related to the W+jets background are discussed in Section 5.6.3.

Sub-sample	$\sigma \times BR$ [pb] (unfiltered)	$\sigma \times BR$ [pb] (AKT10-filtered)
$W(e\nu)$+Np0	8136.8	-
$W(e\nu)$+Np1	1791.5	0.71565
$W(e\nu)$+Np2	541.60	1.9920
$W(e\nu)$+Np3	146.65	2.2144
$W(e\nu)$+Np4	37.334	1.4867
$W(e\nu)$+Np5 (incl.)	11.355	1.1185
$W(\mu\nu)$+Np0	8133.4	-
$W(\mu\nu)$+Np1	1792.7	0.70640
$W(\mu\nu)$+Np2	541.27	1.9221
$W(\mu\nu)$+Np3	146.49	2.1249
$W(\mu\nu)$+Np4	37.341	1.4169
$W(\mu\nu)$+Np5 (incl.)	11.364	1.0612
$W(\tau\nu)$+Np0	8135.7	-
$W(\tau\nu)$+Np1	1793.7	0.70468
$W(\tau\nu)$+Np2	541.24	1.9309
$W(\tau\nu)$+Np3	146.48	2.1416
$W(\tau\nu)$+Np4	37.344	1.4297
$W(\tau\nu)$+Np5 (incl.)	11.477	1.0705

Table 3.7.: Cross-section times branching ratio $\sigma \times BR$ for unfiltered and filtered W+LF samples. Sample information provided by the ATLAS Top Working Group [159].

Background from Z+jets Events

Events with Z bosons produced in association with jets constitutes another, albeit smaller, background to the search presented in this thesis. Z+jets events are generated with ALPGEN interfaced with PYTHIA v6.426 using the same configuration as for the generation of the W+jets samples. The different Z+LF and Z+HF subsamples and the corresponding values of $\sigma \times BR$ are given in Tables 3.9 and 3.10, respectively. The k-factor for the NNLO cross-section calculated with FEWZ is 1.1800 for all samples [185]. The uncertainty on the cross-section for this back-

Sub-sample	$\sigma \times BR$ [pb] (unfiltered)	$\sigma \times BR$ [pb] (AKT10-filtered)
$W + b\bar{b}$+Np0	52.237	0.012462
$W + b\bar{b}$+Np1	45.628	0.11981
$W + b\bar{b}$+Np2	23.955	0.28254
$W + b\bar{b}$+Np3 (incl.)	13.633	0.73213
$W + c\bar{c}$+Np0	149.39	0.013282
$W + c\bar{c}$+Np1	143.90	0.22439
$W + c\bar{c}$+Np2	84.227	0.69188
$W + c\bar{c}$+Np3 (incl.)	44.277	1.7859
$W + c$ (or $\bar{c}$)+Np0	758.93	0.087468
$W + c$ (or $\bar{c}$)+Np1	274.47	0.47215
$W + c$ (or $\bar{c}$)+Np2	71.643	0.56999
$W + c$ (or $\bar{c}$)+Np3	16.482	0.37909
$W + c$ (or $\bar{c}$)+Np4 (incl.)	4.7824	0.29910

Table 3.8.: Cross-section times branching ratio $\sigma \times BR$ for unfiltered and filtered W+HF samples. Sample information provided by the ATLAS Top Working Group [159].

ground is given in Section 5.6.3. No special filtered samples are produced since Z+jets events constitute one of the smallest background components in the signal region (Section 6.1.1).

Sub-sample	$\sigma \times BR$ [pb]
$Z(e^+e^-)$+Np0	718.97
$Z(e^+e^-)$+Np1	175.70
$Z(e^+e^-)$+Np2	58.875
$Z(e^+e^-)$+Np3	15.636
$Z(e^+e^-)$+Np4	4.0116
$Z(e^+e^-)$+Np5 (incl.)	1.2592
$Z(\mu^+\mu^-)$+Np0	719.16
$Z(\mu^+\mu^-)$+Np1	175.74
$Z(\mu^+\mu^-)$+Np2	58.882
$Z(\mu^+\mu^-)$+Np3	15.673
$Z(\mu^+\mu^-)$+Np4	4.0057
$Z(\mu^+\mu^-)$+Np5 (incl.)	1.2544
$Z(\tau^+\tau^-)$+Np0	718.87
$Z(\tau^+\tau^-)$+Np1	175.76
$Z(\tau^+\tau^-)$+Np2	58.856
$Z(\tau^+\tau^-)$+Np3	15.667
$Z(\tau^+\tau^-)$+Np4	4.0121
$Z(\tau^+\tau^-)$+Np5 (incl.)	1.2560

Table 3.9.: Cross-section times branching ratio $\sigma \times BR$ for Z+LF samples. Sample information provided by the ATLAS Top Working Group [159].

Sub-sample	$\sigma \times BR$ [pb]	Sub-sample	$\sigma \times BR$ [pb]
$Z(e^+e^-) + b\bar{b}$+Np0	6.5083	$Z(e^+e^-) + c\bar{c}$+Np0	11.763
$Z(e^+e^-) + b\bar{b}$+Np1	3.2927	$Z(e^+e^-) + c\bar{c}$+Np1	7.1280
$Z(e^+e^-) + b\bar{b}$+Np2	1.2544	$Z(e^+e^-) + c\bar{c}$+Np2	3.3603
$Z(e^+e^-) + b\bar{b}$+Np5 (incl.)	0.61711	$Z(e^+e^-) + c\bar{c}$+Np2 (incl.)	1.7106
$Z(\mu^+\mu^-) + b\bar{b}$+Np0	6.5056	$Z(e^+e^-) + c\bar{c}$+Np0	11.795
$Z(\mu^+\mu^-) + b\bar{b}$+Np1	3.2904	$Z(e^+e^-) + c\bar{c}$+Np1	7.1123
$Z(\mu^+\mu^-) + b\bar{b}$+Np2	1.2601	$Z(e^+e^-) + c\bar{c}$+Np2	3.3708
$Z(\mu^+\mu^-) + b\bar{b}$+Np3 (incl.)	0.61882	$Z(e^+e^-) + c\bar{c}$+Np3 (incl.)	1.7059
$Z(\tau^+\tau^-) + b\bar{b}$+Np0	6.5062	$Z(e^+e^-) + c\bar{c}$+Np0	11.760
$Z(\tau^+\tau^-) + b\bar{b}$+Np1	3.2935	$Z(e^+e^-) + c\bar{c}$+Np1	7.1410
$Z(\tau^+\tau^-) + b\bar{b}$+Np2	1.2485	$Z(e^+e^-) + c\bar{c}$+Np2	3.3582
$Z(\tau^+\tau^-) + b\bar{b}$+Np3 (incl.)	0.61363	$Z(e^+e^-) + c\bar{c}$+Np3 (incl.)	1.7046

Table 3.10.: Cross-section times branching ratio $\sigma \times BR$ for Z+HF samples. Sample information provided by the ATLAS Top Working Group [159].

Background from Diboson Production

The background from diboson (WW, WZ, ZZ) production with up to three extra jets in the ME is simulated with the SHERPA [186] v1.4.1. generator using the CT10 [168] PDF set and taking into account the masses of b- and c-quarks. All subsamples are normalised to calculations at NLO in α_s obtained with MCFM [187] and documented in [185]. The simulated values for $\sigma \times BR$ and the k-factors are summarised in Table 3.11. The uncertainty on the cross-section for this background component is given in Section 5.6.3.

Sub-sample	$\sigma \times BR$ [pb]	k-factor
$WW \to e\nu qq$	7.2854	1.0600
$WW \to \mu\nu qq$	7.2974	1.0600
$WW \to \tau\nu qq$	7.2741	1.0600
$WZ \to e\nu qq$	1.4648	1.0500
$WZ \to \mu\nu qq$	1.4634	1.0500
$WZ \to \tau\nu qq$	1.4523	1.0500
$ZW \to eeqq$	1.9036	1.0500
$ZW \to \mu\mu qq$	1.9057	1.0500
$ZW \to \tau\tau qq$	1.9152	1.0500
$ZZ \to eeqq$	0.24672	1.0000
$ZZ \to \mu\mu qq$	0.24757	1.0000
$ZZ \to \tau\tau qq$	0.24167	1.0000

Table 3.11.: Cross-section times branching ratio $\sigma \times BR$ and k-factors for the diboson samples. Sample information provided by the ATLAS Top Working Group [159].

3.5. Summary

The Large Hadron Collider (LHC) is a *pp* collider that has been operating at a centre-of-mass energy of $\sqrt{s}$ =8 TeV in 2012, reaching a peak luminosity of $\mathcal{L} = 7.73 \cdot 10^{33}$ cm^{-2} s^{-1}. The ATLAS detector is one of two general-purpose detectors at the LHC suited for a wide range of new physics searches and precision measurements. It consists of a mostly silicon-based tracking detector surrounded by a calorimeter system and a muon spectrometer and is equipped with a fast and efficient trigger and data-acquisition (TDAQ) system specifically designed for the high luminosities at the LHC. The data is stored and processed using a world-wide computing grid. Monte Carlo (MC) simulations of the *pp* collisions and subsequent interactions with the detector material are another vital part of particle-physics analyses. The MC samples used in this thesis have been described in detail in the final sections of this chapter.

4. Reconstruction and Identification of Physics Objects

The information from the various ATLAS subdetectors is used to reconstruct and identify a number of physics objects, such as electrons, muons and hadronic jets, which are used to select collision events for further analysis. In the following, a detailed account of the objects used in the search presented in this thesis is given. The reconstruction, identification and calibration procedures discussed here are based on the recommendations of the ATLAS Top Working Group and the respective Combined Performance groups, unless otherwise stated.

4.1. Electrons

4.1.1. Reconstruction, Identification and Isolation

Electrons in the central region of the detector are reconstructed by matching EM calorimeter clusters to ID tracks. The geometric coverage of the ID limits the acceptance region for these electrons to $|\eta^{cl}| < 2.47$ where η^{cl} is the pseudorapidity of the EM cluster. Note that it is possible to reconstruct electrons up to $|\eta^{cl}| < 4.9$ using the EM forward calorimeters. In this thesis, only central electrons are selected and hence only these are discussed in the following.

The electron **reconstruction** starts from seed clusters that are built from radial EM calorimeter towers of size[1] $\Delta\eta \times \Delta\phi = 0.025 \times 0.025$ using a sliding-window algorithm [188]. Track candidates for the reconstruction of central electrons are selected from ID tracks with $p_T > 0.4$ GeV within a $\Delta R < 0.3$ cone around the seed-cluster barycentre based on the differences in η and ϕ between the seed cluster and the track extrapolated to the middle layer of the EM calorimeter. The ID hits associated with the selected track candidates are refitted using the Gaussian Sum Filter (GSF) [189] algorithm, which yields a more accurate estimate of the track parameters compared to the standard ATLAS Global χ^2 Track Fitter [190] by taking into account non-linear bremsstrahlung effects. The track-cluster matching is repeated using the refitted track parameters with tighter matching and additional track-quality criteria. The clusters of the re-

[1] This size corresponds to the granularity of the EM accordion calorimeter middle layer.

sulting electron candidates are built around the seed clusters to form clusters of 3×7 (3×5) cells in the barrel (endcap) of the EM accordion calorimeter. Further details on the reconstruction of electron candidates can be found in Section 3 of [191].

The electron four-momentum is determined using the angular coordinates η^{trk} and ϕ^{trk} of the track, which are known to higher precision than those of the EM cluster. The energy is set to the cluster energy E^{cl}, which is calibrated to the EM scale, as explained in Section 4.1.2, and the transverse energy is calculated as $E_T = E^{cl}/\cosh(\eta^{trk})$.

Various **identification** criteria are imposed on the reconstructed electron candidates to select *prompt* electrons. These are electrons from the decays of W- and Z-bosons that are produced in the primary hard-scattering process or, in the case of W-bosons, in the decay of a top quark. Electrons from other sources must be rejected effectively. These can be broadly classified into *non-prompt* electrons from photon conversion into electron-positron pairs, semileptonic decays of heavy-flavour hadrons or in-flight decays of charged pions, and *"fake"* electrons. The latter are associated with hadronic jets that have a large electromagnetic component due to decays such as $\pi \to \gamma\gamma$ and are falsely reconstructed as electrons.

A set of discriminating variables is used to distinguish prompt electrons from the background of non-prompt and "fake" electrons. They comprise shower-shape variables of the EM cluster as well as track quality and track-cluster matching variables. Three electron quality categories with different levels of background rejection are defined by successively adding more variables and tightening the selection criteria on existing ones: `loose`, `medium` and `tight`. The three categories are strictly inclusive, the `tight` category being a subset of the `medium` category, the latter being a subset of the `loose` category. A complete overview of the categories and definitions of the discriminating variables is given in Section 4 of [191].

The electrons used in this search are required to be in the `tight` category with the additional requirement that the *longitudinal impact parameter* z_0 must be smaller than 2 mm. The longitudinal impact parameter is defined as the z-coordinate of the point of closest approach. A schematic representation is given in Figure 4.3 of Section 4.3.5. Electrons must also fulfill $E_T > 25$ GeV and be within $|\eta| < 2.47$, excluding the transition region $1.37 < |\eta| < 1.52$ between the barrel and endcap calorimeters, which suffers from a degraded electron energy resolution due to the large amounts of un-instrumented material.

In addition, an **isolation** requirement is imposed on all electrons used in the search presented in

this thesis to further suppress the background from non-prompt and "fake" electrons, the main source of which is QCD multi-jet production (Section 5.5.2). An electron is considered isolated if the sum of the transverse momenta of all tracks within a cone with radius $\Delta R = 10\ \text{GeV}/E_T$ centered on the electron cluster is smaller than 5% of the transverse energy E_T of the electron. Only tracks with $p_T^{trk} > 1$ GeV and at least four hits in either the pixel detector or the SCT are considered. They must be associated with the primary vertex (Section 3.2.2) to make the isolation criterion more robust against pile-up. The electron track itself is excluded from the sum. This isolation concept is known as **mini-isolation** [192] and was first used in ATLAS in the search for resonances decaying to $t\bar{t}$ final states at $\sqrt{s} = 7$ TeV [39]. With its variable cone size, it provides a consistently high signal efficiency for electrons from the leptonic decays of highly-energetic top quarks for which the average angular separation between the electron and the b-jet decreases with increasing p_T^{top}.

4.1.2. Energy Scale and Resolution

The energy of the EM cluster is calibrated to correctly account for the energy of the electron that initiated the EM shower in the calorimeter [193]. This energy scale is referred to as the **EM scale**. It is established via test beam measurements with additional corrections derived from simulations and collision data: The MC-based calibration uses a multivariate algorithm [194] to correct the cluster energy for losses in the material upstream of the EM calorimeter, energy deposited outside of the cluster (lateral leakage) and losses for highly-energetic showers not contained within the EM calorimeter. Further corrections derived from collision data are described in Section 6 of [193]. Finally, an in-situ calibration is performed using $Z \to e^+e^-$ events: The energy of electrons in data is scaled so that the *peak* of the Z-boson invariant-mass distribution is centered at its known mass. Moreover, the energy of simulated electrons is smeared so that the *width* of the distribution in MC events matches that measured in data. After the calibration, the energy scale is known to an accuracy of 0.03-0.2% (0.3-2.3%) for electrons with $E_T = 40$ GeV (200 GeV), the exact values depending on the pseudorapidity range. The energy resolution is around 2.5% at $E_T = 25$ GeV and drops to below 1% for $E_T > 200$ GeV.

4.1.3. Single-Electron Triggers

The analysis presented in this thesis uses two single-electron triggers to select events in the e+jets final state: The first trigger, `EF_e60_medium1`, accepts all events with at least one EF

electron with $E_T > 60$ GeV that passes the EF `medium` quality requirements.[2] The second trigger, `EF_e24vhi_medium1`, has a lower E_T threshold of 24 GeV, combined with a fixed-cone isolation requirement: The transverse momentum sum of all tracks (excluding the electron track) within a cone with radius $\Delta R < 0.2$ around the electron must be less than 10% of the electron transverse energy. Only tracks with $p_T > 1$ GeV associated with the primary vertex are considered. This isolation requirement is necessary to keep the trigger rates for this lower E_T trigger threshold at a manageable rate without *prescaling* the trigger, that is without limiting the trigger output to a fraction 1/N of all events passing the trigger requirements. `EF_e24vhi_medium1` and `EF_e60_medium1` are the lowest un-prescaled isolated and non-isolated single-electron triggers, respectively. In the analysis presented in this thesis they are used in an **OR combination**, meaning that an event is accepted for further analysis if it accepted by at least one of them.

4.1.4. Efficiencies and Corrections Applied to MC Events

The overall efficiency ϵ_{total} for selecting an electron is the product of the efficiency of the electron being correctly reconstructed (ϵ_{reco}), the efficiencies of it passing the identification and isolation requirements (ϵ_{id} and ϵ_{iso}, respectively) and the trigger efficiency (ϵ_{trig}) in the case that an electron trigger is used, $\epsilon_{\text{total}} = \epsilon_{\text{reco}} \cdot \epsilon_{\text{id}} \cdot \epsilon_{\text{iso}} \cdot \epsilon_{\text{trig}}$. For electrons with $E_T > 25$ GeV, all efficiencies are measured in $Z \to e^+e^-$ events using a **tag-and-probe method** to obtain a "clean and unbiased sample of electrons" [191]: One electron, which is required to pass a set of `tight` selection criteria, is used to *tag* the event. The second electron, which is initially only required to pass the `loose` selection, is used to *probe* the efficiency of interest. Further requirements are imposed to reduce other electron backgrounds such as "fake" or conversion electrons. The details of the tag-and-probe selection depend on the efficiency that is to be measured and are described in the references given in the following paragraphs.

The efficiencies in data and MC events are determined by the same method. For each type of efficiency, a **scale factor (SF)** is defined as $\text{SF} = \frac{\epsilon(\text{data})}{\epsilon(\text{MC})}$. The scale factors, which are parameterised in E_T and η of the electron, are applied as multiplicative corrections to the MC event weight to bring the MC efficiencies in agreement with those measured in data. All scale factors are found to be close to unity within a few percent.

The determination of the efficiencies and scale factors for the reconstruction and identification

[2] The electron quality categories at the EF are defined in the same way as those for offline electrons except that slightly looser selection criteria are applied on most variables.

of electrons that are well separated from hadronic jets, that is electrons for which the separation $\Delta R(e, \text{jet})$ from the closest anti-k_T $R = 0.4$ jet[3] is smaller than 0.4, is described in [191]. The search presented in this thesis also uses electrons *within jets* as described in [195] and in Section 5.2. The derivation of the identification scale factors for these electrons is described in Section 4 of [195]. The scale factors are obtained using the same method as in [191] but allowing $\Delta R(e, \text{jet}) < 0.4$. For $\Delta R(e, \text{jet}) < 0.6$ these scale factors are also parameterised in $\Delta R(e, \text{jet})$ and the transverse momentum p_T^{jet} of the closest jet in addition to the usual parameterisation in E_T and η of the electron [195]. This additional binning allows for a better understanding of the electron identification in highly boosted top-quark decay topologies where the distance between the electron and the b-jet from the leptonic top-quark decay decreases with increasing transverse momentum of the top-quark (and hence the b-jet). The reconstruction efficiency is found to be 98-99% for electrons with $E_T > 25$ GeV and the corresponding scale factors differ by at most 1-2% from unity with an uncertainty of less than 0.5%. The identification efficiency for `tight` electrons is around 70% for $E_T = 25$ GeV and rises to above 90% for $E_T > 80$ GeV. The corresponding scale factors agree with unity within 4% with uncertainties of up to 2% for electrons with $\Delta R(e, \text{jet}) > 0.4$ [191] and up to 8% for $\Delta R(e, \text{jet}) < 0.4$ [195]. The uncertainty in the latter case is dominated by the statistical uncertainty, which is larger than in the former case due to the additional binning in $\Delta R(e, \text{jet})$ and p_T^{jet}.

The efficiency of mini-isolation is evaluated in $Z \to e^+e^-$ events on `tight` probe electrons. It ranges between 90% for $E_T = 25$ GeV and around 100% for $E_T > 40$ GeV; the scale factors are within 1% of unity with an uncertainty below 0.5% [196]. An additional uncertainty of 2% has been added in quadrature to account for the known differences between $Z \to e^+e^-$ events and the denser topologies of $t\bar{t}$ events [196]. It has been evaluated by comparing tag-and-probe results from an inclusive $Z \to e^+e^-$ sample with results obtained on a $Z \to e^+e^-$ subsample with at least three additional jets [2].

The trigger efficiencies and scale factors are measured on `tight`, mini-isolated probe electrons [197, 196]. For the OR combination of `EF_e2vh4i_medium1` and `EF_e60_medium1`, the trigger efficiency ranges between around 90% for $E_T = 25$ GeV and around 98% for $E_T > 100$ GeV. The scale factors are found to be in the range 0.95-1.1 with uncertainties of 0.5-2.5% depending on the (E_T, η) bin.

[3] For a definition of the different types of hadronic jets see Section 4.3.1.

4.2. Muons

4.2.1. Reconstruction, Identification and Isolation

The design of the ATLAS detector allows for *stand-alone* muon reconstruction and identification using information from the MS only. Both the muon momentum resolution and identification efficiency are, however, considerably improved by taking into account additional tracking information from the ID. Throughout this thesis, *combined* muons are used: The ID and MS tracks are reconstructed independently and the reconstruction starts from stand-alone MS tracks for which matching ID tracks are identified based on a χ^2 minimisation that takes into account the differences between the ID and MS track parameters [198]. Three different algorithms have been developed to combine the ID and MS track objects [199]. The muons used in this thesis have been reconstructed with the `MuID` algorithm, which performs a global refit of the muon track using both ID and MS hits. The use of ID tracks limits the acceptance region for combined muons to $|\eta| < 2.5$. In addition, the muon transverse momentum is required to be greater than 25 GeV throughout this thesis.

Only combined `MuID` muons passing a certain number of quality criteria are considered for further analysis. These include various hit requirements on the ID track [199] as well as the requirement that the longitudinal impact parameter with respect to the primary vertex must be smaller than 2 mm. In addition to these criteria, which follow the recommendations of the Top Working Group, the analysis presented in this thesis uses the requirement that the significance[4] of the *transverse impact parameter* relative to the primary vertex, $|d_0/\sigma_{d_0}|$, is smaller than 3. This requirement has been added in order to further reduce the QCD multi-jet background in the signal regions while preserving the signal efficiency. The transverse impact parameter is defined as the distance between the track and the primary vertex at the point of closest approach in the $r - \phi$ projection and visualised in Figure 4.3 of Section 4.3.5.

The muons used in the search presented in this thesis are required to be isolated in order to suppress the background from sources of non-prompt muons.[5] The same **mini-isolation** requirement as for electrons (Section 4.1.3) is used, with the isolation cone centred on the muon ID track.

[4] The significance of the impact parameter "is defined as the ratio of the signed impact parameter to its total error" [139].

[5] Unlike in the case of electrons, hadronic jets faking a muon signature play a negligible role, because the reconstruction of combined muons does not rely on calorimeter information.

4.2.2. Momentum Scale and Resolution

The muon momentum scale and resolution in simulated events are corrected to those measured in data using a $Z \to \mu^+\mu^-$ tag-and-probe method as described in Section 5 of [199]. The corrections are derived separately for the ID and MS momenta and then propagated to the combined muon momentum. The scale corrections to the simulated ID track momenta are found to be below 0.1% while those for the MS track momenta range between 0.1% and 0.4% depending on the detector region. The resolution smearing corrections are below 10% and below 15% for the ID and MS track momenta, respectively.

4.2.3. Single-Muon Triggers

The analysis presented in this thesis relies on two single-muon triggers to select events in the μ+jets final state. The `EF_mu36_tight` trigger requires a single muon with $p_T > 36$ GeV. No isolation requirement is imposed. The `EF_mu24i_tight` trigger uses a lower p_T threshold of 24 GeV in combination with a fixed-cone isolation requirement identical to the one in Section 4.1.3, except that here the transverse momentum sum of all tracks must be less than 12% of the muon transverse momentum. `EF_mu24i_tight` and `EF_mu36_tight` are the lowest un-prescaled isolated and non-isolated single-muon triggers, respectively. Like the two electron triggers, these two triggers are used in an OR combination in the search presented in this thesis. For further technical details on these triggers see Section 2 of [143].

4.2.4. Efficiencies and Corrections Applied to MC Events

Like in the case of electrons discussed in Section 4.1.4, the efficiencies and scale factors for the reconstruction, identification, isolation and trigger selection are derived using a tag-and-probe method in $Z \to \mu^+\mu^-$ events.

The measurement of the reconstruction and identification efficiencies and scale factors for combined `MuID` muons is described in [199]. The scale factors are provided in bins of the muon charge and the η and ϕ coordinates.[6] The efficiencies in both data and MC events are found to be around 97% and the scale factors are within less than 5% of unity. The total uncertainty on the scale factors is calculated as the quadratic sum of the statistical and various systematic uncertainties of the tag-and-probe method. These include uncertainties on the data-driven background estimate and the selection criteria for the $Z \to \mu^+\mu^-$ event selection. For further details

[6] No p_T binning is used as the scale factor dependence in this variable is found to be negligible [199].

see Section 4.1.4 of [199]. Unlike the scale factors, the systematic uncertainty is p_T-dependent. It is of the order of 0.2% in the low p_T-regime and rises to around 1% at 1 TeV. The increase of the uncertainty with the transverse momentum is mostly driven by the reliability of the simulation of muon energy losses at large energies [200].

The efficiency of the mini-isolation requirement is also estimated using a $Z \to \mu^+\mu^-$ tag-and-probe method. The tag muon is required to pass the isolation requirement and the isolation efficiency is determined as the fraction of events in which the probe muon is isolated as well. Particular emphasis is placed on the performance in dense environments, similar to those in $t\bar{t}$ events. To study this performance, the selected $Z \to \mu^+\mu^-$ sample is divided into exclusive subsamples with one or more additional hard jets and the efficiencies in data and MC events are evaluated and compared separately within each subsample. The scale factors are found to be within less than 0.5% from unity in all distributions considered, the main difference coming from the comparison between the inclusive $Z \to \mu^+\mu^-$ sample and the subsample with at least three extra jets. Hence an isolation scale factor of 1.000 ± 0.005 is used for all simulated muons [196, 2].

The muon trigger efficiency is measured in $Z \to \mu^+\mu^-$ events using the tag-and-probe method described in [143] on mini-isolated probe muons [196]. The trigger efficiency for the OR of `EF_mu24i_tight` and `EF_mu36_tight` is found to be around 70% in the barrel and around 86% in the endcap region for $p_T > 25$ GeV and thus considerably lower than the corresponding values for the electron triggers, discussed in Section 4.1.4. This is a result of the limited geometric coverage of the muon trigger system, as explained in Section 3.2.4. The scale factors for the trigger efficiency are in the range 0.95 - 1.1 with uncertainties below 2%. Various sources of systematic uncertainties have been taken into account, including the dependence on pile-up interactions and the angular correlation between the two muons from the Z boson decay. A complete overview can be found in Section 6.1 of [143].

4.3. Hadronic Jets

Hadronic jets are localised groups of particles or energy deposits in a subdetector that are typically associated with the hadron shower initiated by a single final-state parton. This section deals with their reconstruction and calibration as well as with the identification of b-quark jets.

4.3.1. Reconstruction

Jets are defined by the *jet algorithm* used for their reconstruction and the *type of objects* chosen as input to this algorithm. Hence various *jet collections* may be defined for a single collision event.

Input Objects

Based on the type of input objects, the following types of jets are defined within ATLAS: **Truth-particle jets** are reconstructed from simulated particles with a lifetime τ that meets the requirement $c\tau > 10$ mm, but excluding muons and neutrinos as those leave little or no measurable energy deposits in the calorimeter.

Track jets are reconstructed from ID tracks and hence contain contributions from charged particles only. The input tracks are required to have a transverse momentum greater than 0.5 GeV and at least one (six) hits in the pixel (SCT) subdetector. In order to suppress contributions from pile-up tracks, only tracks associated with the vertex of the hard interaction are considered. This is achieved by imposing requirements on the longitudinal and transverse impact parameters, respectively: $|z_0 \sin\theta| < 1.5$ mm and $d_0 < 1.5$ mm.

Calorimeter jets are built from either towers or topological clusters of calorimeter cells, excluding clusters with negative energy. **Tower jets** consist of radial towers of calorimeter cells with a standard area of $\Delta\eta \times \Delta\phi = 0.1 \times 0.1$ in the $\eta - \phi$ plane. Details of the tower formation can be found in Section 6 of [201]. Tower jets are mostly used at trigger level as the reconstruction of calorimeter towers is considerably faster than that of topological clusters.

Calorimeter jets built from topological clusters are used in most physics analyses in ATLAS, including the analysis presented in this thesis. The topological clusters are designed to follow the shower development in the calorimeter while suppressing calorimeter noise. Their formation starts from seed cells with a signal-to-noise ratio (SNR) greater than 4. Neighbouring cells with SNR ≥ 2 are included iteratively. The SNR is calculated from the absolute energy deposited in a calorimeter cell divided by the RMS of the energy distribution. The latter is obtained from events triggered at random bunch crossings. In the last step of the cluster formation, a ring of "guard cells", consisting of all cells neighbouring the proto-cluster, is added. A splitting procedure based on the presence of multiple energy maxima in a cluster is applied to better separate showers initiated by close-by partons. Further details can be found in [188]. The

cluster energy is taken as the sum of energies of its constituent cells, its mass is set to zero and its angular position is obtained from the energy-weighted averages of the η- and ϕ-coordinates of the constituent cells. The minimum size of a topological cluster is $\Delta\eta \times \Delta\phi = 0.3 \times 0.3$ for a topological cluster consisting of a single seed cell surrounded by a ring of "guard cells" and assuming a cell size of $\Delta\eta \times \Delta\phi = 0.1 \times 0.1$ in the central region of the calorimeter.

Jet Algorithms

Various algorithms have been developed to reconstruct jets from a given set of input objects. The most common jet algorithms used by the LHC experiments today are **sequential recombination algorithms** in which the input objects or *proto-jets* are combined iteratively based on two metrics. For input objects i and j these are defined as follows:

$$d_{i,j} = \min\{p_{T,i}^{2n}, p_{T,j}^{2n}\} \cdot \Delta R_{i,j}^2 \tag{4.1}$$

$$d_{i,B} = p_{T,i}^{2n} \cdot R_0^2, \tag{4.2}$$

where $\Delta R_{i,j} = \sqrt{(y_i - y_j)^2 + (\phi_i - \phi_j)^2}$ denotes the angular distance between the two objects[7] and the user-defined parameters n and R_0 characterise the jet algorithm as explained below. In each recombination step, the smallest among all values of the metrics $d_{i,j}$ and $d_{i,B}$ is determined. If it belongs to a pairwise distance $d_{i,j}$, the two respective objects are combined into one by adding their four-vectors. This recombination approach is referred to as the *E-scheme* because the energy of the combined object is just the sum of the energies of the individual objects. If the smallest value belongs to an object-beam distance $d_{i,B}$, the object is considered a final jet and removed from the list of objects. The procedure is repeated with the updated list of proto-jets until some terminating condition is met. For all jet algorithms considered in this thesis, this is the case when all proto-jets have been combined into final jets. These algorithms are denoted as *inclusive*.

The clustering sequence defined by Equations 4.1 and 4.2 depends on two parameters which determine the properties of the resulting jet collection: The parameter n defines the clustering strategy: For $n = 0$, the two metrics $d_{i,j}$ and $d_{i,B}$ are independent of the transverse momenta of the proto-jets and the recombination is based purely on the angular separation variables $\Delta R_{i,j}$ with close-by objects being clustered first. This jet algorithm is known as the **Cambridge-**

[7] Note the difference between this definition and that in Equation 3.3 where the pseudorapidity η is used instead of the rapidity y. The two metrics are identical for massless objects but differ for proto-jets in later recombination steps which typically have non-negligible masses, a result of the use of the E-scheme recombination, see text.

Aachen (C/A) algorithm [202, 203]. The case $n = 1$ corresponds to the k_T **algorithm** [204, 205]. In this case, the clustering is based on both angular separation and transverse momentum and starts with the recombination of close-by, soft objects. This clustering sequence is sometimes described as a reversal of the angular- and momentum-ordered QCD parton shower which evolves from hard, wide-angle radiation, emitted early in the shower evolution, towards softer, smaller-angle emissions. Finally, the case $n = -1$ defines the **anti-k_T algorithm** [206], the most commonly used jet algorithm within ATLAS. In contrast to the k_T algorithm, jets are built starting from hard, well-separated objects. Hence the axes of the final jets are established within the first few recombination steps and the jets grow around these directions as softer and close-by particles are added. The resulting jets are approximately circular in the $\eta - \phi$ plane.

The second parameter in Equation 4.2, R_0, determines the size of the jets in the $\eta - \phi$ plane. In the following, jets with $R_0 \geq 0.8$ are referred to as **large-R jets**, those with smaller values of R_0 (typically 0.6 and below) as **small-R jets**. All jet collections for which R_0 is a *constant* parameter, such as those used in the search presented in this thesis, are collectively referred to as **fixed-R jets**. A generalisation of the clustering sequence in Equations 4.1 and 4.2, so-called **Variable-R jets** [5], for which R_0 becomes a function of the transverse momentum of the proto-jets are briefly discussed in the outlook (Chapter 9).

Jets reconstructed from the same input using different algorithms may differ notably in properties such as their size, shape and multiplicity. Hence the choice of jet algorithm usually depends on the requirements of a specific analysis, such as the final state and kinematic regime of interest. All jet algorithms, however, are required to meet a set of basic requirements [207]. In particular, the outcome of the jet clustering must not be affected by the splitting of an input object into two softer, collinear daughter objects (*collinear safety*) nor by the presence or absence of additional soft input particles, such as soft gluons (*infrared safety*[8]). These requirements are met by all jet algorithms discussed in this thesis.

The jet collections used in this thesis have been reconstructed with the FastJet software package [208, 209] which provides implementations of the most common algorithms, along with a number of extensions or *contribs* by external developers. The latter include an implementation of the Variable-R algorithm mentioned above.

[8] This requirement is important with regard to the ghost association techniques discussed in the following sections.

4.3.2. Mass and Substructure of Large-R Jets

The properties of large-R jets are of central importance in analyses involving highly-energetic, hadronically-decaying heavy particles, collectively referred to as *boosted objects*. The particle showers initiated by the hadronic decay products of boosted objects are collimated in the direction of the mother particle and tend to merge into a single jet with a characteristic **mass** and **substructure**, which can be used to distinguish boosted particle jets from those initiated by a single gluon or a lighter quark. Typically, boosted objects are reconstructed using a jet algorithm with a large R parameter to ensure that all decay products are contained within the jet.

The focus of this and the following section will be on the identification or **tagging** strategies for boosted top quarks that are used in the search presented in this thesis. More extensive summaries of the **top tagging** strategies developed by the ATLAS and CMS collaborations can be found in [210, 211] and [212], respectively. It should also be noted that similar techniques have been developed for the identification of boosted Higgs and W/Z bosons [213, 214].

An important discriminating variable that is used in the search presented in this thesis is the **jet mass**. It is expected to be close to m_{top} for a fully contained top jet and significantly smaller for jets from single gluons or lighter quarks. The jet mass is calculated as the mass of the four-momentum obtained by summing the four-momenta of all jet constituents, according to the E-recombination scheme introduced in the previous section. It should be noted that the jet mass does not arise from the masses of the constituents, which are massless, but depends upon the angular separation between them: The combined invariant mass m_{12} of two massless four-vectors, p_1 and p_2 with $m_1^2 = 0 = m_2^2$ is given by

$$m_{12}^2 = (p_1 + p_2)^2 = 2 \cdot E_1 \cdot E_2 \cdot [1 - \cos(\alpha_{12})], \tag{4.3}$$

where E_1, E_2 are the respective energies and α_{12} denotes the angle between the two four-vectors. Hence a large-R jet resulting from the merging of two separate, highly energetic small-R jets tends to be more massive than, for example, a gluon jet which has a more homogeneous energy distribution.

In addition to the jet mass, the substructure of jets can be analysed to identify jets resulting from boosted particle decays. Various substructure variables have been developed to identify

subjets or hard splittings within a large-R jet. An overview of commonly used variables can be found in [215]. The search presented in this thesis relies on a single substructure variable. The **first k_T splitting scale** $\sqrt{d_{12}}$ is obtained by reclustering the constituents of the anti-k_T $R = 1.0$ jet with the k_T algorithm. The separation $d_{12} = \min\{p_{T,1}^2, p_{T,2}^2\} \cdot \Delta R_{1,2}^2$ (see Equation 4.1 with $n = 1$) between the two proto-jets in the last recombination step is expected to be large for a two body decay, such as $t \to Wb$, which results in two (or three, depending on whether the two jets from the W-boson can be distinguished) distinct, hard subjets. These subjets typically correspond to the two proto-jets of the last k_T recombination step since the k_T algorithm clusters the hardest objects last, as explained above. In contrast, the splitting scale tends to be small for the more homogeneous jets initiated by a single lighter quark or gluon. This is illustrated in Figure 4.1b in the next section.

4.3.3. Mitigation of Pile-up Effects

Pile-up affects both the multiplicity and the properties of the reconstructed jets in an event. Various techniques have been developed to mitigate the effects of pile-up in order to isolate the kinematics of the hard interaction of interest. The search presented in this thesis relies on two techniques in particular, which are presented in the following. An additional pile-up correction is applied to small-R jets in the context of the calibration procedure discussed in Section 4.3.4.

Grooming Techniques

Grooming algorithms are designed to remove soft, wide-angle contamination related to pile-up and the UE from a given jet in order to increase the discriminating power of the jet mass and substructure variables. Three types of grooming algorithms are used by the LHC experiments: **trimming** [216], **pruning** [217] and **filtering** [218]. While pruning is the most common grooming technique within the CMS collaboration, analyses within ATLAS, including the search presented in this thesis, rely mostly on trimming which will hence be the focus of this section.

The trimming algorithm runs the k_T algorithm with a small size parameter R_{sub} on the constituents of a given ungroomed jet with transverse momentum p_T^{jet}. All k_T subjets with a transverse momentum fraction p_T^i / p_T^{jet} smaller than some threshold f are discarded. The constituents of the remaining subjets form the trimmed large-R jet. Throughout this thesis, the trimming parameters are $R_{\text{sub}} = 0.3$ and $f = 0.05$, which are the default parameters used by ATLAS during Run 1 [215].

The effect of trimming on the jet mass and the first k_T splitting scale, $\sqrt{d_{12}}$, is illustrated in Figure 4.1 for anti-k_T $R = 1.0$ jets built from clusters calibrated to the LCW scale (Section 4.3.4) and with with $500 < p_T^{\text{jet}} < 1000$ GeV on a $Z' \to t\bar{t}$ signal and a QCD multi-jet MC sample, respectively. The difference between trimmed (dashed lines) and ungroomed jets (dotted lines) is especially significant for the jet mass distributions in Figure 4.1a, which are particularly susceptible to the soft, wide-angle contaminations from pile-up according to Equation 4.3: For ungroomed jets, the signal mass distribution, which is expected to show a peak at m_{top}, corresponding to boosted top quarks for which the decay products are fully contained within a single jet, is shifted to around 200 GeV. Trimming restores the top-quark mass peak to its expected position and visibly improves the mass resolution around m_{top}. The second, smaller peak at m_W corresponds to hadronic top-quark decays in which the hadronic decay products from the W-boson are merged into an anti-k_T $R = 1.0$ jet, but the corresponding b-jet is reconstructed separately. In addition, the masses of jets from the QCD multi-jet background are greatly reduced, with the peak of the corresponding distribution shifted from around 150 GeV in the case without grooming to around 50 GeV when trimming is applied. As a result, the separation between top jets from the $Z' \to t\bar{t}$ signal and other jets from the QCD multi-jet background is significantly improved. A similar, albeit smaller improvement is observed for the distribution of the $\sqrt{d_{12}}$ variable in Figure 4.1b.

The mass and first k_T splitting scale of trimmed anti-k_T $R = 1.0$ jets serve as effective discriminants between jets associated with boosted hadronic top-quark decays and those initiated by lighter quarks or gluons, as illustrated in Figure 4.1. The selection criteria for large-R jets used in the search presented in this thesis are summarised in Section 5.2.2.

Jet Vertex Fraction

No grooming techniques have been applied to small-R jets within ATLAS during Run 1 as their smaller areas[9] make them less susceptible to the effects of pile-up. It is, however, necessary to reject extra jets originating from additional parton interactions (in-time pile-up) in order to reduce the combinatorial background in the event reconstruction (Section 5.4).

This is achieved by means of a track-based variable, the **jet vertex fraction (JVF)** [219] which is calculated for each jet with respect to the primary vertex of the hard interaction. The JVF is determined by first matching ID tracks to a given jet by means of a process called *ghost*

[9] See Section 4.3.4 for a definition of jet areas.

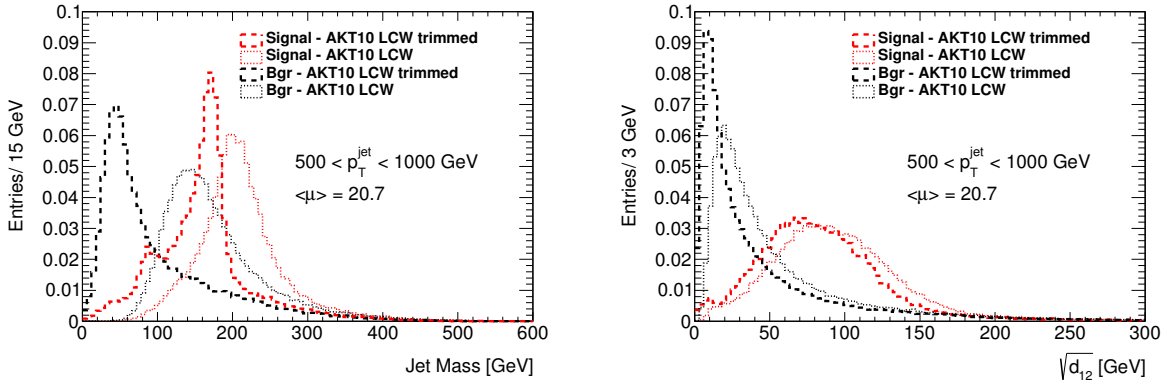

(a) **(b)**

Figure 4.1.: Comparison of trimmed (dashed lines) and ungroomed (dotted lines) anti-k_T $R = 1.0$ LCW jets with $500 < p_T^{\text{jet}} < 1000$ GeV for (a) the jet mass, and (b) the first k_T splitting scale $\sqrt{d_{12}}$ on simulated $Z' \to t\bar{t}$ signal and QCD multi-jet background events. All distributions are normalised to unity. Plots produced by the author but equivalent in content and style to figures in [215].

association. For each track a **ghost track** is created using the η and ϕ coordinates of the original track but setting the mass and transverse momentum of the ghost track to negligible values ($\mathcal{O}(10^{-100})$ GeV). These new objects are then added to the list of input objects for the jet clustering. In the case of an infrared jet algorithm, this does not affect the result of the jet clustering. The tracks corresponding to the ghost tracks that have been clustered into a given jet are considered matched to this jet. The JVF is then calculated as the ratio of the sum of the transverse momenta of the associated tracks that originate from the primary vertex to the sum of the transverse momenta of *all* associated tracks, independent of their origin. A JVF value close to one means that the jet most likely originates from the hard interaction whereas a value close to zero is characteristic for pile-up jets. For the search presented in this thesis, small-R jets with $p_T^{\text{jet}} < 50$ GeV are required to have JVF > 0.5. No JVF requirement is imposed on harder jets as these are less likely to originate from pile-up.

4.3.4. Calibration

The calibration of calorimeter jets and its associated uncertainties are of crucial importance for the majority of analyses at hadron colliders. First and foremost, the jet *energy* calibration must correct the energy *scale* of the reconstructed jet to that of the initial parton while optimising the energy *resolution* to allow for a precise reconstruction of the kinematics of the partonic process and the invariant masses of interest. In practice, the energy of the calorimeter jet is corrected to that of its corresponding truth-particle jet using MC simulations. The energy of the latter

may still differ from the energy of the initial parton due to showering and hadronisation effects or if the hadron shower is not fully contained within the jet. This effect can be addressed by an appropriate choice of the distance parameter R_0 (Equation 4.2), which has to be made at the analysis level. The goal of the calibration, in contrast, is to correct the properties of a given calorimeter jet for the various detector effects listed below, which is achieved by restoring its properties to that of the corresponding truth-particle jet. Additional jet *mass* and *substructure* calibrations are needed for analyses using these variables as selection criteria, such as the search presented in this thesis.

The complexity of the processes involved in the formation, detection and reconstruction of the hadron shower in the calorimeters requires sophisticated, multi-stage calibration methods to correct the jet energy, mass and substructure for a number of effects, which will be discussed in the following subsections:

- Calorimeter non-compensation (next section)
- Losses in dead or un-instrumented detector material
- Leakage of hadronic showers outside the calorimeter
- Losses due to energy deposits in cells failing the SNR requirements for the topological cluster formation (Section 4.3.1)
- Pile-up.

A sizeable number of uncertainties are associated with the different calibration methods. They are typically among the systematic uncertainties with the largest impact for analyses involving hadronic jets, in particular those involving large-R jets and substructure techniques, and much effort has been invested to optimise the calibration methods in order to minimise them. Details of the various uncertainties and their impact on the results of the search for resonances in $t\bar{t}$ final states are discussed in Section 5.6.2.

The Local Cluster Weighting Scheme

The calibration of both small-R and large-R calorimeter jets starts from topological clusters with energies at the EM scale (Section 4.1.2). This energy scale correctly represents the energy of EM clusters but not that of hadronic clusters because the energy of the hadronic shower is partly dissipated via nuclear processes, discussed in Section 3.2.3, that are hard to detect in the calorimeter. This effect is known as calorimeter *non-compensation*. To correct for the

lower calorimeter response to hadronic showers as well as for further energy losses due to noise thresholds and losses in dead material, a **Local Cluster Weighting (LCW) scheme** [220, 221] is applied: Topological clusters are assigned probabilities, classifying them as either EM or hadronic based on a number of cluster-shape variables. The energy of the calorimeter cells in a cluster is then corrected by a weighting factor that is derived from MC simulations of single pions and validated in test beam measurements. The weighting factor depends on the above-mentioned probability of the cluster being hadronic and is further parameterised as a function of the cell energy density and the cluster energy. Additional corrections for losses due to the SNR threshold applied in the selection of input cells for the cluster formation (Section 4.3.1) and energy losses in dead material are applied.

The LCW calibration corrects the energy of the topological clusters used as input to the jet algorithm for calorimeter effects, *independent* of the specific choice of jet algorithm. The subsequent calibration steps are applied at the level of the reconstructed jets to correct the jet energy to that of the parton by which it was initiated. This energy scale is referred to as the **Jet Energy Scale (JES)**. The JES calibration can be applied to jets reconstructed from clusters at the EM or LCW scale. Accordingly, the overall jet energy calibration is either referred to as EM+JES or LCW+JES. The advantages of the LCW+JES scheme over the simpler EM+JES scheme lies in its improved jet energy resolution and the reduced flavour dependence of the jet response [201]. Importantly, it not only corrects the overall jet energy scale but also restores the jet energy profile, a feature that is particularly important for analyses relying on jet substructure variables that are sensitive to the energy distribution within the jet. The energies of the calorimeter jets used in the search presented in this thesis are all calibrated using the LCW+JES scheme.

Jet Energy Scale Calibration of Small-R Jets

The energy scale of small-R jets in both data and MC events is calibrated in the following steps which are documented in [222] and outlined below:

- Origin correction
- Pile-up correction
- JES calibration (+ pseudorapidity correction)
- Global sequential calibration
- Residual corrections derived in-situ (applied to data only).

First, an **origin correction** is applied to change the jet direction such that it points to the primary vertex instead of the nominal interaction point in the detector centre. This is achieved by recalculating the four-momenta of the constituent topological clusters using the η- and ϕ-coordinates of the vector connecting the primary vertex to the cluster barycentre while keeping the mass and energy the same. The corrected jet four-momentum is then obtained as the sum of the corrected four-momenta of its constituents. The origin correction significantly improves the resolution in the η-coordinate of the jet direction [222] due to the finite length of the *beam spot* along the beam line. The beam spot or *luminous region* is the ellipsoid region around the interaction point in which pp interactions take place. During Run 1, this ellipsoid had a size of around 15 μm in the x- and y-direction and 45-50 mm in the z-direction [223]. Hence the position of the primary vertex along the beam line may vary significantly between events.

Next, a **pile-up correction** is applied to correct the jet energy and momentum for additional energy deposits from pile-up that have been absorbed into the jet. This correction is completely data-driven and applied on a jet-by-jet basis using the *jet area* as a measure of the susceptibility of a given jet to pile-up. The jet area is calculated by adding *ghost particles* to the event. These are neutral particles with negligible transverse momentum ($p_T = \mathcal{O}(10^{-100})$ GeV)[10] that are uniformly distributed in a fine $\eta - \phi$ grid. The addition of ghost particles has a negligible effect on the jet four-momenta but artificially increases the particle density in the event, thus allowing for the visualisation of jet areas based on how ghost particles are distributed between different jets in the η-ϕ plane. The number of ghost particles in a jet serves as a measure of the (scalar) jet area A^{jet}. The pile-up activity is measured by the median p_T density ρ in an event (see Section 6.2 in [219] for an exact definition) and treated as a small, uniform energy background. Under this assumption, the pile-up contribution to the transverse momentum p_T^{jet} of a jet with area A^{jet} is given by the product $\rho \cdot A^{\text{jet}}$. The corrected jet four-momentum $\mathbf{P}^{\text{jet,corr}}$ is then obtained as follows, preserving the jet direction:

$$\mathbf{P}^{\text{jet,corr}} = \left(\frac{p_T^{\text{jet}} - \rho \cdot A^{\text{jet}}}{p_T^{\text{jet}}} \right) \cdot \mathbf{P}^{\text{jet}}. \tag{4.4}$$

Additional residual corrections, parameterised in the number of primary vertexs, N_{PV}, and the number of interactions per bunch crossing, $< \mu >$, are applied to minimise the pile-up dependence that remains after the area correction. A full account of the procedure is given in [219]. The pile-up corrections significantly improve the jet energy resolution, which is diluted

[10] This procedure is similar to the ghost track association procedure discussed in Section 4.3.3.

by the pile-up energy deposits in the case of uncorrected jets.

Following the origin and pile-up corrections to the jet four-momentum, the (fully MC-based) **JES calibration** restores the energy of the reconstructed jet to that of the corresponding truth-particle jet. This calibration relies on the *jet energy response*

$$\mathcal{R}(E^{\mathrm{LCW}}_{\mathrm{corr.}}, \eta_{\mathrm{uncorr.}}) = \frac{E^{\mathrm{LCW}}_{\mathrm{corr.}}}{E^{\mathrm{truth}}}, \tag{4.5}$$

which is parameterised in terms of the pile-up corrected energy of the reconstructed jet at the LCW scale, $E^{\mathrm{LCW}}_{\mathrm{corr.}}$, and its η-coordinate *before* the origin correction,[11] $\eta_{\mathrm{uncorr.}}$. It is used to derive multiplicative correction factors, parameterised in the same variables, that are used to correct the jet energy $E^{\mathrm{LCW}}_{\mathrm{corr.}}$ to the LCW+JES scale. Details on the calculation of the correction factors are given in Section 8.3 of [201]. The jet energy response is measured in inclusive dijet MC samples with simulated pile-up [222] using all isolated calorimeter jets with a corresponding isolated truth-particle jet within $\Delta R < 0.3$. A calorimeter jet is considered isolated if there are no other calorimeter jets with $p_T > 7$ GeV within $\Delta R < 2.5 \cdot R$, where R is the distance parameter of the jet algorithm. Details on the jet selection and matching procedure can be found in Section 4.1 of [222].

The comparison between matched calorimeter and truth-particle jets is also used to further correct the origin-corrected pseudorapidity for local biases in poorly instrumented detector regions. Details on this **pseudorapidity correction** are given in Section 8.4 of [201].

Further corrections based on global jet properties, such as the information about associated ID tracks or activity in the MS behind the jet, have been developed in ATLAS during Run 1. These **global sequential (GS) corrections** [224] considerably improve the jet energy resolution and reduce the flavour dependence of the JES. They are, however, not applied to the jets used in the search presented in this thesis, since they had not been finalised by the time the final search strategy was formulated.

The final stage of the jet energy calibration consists of various **residual corrections**, which are applied in the form of calibration factors. These are derived in-situ by exploiting the transverse

[11] The JES calibration is designed to correct for response differences in different detector regions. The uncorrected η-coordinate, that is the coordinate evaluated with respect to the origin of the detector coordinate system, is the appropriate choice for the definition of the detector regions.

momentum balance between a hadronic jet and a well-calibrated reference object:

$$r = \frac{p_T^{\text{jet}}}{p_T^{\text{ref.}}}. \tag{4.6}$$

The ratio r is also referred to as the *in-situ jet response*. The calibration factors are based on the double ratio $r_{\text{data}}/r_{\text{MC}}$ calculated from the responses measured in data and MC events, respectively. They are applied to jets in data events only.

Various in-situ calibration methods based on different reference objects are combined to achieve a precise JES determination and optimal energy resolution over a large transverse momentum and pseudorapidity range. They are also used to evaluate many of the JES uncertainties discussed in Section 5.6.2.

First, any remaining differences in the energy response between jets in the central ($|\eta_{\text{corr.}}| < 0.8$) and forward ($0.8 < |\eta_{\text{corr.}}| < 2.4$) calorimeter regions are corrected using **dijet events** with one jet in the forward region balanced against a reference jet in the central region. This method is referred to as **η-intercalibration** and documented in [225]. The corresponding correction factors are generally below 2%. Next, **Z+jet** and **γ+jet events** are used to derive residual energy correction factors for central jets with $20 \leq p_T^{\text{jet}} \leq 200$ GeV (Z+jet) and $30 \leq p_T^{\text{jet}} \leq 800$ GeV (γ+jet) [226]. Finally, **multi-jet events** in which a single high-p_T jet recoils against a reference system of several low-p_T jets is used to derive corrections for jets with transverse momenta in the range $300 \leq p_T^{\text{jet}} \leq 1700$ GeV. The jets in the recoiling system have been fully calibrated using all previous in-situ corrections. For further details on the multi-jet balance calibration see [225]. The ratio of the response r measured in data and MC events using the the Z+jet, γ+jet and multi-jet balance techniques is shown Figure 4.2a as a function of p_T^{jet}. The combined result, which is also shown in the plot, is obtained as the weighted average of the individual results with weights derived from a χ^2-minimisation of the response ratios in each p_T bin, see Section 13.2 in [227] for details. The ratio is consistent with unity within 1% and the results obtained with the different methods are in very good agreement. For the derivation of the combined uncertainties see Section 5.6.2.

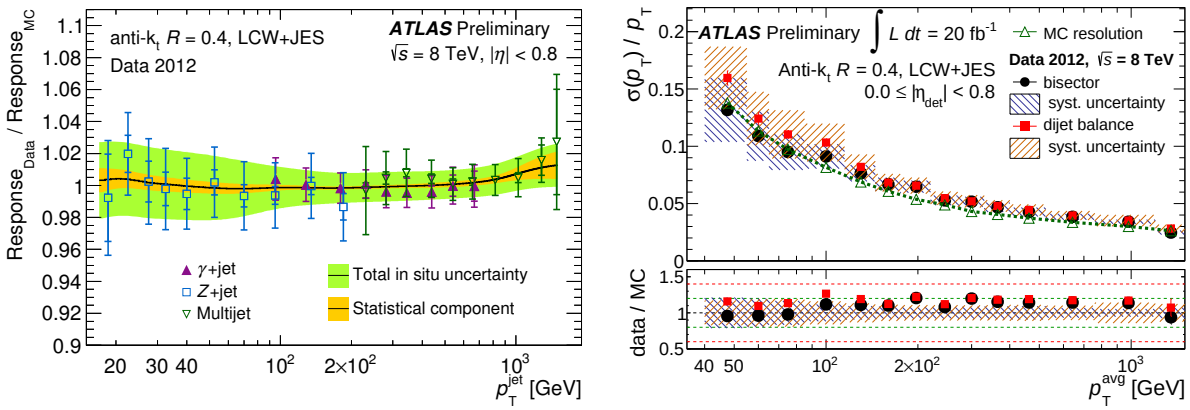

(a) (b)

Figure 4.2.: (a) Ratio of the jet responses (defined in Equation 4.6) in data and MC events as a function of p_T^{jet} for the Z+jet, γ+jet and multi-jet balance techniques and their combination (black line). The green and orange bands mark the total in-situ uncertainty and its statistical component, respectively. The results are derived for anti-k_T $R = 0.4$ jets calibrated to the LCW+JES scale. Taken from [228]. (b) Fractional jet energy resolution $\sigma(p_T)/p_T$ for central ($|\eta_{\text{corr.}}| < 0.8$) anti-$k_T$ $R = 0.4$ jets calibrated to the LCW+JES scale including in-situ corrections. The results measured in data using the in-situ methods described in the text are compared to the resolution in MC events. Taken from [225].

Jet Energy Resolution of Small-R Jets

The **jet energy resolution (JER)** is dominated by two effects: electronic detector noise and pile-up. Their impact on the fractional energy or transverse momentum resolution,[12] $\sigma(p_T^{\text{jet}})/p_T^{\text{jet}}$, is largest at low values of p_T^{jet}, where their relative contribution to the jet energy is largest. The jet energy resolution is measured in dijet events using two different techniques, the dijet balance and the bisector method, which are both described in [225]. The results are shown in Figure 4.2b for central jets calibrated to the LCW+JES scale including all in-situ corrections described above. The fractional resolution is below 10% for $p_T^{\text{jet}} > 100$ GeV and the values observed in data and MC events agree within less than 2%. The same holds for larger pseudorapidity values [225]. Therefore, no energy smearing is applied to jets in MC events. Instead, the jet energy resolution is taken into account as a systematic uncertainty, as described in Section 5.6.2.

Jet Energy Scale Calibration of Trimmed Large-R Jets

The energy scale of trimmed large-R jets is calibrated in a similar way to that of small-R jets: Starting from the LCW scale, the LCW+JES calibration is derived on MC events by comparing the energy response of the calorimeter jet to that of the associated truth-particle jet, using

[12] The two terms are often used equivalently: The transverse momentum is calculated from both the jet energy and pseudorapidity. Its resolution is dominated by the jet energy resolution because the pseudorapidity resolution is much smaller, in particular after the origin correction discussed above.

exactly the same approach as described in the previous section. In contrast to small-R jets, however, no pile-up correction is applied as the effects of pile-up are largely reduced by the trimming procedure already.

The in-situ calibration of large-R jets relies on the comparison of the transverse momentum of a calorimeter jet to that of a well-calibrated reference object on both data and MC events. Like the in-situ calibration of small-R jets, the double ratio $r_{\text{data}}/r_{\text{MC}}$ of the in-situ jet responses defined in Equation 4.6 is used to derive the in-situ corrections and the systematic uncertainties discussed in Section 5.6.2.

Two approaches, relying on different types of reference objects, are used: The *track-jet double-ratio method* uses track jets as reference objects. These are matched to calorimeter jets based on their angular separation ΔR, which is required to be smaller than 0.3 for a matching. This approach is motivated by the fact that the instrumental uncertainties on the energy and momentum scale of track jets are uncorrelated to those of calorimeter jets and that the track selection criteria, described in Section 4.3.1, render track jets less susceptible to the effects of pile-up. A full account of the method is given in Section 3.3 of [201]. The precision of the jet momentum scale determination that can be reached with this method is limited to 3-7% due to inefficiencies in the track finding and uncertainties regarding the MC simulation of the ratio of neutral and charged jet constituents [222]. Therefore, a second method, the *γ-jet balance method* [229] has been introduced which uses a highly energetic photon recoiling against a single large-R jet as a reference object. The uncertainty on the transverse momentum scale determined with this method is 2-3%.

Jet Mass Scale Calibration of Trimmed Large-R Jets

The mass of large-R jets plays a key role as a discriminating variable in the identification of boosted objects. The **jet mass scale (JMS)** must therefore be calibrated separately once the full JES calibration has been applied. The JMS calibration is based on the same principle as the MC-based JES calibration described in Section 4.3.4: The *jet mass response*

$$\mathcal{R}(E^{\text{LCW+JES}}, \eta_{\text{uncorr.}}) = \frac{m^{\text{LCW+JES}}}{m^{\text{truth}}} \tag{4.7}$$

is evaluated on a sample of simulated dijet events and correction factors are derived from the mean of a Gaussian fit of the response distribution in each jet energy and pseudorapidity bin.

The JMS is validated in-situ using the track-jet double-ratio method described in the previous section. This method is also used to determine the fractional uncertainty on the JMS, which is evaluated as a function of p_T^{jet}, η^{jet} and the ratio $m^{\text{jet}}/p_T^{\text{jet}}$ and is of the order of 4-6% for $|\eta^{\text{jet}}| < 0.8$ and around 10% for jets with $|\eta^{\text{jet}}| = 2.0$, $p_T^{\text{jet}} > 1$ TeV and $m^{\text{jet}}/p_T^{\text{jet}} = 0.6$ [222]. The same method is used to derive an uncertainty on the first k_T splitting scale, $\sqrt{d_{12}}$.

Jet Energy and Mass Resolution of Trimmed Large-R Jets

The fractional jet energy resolution and **jet mass resolution (JMR)** of large-R jets are measured in SM $t\bar{t}$ and high-mass Z' MC samples by comparing the energy (mass) of the reconstructed calorimeter jet to that of the corresponding[13] truth-particle jet: The JER is taken as the width of a Gaussian function that is fitted to the distribution of the fractional differences $(E^{\text{reco}} - E^{\text{truth}})/E^{\text{truth}}$. It ranges between 5% for $p_T^{\text{reco}} = 300$ GeV and 3% for $p_T^{\text{reco}} > 900$ GeV [230]. The JMR is measured in the same way using the distribution of the relative mass differences. It is around 7% over the whole p_T^{reco} range [230].

4.3.5. b-tagging

The identification or *tagging* of jets initiated by b-quarks, referred to as *b-jets* in the following, plays a key role in searches for new physics in the $t\bar{t} \to (W^+b)(W^-\bar{b})$ final state that is studied in this thesis. A number of dedicated algorithms have been developed to select b-jets with a high efficiency while minimising the number jets from light- and c-flavour partons that are mis-identified as b-jets.[14] They exploit characteristic properties of the b-hadron decay within the jet: After hadronisation, the b-hadron still carries around 70% of the original b-quark momentum [231]. Its comparatively large mass of > 5 GeV results in its decay products typically having large angles and transverse momenta with respect to the jet axis. Most importantly, the lightest b-hadrons can only decay via the weak force, giving them a relatively long lifetime of the order of 1.5 ps or $c\tau = 450$ μm [231]. Taking into account the relativistic boost factor $\beta\gamma$ this translates into an average decay length of $\beta\gamma c\tau \approx 3$ mm for a b-hadron in a jet with $p_T^{\text{jet}} = 50$ GeV and $\beta\gamma c\tau \approx 3$ cm for $p_T^{\text{jet}} = 500$ GeV. Hence the decay vertex can be reconstructed as a displaced, **secondary vertex**, as illustrated in Figure 4.3. Its associated tracks have large impact parameters d_0 and z_0 with respect to the primary vertex.

The properties of the b-hadron decay products may also be exploited in the b-tagging. The decay

[13] The jets are matched based on the same criteria as in the case of the MC-based JES calibration
[14] In this context, the term light-flavour jet refers to all jets initiated by d-, u- or s-quarks or gluons.

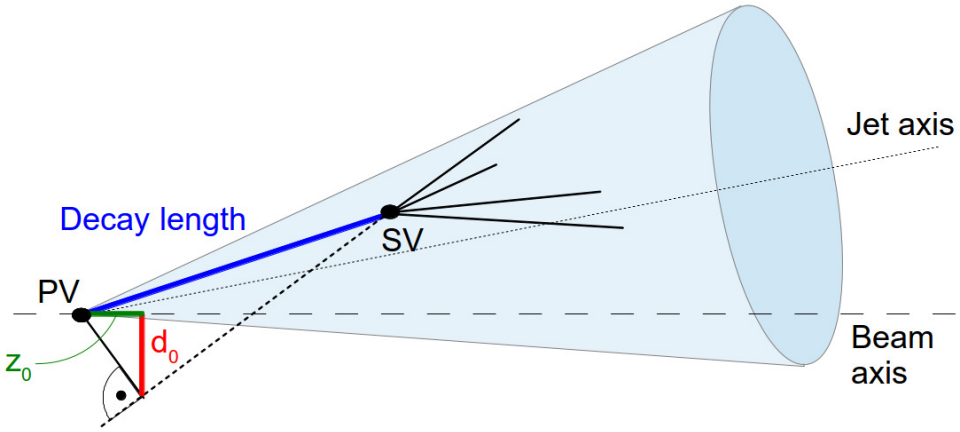

Figure 4.3.: Schematic illustration of the secondary vertex (SV), decay length and impact parameters d_0 and z_0 for a b-hadron decay within a jet emanating from the primary interaction vertex (PV).

of hadrons containing c-quarks, such as D-mesons, results in a displaced, **tertiary vertex** that is roughly in line with the primary vertex and secondary vertex. It is less significant than the secondary vertex due to the smaller mass and shorter decay length of c-hadrons. Furthermore, a soft muon inside a jet may indicate a semileptonic decay of a b-hadron.

Input to b-tagging Algorithms

All b-tagging algorithms rely crucially on the reconstruction and identification of three types of objects: vertices, ID tracks and jets. First, the primary vertex is selected among all vertices with ≥ 5 tracks as the one with the largest transverse momentum sum of associated tracks to ensure that it is the vertex of the hard interaction and not a PU vertex. The track quality requirements are designed to select only well-measured tracks while rejecting those from the decays of long-lived particles, such as K_s and Λ hadrons, tracks originating from interactions with the detector material and falsely reconstructed tracks. A track is required to have $p_T^{trk} > 1$ GeV, pass various hit requirements [232] and its impact parameters with respect to the primary vertex must fulfill $|d_0| < 1$ mm and $|z_0| \sin\theta < 1.5$ mm.

The jet direction and transverse momentum are used to determine the set of tracks associated to the jet that are to be used as input to the b-tagging algorithms. Tracks passing the above quality requirements are matched to a jet based on their angular separation $\Delta R(\text{trk}, \text{jet})$ from the jet axis, which is required to be smaller than an upper limit R_{cut}. The value of R_{cut} decreases with p_T^{jet} to account for the collimation of the hadron shower with increasing energy of the initial parton and minimise the number of associated tracks not stemming from the b-hadron decay.[15]

[15]The exact formula for the dependence of R_{cut} on p_T^{jet} is given in Equation (1) of [233].

If a track fulfills the matching criteria for more than one jet, it is associated with the jet closest in ΔR.

The b-tagging algorithms are run only on small-R jets, most commonly calibrated anti-k_T $R = 0.4$ calorimeter jets, which are also used in the search presented in this thesis. The use of alternative jet collections, in particular track jet collections, for b-tagging is discussed in the outlook (Chapter 9).

The `MV1` Tagger

The b-tagging algorithms used within ATLAS can be roughly classified based on the b-hadron decay properties that are used as discriminating variables. Simple b-tagging algorithms such as `IP3D` and `SV1` rely on the impact parameter significance and secondary vertex properties, such as the decay length, respectively. The more sophisticated `JetFitter` algorithm exploits the topology of the b- and c-hadron decays, using a Kalman filter [234] to find a common line connecting the secondary vertex and tertiary vertex with the primary vertex of the jet. These algorithms are documented in [232].

The b-tagging algorithm chosen for the search presented in this thesis, the so-called **`MV1` tagger** [232], combines the results of the `IP3D`, `SV1` and `JetFitter` algorithms by using them as input to an artificial neural network (ANN) that returns a *tag weight* for each jet, which quantifies how similar the jet properties are to those of a b-jet. Different *working points* are defined based on the threshold weight above which a jet is considered a b-jet. The search presented in this thesis uses a working point for which on average 70% of all b-jets with $p_T^{jet} > 20$ GeV and $|\eta| < 2.5$ in a $t\bar{t}$ MC sample are tagged by `MV1` [232].

`MV1` Tagging Efficiencies and Scale Factors

The b-tagging efficiency ϵ_b depends on the transverse momentum and, to a smaller extent, the pseudorapidity of the jet. The same holds for the efficiencies ϵ_c and ϵ_l for tagging c- and light-flavour jets, respectively. The three efficiencies are shown in Figure 4.4a as a function of p_T^{jet}. Each of the efficiencies ϵ_b, ϵ_c and ϵ_l are determined in both data and MC events, and scale factors binned in p_T^{jet} (and η^{jet} in the case of the light-flavour mistag rate) are derived to correct the efficiencies predicted by MC simulations to those measured in data.

The **b-tagging efficiency** ϵ_b and the corresponding scale factors are measured by three different methods, described in detail in [235], which are combined to achieve results with optimal

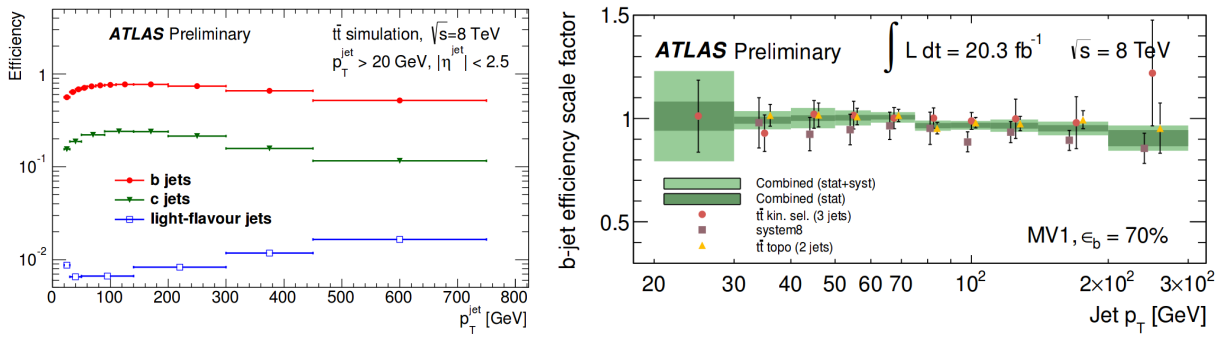

(a) **(b)**

Figure 4.4.: (a) Efficiency of the `MV1` tagger at the 70% working point to select b-, c- and light-flavour jets as a function of p_T^{jet}. (b) The corresponding b-tagging efficiency scale factors as a function of p_T^{jet} derived with the *system8*, *tag-and-probe* ($t\bar{t}$ topo) and *kinematic selection* ($t\bar{t}$ kin. sel.) methods and their combination as described in the text. Both taken from [235].

precision over a large p_T^{jet} range: The *system8* method relies on events with at least one jet containing a muon. This sample is naturally enriched in b-jets with semileptonic b-hadron decays as explained above. Three uncorrelated selection criteria are used to define a system of eight equations, each describing the number of events passing a certain combination of the three selection criteria. The system, which is fully constrained, can be solved for its eight unknowns, including the b-tagging efficiency of interest. The other two methods use dileptonic $t\bar{t}$ events, which provide a sample of b-jets with inclusive b-hadron decays, that is jets containing b-hadrons decaying to any possible final state. A particular advantage of using $t\bar{t}$ events for the b-tagging efficiency calibration is that they can be used to extend the measurement to b-jets with transverse momenta above 300 GeV and with small angular separation from other jets in the event, as expected in boosted object decays, see for example Section 5.1. Such extended calibrations are currently in preparation within ATLAS [236] but have not been available by the time the results presented in this thesis were published.

The *tag-and-probe* method relies on opposite-sign $e\mu$ events with at least one b-tagged jet, which is used to identify (*tag*) an event as a dileptonic $t\bar{t}$ event. Simple kinematic criteria are used to select the b-jet from the second top-quark decay on which the b-tagging efficiency is measured (*probed*). The other method, referred to as the *kinematic selection* method, relies on opposite-sign $e\mu$ events with exactly three jets in the final state.[16] It is based on the assumption that the number of b-tagged jets measured in data is the sum of the number of b-jets that are correctly tagged and the number of c- and light-flavour jets that are falsely tagged. The b-tagging

[16] This selection takes into account the fact that the two leading jets are not necessarily the two b-jets from the $t\bar{t}$ decay since ISR/FSR or pile-up interactions may lead to additional, mostly light-flavour jets in the event.

efficiency can then be calculated from the observed fraction of b-tagged jets in data and the flavour fractions and mistag efficiencies derived from MC simulations, where additional correction factors are applied to correct the mistag efficiencies in MC simulations to those determined in data. The results from the three scale factor measurements are combined using a maximum likelihood method based on the assumption that the measurements follow an underlying Gaussian probability density distribution centered on the true value of the scale factor in each p_T^{jet} bin. Details of the likelihood method are given in Section 6 of [235]. The scale factors and their uncertainties obtained with the three methods and their combination for the 70% working point of the MV1 tagger are shown in Figure 4.4b. The scale factors are in the range $0.9 - 1.0$ with uncertainties as small as 2% in the medium p_T^{jet} range.

The **c-tagging efficiency** ϵ_c and scale factors are determined in a sample of jets containing $D^{*\pm}$ mesons. The results are extrapolated to inclusive c-jets, that is c-jets containing any type of c-hadron. For details of the method see Section 4 of [237]. The final scale factors are around 0.9 with uncertainties in the range 8-15%.

The light-flavour tagging efficiency ϵ_l, more commonly referred to as the **mistag rate**, and the corresponding scale factors are measured in multi-jet events using the *negative tag method* described in Section 5 of [237]. The mistag rate ranges between 0.5% and 2%. The scale factors are greater than unity with relative uncertainties between 15% and 43%.

The efficiency scale factors, SF_x^{eff} with $x \in \{b, c, \text{light}\}$, are applied as multiplicative corrections to the event weight, one for each tagged jet of flavour type x. In order to preserve the event yields before b-tagging, additional **inefficiency scale factors**, defined as

$$\text{SF}_x^{\text{ineff}} = \frac{1 - \epsilon_x^{Data}}{1 - \epsilon_x^{MC}} = \frac{1 - \text{SF}_x^{\text{eff}} \cdot \epsilon_x^{MC}}{1 - \epsilon_x^{MC}}, \tag{4.8}$$

are applied for each un-tagged jet of flavour type x. The tagging efficiency ϵ_x^{MC} for a jet of flavour type x is derived in $t\bar{t}$ MC events and corrected for effects of close-by leptons and jets in boosted top-quark decays using correction factors derived on additional $Z'_{\text{TC2}} \to t\bar{t}$ and $g_{KK} \to t\bar{t}$ MC samples, as described in Section 5.1.2 of [2].

4.4. Missing Transverse Energy

The missing transverse energy E_T^{miss}, which has been introduced in a general form in Section 3.2.1, is an important signature in many searches for new physics. It arises in the presence

of undetected particles, such as neutrinos in SM processes or hypothetical new particles predicted, for example, by supersymmetry. False E_T^{miss} signatures may result from incomplete geometric detector coverage, finite detector resolution, detector noise or dead regions in the detector. It is crucial to properly account for these effects in the reconstruction of E_T^{miss}.

The missing transverse energy is calculated as the vector sum of the transverse energies of topological clusters in the calorimeters and muons reconstructed in the MS. In addition, ID tracks are used to recover low-p_T charged particles that do not reach the calorimeter as well as muons in regions outside the coverage of the MS. The energies of calorimeter clusters associated with high-p_T electrons or small-R jets are replaced by the corresponding calibrated quantities using the calibrations described in the previous sections. Details of the procedure can be found in [238] and [2].

4.5. Summary

The reconstruction of various physics objects from the energy signatures in the different ATLAS subdetectors has been described, along with strategies for their identification and calibration. The search presented in this thesis relies on a number of different objects to select and reconstruct events with a semileptonically decaying $t\bar{t}$ pair: Isolated, high-p_T electrons and muons, large missing transverse energy as well as hadronic jets with two different R parameters: anti-k_T jets with $R = 0.4$ (anti-k_T $R = 4$ jets), and trimmed anti-k_T jets with $R = 1.0$ (anti-k_T $R = 10$ jets). Moreover, algorithms for the identification of b-jets, which are applied to anti-k_T $R = 4$ jets only, play a crucial role in the selection of $t\bar{t}$ events.

5. Analysis Strategy

The search for new resonances decaying to pairs of top quarks ($t\bar{t}$) is designed to identify collision events with a detector signature consistent with that of a heavy-particle decay $X \to t\bar{t}$, the **signal** process. Based on the characteristic properties of the $t\bar{t}$ final state, described below, an *event selection* strategy is developed which is optimised to provide a high selection efficiency for potential signal events while rejecting **background** events from known SM processes with detector signatures similar to those of the predicted signal events. Twelve independent **search channels** or **signal regions** are defined through a number of object and event selection criteria (Section 5.3). A statistical analysis, which is designed to find and quantify any deviations of the observed data from the SM prediction, is then carried out in these signal regions (Chapter 7).

The signal regions are not fully depleted of background events from SM processes. These background contributions have to be estimated using MC simulations (Section 3.4.2) or data-driven methods (Section 5.5). In a search conducted in the single-lepton plus jets final state of $t\bar{t}$ decays (Section 5.1), the following background processes have to be taken into account:

- SM $t\bar{t}$ production
- Single-top production
- Vector-boson production in association with $t\bar{t}$ ($t\bar{t}V$, where $V = W, Z$)
- Vector-boson production in association with hadronic jets (V+jets)
- Vector-boson pair production (WW, WZ, ZZ)
- QCD multi-jet production.

The background from SM $t\bar{t}$ production is an *irreducible* background in the search presented in this thesis as the event selection criteria are tailored towards the identification of events with a $t\bar{t}$ pair, irrespective of whether this $t\bar{t}$ pair originates from SM production or from the decay of a massive resonance. It is therefore the dominant background contribution in the signal regions as will be shown in Chapter 6. All other background processes listed above are considered *reducible*.

The event selection criteria for the signal regions are optimised to suppress these background components as effectively as possible. This is necessary because the production cross-sections of many of these processes are several orders of magnitude larger than that of SM $t\bar{t}$ production, as illustrated in Figure 5.1. For example, the cross-sections for W+jets and Z+jets production (upper two green lines) are 2-3 orders of magnitude larger than that of SM $t\bar{t}$ production (lower red line), which in turn is several orders of magnitude larger than the production cross-sections of most signal processes under consideration (Section 3.4.1).

The signal regions are analysed for deviations of the observed data from the SM prediction. The simplest possible statistical analysis, often referred to as the *cut-and-count method*, is the comparison of the expected event yields in a signal region, based on the estimation of SM background processes, with the corresponding yields observed in data. This simple method has two major drawbacks: Firstly, its sensitivity to signal processes with a small cross-section, for which the predicted ratio $S/\sqrt{B}$ of signal yields S to background yields B is much smaller than one, is limited. Secondly, it is not possible to distinguish between different signal models or masses with this method.

Therefore, a more sophisticated approach is chosen, which relies not only on the overall yields in a signal region but also on the shape of the (binned) distribution of a discriminating variable. In the search presented in this thesis, the invariant mass of the $t\bar{t}$ pair, $m_{t\bar{t}}$, is used as a discriminating variable. It is reconstructed from the properties of selected physics objects in the event. The *event reconstruction* is described in Section 5.4.

Resonant $t\bar{t}$ production via one of the BSM processes discussed in Section 2.5 is expected to manifest itself as a localised deviation ("bump") of the mass distribution or *spectrum* observed in data from the smooth, falling distribution predicted by the SM, the position of the deviation being determined by the mass of the hypothetical resonance. The agreement between the observed and expected spectrum is quantified via comparison of the observed and expected yields in mass windows of varying width and position across the $m_{t\bar{t}}$ spectrum. The method can thus be seen as an extension of the cut-and-count approach, the combination of the results from different mass windows enhancing the overall sensitivity of the search. Details of the statistical analysis of the results are given in Chapter 7.

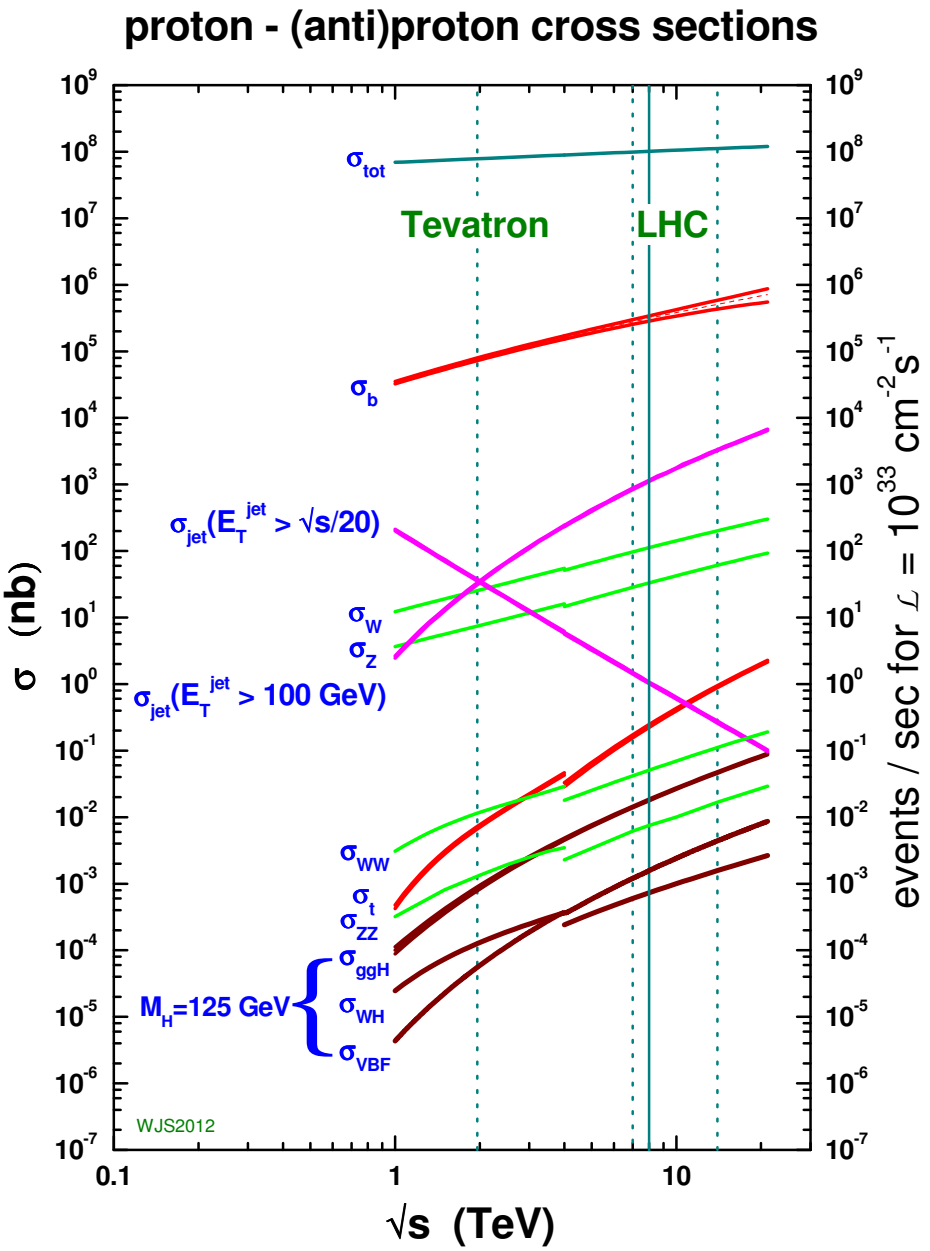

Figure 5.1.: Production cross-sections for various Standard Model processes at the LHC and the Tevatron as a function of the centre-of-mass energy $\sqrt{s}$. The solid blue vertical line marks $\sqrt{s} =$ 8 TeV for the LHC data-taking period in 2012. The magenta lines show the cross-sections for QCD multi-jet production for different requirements on the transverse energy E_T of the leading jet. The green lines mark the inclusive production cross-sections for single and pair production of W and Z bosons, respectively. The lower red line corresponds to the inclusive production cross-section for top quarks from both $t\bar{t}$ and single-top production. The discontinuity in several cross-section lines at $\sqrt{s} = 4$ TeV is due to the switch from $p\bar{p}$ production to pp production. Taken from [239].

5.1. The ℓ+jets Final State and Its Decay Topologies

The search for new resonances decaying to $t\bar{t}$ pairs is conducted in the **single-lepton plus jets** (ℓ+jets) final state, introduced in Section 2.2.3. This final state is characterised by the presence of a single, isolated (charged) lepton[1] with large transverse momentum, stemming from the leptonically decaying W-boson, large missing transverse momentum, associated with the corresponding neutrino, and a certain number of hadronic jets. It is often referred to as the **golden channel** for searches and measurements in $t\bar{t}$ events. The leptonic signature can be used to effectively suppress the large background contribution from QCD multi-jet events, which dominates the (non-$t\bar{t}$) background in the *fully hadronic* final state due to its large cross-section. Compared to the *dilepton* final state, which has a branching fraction of only $\approx 7\%$, its larger branching fraction of $\approx 34\%$ results in a larger number of events in this decay channel available for further analysis.[2]

ATLAS has conducted resonance searches in both the fully hadronic [40] and dilepton [41] $t\bar{t}$ final states using data collected in 2011 at $\sqrt{s} = 7$ TeV, in addition to a search in the ℓ+jets final state [39]. The search in data collected in 2012 at $\sqrt{s} = 8$ TeV focuses on the ℓ+jets final state as the final state with the highest sensitivity to new resonances. This search will be the topic of this thesis.

The detector signature of $t\bar{t}$ events in the ℓ+jets final state depends on the transverse momenta of the top quarks, as illustrated in Figure 5.2. At low transverse momenta, the decay products of the top quarks are generally well separated in the detector and can be reconstructed individually: The hadronic top-quark decay results in three separate jets, one of which is a b-jet. The lepton from the decay of the other top quark is usually well separated from the corresponding b-jet. This decay topology, shown in the left pictogram of Figure 5.2, will be referred to as the **resolved topology** in the following.

As the transverse momenta of the top quarks increase, their decay products appear increasingly collimated in the direction of the respective mother particle in the laboratory frame. The angular separation ΔR between the b-quark and the W-boson from the top quark and that between the two decay products of the W-boson decreases inversely with the transverse momentum of the

[1] In the following "lepton", denoted as ℓ, refers to either an electron or muon (or their respective anti-particles). As explained in Section 2.2.3, τ-lepton decays are not explicitly considered here.

[2] Both numbers refer to final states with electrons and muons, including those from leptonically decaying τ-leptons, as explained in Section 2.2.3.

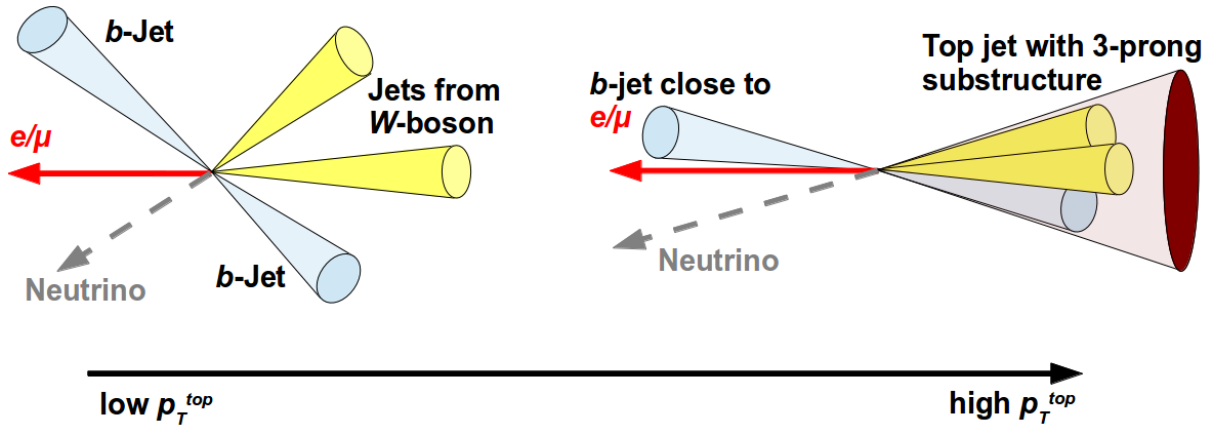

Figure 5.2.: Decay topologies of $t\bar{t}$ events in the ℓ+jets final state for different values of the transverse momenta of the top quarks, p_T^{top}, assuming the momentum vectors of the top and the anti-top quark are of similar magnitude and roughly opposite direction as expected for the decay $X \to t\bar{t}$ of a massive resonance X. Left: resolved decay topology for low p_T^{top}. Right: boosted decay topology for high p_T^{top}.

top quark and the W-boson, respectively, as illustrated in Figure 5.3. This behaviour can be parameterised by the following simple, empirical formula[3] for the average angular separation $\Delta R(a,b) = \sqrt{\Delta y(a,b) + \Delta\phi(a,b)}$ of the decay products in the two-body decay $X \to a + b$:

$$\Delta R(a,b) \approx \frac{2m^X}{p_T^X}, \tag{5.1}$$

where X denotes a heavy particle, such as a top quark or W-boson, with mass m^X and transverse momentum p_T^X. This formula describes the key property of boosted particle decays that dictates the reconstruction and identification strategies discussed in the following.

The increasing collimation of the decay products and the resultingly higher probability for overlap between the corresponding objects affect various aspects of the object reconstruction and identification:

- The hadron showers from the three quarks from the hadronic top-quark decay merge into a single, large jet with a 3-prong substructure.
- The b-jet from the hadronic top-quark decay is close to or even merged with the light-quark jets from the W-boson decay. Hence the b-hadron decay products are no longer separated from other hadronic activity in the event, leading to a reduction of the discriminating power of the variables used by the b-tagger. This is reflected in a decrease of the b-tagging efficiency with increasing transverse momentum of the b-jet from the top-quark decay, as

[3] This formula is given, for example, in [215].

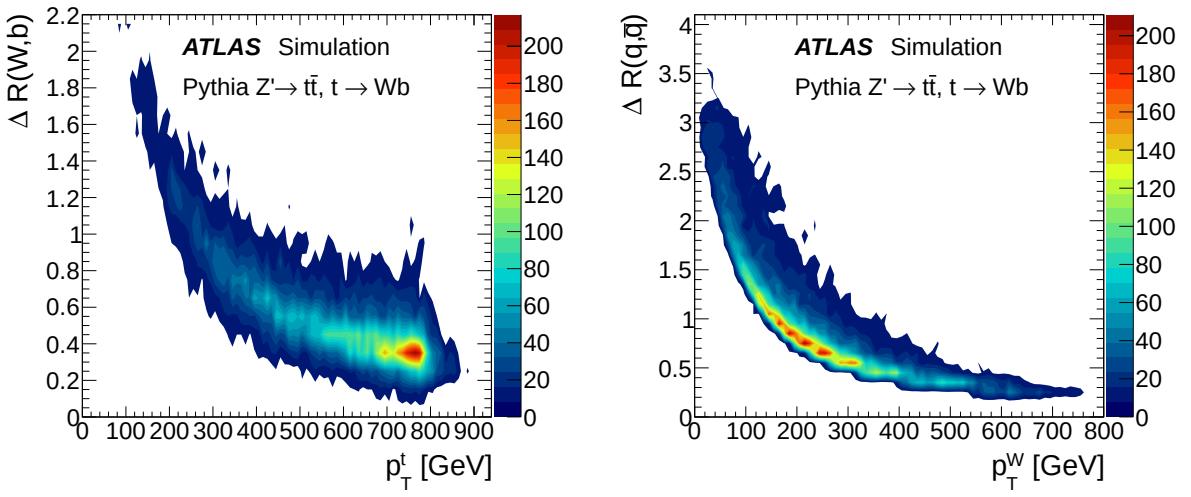

(a) $t \to Wb$ **(b)** $W \to q'\bar{q}$

Figure 5.3.: Angular separation ΔR of the decay products in the two-body decays (a) $t \to Wb$, and (b) $W \to q'\bar{q}$ as a function of the transverse momentum of the top quark and the W boson, respectively. Taken from [215].

illustrated in Figure 4.4a.

- The electron or muon from the leptonic W-boson decay is close to the corresponding b-jet. The increased hadronic activity in its vicinity makes it more likely to fail traditional fixed-cone isolation requirements (see Sections 4.1.3 and 4.2.3). It is also possible that the electron or muon is found within the b-jet.

The decay topology in which the three jets from the hadronic top-quark decay are merged into a single jet, as shown in the right pictogram of Figure 5.2, will be referred to as the **boosted topology** in the following.

It should be noted that there is also an *intermediate topology*, where only two of the jets from the hadronically decaying top quark, typically those from the decay of the W boson, are merged while the third jet is reconstructed separately. In previous iterations of the search discussed in this thesis, events falling into this category were selected by applying all selection criteria for the resolved topology (Section 5.3.5), with the exception that events with only three small-R jets, instead of four or more, were accepted if one of the jets had a mass greater than 60 GeV [39, 174]. It was not possible to use this selection criterion in the search presented in this thesis because at the time the search was conducted no final mass calibration for small-R jets was available within ATLAS. A comparison of the signal efficiencies for the resolved, intermediate and boosted event categories in the last iteration of the search [174] indicates that the selection efficiency for signal events with a resonance mass of 2 TeV is reduced by around 10% if events in the intermediate

category are not considered. The effect is negligble for resonance masses below 1 TeV.

Based on the considerations discussed in this section, four mutually exclusive signal regions are defined through the event selection criteria given in Section 5.3: Events are classified as belonging to either the e+jets channel or the μ+jets channel and falling into either the resolved or boosted category. A further classification into three different b-tagging categories is introduced in Section 5.4.5. Thus, twelve mutually exclusive signal regions are defined for the search.

5.2. Object Selection

The reconstruction and identification of the physics objects used in this search has been described in Section 4. In the following, the selection criteria imposed on these objects are summarised and motivated with regard to the search strategy defined above.

5.2.1. Lepton Selection

The reconstruction, identification and selection criteria for the electrons and muons used in this search have been described in Sections 4.1.1 and 4.2.1, respectively. Both types of leptons are required to have $p_T > 25$ GeV to ensure that the respective lepton triggers, described in Section 5.3.2, are operating at maximum efficiency. The `tight` quality requirements imposed on both electrons and muons are chosen to suppress the background from non-prompt and "fake" leptons in QCD multi-jet events as effectively as possible. The mini-isolation criteria for both electrons and muons rely on isolation cones with a size $\Delta R \propto (p_T^\ell)^{-1}$ that automatically adapts to the transverse momentum scale of the lepton from the top-quark decay, thus taking into account the decreasing angular separation between the lepton and the b-jet from the semileptonic top-quark decay according to Equation 5.1.

5.2.2. Jet Selection

The two different $t\bar{t}$ decay topologies introduced in Section 5.1 require the use of two different jet collections in the event selection and reconstruction.

In the case of the resolved topology, only small-R jets are used to reconstruct the individual hadronic decay products of the top quarks. The small-R jets chosen for the search presented in this thesis are anti-k_T $R = 0.4$ jets (Section 4.3.1) which are reconstructed from topological clusters in the calorimeter and calibrated according to the LCW+JES scheme (Section 4.3.4). They are required to have $p_T > 25$ GeV and $|\eta| < 2.5$. Central, low-p_T jets ($p_T < 50$ GeV

and $|\eta| < 2.4$) are also required to have a jet vertex fraction JVF > 0.5 to reject jets from pile-up vertices (Section 4.3.3). Only selected jets that also pass the overlap removal procedure described in Section 5.2.3 are kept for further analysis.

In the boosted topology, a large-R jet collection is required in addition to the small-R jet collection (which is used to identify the two b-jets) to reconstruct the boosted, hadronically decaying top quark, the decay products of which are merged into a single hadronic jet. The R-parameter of the large-R jet collection determines the threshold of the top-quark transverse momentum above which the top-quark decay products can be expected to be contained within such a jet. The search presented in this thesis relies on trimmed anti-k_T jets with $R = 1.0$ which are required to have $p_T > 300$ GeV.[4] Based on Equation 5.1, the W-boson and b-quark from the top-quark decay are likely to be found within $\Delta R(W, b) < 1.0$ for $p_T^{\text{top}} > 350$ GeV, although overlap between the hadron showers of the three quarks from the hadronic top-quark decay may occur at lower values of p_T^{top}. This is taken into account through the lower p_T threshold of 300 GeV. In addition, the jets are required to have $m > 100$ GeV and $\sqrt{d_{12}} > 40$ GeV (Sections 4.3.2 and 4.3.3) to identify them as top jets and suppress the background from QCD multi-jet events with high-p_T jets initiated by gluons or lighter quarks (Section 4.3.3). Finally, large-R jets are required to be within $|\eta| < 2.0$. This requirement, which is tighter than that imposed on small-R jets, is needed to minimise the number of jets for which the corresponding track jets, which are used as reference objects in the energy and mass calibration as well as the energy and mass resolution measurements (Sections 4.3.4–4.3.4), are not fully contained within the geometric coverage of the ID.

5.2.3. Treatment of Overlap between Leptons and Jets

Overlap between reconstructed leptons and jets occurs in both the boosted and non-boosted event topologies, for example because a (prompt) lepton and a jet from the hard-scattering process happen to be emitted into the same detector region. Moreover, overlap occurs if a non-prompt lepton from a heavy-flavour decay within a hadron shower passes the above selection criteria or if a hadron shower with a large EM component is reconstructed both as a jet and as an electron. An overlap removal procedure is needed to resolve ambiguities in the object identification and to suppress events with non-prompt leptons.

The search presented in this thesis relies on a novel overlap removal strategy that has been

[4] This transverse momentum threshold is increased to 380 GeV for certain events due to trigger requirements. For details see Section 5.3.2.

developed specifically for this search to reduce efficiency losses at large invariant $t\bar{t}$ masses where the top quarks are boosted and the angular separation $\Delta R(\ell, j)$ between the lepton and the b-jet from the semileptonic top-quark decay is small. It consists of two subsequent steps: an electron-jet and a muon-jet overlap removal procedure.

The electron-jet overlap removal procedure is applied to all electrons passing the above selection criteria and all fully calibrated anti-k_T $R = 0.4$ jets in the event before the application of any jet selection criteria. An electron and a jet are considered for overlap removal if the jet is the closest jet to the electron and is within $\Delta R(e, j) < 0.4$ from the position of the electron cluster. In this case, the electron four-momentum is subtracted from the jet four-momentum. Moreover, if the electron track was included in the JVF calculation of the original jet, the JVF is recalculated without the electron track. Next, the jet selection criteria described in the previous section are applied to the recalculated jet object (and all other jets in the event) and the jet is removed if it fails these criteria.

If the jet passes the selection criteria, the angular separation $\Delta R(e, j)$ between the electron and the jet is recalculated using the new jet four-momentum. If $\Delta R(e, j) < 0.2$, the electron cluster has a high probability of originating from the hadron shower. Consequently the electron is removed from the list of electron candidates to be considered in the event selection and its four-momentum is added back to the jet four-momentum. If $\Delta R(e, j) \geq 0.2$, both the electron and the jet are kept and the recalculated jet four-momentum is used in all subsequent analysis steps.

In previous iterations of the analysis [39, 174], only selected jets were considered for overlap removal and the jet closest to a selected electron would be removed if within $\Delta R(e, j) < 0.2$ from the electron, followed by the requirement that all selected electrons within $0.2 \leq \Delta R(e, j) < 0.4$ of any remaining jet be removed. Hence either the b-jet or the electron from the semileptonically decaying top quark would be removed if the two objects were within $\Delta R(e, j) < 0.4$, leading to significant efficiency losses at large values of $m_{t\bar{t}}$. Compared to this old strategy, the new electron-jet overlap removal procedure described above leads to an improvement of the selection efficiency for signal events in the e+jets channel with the boosted-topology selection between 10% at $m_{t\bar{t}}^{\text{reco}} = 1$ TeV and $> 50\%$ for $m_{t\bar{t}}^{\text{reco}} > 2$ TeV [2].

Following the electron-jet overlap removal, the overlap between muons and jets is addressed. A veto on muons with a small angular distance $\Delta R(\mu, j)$ to a selected jet is necessary to reject non-

prompt muons from heavy-flavour decays within hadronic jets, thereby reducing the background from QCD multi-jet events. In previous iterations of the analysis [39, 174], a selected muon was removed if it was within $\Delta R(\mu, j) < 0.1$ of a selected anti-k_T $R = 0.4$ jet. In the search presented in this thesis, this requirement is loosened to remove only muons for which

$$\Delta R(\mu, j) < 0.04 + \frac{10 \text{ GeV}}{p_T^{\mu}}. \tag{5.2}$$

The p_T^{μ}-dependent threshold reflects the increasing collimation of the top-quark decay products according to Equation 5.1. The parameters have been been derived on Z' MC samples and optimised to achieve a constantly high signal efficiency of around 96% across the whole invariant mass range [240].

No overlap removal between leptons and large-R jets is applied but the boosted-topology selection, described in Section 5.3.4, includes a requirement on the angular separation between the selected lepton and the selected large-R jet which ensures that they are well separated in the detector.

5.3. Event Selection

Collision events[5] must pass a number of selection requirements to be considered as signal candidate events. First, general quality requirements, referred to as *preselection* criteria, are applied (Section 5.3.1). Furthermore, events are required to have passed the selection criteria of at least one of a specific set of triggers, indicating that their detector signature shows certain characteristics compatible with the final state of interest. Details of the trigger selection are given in Section 5.3.2. Following the quality and trigger requirements, object-related selection criteria specific to the ℓ+jets final state are applied. These include requirements common to both the resolved and boosted decay topologies, such as the presence of a single lepton and a missing energy signature compatible with that expected for a leptonic W-boson decay (Section 5.3.3). Finally, selection criteria specific to the boosted and resolved decay topology, respectively, are imposed. These include requirements on the type and number of jets in the event and the separation between objects. Events are first tested against the criteria for the boosted decay topology (Section 5.3.4). Only events that fail these criteria are tested against those for the resolved topology (Section 5.3.5) to avoid overlap between the different signal regions.

[5] Unless otherwise stated, all selection criteria are applied to both real data and simulated events.

5.3.1. Event Preselection

Only events passing a number of general quality requirements are accepted for further analysis. These requirements are imposed to exclude events suffering from temporary subdetector malfunctions, such as noise bursts in the LAr calorimeter or corrupted data from the tile calorimeter, and events with incomplete detector information. Data events are also required to belong to a luminosity block contained in the Good Runs List (Section 3.2.7), to ensure that they are of sufficient quality.

Events that are not associated with a collision but with external effects, such as cosmic rays or background radiation in the cavern,[6] are suppressed through the requirement that the primary vertex must have at least four associated tracks with $p_T^{\text{trk}} > 400$ MeV.

5.3.2. Trigger Selection

Next, events are required to have fired at least one of a certain set of triggers. The choice of triggers for an analysis is naturally based upon one or several characteristics of the final state under consideration, the trigger selection thus acting as a preselection of events that may potentially be associated with the signal process of interest. A natural trigger choice for $t\bar{t}$ events in the ℓ+jets final state are single-lepton triggers. To maximise the selection efficiency over the largest possible range of the $t\bar{t}$ invariant mass, the unprescaled single-lepton triggers with the lowest transverse momentum threshold available are used: `EF_e24vhi_medium1` in the e+jets channel and `EF_mu24i_tight` in the μ+jets channel, which have been defined in Sections 4.1.3 and 4.2.3, respectively. The lepton selection for these triggers includes an isolation requirement which leads to a decrease of the trigger efficiency for leptons from the decays of boosted top quarks that are close to the corresponding b-jet. This is reflected in a decrease of the trigger efficiency with increasing (true) $t\bar{t}$ invariant mass,[7] $m_{t\bar{t}}^{\text{true}}$, for $Z' \to t\bar{t}$ signal events, as illustrated in Figure 5.4 (blue curves). Here the trigger efficiency is defined as the fraction of events passing all offline selection criteria with the exception of the trigger requirements (resolved- and boosted-topology selection combined) that are also selected by the trigger under consideration.

To obtain a stable trigger efficiency over the whole mass range, the above triggers are combined with the single-lepton triggers `EF_e60_medium1` and `EF_mu36_tight`, respectively. These

[6] Cavern background radiation originates from soft, inelastic interactions between the proton beams or the collision products with the cavern walls or detector shieldings. It consists mostly of slow, low-energy neutrons and photons. For more information see for example [241].

[7] The true $t\bar{t}$ invariant mass is calculated in MC events from the four-momenta of the top quarks from the resonance decay after the emission of final-state radiation.

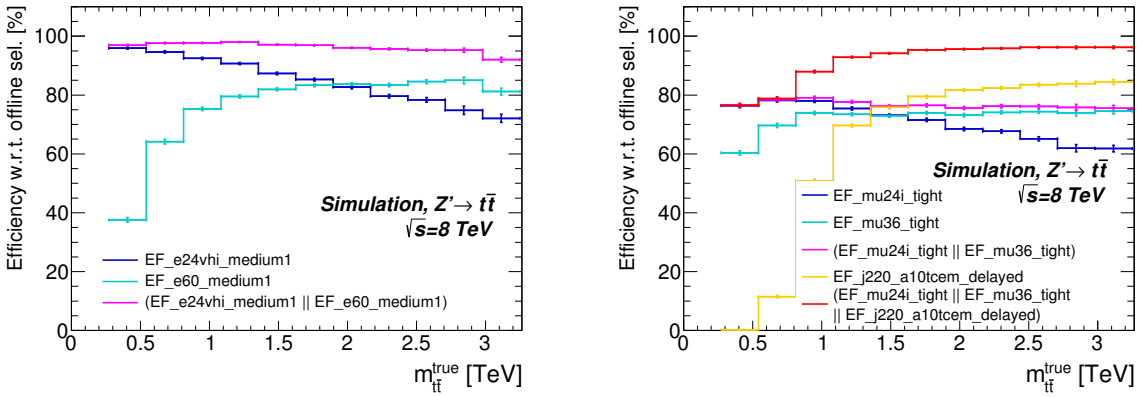

(a) (b)

Figure 5.4.: Efficiency of the isolated and non-isolated single-lepton triggers and their OR combination as a function of the invariant mass of the reconstructed $t\bar{t}$ system for (a) the electron triggers and (b) the muon triggers. The efficiencies are evaluated with respect to the full offline selection (resolved- and boosted-topology selection combined) of the e- and μ+jets channel, respectively. All $Z' \to t\bar{t}$ MC samples listed in Section 3.4.1 are used. Events passing `EF_j220_a10tcem_delayed`, but none of the single-muon triggers, are scaled by a factor of 17.4/20.3 to account for the lower integrated luminosity of the delayed stream in the calculation of the efficiencies involving `EF_j220_a10tcem_delayed`.

triggers have no lepton isolation requirements and accordingly higher transverse momentum thresholds to compensate for the higher rates of non-prompt, non-isolated leptons passing the trigger requirements. The higher thresholds leads to a lower selection efficiency for signal events, especially in the lower invariant mass range, compared to the triggers with lower thresholds, as shown in Figure 5.4 (cyan curves). The OR combinations (`EF_e24vhi_medium1 || EF_e60_medium1`) and (`EF_mu24i_tight || EF_mu36_tight`), respectively, yield stable trigger efficiencies over the whole invariant mass range (magenta curves). Events are therefore required to pass either `EF_e24vhi_medium1` or `EF_e60_medium1` (`EF_mu24i_tight` or `EF_mu36_tight`) to be considered for the e+jets channel (μ+jets channel).

A comparison of Figures 5.4a and 5.4b shows that the overall single-muon trigger efficiency is only around 80% compared to $> 95\%$ in the case of the electron trigger combination, a consequence of the limited geometric coverage of the muon trigger system (see Sections 3.2.4 and 4.2.4). To increase the selection efficiency for events in the μ+jets channel, a single large-R jet trigger from the delayed stream (Section 3.2.6), `EF_j220_a10tcem_delayed`, is used in addition to the single-muon triggers described above. At the EF, this trigger is fired by events with at least one (ungroomed) anti-k_T $R = 1.0$ jet at the EM scale that has $p_T^{\text{jet,EF}} > 220$ GeV.

In Figure 5.5a, the efficiency of `EF_j220_a10tcem_delayed` is shown as a function of the trans-

verse momentum of the leading trimmed and calibrated anti-k_T $R = 1.0$ jet in data, QCD dijet events simulated with PYTHIA8, and SM $t\bar{t}$ events simulated as described in Section 3.4.2. No object-specific requirements are imposed on these events, hence the data sample is dominated by QCD multi-jet events. In the former two cases, the trigger reaches its full efficiency of $> 99\%$ at ≈ 300 GeV. In the latter case, the efficiency plateau is reached at ≈ 380 GeV. To ensure a maximum trigger efficiency and an optimal agreement between the efficiencies in data and MC events, the transverse momentum threshold for large-R jets in the boosted-topology selection is raised to 380 GeV for events in the μ+jets channel that fail the muon triggers but pass the jet trigger.

The data collected by this trigger is part of the delayed data stream, discussed in Section 3.2.6. Similar single large-R jet triggers in the prompt data stream have tighter threshold requirements on $p_T^{\text{jet,EF}}$ to keep the event rates below the maximum rate that can be handled by the processing units available for prompt data reconstruction. For example, the lowest un-prescaled single large-R jet trigger in the prompt data stream, `EF_j360_a10tcem`, has a threshold of $p_T^{\text{jet,EF}} > 360$ GeV and reaches its efficiency plateau only for $p_T^{\text{jet}} \approx 450$ GeV. Data in the delayed stream has only been recorded during part of the 2012 data-taking period, the delayed stream dataset amounting to 17.4 fb^{-1}, compared to 20.3 fb^{-1} for the full dataset. Events may belong to both the prompt and the delayed stream. To avoid duplication of data events in the event selection, only events in the delayed stream that fail the single-muon trigger requirements are checked against the jet trigger decision.

The efficiency of `EF_j220_a10tcem_delayed` on $Z' \to t\bar{t}$ signal events passing the full offline selection, excluding the trigger requirements, is shown in Figure 5.4b (orange curve), along with that for the OR combination of `EF_j220_a10tcem_delayed` with the two muon triggers (red curve). Events passing `EF_j220_a10tcem_delayed`, but none of the muon triggers, are scaled by a factor of 17.4/20.3 to account for the lower integrated luminosity of the delayed stream. The addition of the delayed-stream trigger significantly increases the trigger efficiency with respect to the offline selection for events with $m_{t\bar{t}}^{\text{true}} > 0.8$ TeV. For signal events with $m_{t\bar{t}}^{\text{true}} > 1.5$ TeV, this efficiency is greater than 95% for the OR combination of the three triggers.

In Figure 5.5b, the product of the selection efficiency times acceptance times branching ratio, BR($t\bar{t} \to \mu$+jets), is shown as a function of the true $t\bar{t}$ invariant mass for $Z' \to t\bar{t}$ signal events in the μ+jets channel with the boosted-topology selection, both with and without the addition of the delayed-stream jet trigger. The addition of the delayed-stream trigger increases the overall

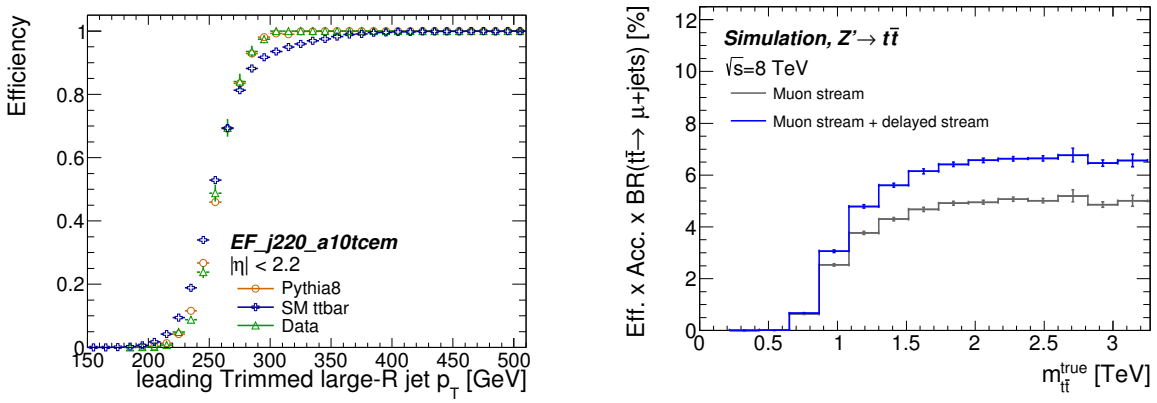

(a) (b)

Figure 5.5.: (a) Efficiency of `EF_j220_a10tcem_delayed` as a function of the transverse momentum of the leading trimmed and calibrated anti-k_T $R = 1.0$ jet in data, QCD dijet events simulated with PYTHIA8, and SM $t\bar{t}$ events simulated as described in Section 3.4.2. Taken from [2]. (b) Selection efficiency times acceptance times branching ratio, BR($t\bar{t} \to \mu$+jets), for $Z' \to t\bar{t}$ signal events in the μ+jets channel with the boosted-topology selection with and without the addition of the delayed-stream jet trigger `EF_j220_a10tcem_delayed`. Plot produced by the author but equivalent in content and style to Figure 5 in [2].

efficiency for the boosted-topology selection in the μ+jets channel by roughly 20%. The use of the delayed-stream trigger in the e+jets channel was investigated but the improvements were found to be marginal [2], hence this trigger is only used in the μ+jets channel.

5.3.3. Common Object-related Selection

The categorisation of events as belonging to either the e+jets or the μ+jets channel is made based on the presence of exactly one electron or exactly one muon in the event, where the respective lepton is required to pass the object selection criteria summarised in Section 5.2.

Only events that have been selected by either the `EF_e24vhi_medium1` or `EF_e60_medium1` trigger are considered for the selection specific to the e+jets channel. These events are required to contain exactly one selected electron, which must be matched to an EF electron object that fired either `EF_e24vhi_medium1` or `EF_e60_medium1`. The two objects are considered matched if their angular separation ΔR is smaller than 0.15. Events in which at least one selected muon is found in addition to the electron are vetoed to suppress contributions from background processes such as diboson production.

In the case of the μ+jets channel, events in the prompt stream that pass the `EF_mu24i_tight` or `EF_mu36_tight` triggers or events in the delayed stream that fail the lepton trigger requirements but are selected by the large-R jet, trigger `EF_j220_a10tcem_delayed`, are considered for further

analysis. These events must contain exactly one selected muon; events with at least one selected electron in addition to the muon are rejected. If the event was recorded by one or both of the single-muon triggers, the muon must be within $\Delta R < 0.15$ of an EF muon object that fired either `EF_mu24i_tight` or `EF_mu36_tight`. No trigger matching criterion is imposed on events selected by the single large-R jet trigger.

Events in both the e- and μ+jets channels are required to have $E_T^{\text{miss}} > 20$ GeV to reject background events from sources of non-prompt leptons or "fake" electrons in which missing transverse energy arises from the detector effects described in Section 4.4. This requirement alone, however, does not provide sufficient suppression of QCD multi-jet events in which secondary neutrinos from semileptonic decays of heavy-flavour hadrons result in large E_T^{miss}. Hence a second requirement, $E_T^{\text{miss}} + m_T^W > 60$ GeV, is imposed. It relies on the transverse mass of the leptonically-decaying W-boson, defined as

$$m_T^W = \sqrt{2 \cdot p_T^\ell \cdot E_T^{\text{miss}} \cdot (1 - \cos\phi_{\ell\nu})}, \tag{5.3}$$

where p_T^ℓ is the magnitude of the transverse momentum vector of the selected lepton, and $\phi_{\ell\nu}$ is the angle between the lepton transverse momentum vector and the direction of E_T^{miss}. Events in which the lepton and missing transverse energy result from the leptonic decay of an on-shell W-boson from the hard scattering or the decay of a top quark tend to have large values of m_T^W in contrast to those in which missing energy arises from a neutrino from the semileptonic decay of a heavy-flavour hadron. The above selection requirements on E_T^{miss} and m_T^W are recommended by the ATLAS Top Working Group and are also used in other searches and measurements involving $t\bar{t}$ pairs decaying to the ℓ+jets final state, for example [172, 242]. Alternative requirements involving these two variables have been investigated for the search presented in this thesis but have not been [243] as they did not lead to an improvement of the signal significance in the signal regions [243].

Moreover, events are rejected if they contain at least one small-R jet with $p_T > 20$ GeV that is flagged as arising from non-collision background such as calorimeter noise, cosmic rays or interactions between a proton beam and residual gas in the beam pipe. This procedure is known as *jet cleaning*. The criteria used to identify these background jets are described in Section 7 of [201]. At this point, the selection criteria for the boosted and resolved topologies diverge.

5.3.4. Boosted-topology Selection

Each event is first tested against the selection criteria for the boosted topology: Events in this category are required to have at least one selected anti-k_T $R = 0.4$ jet within $\Delta R < 1.5$ from the selected lepton. This reflects the fact that the b-jet from a boosted, semileptonically decaying top quark is expected to be close to the leptonically decaying W-boson, and hence close to the corresponding lepton. If more than one jet meets this requirement, the one with the highest transverse momentum is selected as the b-jet candidate for the event reconstruction (Section 5.4.2). It is labelled j_{sel} in the following.

In addition, there must be at least one selected anti-k_T $R = 1.0$ jet which is taken to correspond to the hadronically decaying top quark. The momenta of the top and anti-top quark from the decay of a heavy resonance are expected to be of similar magnitude with approximately opposite directions in the laboratory frame, as dictated by momentum conservation for the two-body decay of a heavy particle produced approximately at rest in the laboratory frame. If the top quarks are sufficiently boosted, their collimated decay products will also be well separated in the detector. This is reflected by the requirement that the angular separation ΔR between the anti-k_T $R = 1.0$ jet and j_{sel} must be greater than 1.5. Similarly, $\Delta\phi$ between the anti-k_T $R = 1.0$ jet and the selected lepton must be greater than 2.3. If there is more than one selected anti-k_T $R = 1.0$ jet that meets these criteria, the one with the largest transverse momentum is taken as the hadronically-decaying top-quark candidate in the following. All selection criteria related to the angular separation between the different objects in the boosted decay topology have already been used in previous iterations of the search presented in this thesis [39, 174].

Finally, there must be at least one b-tagged anti-k_T $R = 0.4$ jet in the event matched to either of the two reconstructed top-quark candidates, as described in Section 5.4.5.

5.3.5. Resolved-topology Selection

Events that fail the selection criteria of the boosted decay topology are tested against the selection criteria of the resolved topology: Events are required to have at least four selected anti-k_T $R = 0.4$ jets, at least one of which must be b-tagged. Moreover, the outcome of the kinematic χ^2 fit in the event reconstruction in the resolved topology, described in Section 5.4.3, is used to quantify how well the kinematics of the event in question match those expected for the ℓ+jets final state of a $t\bar{t}$ event. Only events for which $\log_{10}\chi^2 < 0.9$ are accepted for the resolved-

topology selection. This selection criterion, which was not used in previous iterations of the search presented in this thesis [39, 174], was introduced to reduce contributions from non-$t\bar{t}$ background processes and from $t\bar{t}$ events in which the $t\bar{t}$ pair is incorrectly reconstructed, for example because a small-R jet from pile-up or initial-state radiation is used in the reconstruction instead of one of the four jets from the decays of the two top quarks (Section 5.1). These incorrectly reconstructed $t\bar{t}$ events, which form the *combinatorial background*, worsen the resolution of the $t\bar{t}$ invariant mass distribution for signal events, thus reducing the sensitivity of the search. The value of the upper bound imposed on $\log_{10}\chi^2$ has been optimised to achieve an optimal signal significance, defined here as $S/(S+B)$, across the whole $t\bar{t}$ invariant mass spectrum. Details of the optimisation procedure can be found in [244]. It has been verified by a comparison to data that the distribution of the variable $\log_{10}\chi^2$ is well described by the total background estimate in the signal regions for the resolved topology, as shown in Figure 6.1 in Section 6.1.2.

5.3.6. Selection Efficiency

The product of the selection efficiency times acceptance times branching ratio for the four signal models described in Section 2.5 is shown in Figure 5.6 as a function of the true $t\bar{t}$ invariant mass, $m_{t\bar{t}}^{\text{true}}$. The branching ratio for the decay $t\bar{t} \to \ell$+jets, where $\ell = e$ or μ, is 17% for each lepton flavour [52]. This number includes contributions from top quark decays which result in a τ-lepton that decays leptonically to a single electron or muon (in addition to neutrinos).

The overall efficiency times acceptance (solid lines) is dominated by the efficiency times acceptance of the resolved-topology selection in the range $m_{t\bar{t}}^{\text{true}} < 1.0$ TeV. The smaller values at low $m_{t\bar{t}}^{\text{true}}$ are mostly due to the threshold criteria on the transverse momenta of leptons and jets. The probability for an event to pass the boosted-topology selection (dashed lines) increases steadily for $m_{t\bar{t}}^{\text{true}} > 0.5$ TeV because higher values of $m_{t\bar{t}}^{\text{true}}$ correspond to more energetic top quarks for which the products of the hadronic decay are more collimated and hence more likely to be merged into a single large-R jet that passes the selection criteria described in Section 5.2.2. Events in the boosted-topology category clearly dominate the selected event sample for $m_{t\bar{t}}^{\text{true}} > 1.5$ TeV, a result of the collimation of the decay products from the hadronic top-quark decay and the fact that events passing the boosted-topology selection are not considered for the resolved-topology selection.

Clear differences between the e- and the μ+jets channels are observed for $m_{t\bar{t}}^{\text{true}} > 1.5$ TeV,

with the efficiency times acceptance in the latter case being up to a factor of two higher than in the former case. This is a consequence of the differences in the overlap removal procedures for electrons and muons: In the case of the electron-jet overlap removal, the electron is removed if $\Delta R(e, j) < 0.2$, whereas the muon-jet overlap removal criterion in Equation 5.2 allows for $t\bar{t}$ events with a much smaller angular separation between the muon and the b-jet to be accepted for further analysis.

Furthermore, at large values of $m_{t\bar{t}}^{\text{true}}$, the selection efficiency in both channels is limited by the b-tagging efficiency [245] which decreases notably with increasing transverse momentum of the b-jet from the top-quark decay as shown in Figure 4.4a. The reasons for this effect have been discussed in Section 5.1. Alternative b-tagging strategies that rely on track jets with R-parameter values smaller than 0.4 [246] or an improved version of the MV1 tagger, MVb, which has been specifically designed for dense decay topologies [233], have been developed within ATLAS but had not been fully commissioned by the time the analysis strategy for this search was finalised and are therefore not used here.

A comparison between the four resonance models in Figure 5.6 shows that the efficiency times acceptance at any given mass point is largest for the spin-2 resonance, G_{KK}. This is a consequence of the fact that the top quarks from this resonance decay are more centrally distributed compared to the spin-1 resonances, Z' and g_{KK}, which results in a higher fraction of top quarks at larger pseudorapidities, as illustrated in Figure A.1 in the appendix.

5.4. Event Reconstruction

The selected events in the four categories - the e- and μ+jets channels with each the boosted- and resolved-topology selection - are reconstructed based on the assumption that the final state signature stems from the semileptonic decay of a $t\bar{t}$ pair. The aim is to reconstruct the invariant mass of the $t\bar{t}$ system, $m_{t\bar{t}}^{\text{reco}}$, from the selected objects in order to study the $m_{t\bar{t}}^{\text{reco}}$ spectrum and search it for deviations from the SM expectations. The reconstruction strategies naturally differ between the boosted and resolved event topologies.

5.4.1. Neutrino Reconstruction

In both cases, the first reconstruction step is the determination of the four-momentum of the neutrino. Its transverse momentum is taken to be the E_T^{miss} vector, assuming that all other possible sources of E_T^{miss}, such as energy losses in dead material or secondary neutrinos from

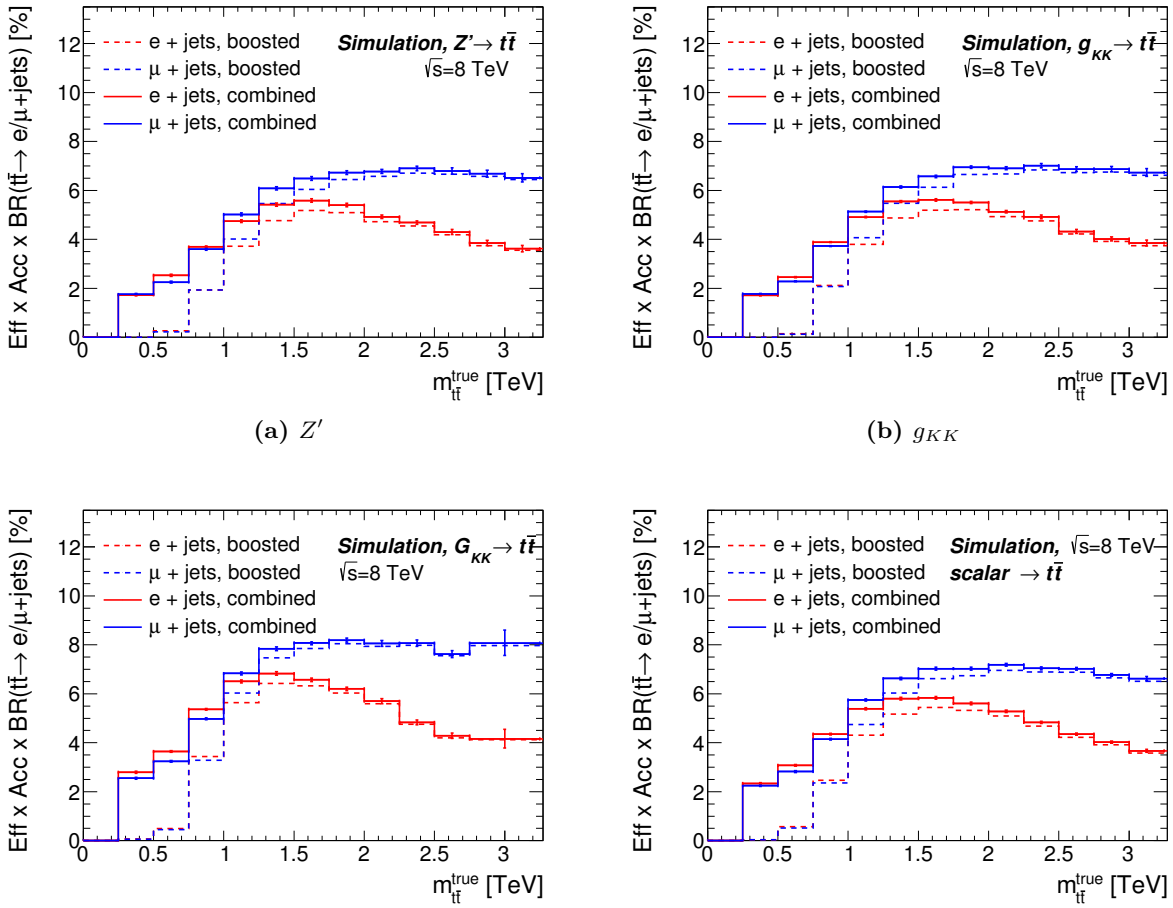

(a) Z' **(b)** g_{KK}

(c) G_{KK} **(d)** Scalar

Figure 5.6.: Selection efficiency times acceptance times branching ratio for the four benchmark models described in Section 2.5: (a) Z', (b) g_{KK}, (c) G_{KK}, and (d) scalar resonance. The respective products are given as a function of the true $t\bar{t}$ mass and for both the combined boosted- and resolved-topology selection (solid lines) and for the boosted-topology selection alone (dashed lines).

heavy-flavour decays, have been already accounted for by the calibration of the other reconstructed objects in the event. The longitudinal momentum component, p_z^ν, cannot be measured directly because the longitudinal momentum of the centre-of-mass frame of the hard interaction with respect to the laboratory frame is unknown (Section 3.2.1). It can, however, be calculated from the kinematic constraint that the sum squared of the four-momenta of the neutrino and the charged lepton from the on-shell decay of a W-boson must yield the W-boson mass, m_W: $m_W^2 = (p^\nu + p^{\text{lep}})^2$. Since m_W is known and the four-momentum of the charged lepton has been fully reconstructed, this quadratic equation can be solved for p_z^ν. If only one real solution exists, the neutrino four-momentum can be reconstructed without ambiguity given that $m^\nu \approx 0$. If the equation has no real solution, the E_T^{miss} vector is scaled and rotated by the minimum amount necessary to produce exactly one real solution.[8] If two real solutions are found, the one with the smallest $|p_z^\nu|$ is used in the boosted-topology case. In the resolved-topology reconstruction, the choice is made by the χ^2 algorithm (Section 5.4.3).

5.4.2. Event Reconstruction in the Boosted Topology

Events within the boosted-topology category can straightforwardly be reconstructed by taking the leading large-R jet as the hadronically-decaying (merged) top quark and reconstructing its leptonically decaying counterpart from the neutrino, the charged lepton and previously selected small-R jet, j_{sel} (Section 5.3.4). The invariant mass $m_{t\bar{t}}^{\text{reco}}$ is then calculated from the four-momentum sum of these four objects.

5.4.3. Event Reconstruction in the Resolved Topology

The reconstruction of events in the resolved-topology category is more involved since there are many possible ways to pick four out of the four or more selected small-R jets and assign them to the leptonically- and hadronically-decaying top quarks. Like in the case of the neutrino reconstruction, kinematic constraints are used to identify the optimal assignment. This is achieved by means of a χ^2 function:

$$\begin{aligned}\chi^2 = &\left[\frac{m_{jj} - m_W}{\sigma_W}\right]^2 + \left[\frac{m_{jjb} - m_{jj} - m_{t_h - W}}{\sigma_{t_h - W}}\right]^2 + \left[\frac{m_{j\ell\nu} - m_{t_\ell}}{\sigma_{t_\ell}}\right]^2 \\ &+ \left[\frac{(p_{T,jjb} - p_{T,j\ell\nu}) - (p_{T,t_h} - p_{T,t_\ell})}{\sigma_{\text{diff}\, p_T}}\right]^2,\end{aligned} \tag{5.4}$$

[8] This procedure is justified considering that a mis-measurement of E_T^{miss} is the most likely cause for the lack of a solution to the momentum equation.

which is calculated from the four-momenta of the neutrino, the charged lepton and four selected small-R jets [2]. The first term expresses the fact that, since the W-boson from one top quark decays hadronically, there must be two jets with a combined invariant mass, m_{jj}, close to m_W. By the same logic, there must be a third jet which, in combination with the two jets from the W-boson decay, yields an object with an invariant mass, m_{jjb}, close to the mass of the hadronically decaying top quark, t_h. Instead of using the absolute mass difference $m_{jjb} - m_{\text{top}}$, though, which would be heavily correlated with the first term, the invariant two-jet mass of the first term is subtracted from the three jet mass m_{jjb} to yield the term in the form quoted above. The third term expresses the equivalent mass constraint for the leptonically decaying top quark, t_ℓ. Finally, the last term constrains the transverse momenta of the two reconstructed top quarks to be similar, as expected for resonant $t\bar{t}$ production.

The values of the parameters of the χ^2 function have been evaluated on Z' signal MC events in which the jets, the electron or muon, and the reconstructed neutrino have been matched to the four quarks, the electron or muon and the neutrino from the hard process in order to find the right assignment. A quark is considered matched to a jet if it is within $\Delta R < 0.4$ from the jet axis. The matching criterion for reconstructed electron or muon to its counterpart from the hard process is the same as that for the matching of quarks to jets. In the case of the neutrino, the angular difference $\Delta\phi$ to the E_T^{miss} vector is required to be smaller than one. Among all events passing the resolved-topology selection roughly 70% (55%) of the Z' signal events with $m_{Z'} = 750$ GeV ($m_{Z'} = 500$ GeV) have all six decay products matched to a corresponding detector-level objects [2]. The values of the central parameters m_W, $m_{t_h - W}$, m_{t_ℓ} and $(p_{T,t_h} - p_{T,t_\ell})$ as well as the corresponding width parameters σ_W, $\sigma_{t_h - W}$, σ_{t_ℓ}, $\sigma_{\text{diff}\, p_T}$ are obtained from the fit of a Gaussian function to the relevant kinematic distributions. The fitted parameter values are: $m_W = 82.4$ GeV, $m_{t_h - W} = 89.0$ GeV, $m_{t_\ell} = 166.0$ GeV, $(p_{T,t_h} - p_{T,t_\ell}) = 0.43$ GeV, $\sigma_W = 9.6$ GeV, $\sigma_{t_h - W} = 15.7$ GeV, $\sigma_{t_\ell} = 17.5$ GeV and $\sigma_{\text{diff}\, p_T} = 46.1$ GeV [2].

All possible permutations of small-R jets and both neutrino solutions (if there is more than one) are tested and the combination that minimises χ^2 is chosen for the reconstruction of $m_{t\bar{t}}^{\text{reco}}$. The number of permutations to be tested is reduced by requiring that any b-tagged jets can only be assigned to either of the b-quarks from the top-quark decays. Studies on Z' and g_{KK} signal MC events in which all six decay products from the two top quarks have been matched to a counterpart reconstructed at detector level show that the χ^2 minimisation succeeds in choosing the correct assignment in over 80% of the events [2]. For G_{KK} and scalar resonance signal events,

smaller values of 60-70% are found. This is a consequence of the higher rates of ISR from the gg initial states of these signal processes compared to the $q\bar{q}$ initial states of the other two signal processes, resulting in larger jet multiplicities in the event and hence a larger combinatorial background in the reconstruction.

5.4.4. Reconstructed $t\bar{t}$ Invariant Mass Distributions and Experimental Resolution

The reconstructed $t\bar{t}$ invariant mass distributions for different signal samples for all events that pass the resolved- and boosted-topology selection, respectively, are shown in Figures 5.7 and 5.8. As expected, the mass distributions peak at the resonance mass of the respective samples. Most distributions exhibit tails towards lower masses which are especially significant for broader resonances and larger resonance masses. They are caused by two effects: Firstly, final-state radiation (FSR) from any of the objects in the $t\bar{t}$ system that is not included in the reconstruction, for example because it results in an extra high-p_T jet, leads to lower values of $m_{t\bar{t}}^{\text{reco}}$. This effect is particularly important at high resonance masses where the top quarks and their decay products are more energetic and hence the probability for the emission of hard gluon radiation is higher. The second effect is a result of the finite resonance width in combination with the shape of the parton luminosity functions: The finite width Γ_X allows for a resonance to be produced with a mass slightly below or above its nominal mass value m_X, according to the common Breit-Wigner function for resonant particle production. The steeply falling parton luminosities shown in Figure 2.2b lead to notable differences in the probabilities for a resonance to be produced slightly below or above its nominal mass values, thus causing the convolution of the Breit-Wigner curve with the parton luminosity distribution to be skewed towards lower resonance masses, an effect sometimes referred to as the "parton luminosity tail". This is reflected in the distribution of $m_{t\bar{t}}^{\text{reco}}$ and is especially notable for the g_{KK} resonances, the broadest resonances under consideration. The two effects are illustrated in Figure A.4 in the appendix which shows the generator-level mass distributions for the 1.0 TeV and 2.0 TeV mass points of the four benchmark models before and after the emission of FSR.

The experimental resolution of the reconstructed $t\bar{t}$ invariant mass, $m_{t\bar{t}}^{\text{reco}}$, which depends on the energy, momentum and mass resolution of the different reconstructed objects, for example small-R and large-R jets, in the detector, is defined as the width of a Gaussian fit to the distribution

$$\frac{m_{t\bar{t}}^{\text{reco}} - m_{t\bar{t}}^{\text{true,FSR}}}{m_{t\bar{t}}^{\text{true,FSR}}}, \tag{5.5}$$

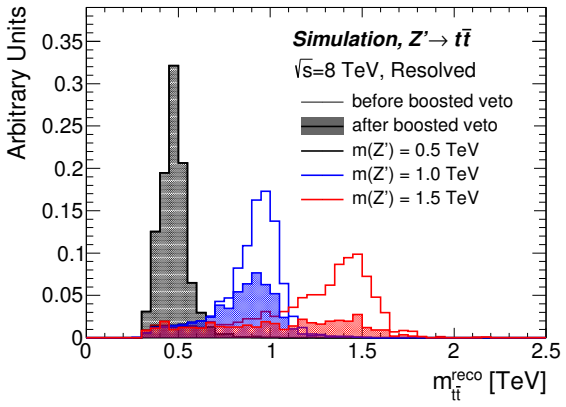

(a) Z'

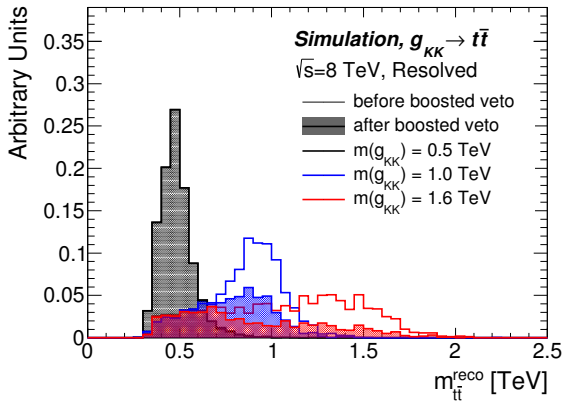

(b) g_{KK}

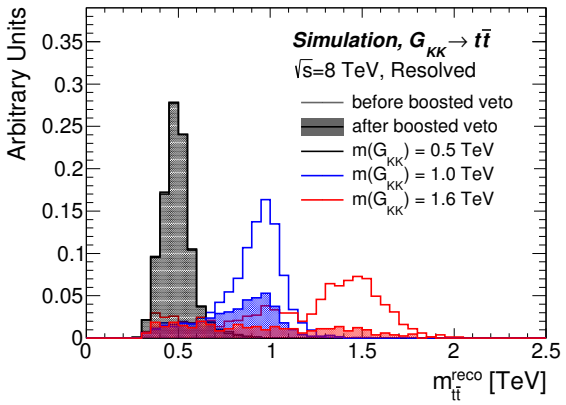

(c) G_{KK}

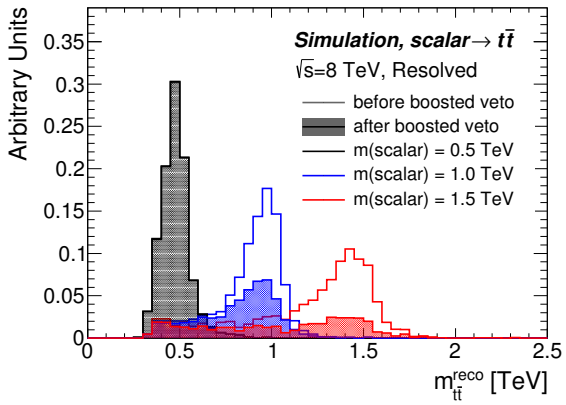

(d) Scalar

Figure 5.7.: Reconstructed $t\bar{t}$ invariant mass distributions for the four signal models considered in the search: (a) Z', (b) g_{KK}, (c) G_{KK}, and (d) scalar resonance. The events satisfy the criteria of the resolved-topology selection before (empty) or after (filled) the veto on events that also pass the boosted-topology criteria. All distributions are normalised to unit area.

where only events in which all reconstructed objects have been correctly assigned to their lepton and quark counterparts in the $t\bar{t}$ final state at generator level are taken into account. The true $t\bar{t}$ invariant mass after FSR, $m_{t\bar{t}}^{\text{true,FSR}}$, is defined as the combined invariant mass of the six $t\bar{t}$ decay products at generator level. The experimental resolution is found to be 8% (6%) for a resonance mass of 0.4 TeV (1.0 TeV) in the resolved topology and 6%, independent of the resonance mass, in the boosted topology [2].

5.4.5. b-tagging Categories

After the leptonically- and hadronically-decaying top-quark candidates have been reconstructed for both boosted- and resolved-topology events, the events in each of the four selection categories are further classified into b-tagging categories: The first b-tagging category contains events

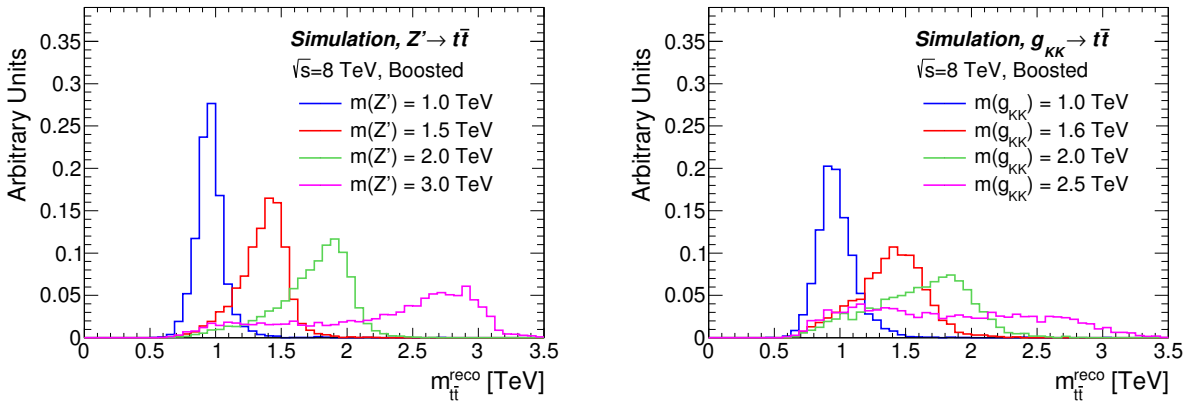

(a) Z'

(b) g_{KK}

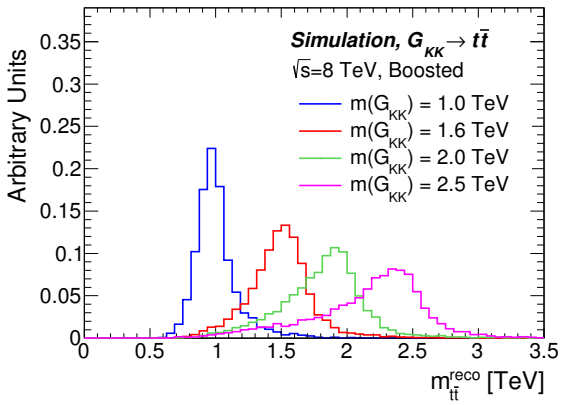

(c) G_{KK}

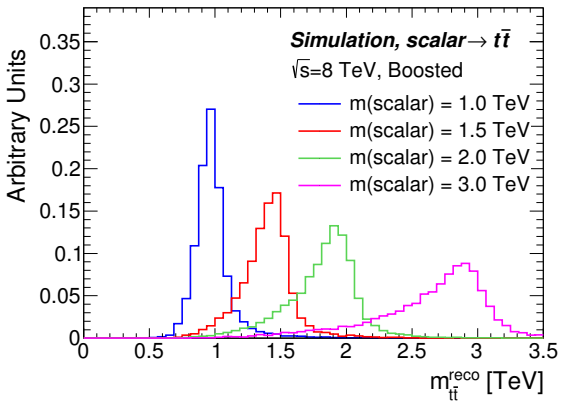

(d) Scalar

Figure 5.8.: Reconstructed $t\bar{t}$ invariant mass distributions for the four signal models considered in the search: (a) Z', (b) g_{KK}, (c) G_{KK}, and (d) scalar resonance. All events satisfy the criteria of the boosted-topology selection. All distributions are normalised to unit area.

in which both top-quark candidates have a matching b-tagged jet. Events in categories two and three have only the hadronically-decaying or semileptonically-decaying top-quark candidate matched to a b-tagged jet, respectively. For events with a resolved decay topology, a b-tagged jet is considered matched to a top-quark candidate if it was assigned to it by the χ^2 algorithm. In the case of boosted-topology events, the hadronically-decaying top quark is considered matched to a b-tagged jet if its corresponding large-R has a b-tagged small-R jet within $\Delta R < 1.0$. The semileptonically-decaying top-quark candidate is considered matched if the selected small-R jet, j_{sel}, is b-tagged. After the b-tagging categorisation, there are twelve mutually exclusive event categories which define the signal regions of this search.

5.5. Data-Driven Estimation of Background Processes

The majority of background processes, including SM $t\bar{t}$ production, by far the largest background component in this analysis (Section 6.1.1), are estimated relying purely on MC simulations. Details of the MC generators and settings used for the simulation of the various processes have been given in Section 3.4.2. MC generators are essential tools in high-energy physics with a great predictive power. Nevertheless, they are based on theoretical assumptions, approximations and modelling choices, and their predictions must be interpreted with care and validated against real data where possible.[9] Moreover, systematic uncertainties have to be introduced to account for those modelling choices and theoretical uncertainties, as described in Section 5.6. In certain cases, therefore, partly or fully data-driven approaches have been found to yield a more reliable background prediction with smaller systematic and statistical uncertainties. In the analysis presented here, data-driven techniques are used in the estimation of two background components: In the case of the W+jets background, data is used to derive scale factors that are applied to events simulated with the Alpgen MC generator to correct the overall normalisation and individual flavour fractions (Section 3.4.2). A purely data-driven technique is used to estimate the background from QCD multi-jet production (Section 5.5.2). Note that a data-driven derivation of the (irreducible) background from SM $t\bar{t}$ production is not possible in this analysis, as explained in Section 2.2.1.

5.5.1. Background from W+jets

The background from W+jets events is estimated using MC simulations to predict its shape, and scale factors derived from data to correct its overall normalisation and the individual flavour fractions. Events are genererated with the Alpgen MC generator as described in Section 3.4.2. Scale factors are then derived from data in an iterative two-step process based on the official recommendations of the ATLAS Top Working Group for analyses using the full 2012 ATLAS dataset [196]. The official W+jets scale factors that are derived centrally by this group cannot be used in this analysis because various selection criteria, such as the isolation requirement for electrons or the entire boosted-topology selection, deviate from the default selection criteria used by the ATLAS Top Working Group. Hence the scale factors needed to be rederived as described

[9] It is no coincidence that the MC generator Pythia carries the name of the (in)famous oracle from Greek mythology that is known for its reliable, though never quite unambiguous predictions. Hence the authors of Pythia conclude their manual with a warning: "You must be very careful when you formulate the questions (...) [a]nd you must be even more careful not to misinterpret the answers" [150].

in the following and documented in [2].

First, a **scale factor for the overall normalisation** is derived by exploiting the **charge asymmetry** in the production of W bosons at proton-proton colliders like the LHC: Positively charged W bosons, W^+, are produced in parton-level processes such as $u\bar{d} \to W^+ + X$, while negatively charged W bosons, W^-, originate from processes such as $d\bar{u} \to W^- + X$, where X stands for any number of final state partons produced in association with the $W^\pm$. The corresponding cross-sections $\sigma(pp \to W^+)$ and $\sigma(pp \to W^-)$ depend on the PDFs of the respective initial-state partons which differ for the u and d valence quarks in the proton, as illustrated in Figure 2.2a. The resultantly higher production rate for W^+ compared to W^- bosons results in an asymmetry in the number of W+jets events with a positively-charged lepton in the final state, N_{W^+}, and that with a negatively-charged lepton, N_{W^-}. Normalisation scale factors are derived by comparing this lepton charge asymmetry between data and MC simulation.

The key observation underlying this approach is that the ratio $r \equiv \sigma(pp \to W^+)/\sigma(pp \to W^-)$ is known to high accuracy [247] and much more precisely than the total cross-section for W+jets events with three or more jets. It can reliably be estimated as the ratio of event yields from W^+ and W^- production in samples generated with the Alpgen MC generator:

$$r_{MC} = \frac{N_{W^+}}{N_{W^-}}. \tag{5.6}$$

Using this result, the total number of W+jets events, $N_W = N_{W^+} + N_{W^-}$, can be calculated from the observed difference between the number of data events with a positively-charged lepton and that with a negatively-charged lepton using the formula:

$$N_{W^+} + N_{W^-} \stackrel{!}{=} \frac{N_{W^+} + N_{W^-}}{N_{W^+} - N_{W^-}} \cdot (D_+^{\text{corr}} - D_-^{\text{corr}}) = \frac{r_{MC} + 1}{r_{MC} - 1} \cdot (D_+^{\text{corr}} - D_-^{\text{corr}}). \tag{5.7}$$

The first equality sign is valid only under the assumption that the charge asymmetry observed in data is equal to that in a pure sample of W+jets events

$$N_{W^+} - N_{W^-} \stackrel{!}{=} D_+^{\text{corr}} - D_-^{\text{corr}}. \tag{5.8}$$

For this assumption to hold, the data yields must be corrected for contributions from other charge-asymmetric processes, such as single-top, $t\bar{t}$+W and diboson production. This is achieved by estimating the yields for these processes using MC simulations and subtracting them from

the data yields to obtain the corrected yields for data events with positively- and negatively-charged leptons. These are denoted as D_{+}^{corr} and D_{-}^{corr}, respectively. Contributions from charge-symmetric processes such as $t\bar{t}$, Z+jets and QCD multi-jet production need not be taken into account as they have no effect on the difference $(D_{+}^{\text{corr}} - D_{-}^{\text{corr}})$ on the right-hand side of Equation 5.7. The **normalisation scale factor** $\mathbf{C}_A$ is obtained by dividing the number $N_{W^+} + N_{W^-}$, derived from the charge asymmetry in data using Equation 5.7, by the corresponding W+jets event yield estimated on ALPGEN MC samples.

This procedure is carried out separately for the electron and muon channels and for the boosted and resolved event topologies. The set of selection criteria used to define the **normalisation region** in each case does not necessarily need to be identical to the one used in the definition of the corresponding signal region. In fact, a looser set of selection criteria that yields a normalisation region enriched with W+jets events is preferred as it leads to smaller statistical uncertainties on the normalisation scale factor C_A. For the resolved topology, all the nominal selection criteria are applied with the exception of the b-tagging requirement. For the boosted topology, in addition to the b-tagging requirement, the requirements on the jet mass, the $\sqrt{d_{12}}$ splitting scale and the angular separation $\Delta\phi(\text{jet}, \ell) > 2.3$ are dropped to sufficiently enhance the fraction of W+jets events in the normalisation regions for the boosted-topology selection. Possible biases introduced by these changes in the boosted selection criteria with respect to those for the boosted signal regions are investigated by rederiving the scale factors in *alternative* normalisation regions. These are obtained by applying each of the dropped selection criteria, one at a time, on top of the requirements for the *nominal* normalisation region. The alternative scale factors are found to be in agreement with the nominal scale factor within their statistical uncertainties [248].

The second step in the data-driven estimation of the scale factors for the W+jets background is the derivation of **correction factors for the relative fractions of processes with different quark flavours** in W+jets events, namely those with $W + b\bar{b}$, $W + c\bar{c}$, $W + c$ and W+light quark final states, respectively. The corresponding correction factors, denoted as $\mathbf{K}^{b\bar{b}}$, $\mathbf{K}^{c\bar{c}}$, $\mathbf{K}^{c}$ and $\mathbf{K}^{\text{light}}$ in the following, are derived from two W+jets enriched regions: The *post-tag* region is defined by applying all selection criteria for the resolved topology except the one on the jet multiplicity, which is changed so that exactly two anti-k_T $R = 0.4$ jets are required. The *pre-tag* region is defined in the same way except that no b-tagging requirement is applied.

The individual correction factors $K^{b\bar{b}}$, $K^{c\bar{c}}$, K^{c} and K^{light} are obtained by comparing the number

of W+jets events in data and MC in the *post-tag* region. This comparison is made separately for events with a positively-charged and those with a negatively-charged lepton. Breaking down the total number of $W^{\pm}$+jets events into the yields for the individual flavour fractions, this comparison can be written as:

$$C_A \cdot N_{\mathrm{MC},W^{\pm}} = C_A \cdot (K^{b\bar{b}} N^{b\bar{b}}_{\mathrm{MC},W^{\pm}} + K^{c\bar{c}} N^{c\bar{c}}_{\mathrm{MC},W^{\pm}} + K^{c} N^{c}_{\mathrm{MC},W^{\pm}} + K^{\mathrm{light}} N^{\mathrm{light}}_{\mathrm{MC},W^{\pm}}) = N_{\mathrm{data},W^{\pm}}, \tag{5.9}$$

where C_A is the normalisation scale factor obtained from the charge asymmetry method described above. $N_{\mathrm{data},W^{\pm}}$ denotes the number of estimated $W^{\pm}$+jets events in data for the post-tag region. It is obtained by deriving the yields for all non-W+jets backgrounds using the data-driven estimate described in Section 5.5.2 for the QCD multi-jets contribution and MC simulations for all other backgrounds. Those yields are then subtracted from the data yields in the post-tag region to obtain $N_{\mathrm{data},W^{\pm}}$.

Two further constraints are needed to determine the four unknown correction factors: The first constraint is imposed by fixing the ratio of the fractions of the $W + b\bar{b}$ and $W + c\bar{c}$ components, which is determined directly from the MC samples. This means that a single correction factor $K^{b\bar{b}/c\bar{c}} \equiv K^{b\bar{b}} = K^{c\bar{c}}$ is derived for both components. This is a reasonable assumption given that the parton-level processes for both final states are similar and any potential MC mis-modelling would be likely to affect both components in a correlated way.

The second constraint comes from the requirement that the flavour fractions in the *pre-tag* region must add up to unity *after* the correction factors are applied, thus preserving the overall normalisation:

$$f^{b\bar{b}}_{MC} \cdot K^{b\bar{b}} + f^{c\bar{c}}_{MC} \cdot K^{c\bar{c}} + f^{c}_{MC} \cdot K^{c} + f^{\mathrm{light}}_{MC} \cdot K^{\mathrm{light}} = 1. \tag{5.10}$$

Here $f^{b\bar{b}}_{MC}$, $f^{c\bar{c}}_{MC}$, f^{c}_{MC} and f^{light}_{MC} are the simulated fractions of the different flavour components derived by comparing the *pre-tag* event yields for the respective MC flavour samples.

With these additional constraints, the correction scale factors $K^{b\bar{b}/c\bar{c}}$, K^{c} and K^{light} can be obtained by solving the following system of linear equations:

$$\begin{pmatrix} C_A \cdot (N^{bb}_{\mathrm{MC},W^-} + N^{cc}_{\mathrm{MC},W^-}) & C_A \cdot N^{c}_{\mathrm{MC},W^-} & C_A \cdot N^{\mathrm{light}}_{\mathrm{MC},W^-} \\ (f_{bb} + f_{cc}) & f_c & f_{ll} \\ C_A \cdot (N^{bb}_{\mathrm{MC},W^+} + N^{cc}_{\mathrm{MC},W^+}) & C_A \cdot N^{c}_{\mathrm{MC},W^+} & C_A \cdot N^{\mathrm{light}}_{\mathrm{MC},W^+} \end{pmatrix} \cdot \begin{pmatrix} K^{b\bar{b}/c\bar{c}} \\ K^{c} \\ K^{\mathrm{light}} \end{pmatrix} = \begin{pmatrix} D_{W^-} \\ 1.0 \\ D_{W^+} \end{pmatrix}. \tag{5.11}$$

The two-step procedure for the derivation of the overall normalisation scale factor C_A and the correction factors for the flavour fractions is then iterated using the corrected flavour fractions in the derivation of the C_A scale factor. This is necessary because a change in the relative fractions of $W + c$ events on the one hand, and $W + c\bar{c}$, $W + b\bar{b}$ and W+light quark flavour events on the other hand affects the value of r_{MC} used in the derivation of C_A.[10] The procedure is repeated until the differences between the scale factors of two subsequent iterations are negligible. This is found to be the case after only ten iterations [1].

The final correction factors for the flavour fractions, which have been derived for the modified signal region with the requirement of exactly two selected anti-k_T $R = 0.4$ jets, are then extrapolated to regions with higher jet multiplicities, namely the signal region, which requires ≥ 4 jets, by keeping their relative ratios fixed while requiring that the overall normalisation in each jet multiplicity bin is preserved. The same correction factors are used for both the boosted- and the resolved-topology selections because flavour fraction scale factors derived separately for the boosted topology have been found to suffer from large statistical uncertainties due to the lower selection efficiency for W+jets events in this case [248].

The final scale factor values and their statistical uncertainties are summarised in Table 5.5.1. The scale factors for the flavour fractions and for the normalisation in the boosted topology are notably different from unity implying a certain degree of disagreement between the MC prediction and the data which is corrected for by the application of the scale factors. Differences of around 10% between the electron and muon channel are observed for individual scale factors. These differences have been investigated and found to be related to small differences in the detector acceptance for electrons and muons as a function of the pseudorapidity [2]. The normalisation scale factors for the resolved topology are compatible with unity within their statistical uncertainties. Although this means that the data-driven method has little effect on the overall yields for the resolved-topology selection, it leads to a reduction of the systematic uncertainties on the W+jets background compared to a purely MC-based background estimate. The treatment of the systematic uncertainties related to the W+jets background is described in Section 5.6.3.

[10] This is mostly due to the fact that the value of r_{MC} is slightly different for $W + c$ events compared to $W + c\bar{c}$, $W + b\bar{b}$ and W+light quark flavour events because the cross-section in the former case has a notable dependence on the PDF of the s-quark [249].

	$K^{b\bar{b}}$, $K^{c\bar{c}}$	K^{c}	K^{light}	C_A (resolved)	C_A (boosted)
e+jets	1.36 ± 0.07	0.71 ± 0.03	0.934 ± 0.005	1.03 ± 0.01	0.89 ± 0.06
μ+jets	1.52 ± 0.08	0.66 ± 0.03	0.873 ± 0.004	0.98 ± 0.01	0.81 ± 0.05

Table 5.1.: Scale factors and their statistical uncertainties for the flavour fractions and the overall normalisation of the W+jets samples for the electron and muon channels. The normalisation scale factors have been derived separately for the resolved- and boosted-topology selection while the same scale factors are used for the correction of the flavour fractions in both topologies. Numbers taken from [2].

5.5.2. Background from QCD Multi-jet Production

Events with purely hadronic final states produced via the strong interaction, referred to as **QCD multi-jet events** in the following, constitute an important background to analyses at hadron colliders because their cross-section exceeds that of other SM processes, such as SM $t\bar{t}$ production, by several orders of magnitude, as illustrated in Figure 5.1. Their contribution to the overall background yield is considerably reduced by selecting only events with one or more isolated leptons in the final state, as in the case of the ℓ+jets selection in this analysis. The `tight` quality and isolation criteria introduced in Sections 4.1 and 4.2 are specifically optimised to reject QCD multi-jet events in the selection process, rendering QCD multi-jet production a minor, though non-negligible, background to this analysis (Section 6.1.1).

There are two ways in which QCD multi-jet events may pass the `tight` lepton identification and isolation criteria: First, real electrons and muons may arise from (semi)leptonic decays inside hadronic jets. Typical sources of such *non-prompt leptons* are semileptonic weak decays of heavy-flavour hadrons, such as B- and D-hadrons, and leptonic decays-in-flight of charged pions and kaons, the latter resulting mostly in muons due to the helicity suppression of the decay to electrons. If the lepton is emitted at a large angle from the jet axis, and if the jet is poorly reconstructed, the lepton may be identified as isolated. These sources of non-prompt leptons contribute to the multi-jet background in both the e+jets and the μ+jets channel. Another source of non-prompt leptons, which contributes to the e+jets channel only, is photon conversion to electron-positron pairs, $\gamma \to e^+e^-$, where the photon arises, for example, from the decay of a neutral pion, $\pi^0 \to \gamma\gamma$, inside the hadronic jet.

The second contribution to the QCD multi-jet background comes from events where a quark or gluon jet is mis-identified as a lepton. These *fake leptons* are significantly more likely to occur in the e+jets channel due to the differences in electron and muon reconstruction described in

Sections 4.1 and 4.2: For example, isolated hadronic jets can be mis-identified as electrons if they contain a large fraction of electromagnetic decays, such as $\pi^0 \to \gamma\gamma$, which lead to large energy deposits in the electromagnetic calorimeter. These effects result in a larger contribution from QCD multi-jet events to the yields in the e+jets channel compared to those in the μ+jets channel, as shown in Table 6.1 in the next chapter.

The diversity of processes contributing to the QCD multi-jet background and their particular dependence on instrumental effects makes this background component especially hard to model adequately in simulations. Moreover, large systematic uncertainties are associated with MC simulations of the hard process itself, especially for large jet multiplicities where higher-order effects need to be taken into account. Finally, MC samples with large event statistics would need to be generated in order to reduce the statistical errors of an MC-based background estimation due to the very small probability for a QCD multi-jet event passing the `tight` lepton selection criteria of the ℓ+jets channel.

Therefore, a data-driven approach, a so-called **Matrix Method**, is used to determine both the normalisation and shape of the QCD multi-jets background in the signal regions as well as its associated statistical and systematic uncertainties. The Matrix Method was first used by the DØ collaboration at the Tevatron [250] and both the ATLAS and CMS collaborations have applied modified versions of this technique in various analyses, see for example [251, 252].

The Matrix Method is based on the comparison between two data samples, the selection criteria for which differ only in the quality requirements imposed on the lepton: The first sample is obtained by applying the full set of requirements for the signal region of a given search channel, including the `tight` lepton quality criteria described in Sections 4.1 and 4.2. The second data sample is defined in the same way except that the `tight` lepton quality criteria are replaced by a looser set of requirements (see below for details). The first sample is therefore a subsample of the second. Both data samples contain QCD multi-jet events as well as events from processes such as SM $t\bar{t}$ and W/Z+jets production with *prompt leptons* originating from the decays of W and Z bosons. The event yields N_L and N_T for the data samples with the `loose` and `tight` lepton definitions, respectively, can then be written as:

$$\begin{aligned} N_L &= N_{\text{prompt}} + N_{\text{multi-jet}} \\ N_T &= \epsilon \cdot N_{\text{prompt}} + f \cdot N_{\text{multi-jet}}. \end{aligned} \tag{5.12}$$

The efficiency ϵ is defined as the probability that a `loose` lepton from prompt sources also passes the `tight` lepton selection criteria. The equivalent probability for a `loose` lepton from the QCD multi-jet background is denoted as the false-identification rate f. If ϵ and f are known, the multi-jet contribution to the signal region can be obtained from the observed event yields in the two data samples by solving Equations 5.12 for $f \cdot N_{\text{multi-jet}}$:

$$f \cdot N_{\text{multi-jet}} = \frac{(\epsilon - 1) \cdot f}{\epsilon - f} \cdot N_T + \frac{\epsilon \cdot f}{\epsilon - f} \cdot N_A. \tag{5.13}$$

Here $N_A = N_L - N_T$ denotes the number of events with an *anti*-`tight` lepton, i.e. a `loose` lepton that fails one or more of the `tight` selection criteria.

For Equation 5.13 to yield a reliable estimate of the QCD multi-jet contribution to the signal region, it is important that the difference $\epsilon - f$, which enters the calculation in the denominator, is sufficiently large to minimise the impact of the statistical uncertainties on ϵ and f on the final yields. The `loose` lepton definition must therefore be chosen such that the corresponding data sample contains a large fraction of QCD multi-jet events compared to the sample obtained for the `tight` lepton definition.

In the μ+jets channel, this is achieved by dropping the isolation requirement on the muon. In the e+jets channel, in addition to dropping the isolation requirement, the `tight` lepton definition is replaced by the looser criteria of the `medium` category (Section 4.1) with an additional veto against electrons from photon conversions. The `loose` electron and muon definitions used in this analysis are based on the recommendations given in [253].

The probabilities ϵ and f are derived separately for each lepton flavour and for both the resolved- and boosted-topology selections: The **efficiency** ϵ is obtained from a sample of simulated SM $t\bar{t}$ events, by far the dominant source of prompt leptons in the signal region, as illustrated in Table 6.1. Contributions from other sources of prompt leptons such as W/Z+jets events can be neglected because their overall contribution to the signal region is small and because the differences in ϵ between the different sources have been found to be negligible [254]. Lepton scale factors derived from $Z \to \ell\ell$ events are applied to correct for differences in lepton efficiencies between simulation and data (Sections 4.1 and 4.2). The efficiency is calculated as the fraction of SM $t\bar{t}$ events in the signal region with only the `loose` lepton selection criteria applied that also pass the `tight` quality requirements. It has been verified by a comparison to data that this efficiency is well modelled in simulated events with the lepton scale factors applied [2].

The **false-identification rate** f is derived from data using a **control region (CR0)** that is enriched in QCD multi-jet events. The selection criteria for CR0 are based on those for the signal region in order to reduce systematic biases due to differences in the event topology and kinematics between signal and control regions. However, a number of selection criteria are changed compared to the signal region definition to suppress contributions from processes other than QCD multi-jet events:

- Events containing a leptonically decaying W boson, such as those from SM $t\bar{t}$ and W+jets production, are suppressed by inverting the requirements on the missing energy E_T^{miss} and the transverse mass of the leptonic W boson M_T^W: E_T^{miss} is now required to be smaller than 20 GeV and the sum $E_T^{\text{miss}} + M_T^W$ to be smaller than 60 GeV.
- For the resolved-topology selection, the contribution from SM $t\bar{t}$ events is further suppressed by removing the requirement on the goodness-of-fit variable χ^2 for the event reconstruction (Section 5.3).
- For the boosted-topology selection, the suppression of SM $t\bar{t}$ and, to a smaller extend, W+jets events is achieved by changing the mass requirement on the large-R jet: The jet mass is required to be less than 70 GeV. Moreover, the requirement on the k_T-splitting scale $\sqrt{d_{12}}$ is dropped entirely and the lower threshold on the transverse momentum of the jet is lowered from 300 GeV in the signal region to 100 GeV in CR0 to further increase the fraction of QCD multi-jet events, which typically have large-R jets with small transverse momenta.

Finally, in order to measure the false-identification rate, the `tight` lepton definition of the signal region is replaced by the `loose` requirements. The remaining contributions from processes other than QCD multi-jet production are estimated using MC simulations and subtracted from the data yields in CR0. The false-identification rate f is then defined as the fraction of data events in CR0 passing the `tight` lepton selection criteria.

The efficiencies ϵ and f are derived in bins of a number of kinematic variables. This is necessary in order to estimate not only the overall yield of the QCD multi-jets background in the signal region but also its shape as a function of the invariant mass of the $t\bar{t}$ system. This is achieved by using Equation 5.13 to calculate a weight for each data event in the `loose` sample. The weight is calculated from the right-hand side of Equation 5.13 by setting $(N_T, N_A) = (1, 0)$ if the event passes the tighter lepton selection criteria and $(N_T, N_A) = (0, 1)$ otherwise. The values of ϵ

and f are determined based on the kinematic properties of the event in question. The choice of kinematic variables for the parameterisation of ϵ and f is based on two considerations. On the one hand, the accuracy of the modelling of the invariant mass distribution increases with the number of kinematic variables that are considered in the reweighting of the data events. On the other hand, the statistical errors on ϵ and f increase as the data events are distributed over more bins. Therefore, only the kinematic variables that have the largest impact on the probabilities ϵ and f are considered. These variables are found to be the transverse momentum of the lepton, and the distance $\Delta R(e, \text{closest jet})$ between the lepton and the jet closest to it. In the case of the false-identification rate f, the transverse momentum of the jet closest to the lepton is used in addition. The efficiency ϵ has been found to exhibit little dependence on this variable [254], hence this additional binning is not used in this case.

The values for ϵ and f for both electrons and muons are shown in Figures 5.9 and 5.10 for the resolved- and boosted-topology selections, respectively. The efficiency ϵ for a `loose` prompt lepton to pass the `tight` lepton selection criteria is found to be close to unity in the majority of bins. This is to be expected as the `tight` lepton definition has been optimised for a high selection efficiency for prompt leptons. Smaller values of ϵ are found for lower values of the transverse momentum of the lepton and for leptons close to or within a jet. This is expected since these leptons tend to be less well reconstructed than isolated leptons or leptons with larger transverse momenta. The values for the false-identification rate f are significantly lower than those for ϵ, as discussed above. Moreover, the false-identification rate in the e+jets channel is on average larger than that in the μ+jets channel which can be explained by the larger number of effects contributing to the QCD multi-jets background in this channel, as discussed at the beginning of this section. The values for ϵ and f agree within statistical uncertainties between the resolved- and boosted-topology selections.

The shape modelling of the invariant mass distribution for the QCD multi-jet background has been validated by comparing the estimated background distributions in the QCD multi-jet enriched control region CR0 to those observed in data. The distributions agree within the overall uncertainty as illustrated in Figure 5.11.

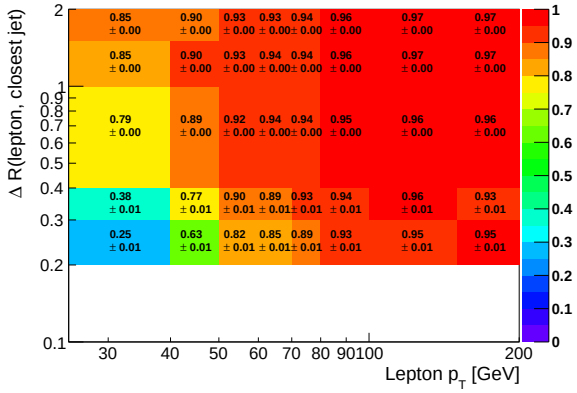

(a) Efficiency ϵ, e+jets channel

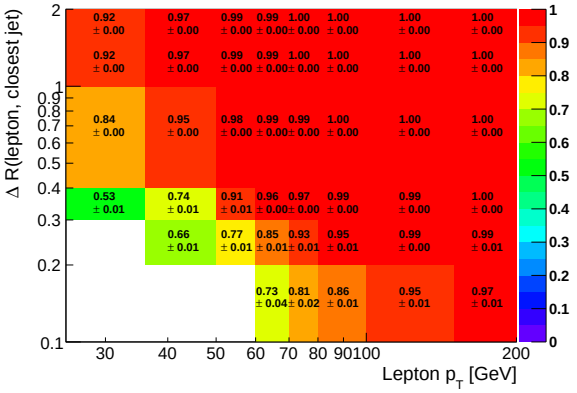

(b) Efficiency ϵ, μ+jets channel

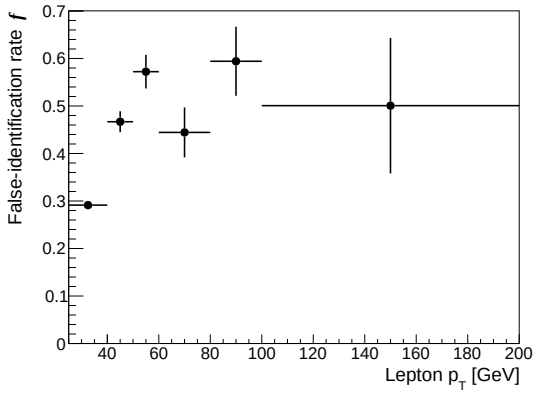

(c) False-identification rate f, e+jets channel, $\Delta R(e, \text{closest jet}) \geq 0.4$

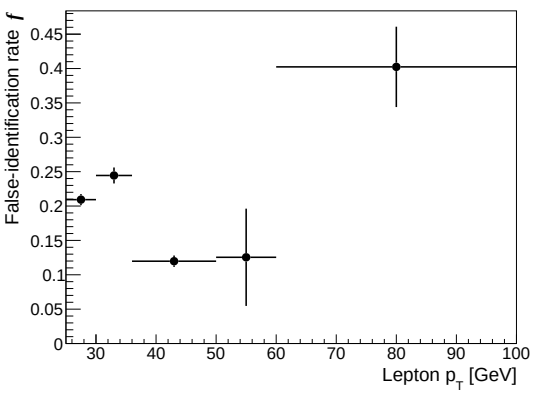

(d) False-identification rate f, μ+jets channel, $\Delta R(\mu, \text{closest jet}) \geq 0.4$

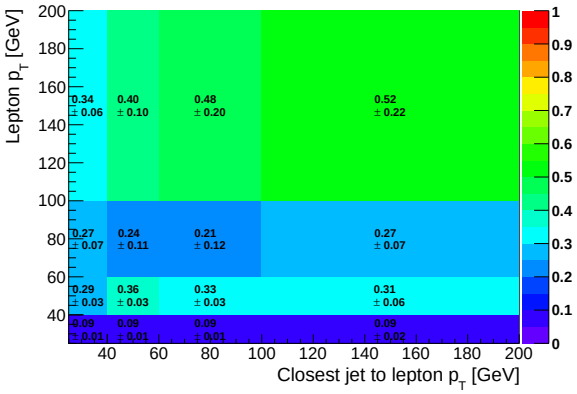

(e) False-identification rate f, e+jets channel, $\Delta R(e, \text{closest jet}) < 0.4$

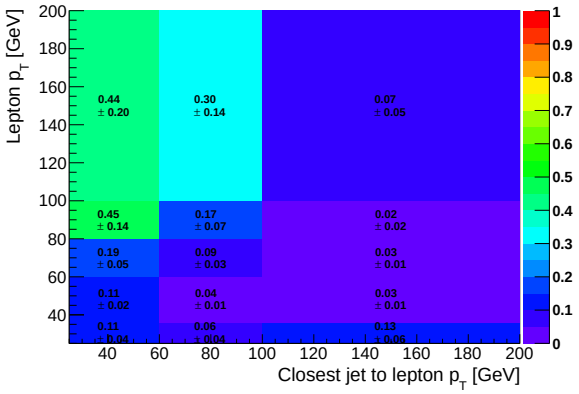

(f) False-identification rate f, μ+jets channel, $\Delta R(\mu, \text{closest jet}) < 0.4$

Figure 5.9.: Resolved-topology selection: (a,b) Efficiency ϵ for `loose` prompt leptons to be identified as `tight`, given as a function of the transverse momentum of the lepton and the distance $\Delta R(e, \text{closest jet})$ between the lepton and the closest jet; (c-f) false-identification rate f for `loose` leptons from the QCD multi-jet background to be identified as `tight` as a function of the transverse momenta of the lepton and the closest jet for the cases $\Delta R(e, \text{closest jet}) \geq 0.4$ and $\Delta R(e, \text{closest jet}) < 0.4$. Numbers taken from [2].

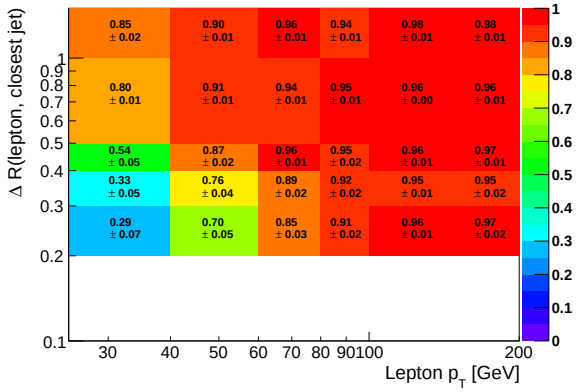

(a) Efficiency ϵ, e+jets channel

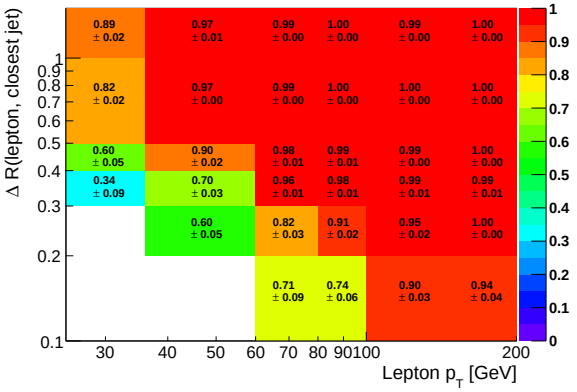

(b) Efficiency ϵ, μ+jets channel

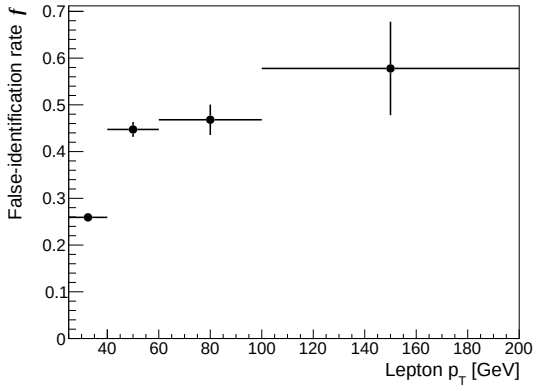

(c) False-identification rate f, e+jets channel, $\Delta R(e, \text{closest jet}) \geq 0.4$

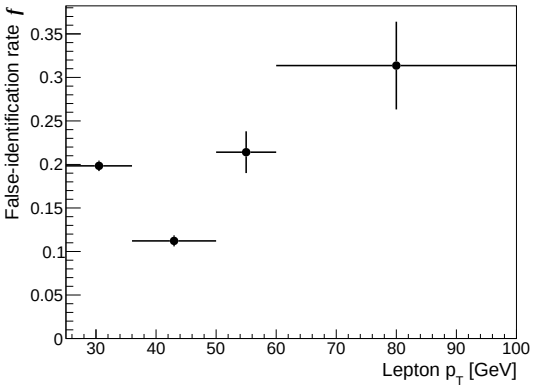

(d) False-identification rate f, μ+jets channel, $\Delta R(\mu, \text{closest jet}) \geq 0.4$

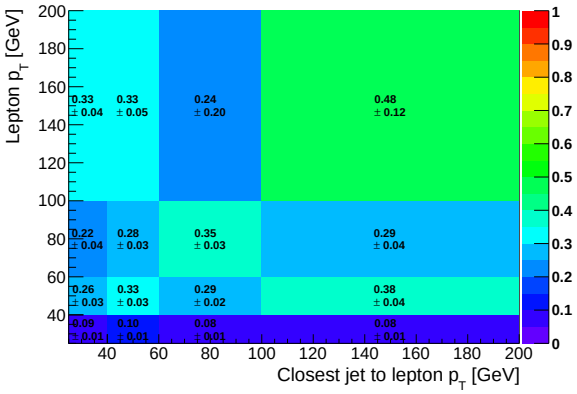

(e) False-identification rate f, e+jets channel, $\Delta R(e, \text{closest jet}) < 0.4$

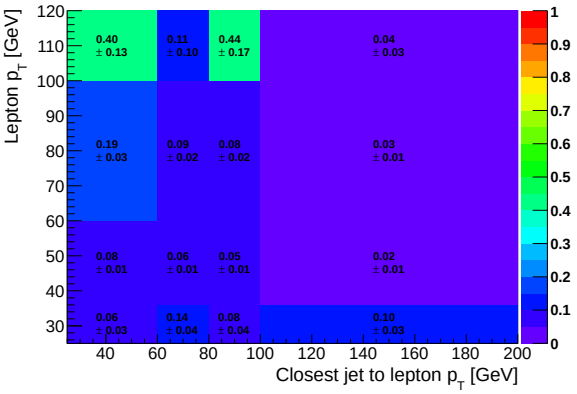

(f) False-identification rate f, μ+jets channel, $\Delta R(\mu, \text{closest jet}) < 0.4$

Figure 5.10.: Boosted-topology selection: (a,b) Efficiency ϵ for `loose` prompt leptons to be identified as `tight`, given as a function of the transverse momentum of the lepton and the distance $\Delta R(e, \text{closest jet})$ between the lepton and the closest jet; (c-f) false-identification rate f for `loose` leptons from the QCD multi-jet background to be identified as `tight` as a function of the transverse momenta of the lepton and the closest jet for the cases $\Delta R(e, \text{closest jet}) \geq 0.4$ and $\Delta R(e, \text{closest jet}) < 0.4$. Numbers taken from [2].

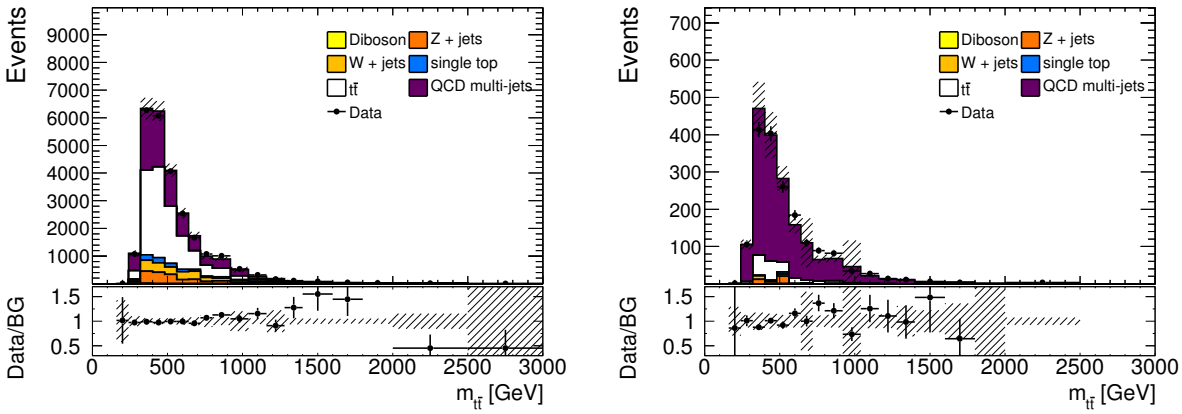

(a) resolved topology, e+jets channel

(b) resolved topology, μ+jets channel

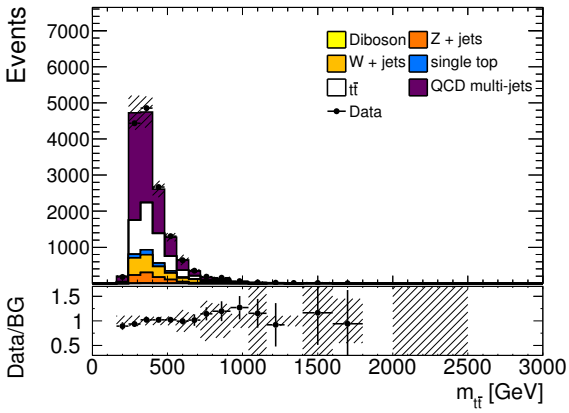

(c) boosted topology, e+jets channel

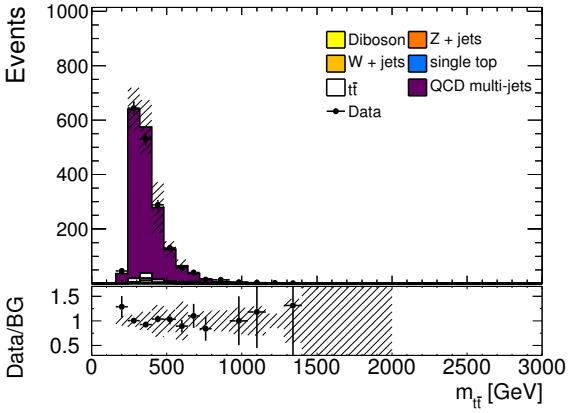

(d) boosted topology, μ+jets channel

Figure 5.11.: Distributions of the invariant mass $m_{t\bar{t}}$ in the QCD multi-jet enriched control regions CR0 for the resolved- and boosted-topology selections in the e+jets and μ+jets channels, respectively. The grey bands represents the total uncertainties on the background estimation as described in Section 5.6. Plots taken from [2].

5.6. Estimation of Systematic Uncertainties

The estimation of systematic uncertainties as well as their treatment in the statistical analysis of the results (see Chapter 7 for details) are core elements of any data analysis: In a search for new physics, the significance of a data deviation from the background expectation is evaluated by taking into account systematic variations in the background estimation which may partially or completely account for the deviation. If no significant deviation is observed and upper exclusion limits on the production cross-section times branching ratio are derived, the systematic uncertainties affect the size of the 1σ and 2σ error bands on the expected limit. These are used to quantify the agreement between observed and expected limits across the invariant mass spectrum. A careful and complete evaluation of the different sources of systematic uncertainties is therefore mandatory.

Systematic uncertainties can be broadly divided into two categories: Uncertainties related to reconstructed objects such as electrons, muons and jets, and uncertainties related to the estimation of the various background processes. In addition, uncertainties on the PDFs and the luminosity measurement are derived.

In a search based on a multi-bin invariant mass spectrum, such as the one presented here, systematic variations can have two effects: They may change the total number of events in the signal region(s) and hence the *normalisation* of the mass spectrum. Or they may alter the *shape* of the mass distribution while leaving the total number of events unaffected, for example by causing events to migrate between mass bins. With the exception of the luminosity uncertainty, which affects only the overall normalisation, all systematic uncertainties presented in the following affect both the shape and the normalisation of the spectrum unless explicitly stated otherwise.

Sections 5.6.1–5.6.4 cover the derivation of the various systematic uncertainties. The impact of the systematic uncertainties on the signal and background yields, the $m_{t\bar{t}}^{\text{reco}}$ spectra as well as the signal strength is discussed in Section 6.2. Systematic uncertainties are treated as uncorrelated in the statistical analysis of the results and care is taken in the definition and estimation of the systematic uncertainties to avoid or reduce correlations.

5.6.1. Uncertainty on the Luminosity Measurement

The integrated luminosity of the ATLAS dataset used in this analysis, i.e. the full dataset collected in 2012 at $\sqrt{s} = 8$ TeV, and its uncertainty have been measured centrally within ATLAS using the techniques described in [255]. The relative uncertainty on the integrated luminosity obtained with this approach is $\pm 2.8\%$ [256]. Since this is a pure normalisation uncertainty, it is applied as a constant shift across the whole $m_{t\bar{t}}^{\text{reco}}$ spectrum for all simulated background and signal samples.

5.6.2. Uncertainties on Reconstructed Objects

The reconstruction, identification and calibration of the various physics objects used in the search are associated with a number of different uncertainties which need to be taken into account in the evaluation of the final analysis result. These uncertainties may affect both the shape and the normalisation of the $m_{t\bar{t}}^{\text{reco}}$ spectrum for all signal and background samples. In particular, energy or transverse momentum variations of objects, such as jets, directly affect $m_{t\bar{t}}^{\text{reco}}$, thus causing events to migrate between $m_{t\bar{t}}^{\text{reco}}$ bins.

Electrons

The main uncertainty related to electrons stems from the uncertainty on the scale factors for the reconstruction, identification, isolation and trigger efficiencies, which have been discussed in detail in Section 4.1.4. The different scale factors are applied as multiplicative corrections to the MC event weight and their uncertainties, which are considered uncorrelated, are added in quadrature to derive the overall uncertainty on the combined electron scale factor. The combined uncertainty is then propagated to the $m_{t\bar{t}}^{\text{reco}}$ spectrum by varying the combined scale factor up and down within its relative uncertainty.

The impact of the uncertainties related to the electron energy scale and resolution corrections described in Section 4.1.2 has been evaluated and found to have a negligible effect on the $m_{t\bar{t}}^{\text{reco}}$ spectrum and the overall yields.

Muons

As in the case of electrons, the uncertainties on the scale factors for the reconstruction, identification, isolation and trigger efficiencies are taken into account. Details of their derivation have been given in Section 4.2.4. The overall uncertainty on the combined muon scale factor is

obtained by adding the uncertainties on the individual scale factors in quadrature. The impact of the uncertainties related to the muon momentum scale and resolution corrections described in Section 4.2.2 have been found to have a negligible effect on the $m_{t\bar{t}}^{\text{reco}}$ spectrum and the overall yields.

b-tagging

The total uncertainties on the scale factors for the b-, c- and light-flavour tagging efficiencies are each related to a large number of different sources that are specific to the method(s) used for the derivation of the respective type of scale factor, as described in Section 4.3.5 and references therein. One possible, accurate way of assessing the effect of each source of scale factor uncertainty on the $m_{t\bar{t}}^{\text{reco}}$ spectrum and the overall yields would be to recalculate a given set of scale factors, binned in p_T^{jet}, $2n$ times, once for each $\pm 1\sigma$ variation of its n sources of uncertainty, and rederive the analysis results in each case. This approach would significantly increase the number of systematic uncertainties of the search and hence the number of nuisance parameters to be considered in the limit setting procedure described in Section 7.2.

The number of uncertainties related to the flavour tagging scale factors can be reduced considerably by reformulating the uncertainties in the context of the so-called **eigenvector (EV) variation method** [257]. For each source of systematic uncertainty, the covariance matrix, an $m \times m$ matrix that describes the correlations between the m bins of the p_T^{jet} distribution,[11] is derived and the sum of all matrices is calculated. Since covariance matrices are symmetric and positive-definite, the eigenvalue problem can be solved and all eigenvalues are non-negative. The corresponding orthogonal eigenvectors can be interpreted as "directions" in which independent variations are to be carried out. The size of each variation is given by the square-root of the corresponding eigenvalue. The number of systematic variations that need to be carried out is thereby reduced to the number of p_T^{jet} bins under consideration.

The eigenvector breakdown has been implemented and tested for all three types of scale factor uncertainties: In the case of b-jets, only four eigenvector variations are found to have a non-trivial effect on the $m_{t\bar{t}}^{\text{reco}}$ spectrum and the overall yields. Hence only these components, labelled `b-tag EV6`, `b-tag EV7`, `b-tag EV8` and `b-tag EV9` in Table 6.2, are kept as input to the limit setting procedure. The scale factor uncertainties related to c- and light-flavour jets are found to have only a small impact on the result. Therefore, no eigenvector breakdown is applied in

[11] In the case of the b-tagging efficiency scale factor, for example, $m = 10$, as can be seen in Figure 4.4b.

those cases. Instead, the scale factors are varied only within their total uncertainty so that only a single uncertainty component is needed in each case. These components are referred to as c-`tag` and `Mistag` in Table 6.2. It should be noted that the uncertainties of the b-, c- and light-flavour tagging scale factors can be considered uncorrelated as the scale factors are derived using completely different calibration approaches (Section 4.3.5).

The data-driven methods for the derivation of the b-, c- and light-flavour tagging efficiencies and scale factors described in Section 4.3.5 suffer from limited statistics for high-p_T jets: The b- and c-tagging scale factors are provided only for $p_T^{\text{jet}} < 300$ GeV, those for the light-flavour mistag rate for $p_T^{\text{jet}} < 750$ GeV. For jets with larger transverse momenta, the respective scale factor for the last calibrated p_T^{jet} bin is used. An additional **extrapolation uncertainty**, derived by the ATLAS Flavour Tagging group in studies carried out on SM $t\bar{t}$ MC samples [258, 259], is applied for these jets. The absolute values for the b-, c- and light-flavour scale factor extrapolation uncertainties are listed in Table 5.2. In the case of the b-tagging efficiency scale factors, this uncertainty is treated as an independent component, referred to as b-`tag high-`p_T in Table 6.2. In the case of the single-component uncertainties on the c-tag and mistag scale factors, the extrapolation uncertainty is added in quadrature to the uncertainty on the scale factor in the last p_T^{jet} bin.

jet-p_T [GeV]	300-500	500-800	800-1200
b-tag scale factor	0.12	0.33	0.27
c-tag scale factor	0.17	0.27	0.30
Mistag scale factor	–	–	0.58

Table 5.2.: Additional scale factor uncertainties for high-p_T jets. The numbers represent the absolute variations to be applied to the respective scale factors. Taken from [258, 2].

Small-R Jets

The variety of different methods involved in the energy calibration of small-R jets (Section 4.3.4) leads to a large number of systematic uncertainties that are associated with the fully calibrated energy scale. Only a reduced number of systematic uncertainties are considered in the derivation of the final search results because the statistical tools can only handle a limited number of nuisance parameters (Section 7.2). In this section, an overview of all systematic uncertainties associated with small-R jets is given along with the considerations involved in the choice of a reduced set of uncertainties.

The three methods used for the **in-situ corrections to the JES**, namely the Z+jet, γ+jet and multi-jet balance calibrations, are each associated with a number of different uncertainties. These include systematic uncertainties on the energy calibration of the electrons or muons from the Z-boson decay and the photon energy calibration.[12] Further uncertainties are related to the choice of the MC generator and the various selection criteria, especially the veto on the presence of a second, subleading jet in Z+jet and γ+jet events. In total, 56 independent sources of systematic uncertainty on the in-situ JES calibration are considered. The full list and further details can be found in [227, 222].

To reduce the number of systematic uncertainties that must be considered in the derivation of the final analysis result, a reduction scheme is recommended by the ATLAS JetEtMiss Working Group. It relies on the same eigenvector approach as used in the case of the b-tagging scale factor uncertainties. Each of the 56 uncertainties associated with the in-situ JES calibration is classified as either statistical, detector related, model related or related to both detector and modelling, based on the source of the uncertainty [227, 222].[13] The uncertainties within each of these four categories are combined using the eigenvector technique described in Section 5.6.2. Only the two to four components with the largest eigenvalues are kept within each category. This approach reduces the number of uncertainties associated with the in-situ corrections, which are considered in this search, from 56 to 12. Further details on the reduction scheme applied for the JES uncertainties can be found in [260]. An additional **high-p_T uncertainty** is applied for jets with transverse momenta above 1500 GeV where the statistical power of the in-situ balance methods is limited and additional single-hadron response measurements are used to calibrate the JES [222].

The uncertainties on the **η-intercalibration** (Section 4.3.4), which are parameterised in both the transverse momentum and the pseudorapidity, are derived separately. Two components, one systematic and one statistical, are used. The dominant source of systematic uncertainty in this case is the MC modelling uncertainty for jets in the forward calorimeter region.

Four uncertainty components are considered with regard to the **pile-up correction**. The first two components describe the uncertainty on the dependence of p_T^{jet} on in-time and out-of-time

[12] The electron and photon energy scales can be assumed to be fully correlated, hence a combined set of uncertainties is used for both.

[13] The definition of these categories is motivated by the desire to make jet-related measurements and their uncertainties comparable between experiments: Statistical and detector-related uncertainties, for example, can be considered as uncorrelated between experiments. Modelling uncertainties, on the other hand, such as those related to the choice of MC generators, are likely to be correlated.

pile-up, quantified by the number of primary vertices in an event, N_{PV}, and the average number of interactions per bunch crossing, $< \mu >$. This dependence is important since the pile-up corrections have been derived with regard to reference pile-up conditions given by the mean conditions in the 2012 dataset, $N_{PV}^{\text{ref}} = 11.8$ and $< \mu >^{\text{ref}} = 20.7$, and the values in individual events are typically different. The third uncertainty component describes the uncertainty on the dependence of the residual pile-up corrections on p_T^{jet}. The last component is associated with the uncertainty on the median p_T density in the event, ρ, used in the jet area correction. Both the dependence of ρ on $< \mu >$ and its sample dependence, evaluated by comparing dijet, γ+jet and Z+jet events in data and MC, are taken into account. Details on the calculation of the four pile-up uncertainties are given in Section 6.7 of [219].

Two additional sources of systematic uncertainty are introduced to take into account the differences in the jet energy response between light-quark and gluon-initiated jets: Gluon-initiated showers tend to have higher particle multiplicities than those initiated by light quarks and consequently their constituents tend to be softer. Moreover, gluon-initated showers are wider on average than those stemming from light quarks, an effect that is amplified by the magnetic field of the ID where softer particles are deflected more than harder ones. Hence jets initiated by light quarks tend to be narrower and penetrate further into the calorimeter than those initiated by gluons and the corresponding calorimeter cells are more energetic and therefore more likely to pass the noise-threshold criteria described in Section 4.3.1. The residual JES calibration is derived on event samples with a ratio of light-quark- and gluon-initiated jets that may differ from that in samples selected by other analyses. To account for this effect, a **flavour composition uncertainty**, derived from the response differences between MC samples containing only light-quark and only gluon jets, respectively, is applied to all jets with the exception of b-jets whose uncertainties are discussed below. An additional **flavour response uncertainty** is used to account for differences observed in the gluon-jet response for different MC generators.[14] The derivation of these flavour uncertainties is described in [227] and [222].

The total fractional JES uncertainty is shown in Figure 5.12 as a function of p_T^{jet} and η^{jet}, along with the individual contributions from the combined in-situ, flavour-composition, flavour-reponse and pile-up uncertainties, respectively. In each case, the combined uncertainties are calculated by adding the relevant, independent components in quadrature. All 21 components discussed above are considered. For the jets in the kinematic range relevant to this analysis

[14] The response of light-quark jets, in contrast, is found to be within good agreement between different generators.

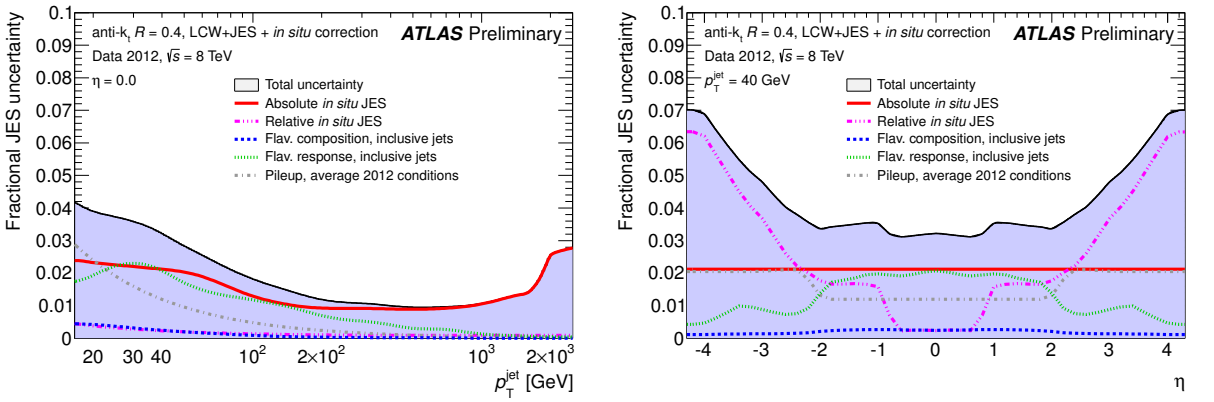

(a) **(b)**

Figure 5.12.: (a) Fractional JES uncertainty as a function of p_T^{jet}, and (b) η^{jet} for anti-k_T $R = 0.4$ jets calibrated with the LCW+JES scheme (including in-situ corrections). The contributions from the individual uncertainty components are also shown. The total uncertainty is obtained by summing the individual components in quadrature. Taken from [228].

($p_T^{\text{jet}} > 25$ GeV, $|\eta^{\text{jet}}| < 2.5$), the total fractional JES uncertainty is always below 4% and below 2% for central jets with $p_T^{\text{jet}} > 100$ GeV.

These numbers serve merely as an illustration of the magnitude of the overall JES uncertainty. The impact of the JES uncertainty on the $m_{t\bar{t}}^{\text{reco}}$ spectrum is evaluated separately for each of its 21 components to avoid overconstraining the JES uncertainty in the profiling procedure discussed in Section 7.2. The impact is evaluated by varying the jet energies and transverse momenta up and down according to the magnitude of the JES uncertainty component under consideration. The energy and transverse momentum variations are performed simultaneously for all (small-R) jets in an event to preserve the information about the correlations between the p_T^{jet} bins for each component.

To further reduce the number of systematic uncertainties that are given as input to the statistics tools only the six out of the 21 components that are found to have a noticeable impact on the results are kept as individual components. The remaining uncertainty components are added in quadrature and treated as a single component, labelled `AKT4 JES (Others)`. An overview of the JES components used in the following is given in Table 5.3.

An additional uncertainty component, `AKT4 JES22 (bJES)`, which is also listed in Table 5.3, must be taken into account for b-jets. It quantifies the uncertainty on the differences in the detector response between b-jets and jets initiated by gluons or lighter quarks. The energy of b-jets with b-hadrons decaying semileptonically into muons is underestimated, firstly because the muon leaves little energy in the calorimeters and secondly because the associated neutrino cannot

Type	Label
In-situ	`AKT4 JES3 (Modelling1)` `AKT4 JES7 (Detector1)`
η-intercalibration	`AKT4 JES12 (EtaInter)`
Pile-up	`AKT4 JES18 (PU Rho)`
Flavour	`AKT4 JES20 (FlavourComp)` `AKT4 JES21 (FlavourResp)`
bJES	`AKT4 JES22 (bJES)`
Other	`AKT4 JES (Others)`

Table 5.3.: Overview of the 7+1 JES and the one bJES uncertainty components considered in the derivation of the final search result.

be detected. These decays occur in roughly 20% of all b-jets [196]. The additional uncertainty related to the JES of b-jets, the so-called **bJES uncertainty**, is derived by measuring the ratio of the response of b-jets and jets initiated by gluons or lighter quarks in dijet and $t\bar{t}$ samples [261]. It is found to be around or below 2% over the whole $p_T^{b-\text{jet}}$ range and is applied to all true b-jets in MC events, not just those that are b-tagged.

The **jet energy resolution uncertainty** is propagated to the final result by artificially smearing the energies of all small-R jets in the event, thus worsening the jet energy resolution. This is achieved by scaling the energy of each jet by a random factor that is taken from a Gaussian distribution with a mean value of 1.0 and a width determined by a smearing factor

$$\text{SmearFac} = \sqrt{(\text{JER}_{\text{MC}} + \Delta\text{JER})^2 - (\text{JER}_{\text{MC}})^2}, \tag{5.14}$$

where JER_{MC} is the jet energy resolution measured in MC events and ΔJER denotes the total uncertainty on the jet energy resolution [262]. Unlike the JES uncertainties, which are taken into account by varying the jet energy up and down, this procedure yields a one-sided uncertainty since the resolution can only be worsened. The statistical tools discussed in Chapter 7, however, require both an "up" and a "down" variation histogram as input. The second histogram is obtained by symmetrising with respect to the nominal $m_{t\bar{t}}^{\text{reco}}$ spectrum: If the value of bin i in the smeared histogram differs by x% from that in the nominal histogram, the corresponding value in the symmetrised histogram is shifted by $-x$%.

The uncertainty related to the choice of the lower boundary on the JVF, which is 0.5 in the nominal selection, has been evaluated by varying this value up and down as prescribed in [263]. The impact on the yields and $m_{t\bar{t}}^{\text{reco}}$ spectrum has been found to be negligible. Hence this

uncertainty is not considered in the derivation of the final results.

Large-R Jets

The measurements of both the energy and mass scales of large-R jets are associated with a number of different uncertainties which must be taken into account in the statistical analysis of the search result. In the case of the **JES uncertainty**, the uncertainties derived with the γ-jet balance and the track-jet double-ratio methods, discussed in Section 4.3.4, are combined. The γ-jet balance method, which yields the more precise determination of the JES, is statistically limited for jets with $p_T^{\text{jet}} > 800$ GeV and invalid for $p_T^{\text{jet}} > 1000$ GeV. This regime is, however, covered by the track-jet double-ratio method. For jets with $p_T^{\text{jet}} \leq 700$ GeV, only the uncertainties from the γ-jet balance method are used. In total, twelve independent uncertainty components, derived in [229], are taken into account. The uncertainty derived with the γ-jet balance method and an additional pile-up uncertainty, derived by the same method, are shown in Figure 5.13a as a function of p_T^{jet}. For jets with $p_T^{\text{jet}} > 700$ GeV, an additional uncertainty is added in quadrature. It is obtained by linear interpolation between the uncertainty derived from the γ-jet balance method at 700 GeV and the uncertainty given by the track-jet double-ratio method at 1100 GeV, as illustrated in Figure 5.13a.

An additional uncertainty arises from differences in the p_T response between large-R jets with different substructure, namely those corresponding to a fully contained hadronically decaying top quark, those associated with a hadronically decaying W-boson and those originating from a single lighter quark or gluon. This **topology uncertainty** is equivalent to the flavour composition uncertainty for small-R jets discussed in Section 5.6.2. It is derived by comparing the p_T response of top-quark and W-jets in a SM $t\bar{t}$ MC sample with jets in the same sample that are not associated with a top quark, and with jets from lighter quarks and gluons in W+jets events in which a leptonically decaying W-boson recoils against a highly-energetic large-R jet. The responses are evaluated as a function of p_T^{reco} in three different pseudorapidity regions. This is illustrated for the central pseudorapidity region ($|\eta| < 0.8$) in Figure 5.13b. The envelope defined by the largest response difference between any two of the four compared samples in each p_T^{reco} bin is then taken as a conservative estimate of the topology uncertainty. For further details see [222].

In total, the impact of 16 independent JES uncertainty components on the analysis results has been studied. Only the topology uncertainty (`AKT10 JES (Topology)`) and a component

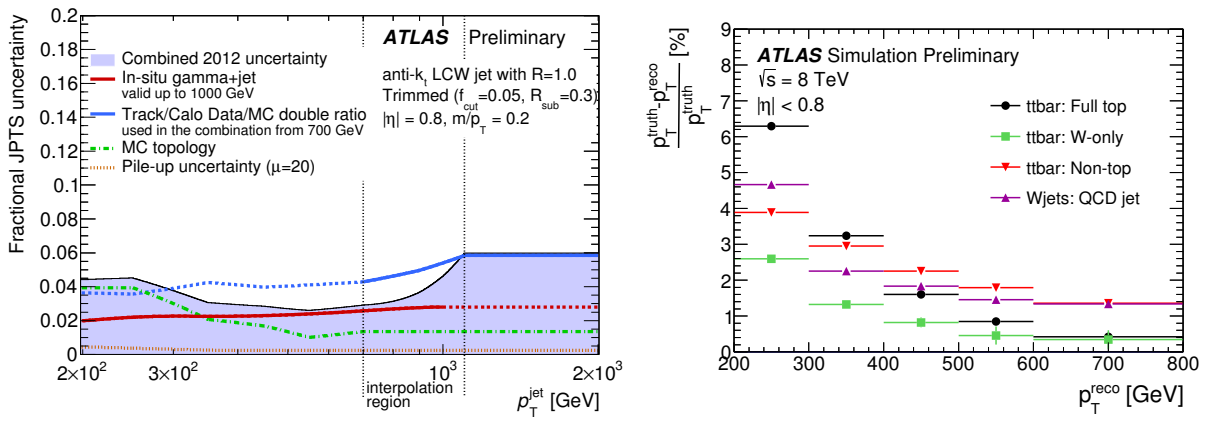

(a) (b)

Figure 5.13.: (a) Fractional jet p_T scale (JPTS) uncertainty for fully calibrated, trimmed anti-k_T $R = 1.0$ jets as a function of p_T. The individual contributions to the combined uncertainty are discussed in the text. (b) Comparison of the p_T response of trimmed anti-k_T $R = 1.0$ jets from different flavour sources (see text) in the central detector region ($|\eta| < 0.8$) as a function of p_T^{reco}. Both taken from [222].

describing the disagreement between data and MC predictions in the γ-jet balance method (`AKT10 JES (Data/MC)`) have been found to have a non-negligible impact on the yields and the $m_{t\bar{t}}^{\text{reco}}$ spectrum. The remaining 14 components are added in quadrature for each jet and treated as a single component (`AKT10 JES (Others)`).

The uncertainties on the JMS and the first k_T splitting scale, $\sqrt{d_{12}}$, are derived using the track-jet double-ratio method, as discussed in Section 4.3.4. Since the two variables are correlated, their values are varied simultaneously within the respective uncertainties to yield a conservative estimate of the combined uncertainty, labelled `AKT10 jet m/d12 scale`.

The impact of the **uncertainties on the jet energy and mass resolution** is evaluated by smearing the reconstructed energy and mass values, respectively, by 20%, as recommended by the ATLAS Jet Substructure Group [264], thus worsening the resolutions. This is achieved using the same approach as in the case of the energy resolution uncertainty for small-R jets discussed in the previous section.

5.6.3. Uncertainties on the Estimation of Background Processes

The background processes relevant to this analysis have been estimated using a number of different approaches ranging from pure MC-based estimations to partly or fully data-driven techniques. Each technique has its own set of systematic uncertainties, for examples those corresponding to the definition of control regions or choices of kinematic cuts on reconstructed

objects. If simulated data is used, uncertainties have to be assigned related to the choice of input parameters to the simulation as well as the choice of the generator itself. These background-specific systematic uncertainties are described in the following sections.

Uncertainties affecting only the SM $t\bar{t}$ Background

The background from SM $t\bar{t}$ production is by far the largest background in all signal regions of this analysis: It makes up between 80 and 90% of the overall background yield in both the boosted- and resolved-topology search channels (Table 6.1). Hence a particularly detailed assessment of its various systematic uncertainties is required.

The uncertainty on the **overall normalisation** of the SM $t\bar{t}$ background is dominated by the uncertainty on the production cross-section, which is calculated at NNLO+NNLL, as discussed in Section 3.4.2. The derivation of the cross-section value and its systematic uncertainties are described in detail in [59]. Three sources of uncertainty on the cross-section are considered: First, the uncertainty due to missing higher-order QCD corrections is determined by varying both the renormalisation scale μ_r and the factorisation scale μ_f independently by factors of 0.5 and 2 from their default values $\mu_r = \mu_f = m_{\text{top}}$. The envelope of the resulting cross-section values is taken as the *scale uncertainty*. Second, an uncertainty due to the choice of the PDF set and the value of the strong coupling constant α_s is derived. These two sources of uncertainty are treated as a single combined *"PDF+α_s" uncertainty* because the conventions concerning the choice of α_s differ between PDF sets. The procedure for deriving this uncertainty is based on the PDF4LHC [265] recommendations, but uses NNLO PDF sets. Third, the dependence of the cross-section on the value of the top-quark mass is evaluated by varying m_{top} by ± 1 GeV from its nominal value of 172.5 GeV to derive the *top mass uncertainty*. The cross-section value and its uncertainties are given in Equation 2.13. Adding the respective uncertainties in quadrature yields a relative cross-section uncertainty of 6.5%, which is applied as a constant shift across the SM $t\bar{t}$ invariant mass spectrum to assess its effect on the overall normalisation of this background.

An additional uncertainty on the **electroweak corrections** to the *differential* SM $t\bar{t}$ cross-section, described in Section 3.4.2, is derived. This uncertainty is evaluated by varying the scale factors by $\pm 10\%$. It affects both the normalisation and the shape of the spectrum.

The uncertainty related to the value of the **top-quark mass** is evaluated by comparing the spectra from POWHEG+PYTHIA samples generated with values of $m_{\text{top}} = 170.0$ GeV and $m_{\text{top}} =$

175.0 GeV, respectively, to the nominal spectrum and scaling the differences by a factor of 0.4 to approximate the current uncertainty on the top-quark mass which is around 1 GeV [52]. The spectra obtained with the alternative m_{top} values are scaled to the nominal cross-section as the top mass uncertainty has already been taken into account in the derivation of the $t\bar{t}$ cross-section uncertainty (see above). Hence this uncertainty affects only the efficiency of the selection.[15]

The choice of the NLO generator for the hard process as well as the choice of the generator for the modelling of the parton shower affects both the shape and the normalisation of the invariant mass spectrum. To account for these differences, two modelling uncertainties are derived by comparing the nominal distributions generated with POWHEG+PYTHIA to those derived with two different combinations of NLO and parton shower generators: A comparison with MC@NLO v4.1 [266, 267, 268]+PYTHIA yields the **generator uncertainty**, and the **parton shower uncertainty** is derived from a comparison to POWHEG+HERWIG.[16] In each case, the absolute difference between the spectra obtained with the nominal and the alternative generator is evaluated bin-wise. It is taken to be the size of both the up and down variations around the nominal spectrum, which yields a conservative estimate of the generator and parton shower uncertainties.

Finally, an **ISR/FSR uncertainty** is derived to account for differences due to the modelling of both initial- and final-state QCD radiation (ISR and FSR). The choice of these modelling parameters affects the number and softness of additional jets in the event which has a direct impact on the selection efficiency and hence the shape and normalisation of the spectrum. The uncertainty is estimated on samples generated with ACERMC [270] v3.8 interfaced with PYTHIA v6.426 by varying a set of internal parameters in PYTHIA to increase or decrease the amount of ISR and FSR, see [271] for details on the parameter settings. In order to obtain the absolute uncertainty with respect to the nominal spectrum, which is generated with POWHEG instead of ACERMC, the ACERMC spectra for the up and down variations of ISR/FSR are compared bin-wise and the 1σ variation with respect to the POWHEG nominal spectrum in a given bin i is calculated as

$$\Delta_i^{ISR/FSR} = \frac{|y_i^{up} - y_i^{dw}|}{2} \cdot \frac{|y_i^{nom}|}{(y_i^{up} + y_i^{dw})/2}, \tag{5.15}$$

where y_i^{up} and y_i^{dw} are the yields obtained from the ACERMC samples with ISR/FSR varied up and down, respectively, and y_i^{nom} denotes the yield for the nominal POWHEG sample.

[15] Note that changes in the selection efficiency may affect both the shape and the normalisation of the spectrum.
[16] Using JIMMY [269] to model the underlying event.

Uncertainties affecting only the W+jets Background

The W+jets background estimation relies on simulated data to model the shape of the $m_{t\bar{t}}^{\text{reco}}$ distributions as well as scale factors derived from real data to determine the overall normalisation and heavy flavour fractions (Section 5.5.1).

The shape of the W+jets background distribution depends on the choice of internal parameters of the ALPGEN MC generator. Two parameters have been found to have a non-negligible impact on the event kinematics [272]:

- **ptjmin**: This parameter is used to set the minimum transverse momentum of the final state partons in the hard process. Its default value is 15 GeV. An alternative value of 10 GeV is used in the uncertainty estimation. The uncertainty related to this parameter change is referred to as W`+jets shape, "ptjmin10"` in the following.
- **iqopt**: This parameter determines the functional form of the factorisation and renormalisation scale. In order to estimate the uncertainty related to this choice, the default function $m_W^2 + \sum p_T^2(jet)$ (`iqopt=1`) is replaced by the function $m_W^2 + p_T^2(W)$ (`iqopt=3`). The corresponding uncertainty is labelled W`+jets shape, "iqopt3"`.

In order to avoid having to regenerate the full set of ALPGEN MC samples for each parameter variation, the change in the event kinematics caused by the change of one of the above parameters is studied on truth MC samples. A reweighting function is derived based on the transverse momentum of the leading jet in the event which has been found to be a good estimator of the event kinematics [272]. The events of the nominal sample are then reweighted according to this function and the resulting invariant mass spectra are normalised to the nominal yield. This is done to avoid any change in the overall normalisation which is assessed in a data-driven way. The **iqopt3** and **ptjmin10** uncertainties are therefore pure shape-changing systematics.

The procedure used to estimate the uncertainties on the data-driven scale factors for the overall normalisation and the heavy flavour fractions has changed considerably since the last iteration of this analysis: Previously, a number of additional uncertainties related to the derivation of those scale factors were introduced and great care had to be taken to avoid any correlations between them, see [174] for details. In the new approach, no explicit systematic uncertainties on the W+jets scale factors are introduced. Instead, the scale factors are rederived for each variation of all the major systematics, such as the JES and b-tagging components, the `iqopt3` and `ptjmin10` shape uncertainties and the PDF uncertainty. These new scale factors are applied

when deriving the spectra for the different systematic variations. This more complex procedure is considered the most accurate way of dealing with scale-factor variations and has the advantage of avoiding the introduction of additional systematic uncertainties and possible correlations with other systematic uncertainties. Moreover, it has the side-effect of slightly reducing the impact of various systematic uncertainties on the $m_{t\bar{t}}^{\text{reco}}$ spectrum [2].

Uncertainties affecting other Electroweak Backgrounds

The combined contribution from the single-top, $t\bar{t}$+V, Z+jets and diboson background processes to the overall background yield is found to be only around 5% in both the boosted- and resolved-topology search channels (Table 6.1). Therefore, only the normalisation uncertainty related to the cross-section uncertainties of the various processes is evaluated by a flat scaling of the respective spectra by 7.7% for the single-top [177, 178, 179], 30% for the $t\bar{t}+V$ [273], 48% for the Z+jets [274] and 34% for the diboson background [275], the latter including uncertainties on the inclusive production cross-section as well as uncertainties related to additional hard jets not stemming from final state partons in the matrix element.

Uncertainties affecting only the Multi-jet Background

The multi-jet background is estimated using the purely data-driven techniques described in Section 5.5.2. As shown in Table 6.1, its contribution to the overall background yield is 5% for the resolved-topology selection in the e+jets channel and around or below 1% for the other channels. This implies that statistical errors take precedence over the systematic uncertainty on the *shape* of the spectrum. Hence only an uncertainty on the overall normalisation is derived. Three types of uncertainties are taken into account: First, alternative definitions of the multi-jet enriched control region CR0, defined in Section 5.5.2, are investigated by removing or changing individual cuts while keeping all other cuts the same. The following changes are made in turn:

1. The selection requirement on $E_T^{\text{miss}} + M_T^W$ is dropped.
2. The selection requirement on E_T^{miss} is dropped.
3. The selection requirement on the significance of the impact parameter d_0 is dropped in the μ+jets channel.
4. The requirement $\log_{10}\chi^2 < 0.9$ is added in the resolved-topology definition for CR0.
5. The jet mass requirement in the boosted-topology selection is changed so that all jets with $m^{jet} \in [50, 100]$ GeV are accepted as opposed to requiring $m^{jet} < 70$ GeV in CR0.

Second, the impact of various systematic uncertainties, which have been found to have a non-negligible impact on the multi-jet background estimation, is investigated. This includes uncertainties on reconstructed objects, such as those related to the JES of small- and large-R jets and the b-tagging efficiency, as well as the $t\bar{t}$ generator and showering uncertainties. Finally, the values derived for the fake rate f and the efficiency ϵ are varied within their respective statistical uncertainties to determine their effect on the overall yields. Table 5.6.3 summarises the impact of the various sources of systematic uncertainties on the overall yield of the multi-jet background. The total impact in the boosted and resolved channels is found to be around 20%.

	Boosted selection yield impact [%]		Resolved selection yield impact [%]	
Systematic Uncertainties	e+jets	μ+jets	e+jets	μ+jets
Alternative MET+MTW	4.03	1.17	3.52	3.05
Alternative MET	9.56	1.61	11.45	4.88
Alternative $S(d_0)$	-	11.40	-	10.69
Alternative jet mass	10.65	14.54	-	-
Alternative χ^2 cut	-	-	10.98	18.52
$t\bar{t}$ Generator dependence	2.66	0.31	6.89	0.57
$t\bar{t}$ Parton shower	5.12	0.24	6.96	0.16
Large-R JES	6.14	0.26	-	-
Small-R JES	6.14	0.54	2.06	0.11
b-tag efficiency	8.39	0.07	4.25	0.18
Stat. uncertainty on ϵ	2.17	0.19	0.13	0.0061
Stat. uncertainty on f	2.94	3.08	4.45	4.58
Total Uncertainty	19.4	18.9	20.1	22.6

Table 5.4.: Impact of the various sources of systematic uncertainty on the yields for the multi-jet background in the CR0 Control Regions for the boosted- and resolved-topology selections. Numbers taken from [2].

5.6.4. PDF Uncertainties

As discussed in Section 2.2.1, PDF sets are derived by a number of groups using approaches that differ in various aspects, such as observables used in the fit to data or the choice of input datasets. Following the recommendations of the PDF4LHC working group [265], three different PDF sets are used in the uncertainty estimation:[17] CT10NLO [168], MSTW2008NLO [67], NNPDF2.3 [276]. Each PDF set has a number of associated uncertainties, which can be broadly subdivided into statistical, experimental, theory and modelling uncertainties, the latter including

[17] These PDF sets have been chosen specifically because each is derived using the widest possible range of available input datasets, namely data from fixed target experiments, the latest combined DIS data from the HERA collider and hadron-collision data from the Tevatron. Moreover, each PDF set is available for a variety of different values of α_s.

uncertainties related to assumptions made in the derivation of the PDFs, such as the parametric form of the input distributions to the fit or the treatment of heavy flavour components.

A PDF set consists of a nominal or central PDF and a set of error or ensemble PDFs corresponding to variations of different PDF parameters. The number N of PDFs differs between PDF sets: $N = 53$ for CT10NLO, $N = 41$ for MSTW2008NLO (version MSTW2008nlo68cl) and $N = 101$ for NNPDF2.3 (version NNPDF23_nlo_as_0118). All members of a PDF set can be accessed via the LHAPDF6 [277] library. Unlike the FORTRAN-based LHAPDF5 interface used in previous iterations of this analysis, this new C++ implementation greatly reduces the memory overhead from the order of gigabytes to the order of megabytes, thus allowing all members of all three PDF sets to be loaded simultaneously into the analysis code. This considerably facilitates the implementation of PDF-related uncertainties and reduces the CPU time required for their calculation.

In order to evaluate the impact of the total PDF-related uncertainty on the final invariant mass distribution, two types of PDF uncertainties, *inter*- and *intra*-PDF uncertainties, are considered, which are derived following the recommendations in [265] and [278].

Intra-PDF uncertainties are calculated separately for each of the three PDF sets by repeating the analysis N times and reweighting each event by a PDF weight defined as [278]:

$$w = \frac{\mathrm{PDF}_a(id1, x1, Q1) \cdot \mathrm{PDF}_a(id2, x2, Q2)}{\mathrm{PDF}_0(id1, x1, Q1) \cdot \mathrm{PDF}_0(id2, x2, Q2)}, \tag{5.16}$$

where $x1$ and $Q1$ ($x2$ and $Q2$) are the momentum fraction and energy scale for the first (second) initial-state parton of type $id1$ ($id2$). PDF_0 denotes the nominal PDF and PDF_a, with $a \in N$, is the error PDF corresponding to a particular parameter variation.

If necessary, each of the N invariant mass distributions obtained from this procedure is rescaled by the inverse of the respective sum of PDF weights, calculated from the weights w of all events *before* applying the selection criteria. This step is applied if the total cross-section of a particular process is to be preserved under the PDF variations, as required in certain cases that are discussed below.

The intra-PDF uncertainty for a given set is then calculated bin-wise as the 1σ standard deviation of all variations around the nominal or central value.[18]

[18] The calculation of the intra-PDF error bands differs slightly for the three PDF sets as the groups use different approaches for the treatment of systematic uncertainties [278, 66, 265].

The **inter-PDF uncertainty** quantifies the difference between PDF sets derived by different collaborations and is calculated as the largest pairwise difference between the three central values. Intra- and inter-PDF uncertainties are then combined into a **total PDF uncertainty** on the invariant mass distribution following the prescription of the PDF4LHC working group: In each bin, the envelope of the three intra-PDF uncertainty bands is determined as follows:

- *upper*(envelope) = max{ *upper*(CT10), *upper*(MSTW2008NLO), *upper*(NNPDF2.3)}
- *lower*(envelope) = min{ *lower*(CT10), *lower*(MSTW2008NLO), *lower*(NNPDF2.3)},

where *upper*(...) and *lower*(...) are the upper and lower edges of the respective error bands. The total PDF uncertainty is then taken as half of the envelope width, as illustrated in Figure 5.14.

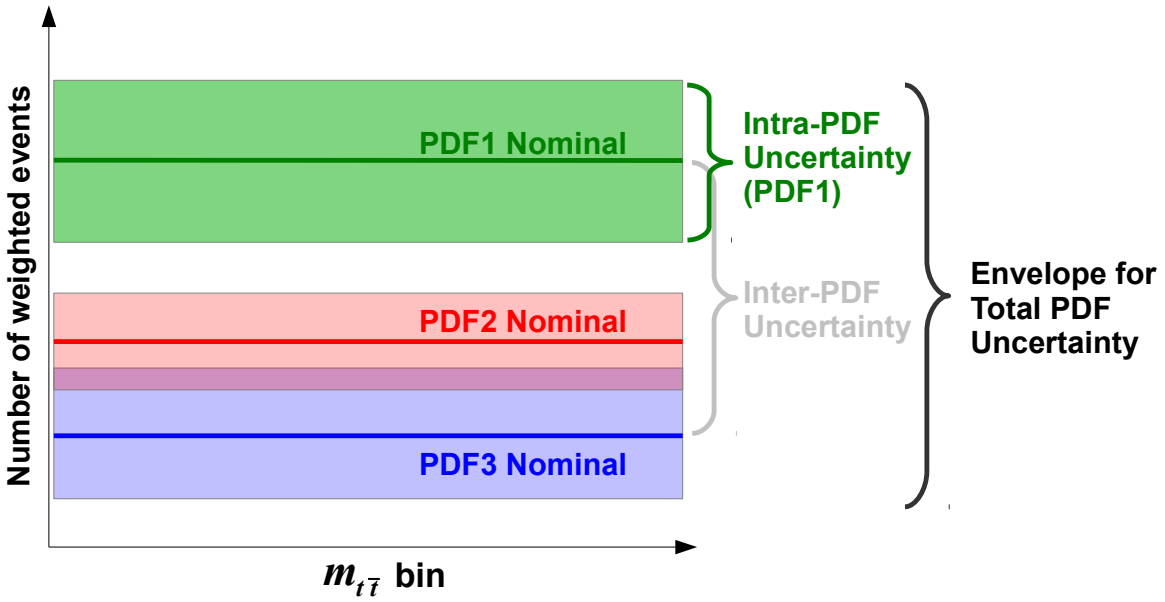

Figure 5.14.: Schematic illustration of the intra- and inter-PDF uncertainties as well as their envelope in a single $m_{t\bar{t}}^{\text{reco}}$ bin. The total PDF uncertainty on the invariant mass spectrum is defined as half the envelope of the three intra-PDF uncertainties. The derivation of the uncertainties is based on the procedure proposed in [265]. A similar illustration can be found in [279].

The PDF uncertainty is evaluated for the SM $t\bar{t}$ and the W+jets background as well as for all signal MC samples. However, only certain aspects of the changes in the invariant mass spectrum are taken into account in each case:

- W+jets: Only the effect on the *shape* of the $m_{t\bar{t}}^{\text{reco}}$ spectrum is taken into account by normalising the mass distributions corresponding to the PDF variations to the yield of the nominal W+jets spectrum (with scale factors applied). The reason for this is that the overall normalisation is determined by data-driven scale factors that are rederived separately for the PDF variations, as described above in Section 5.6.3.

- SM $t\bar{t}$: The uncertainty on the SM $t\bar{t}$ cross-section already includes a contribution from the PDF uncertainty. Therefore only the impact on the *selection efficiency* is considered. The procedure used to remove the effect of the PDF uncertainty on the cross-section when calculating the intra-PDF uncertainty is outlined above.
- BSM signal: Like in the case of the background from SM $t\bar{t}$ production, the effect of the PDF uncertainty on the cross-section is removed because the cross-section is the parameter on which upper limits are derived. Hence only the impact of the PDF uncertainty on the signal efficiency is of interest.

5.7. Smoothing Procedure for Systematic Variations Spectra

The $m_{t\bar{t}}^{\text{reco}}$ spectra corresponding to the $\pm 1\sigma$ variations related to some of the systematic uncertainties discussed above exhibit sizeable fluctuations in certain mass regions where the statistical uncertainty[19] on the background estimate is large. These fluctuations lead to an overestimation of the impact of the affected systematic uncertainties or, in other words, a double-counting of the statistical uncertainty on the background estimate. This effect is particularly severe given the large number of systematic uncertainties considered in this analysis. Moreover, these fluctuations tend to cause the nuisance parameters in the profile likelihood fit that is used to derive the upper cross-section limits (Section 7.2) to be overconstrained and can even prevent the fitting procedure from converging.

A **smoothing** procedure has therefore been developed to mitigate the impact of statistical fluctuations on the $m_{t\bar{t}}^{\text{reco}}$ spectra for the systematic variations. The procedure is designed to yield a more reliable estimate of the systematic variations in regions affected by statistical fluctuations by merging bins for which the MC statistical uncertainty is comparable or larger than the systematic variation. It is applied for all systematic variations except the ones involving scale factor variations which have been found to be less affected by statistical fluctuations. The smoothened spectra are used in all plots in the following sections and in all parts of the statistical analysis discussed in Chapter 7. The following algorithm, described in [2], is used to obtain the smoothened $m_{t\bar{t}}^{\text{reco}}$ spectra for the systematic variations:

[19] This uncertainty is conventionally referred to as "MC statistical uncertainty", despite the fact that some of the background components are estimated from data. It is defined as the Poissonian error $\sqrt{\sum_{i=1}^{N} w_i^2}$ for a bin containing N "raw" background events with weights $\{w_i\}$. Unlike the statistical uncertainty on the expected background yields in the same bin, which is evaluated for a given luminosity, the MC statistical uncertainty is a measure of the statistical power of the event samples that are used to estimate the background yields.

1. Starting from an input $m_{t\bar{t}}^{\text{reco}}$ histogram, $h^{(\text{NP,var})}$, that corresponds to either the up (var = up) or the down (var = dw) variation of a given systematic uncertainty NP, loop over its N bins and identify the one with the largest (relative) MC statistical uncertainty.
2. Test if the (relative) systematic variation in this bin is greater than twice the MC statistical uncertainty in the same bin. If this is the case, the systematic uncertainty is considered (statistically) significant, the current bin is skipped, and the bin with the next largest MC statistical uncertainty is considered. If the systematic uncertainty in the given bin is not significant by the above criterion, the bin is considered for merging with the adjacent bin(s).
3. Merging of a selected bin with an adjacent bin is considered appropriate if either of the following conditions is met:

   a) The systematic variation in the adjacent bin is not significant.
   b) The systematic variation in the new bin that would result from the merging of the two bins is smaller than twice the MC statistical uncertainty in the current bin.

   If both adjacent bins fail both criteria, the current bin is skipped, and the bin with the next largest MC statistical uncertainty is considered. If the current bin has two adjacent bins that are considered appropriate for merging, the one with the larger MC statistical uncertainty is chosen.
4. Following the merging of two bins, the procedure is iterated starting from Step 1 using the new histogram with $N - 1$ bins.
5. The algorithm terminates if, at a given stage, no bin with insignificant systematic variation remains or if all bins have bin merged into a single one.

The result of the smoothing procedure is illustrated in Figure 5.15 for two different systematic variations: The variation histograms for the `AKT4 JES21 (FlavourResp)` uncertainty in the μ+jets channel of the resolved-topology selection (Figure 5.15a) before smoothing exhibit considerable fluctuations for $m_{t\bar{t}} > 700$ GeV due to the limited statistics that is available in the high-mass region for this channel. In the corresponding histogram obtained with the smoothing procedure described above, the bins in this region have been merged into a single one. The extreme case in which the smoothing procedure results in a single bin for the $\pm 1\sigma$ variation histograms is illustrated in Figure 5.15b. Here, the systematic variations after smoothing affect only the normalisation of the spectrum, but no longer its shape.

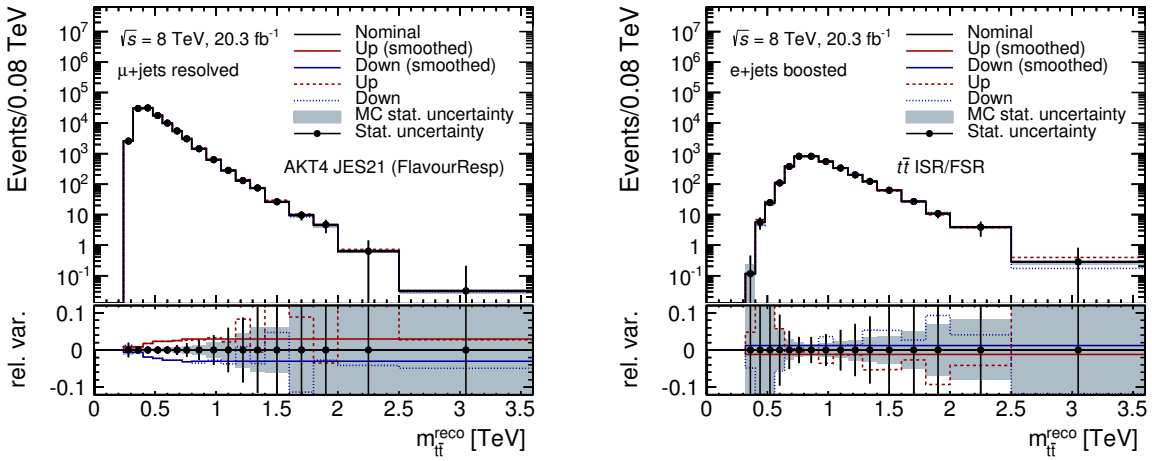

(a) `AKT4 JES21 (FlavourResp)`, μ+jets channel, resolved topology

(b) `ISR/FSR`, e+jets channel, boosted topology

Figure 5.15.: Effect of selected systematic variations on the $m_{t\bar{t}}^{\text{reco}}$ spectrum: (a) `AKT4 JES21 (FlavourResp)` uncertainty in the μ+jets channel of the resolved-topology selection and (b) $t\bar{t}$ `ISR/FSR` uncertainty in the e+jets channel of the boosted resolved-topology selection. The absolute (upper pad) and relative (lower pad) up and down variations are shown both before and after the smoothing procedure is applied. Similar plots, produced by the author, are included in [2].

5.8. Summary

The search for resonant production of $t\bar{t}$ pairs via BSM processes is carried out on the distributions of the invariant mass of the reconstructed $t\bar{t}$ pair, $m_{t\bar{t}}^{\text{reco}}$, in twelve mutually exclusive signal regions. The sensitivity of the search across the whole $m_{t\bar{t}}^{\text{reco}}$ spectrum between 0.4 and 3.0 TeV is optimised by combining two different selection and reconstruction strategies, tailored towards the boosted and resolved $t\bar{t}$ decay topologies, respectively. The expected contributions of SM processes in the signal regions are estimated using both MC-based and data-driven methods. The impact of systematic uncertainties, related to the luminosity measurement, the PDFs, the reconstructed objects and the estimated background components, is studied. The impact on both the normalisation and shape of the $m_{t\bar{t}}^{\text{reco}}$ spectrum is taken into account.

6. Results

The event selection and reconstruction criteria introduced in Sections 5.3 and 5.4 are applied to the full dataset collected by the ATLAS experiment in pp collisions at $\sqrt{s} = 8$ TeV. In this section, the event yields and kinematic distributions in the signal regions observed in data are compared to those of the expected SM background, which is estimated as described in Section 5.5. Moreover, the impact of the systematic uncertainties described in Section 5.6 is studied.

6.1. Comparison of Observed Data with Expected SM Background

The objective of the analysis presented in this thesis is to search for deviations of the observed data from the background that is expected based on SM predictions in the twelve mutually exclusive signal regions defined in Section 5.4.5. As explained at the beginning of Chapter 5, a simple comparison of the observed and expected event yields in the signal regions does not provide sufficient sensitivity to BSM processes for which the production cross section times branching ratio, $\sigma_X \times BR(X \to t\bar{t})$, is small, which is why the search exploits the shape information provided by the $t\bar{t}$ invariant mass distributions in the signal regions. For completeness, in this section the overall event yields are given along with the $m_{t\bar{t}}^{\text{reco}}$ spectra for the individual channels. The statistical analysis, described in detail in Chapter 7, focuses exclusively on these $m_{t\bar{t}}^{\text{reco}}$ spectra.

In addition, a comparison of observed data and expected background contributions for other relevant kinematic distributions is presented. This serves as a vital test of the reliability of the background estimate. Ideally, these cross-checks would be carried out in so-called *control regions* that are defined such that the composition of background processes would be similar to the signal regions while the contribution from potential signal processes would be negligible. In the search presented in this thesis, however, the SM $t\bar{t}$ background constitutes an irreducible background, hence a region depleted in potential signal events would necessarily also be depleted in this background. Therefore, dedicated control regions are used only in the validation of the data-driven background estimates (Section 5.5.2). Instead, the total background estimate is

validated in the signal region using kinematic distributions that are *not* used in the search for BSM resonances. These cross-checks are carried out before the observed event yields and $m_{t\bar{t}}^{\text{reco}}$ spectra are analysed.

6.1.1. Event Yields

The observed and expected event yields after the resolved- and boosted-topology selections are given in Table 6.1, both separately for the e+jets and μ+jets channels and for their combination. The three b-tagging categories are not considered separately here. In total, 223,330 data events pass the selection criteria for the resolved topology, compared to 8,206 data events passing the selection criteria for the boosted topology. These numbers are in good agreement with the expected yields for the SM background: $215,000 \pm 24,000$ for the resolved topology, and $9,200 \pm 1,200$ for the boosted topology, where the total uncertainty on the background estimate is derived by summing all systematic uncertainties and the MC statistical uncertainty in quadrature.[1] In total, 27 times as many events pass the selection criteria for the resolved topology than pass those for the boosted topology, a result of the monotonically decreasing rate for SM $t\bar{t}$ production with increasing $t\bar{t}$ invariant mass.

The expected yields for the individual background components are also listed. The background from SM $t\bar{t}$ production clearly dominates the total SM background, making up more than 85% of the expected yields in each channel. The second largest background contribution in each channel stems from W+jets production, followed by single-top and QCD multi-jet production. The contribution of the latter is larger in the e+jets channels than in μ+jets channels due to the higher rate of "fake" electrons compared to that of "fake" muons, as explained in Section 5.5.2.

6.1.2. Distributions of Selected Kinematic Variables

A comparison between observed data and expected SM background has been carried out for a number of kinematic distributions that are not considered directly in the search for BSM resonances. These cross-checks must include variables on which selection criteria are imposed, such as transverse momenta and pseudorapidities of leptons and jets or the mass and first k_T splitting scale of large-R jets, as well as reconstructed quantities, such as the masses of the hadronically and semileptonically decaying top-quark candidates, t_{had} and t_{lep}, respectively. In this section, only a few representative distributions are shown. In particular, the distributions for $\log_{10}\chi^2$, the new selection variable for the signal regions of the resolved topology (Section 5.3.5),

[1] The complete set of uncertainties considered in the derivation of the final result is listed in Table 6.2.

Resolved-topology selection			
Type	e+jets	μ+jets	Sum
$t\bar{t}$	93,000 ± 11,000	91,000 ± 11,000	184,000 ± 22,000
Single top	3,800 ± 500	3,800 ± 500	7,600 ± 1,000
$t\bar{t}V$	274 ± 40	267 ± 40	541 ± 80
Multi-jet e	5,300 ± 1,100	–	5,300 ± 1,100
Multi-jet μ	–	1,050 ± 240	1,050 ± 240
W+jets	6,600 ± 800	7,100 ± 800	13,700 ± 1,500
Z+jets	1,400 ± 750	650 ± 340	2,000 ± 1,080
Dibosons	320 ± 120	310 ± 120	620 ± 240
Total	110,000 ± 12,000	105,000 ± 12,000	215,000 ± 24,000
Data	114,377	108,953	223,330
Boosted-topology selection			
Type	e+jets	μ+jets	Sum
$t\bar{t}$	4,100 ± 600	4,000 ± 600	8,100 ± 1,200
Single top	138 ± 20	154 ± 20	290 ± 40
$t\bar{t}V$	37 ± 6	38 ± 7	75 ± 13
Multi-jet e	91 ± 18	–	91 ± 18
Multi-jet μ	–	8.6 ± 1.6	8.6 ± 1.6
W+jets	260 ± 50	290 ± 50	550 ± 100
Z+jets	31 ± 16	17 ± 9	48 ± 25
Dibosons	21 ± 8	20 ± 8	41 ± 16
Total	4,700 ± 600	4,500 ± 600	9,200 ± 1,200
Data	4,148	4,058	8,206

Table 6.1.: Observed data and expected background event yields after the resolved- and boosted-topology selections in the e+jets and μ+jets channels. The (total) uncertainty on the expected background yields is derived by summing all systematic uncertainties and the MC statistical uncertainty in quadrature. Published in [1].

are given in Figure 6.1. The full set of distributions is given in [2]. In all cases, good agreement between data and expected SM background is observed within the total uncertainty of the background estimate. This demonstrates that the variables used in the definition of the signal regions are well-modelled and that the reconstruction of the $t\bar{t}$ system yields reliable results.

The distributions of the reconstructed mass of the hadronically and semileptonically decaying top-quark candidates and of the hadronically decaying W-boson candidate for events passing the resolved-topology selection in the e+jets and the μ+jets channels, respectively, are shown in Figure 6.1. In each case, the distribution observed in data agrees well with the set of stacked distributions for the individual background components within the total uncertainty on the background estimate. The background contributions from single-top, $t\bar{t}V$, Z+jets, diboson and QCD multi-jet production, which are found to be small compared to the dominant background

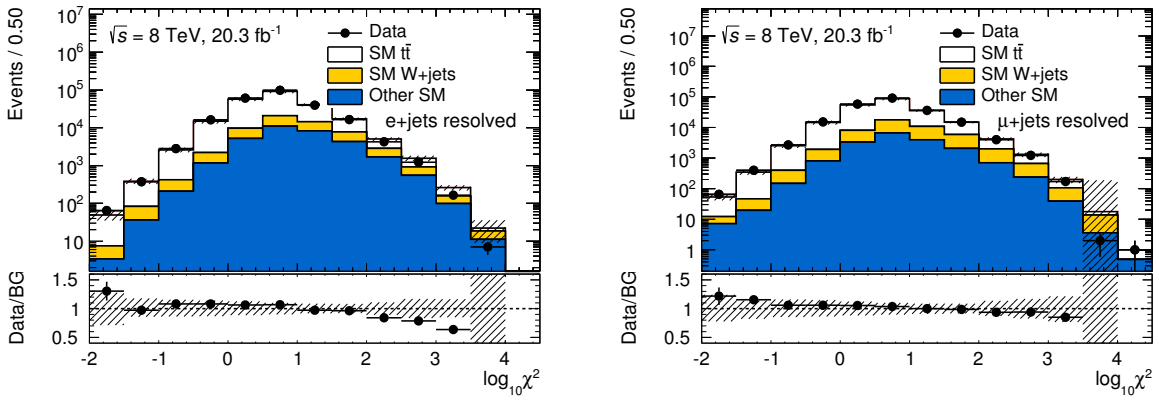

(a) e+jets channel, resolved topology

(b) μ+jets channel, resolved topology

Figure 6.1.: Distributions of kinematic variables for events passing the resolved-topology selection. (a)-(b) Goodness-of-fit variable $\log_{10}\chi^2$ (Section 5.3.5). All selection criteria for the resolved topology are applied with the exception of the requirement $\log_{10}\chi^2 < 0.9$ (Section 5.3.5). Taken from [2].

from SM $t\bar{t}$ production (Table 6.1), are treated as a single component, labelled "Other SM".[2] The total uncertainty on the estimated background is indicated by grey, shaded bands.

The corresponding distributions for the boosted-topology selection are shown in Figure 6.3, where the mass of the hadronically decaying top quark is taken to be the mass of the selected large-R jet. The distributions of the transverse momentum and the first k_T splitting scale of the same jet, which are also used in the definition of the signal regions for the boosted topology, are shown in Figure 6.4. The lower edge of the x-axis range corresponds to the lower thresholds that are imposed on these quantities in the event selection.

6.1.3. Distributions of the Reconstructed $t\bar{t}$ Invariant Mass

The distributions of the reconstructed invariant mass of the $t\bar{t}$ system, $m_{t\bar{t}}^{\text{reco}}$, are given in this section: The $m_{t\bar{t}}^{\text{reco}}$ spectra for the six signal regions that correspond to the three b-tagging categories for the e+jets and μ+jets channels of the resolved-topology selection are shown in Figure 6.5, those for the boosted-topology selection are given in Figure 6.6. In Figure 6.7, the spectra obtained for the combination of the six channels for the resolved and boosted topology, respectively, are shown, along with the spectra resulting from a combination of all twelve channels. The spectra in Figures 6.5 and 6.6 serve as input to the statistical analysis (Chapter 7). In addition, a second set of $m_{t\bar{t}}^{\text{reco}}$ spectra is derived based on the results of a profile-likelihood

[2] This treatment of the SM background as only three distinct components, "SM $t\bar{t}$", "SM W+jets" and "Other SM", is used in all parts of the statistical analysis (Chapter 7) in order to reduce the complexity of the input to the statistical analysis tools.

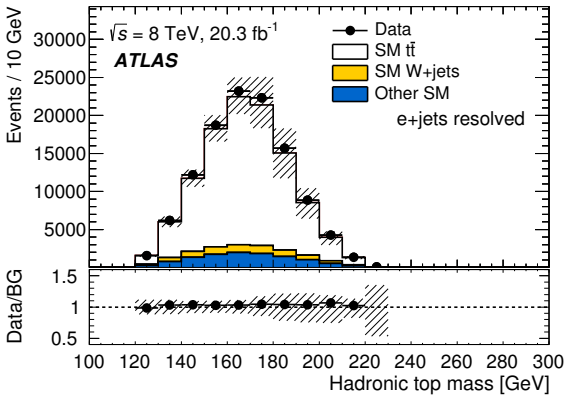

(a) e+jets channel, resolved topology

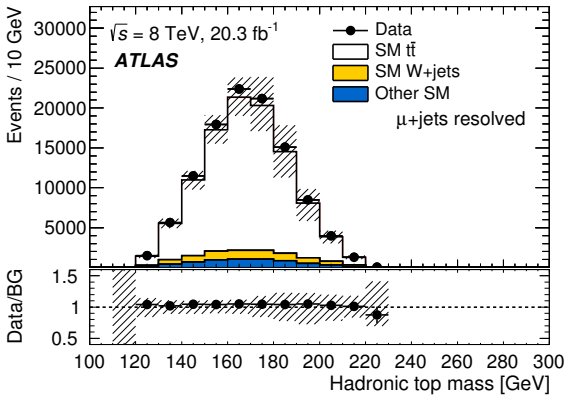

(b) μ+jets channel, resolved topology

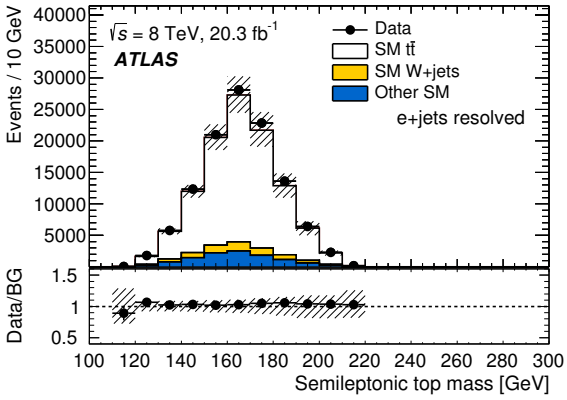

(c) e+jets channel, resolved topology

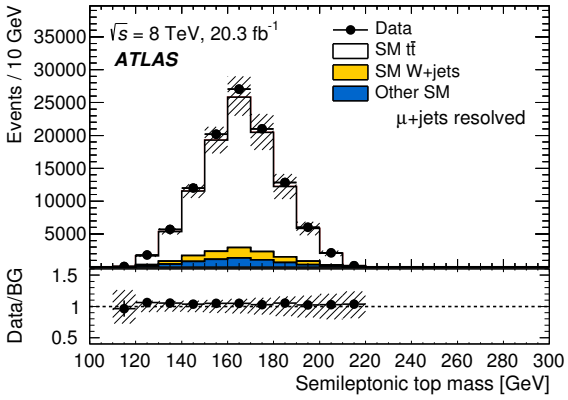

(d) μ+jets channel, resolved topology

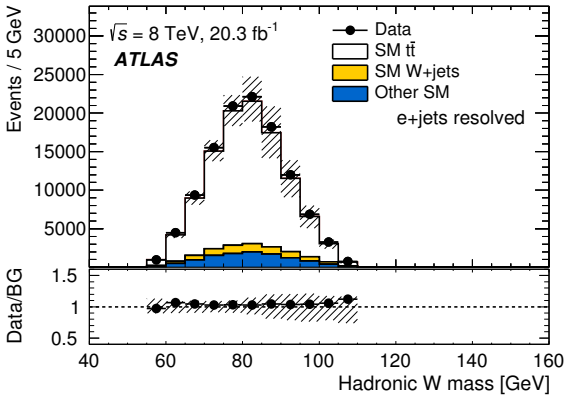

(e) e+jets channel, resolved topology

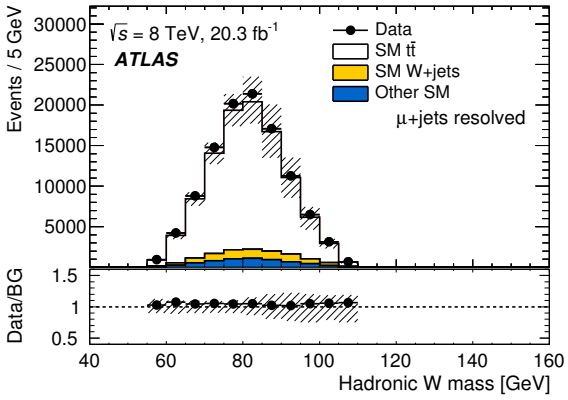

(f) μ+jets channel, resolved topology

Figure 6.2.: Distributions of kinematic variables for events passing the resolved-topology selection. (a)-(b) Reconstructed mass of the hadronically decaying top-quark candidate. (c)-(d) Reconstructed mass of the semileptonically decaying top-quark candidate. (e)-(f) Reconstructed mass of the hadronically decaying W-boson candidate. Published in [1].

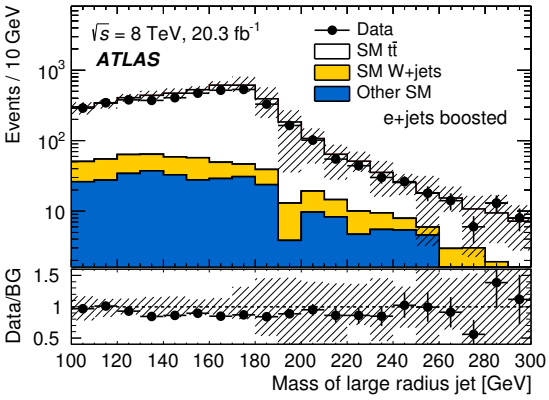

(a) e+jets channel, boosted topology

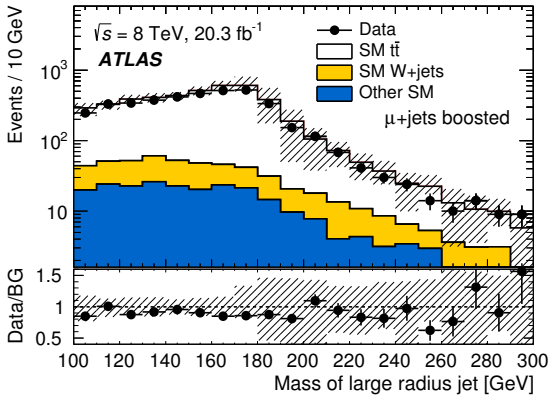

(b) μ+jets channel, boosted topology

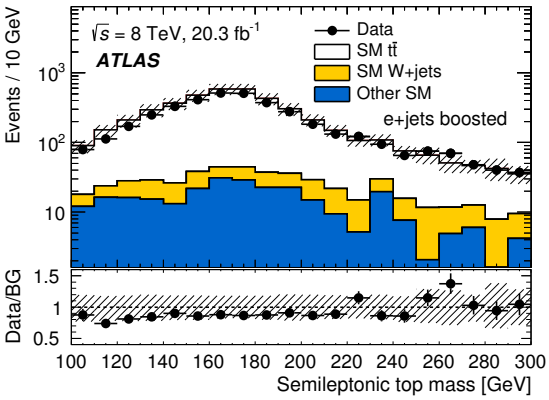

(c) e+jets channel, boosted topology

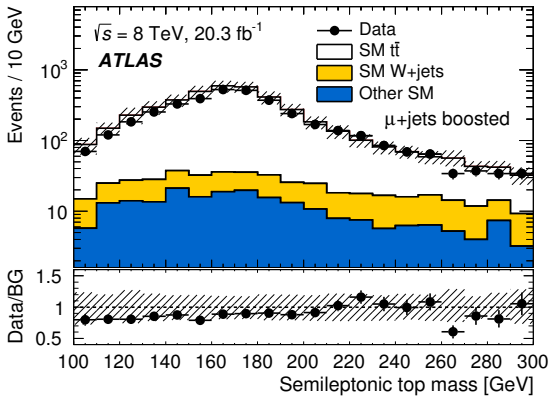

(d) μ+jets channel, boosted topology

Figure 6.3.: Distributions of kinematic variables for events passing the boosted-topology selection. (a)-(b) Reconstructed mass of the large-R jet selected as the hadronically decaying top-quark candidate. (c)-(d) Reconstructed mass of the semileptonically decaying top-quark candidate. Published in [1].

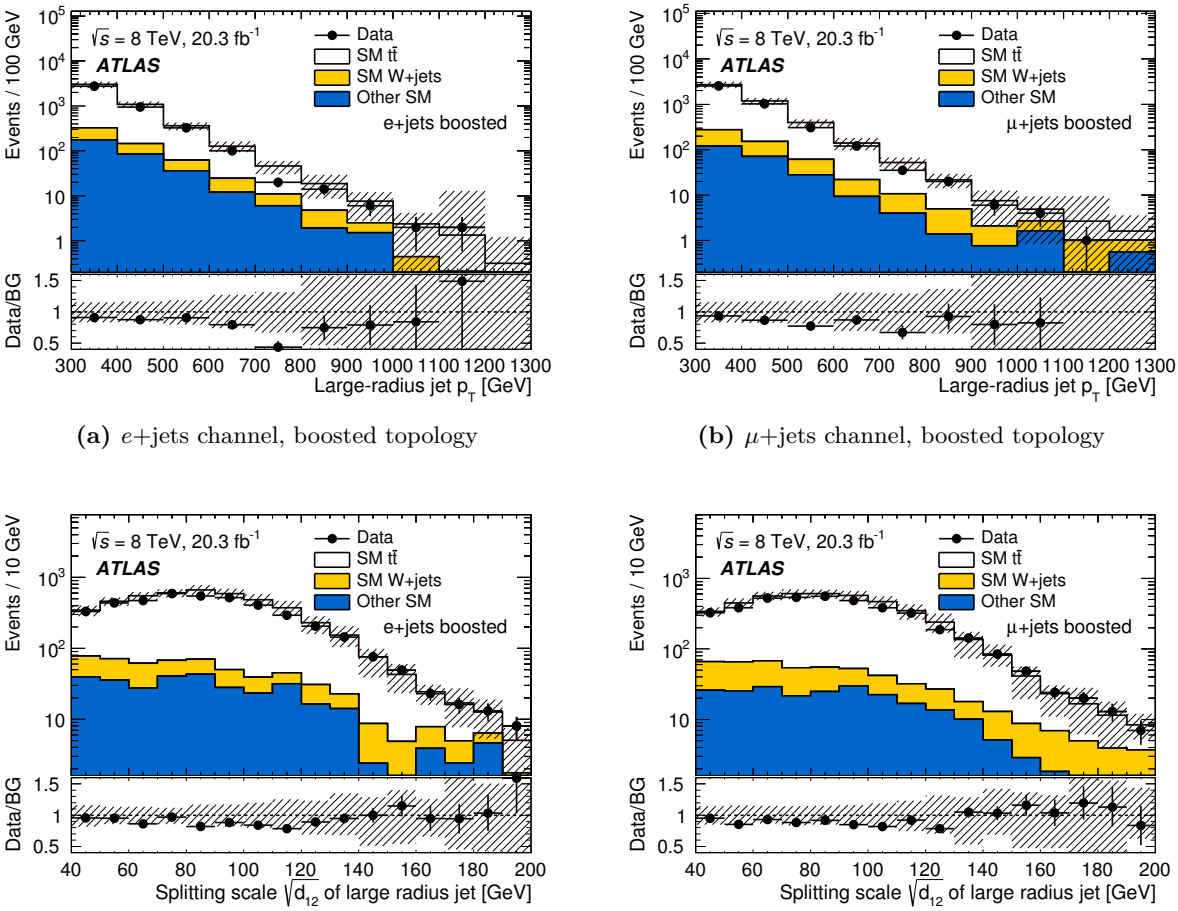

(a) e+jets channel, boosted topology

(b) μ+jets channel, boosted topology

(c) e+jets channel, boosted topology

(d) μ+jets channel, boosted topology

Figure 6.4.: Distributions of kinematic variables for events passing the boosted-topology selection. (a)-(b) Transverse momentum, p_T and (c)-(d) first k_T splitting scale, $\sqrt{d_{12}}$ of the large-R jet selected as the hadronically decaying top-quark candidate. Published in [1].

fit of the expected background to the observed data distributions under the background-only hypothesis. Details are given in Section 7.2.4. The resulting **post-fit spectra** for the combined channels are shown in Figure 6.8 for direct comparison to the corresponding **pre-fit spectra** in Figure 6.7. In all channels, observed data and the expected background distributions are found to be in good agreement with the exception of visible shape differences for $m_{t\bar{t}}^{\text{reco}} \gtrsim 1.5$ TeV: In this region the data yields are systematically lower than the background expectation although the distributions are still consistent within the uncertainties. This effect is discussed further in the context of the derivation of upper cross-section limits in Section 7.2.

6.2. Impact of Systematic Variations

The impact of systematic variations can be quantified in different ways. In Table 6.2, the average **impact on the overall event yields** relative to the nominal yields is given for the expected total SM background and for a hypothetical Z' signal with $m_{Z'} = 1.75$ TeV. The resolved- and boosted-topology selections are considered separately. Only the most relevant systematic uncertainties are listed and only these are taken into account in the statistical analysis of the search results (Chapter 7).

The systematic uncertainty with the largest impact on the expected background yields after the resolved-topology selection is the uncertainty on the normalisation of the SM $t\bar{t}$ background ($t\bar{t}$ `normalisation`), followed by the uncertainty related to the modelling of the PS and fragmentation ($t\bar{t}$ `PS + fragmentation`).

The normalisation uncertainty is also among the uncertainties with the largest impact on the expected background yields after the boosted-topology selection. The dominant systematic uncertainty in this case, however, is the topology uncertainty on the JES of the large-R jets (`AKT10 JES13 (Topology)`). Other uncertainties related to the JES and JMS of the large-R jets also have a considerable impact on the expected background yields. The relative impact of the uncertainties related to the JES of large-R jets on the expected yields for the Z' signal is smaller, a result of the different transverse momentum distributions for top quarks in the SM $t\bar{t}$ background and the signal. The falling $t\bar{t}$ invariant mass and top-quark transverse momentum spectra of the SM $t\bar{t}$ background result in a large fraction of events passing the boosted-topology selection criteria which have top-quark jets produced with transverse momenta close to the kinematic threshold for the boosted-topology selection ($p_T^{\text{jet}} > 300$ GeV). Top quarks from a Z' resonance with $m_{Z'} = 1.75$ TeV, on the other hand, typically have transverse momenta

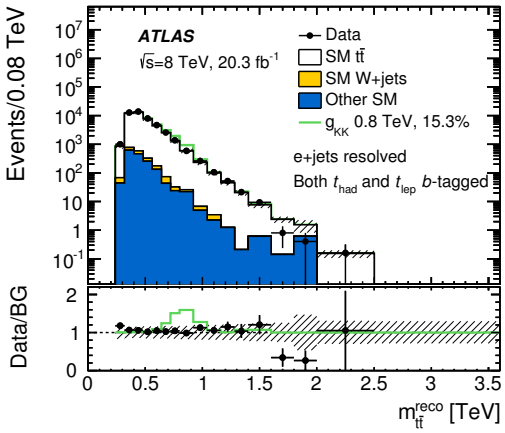

(a) e+jets channel, resolved topology. Both top-quark candidates have b-jets.

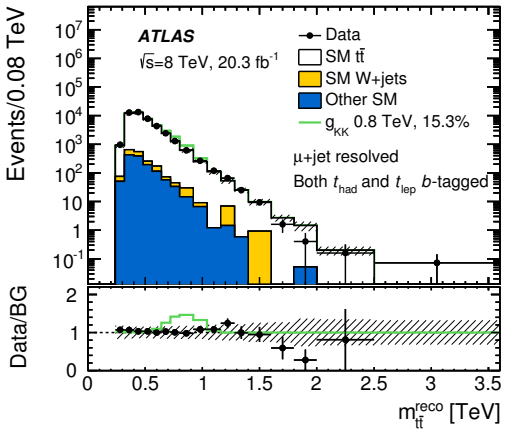

(b) μ+jets channel, resolved topology. Both top-quark candidates have b-jets.

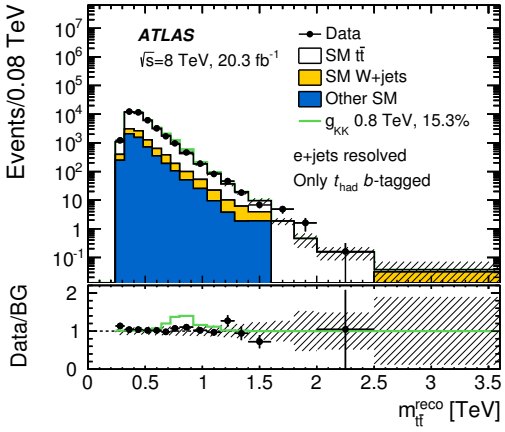

(c) e+jets channel, resolved topology. Only hadronic top-quark candidate has b-jet.

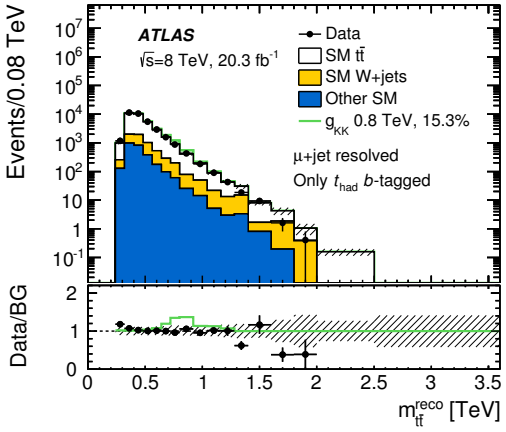

(d) μ+jets channel, resolved topology. Only hadronic top-quark candidate has b-jet.

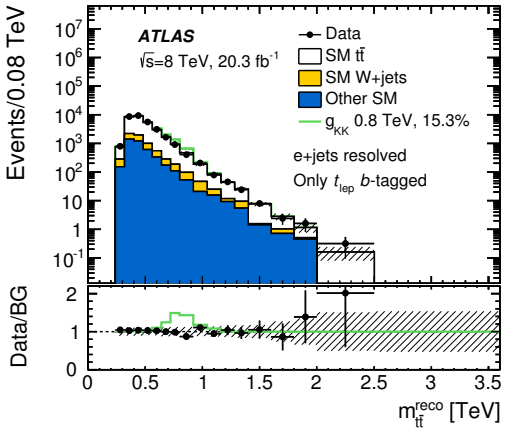

(e) e+jets channel, resolved topology. Only leptonic top-quark candidate has b-jet.

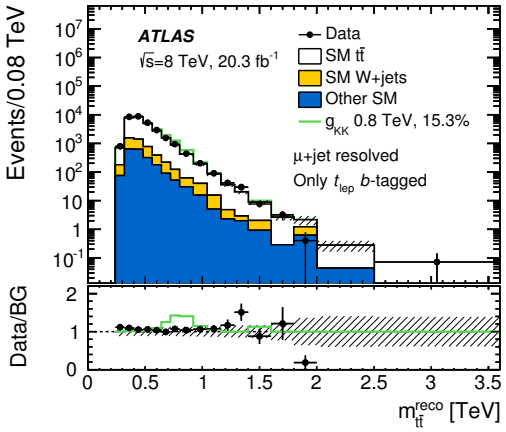

(f) μ+jets channel, resolved topology. Only leptonic top-quark candidate has b-jet.

Figure 6.5.: The $m_{t\bar{t}}^{\text{reco}}$ spectra for the six search channels of the resolved-topology selection *before* the profile-likelihood fit. The distributions observed in data and those estimated for the relevant SM background processes are shown. The grey, shaded bands correspond to the total uncertainty on the background estimate (see text). The green line shows the distribution for a hypothetical KK gluon signal with $m_{g_{KK}} = 0.8$ TeV and $\Gamma_{g_{KK}}/m_{g_{KK}} = 15.3\%$. Published in [1].

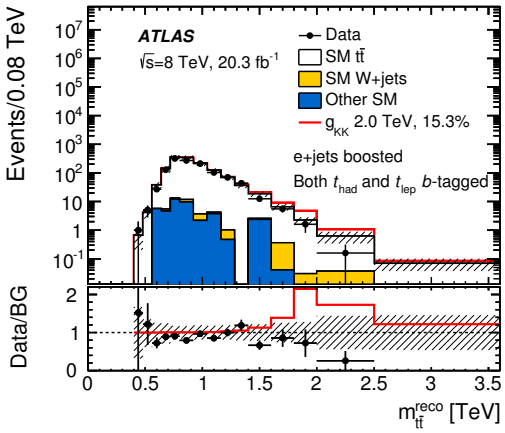

(a) e+jets channel, boosted topology. Both top-quark candidates have b-jets.

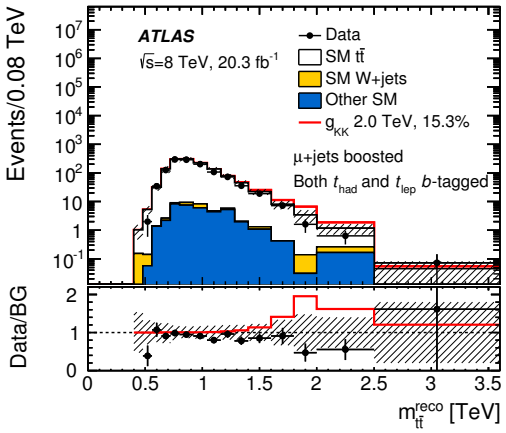

(b) μ+jets channel, boosted topology. Both top-quark candidates have b-jets.

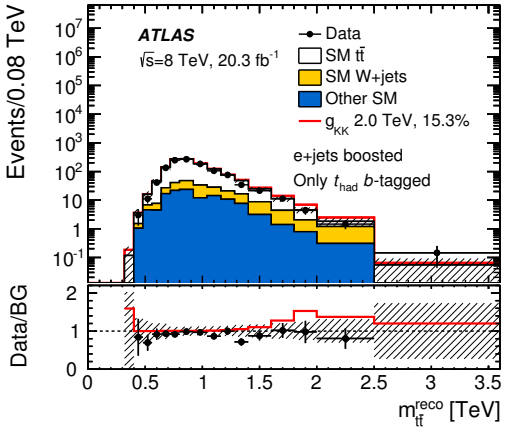

(c) e+jets channel, boosted topology. Only hadronic top-quark candidate has b-jet.

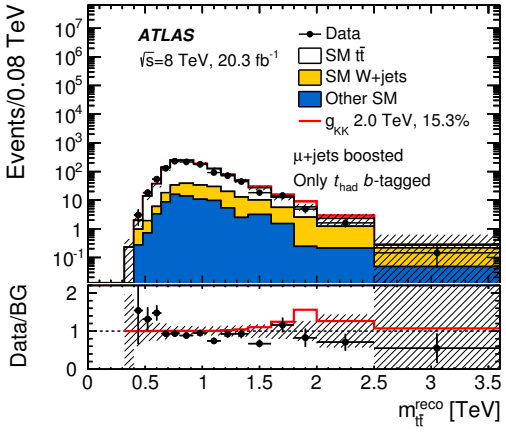

(d) μ+jets channel, boosted topology. Only hadronic top-quark candidate has b-jet.

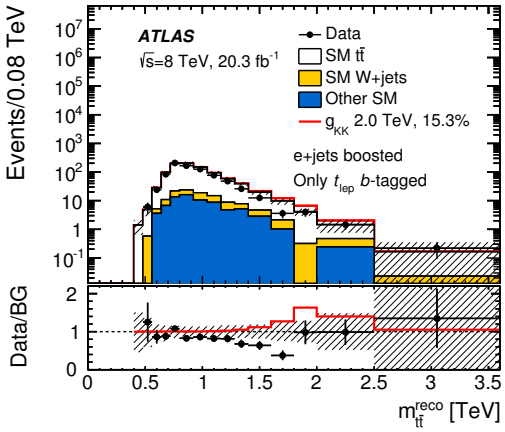

(e) e+jets channel, boosted topology. Only leptonic top-quark candidate has b-jet.

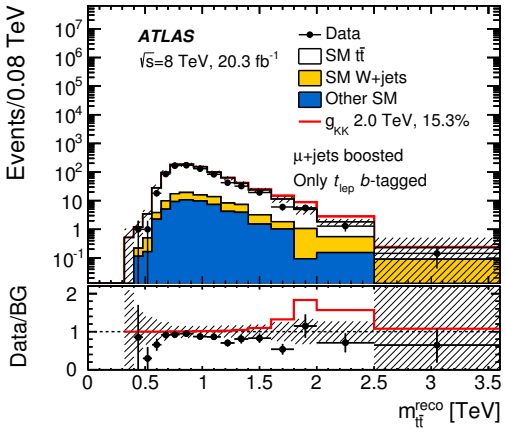

(f) μ+jets channel, boosted topology. Only leptonic top-quark candidate has b-jet.

Figure 6.6.: The $m_{t\bar{t}}^{\text{reco}}$ spectra for the six search channels of the boosted-topology selection *before* the profile-likelihood fit. The distributions observed in data and those estimated for the relevant SM background processes are shown. The grey, shaded bands correspond to the total uncertainty on the background estimate (see text). The red line shows the distribution for a hypothetical KK gluon signal with $m_{g_{KK}} = 2.0$ TeV and $\Gamma_{g_{KK}}/m_{g_{KK}} = 15.3\%$. Published in [1].

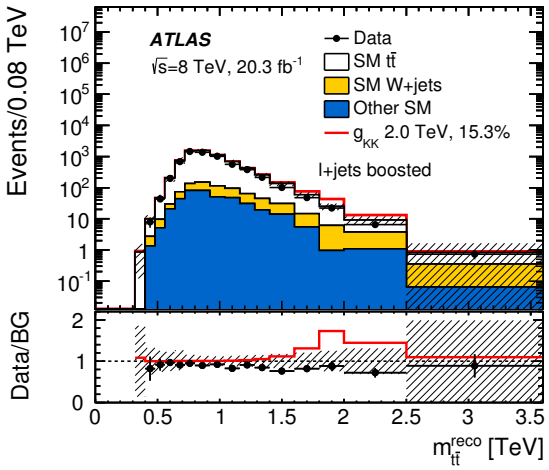

(a) Boosted topology

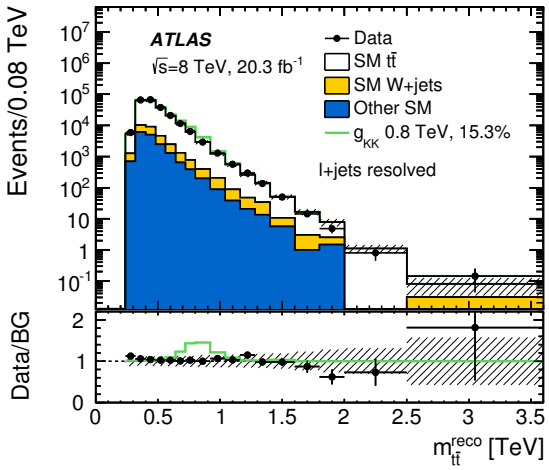

(b) Resolved topology

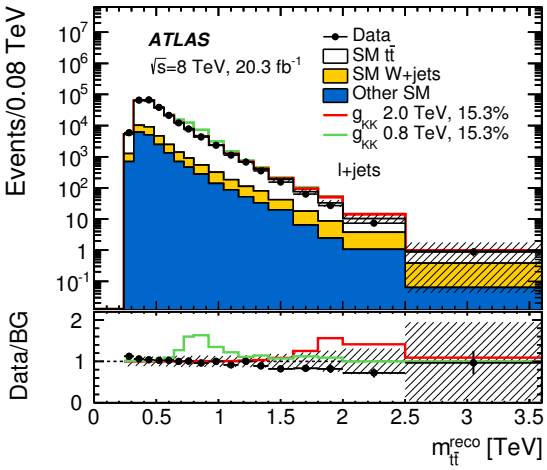

(c) All topology

Figure 6.7.: The $m_{t\bar{t}}^{\text{reco}}$ spectra *before* the profile-likelihood fit summed over (a) the six channels of the boosted-topology selection (b) the six resolved-topology selection (c) all twelve channels. Published in [1].

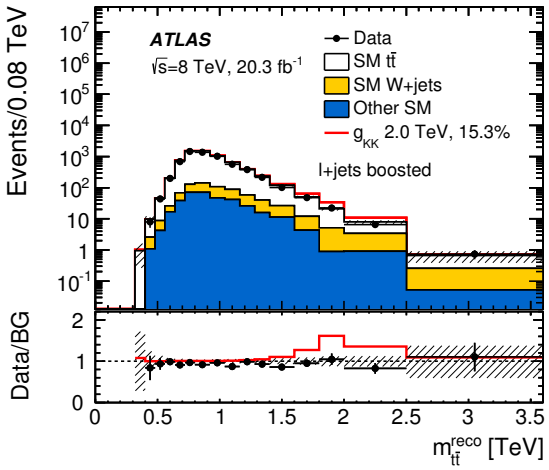

(a) Boosted topology

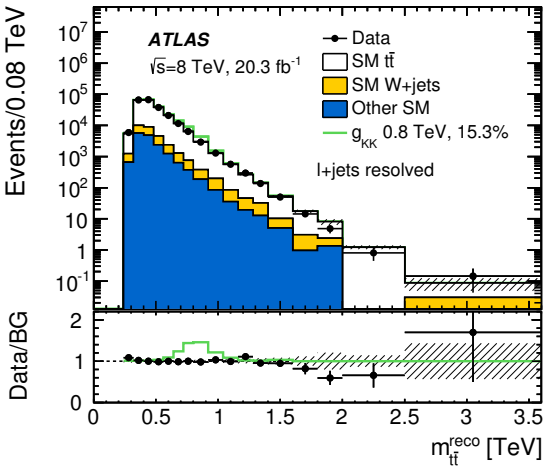

(b) Resolved topology

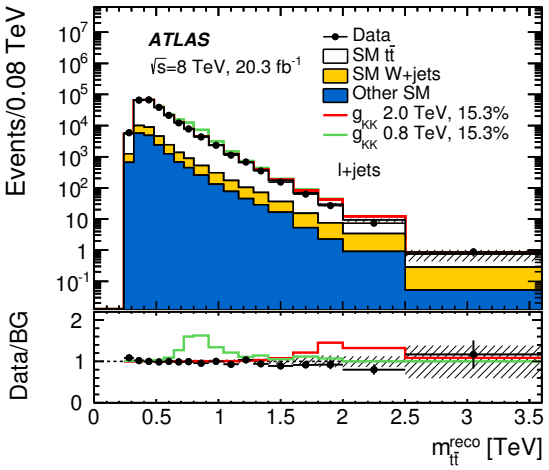

(c) All topology

Figure 6.8.: The $m_{t\bar{t}}^{\text{reco}}$ spectra *after* the profile-likelihood fit (Section 7.2.4) summed over (a) the six channels of the boosted-topology selection (b) the six resolved-topology selection (c) all twelve channels. Published in [1].

around $m_{Z'}/2 \approx 900$ GeV (see also Figure A.2 in the appendix). Thus a variation of the jet energy/momentum scale has a more significant impact on the expected yields for the SM $t\bar{t}$ background than on those for the given signal. The largest impact on the latter stems from the high-p_T b-tagging uncertainty (b-`tag high-`p_T), the role of which with regard to the derivation of the exclusion limits will be discussed in Section 7.2.7. It should be noted that the uncertainties related to large-R jets also affect the yields for the resolved-topology selection which includes a veto on events passing the boosted-topology selection.

Alternative measures for the impact of systematic variations are needed. The **impact on the $m_{t\bar{t}}^{\text{reco}}$ spectra** is of particular relevance for the search presented in this thesis as it allows to gauge the effect of systematic variations on the *shape* of the spectra, as shown, for example, in Figure 5.15. In particular, certain systematic uncertainties may have a small impact in one region of the spectrum but a large impact in another, thus affecting the sensitivity to hypothetical resonances differently depending on the resonance mass. In contrast, the overall yields are only sensitive to changes in the *normalisation* of the spectra. The relevance of systematic variations and the decision about whether to keep them as input to the statistical analyis tools is made based on both the impact on the yields and the spectra.

In addition, the **impact of the corrresponding nuisance parameters on the signal strength** in the profile-likelihood fit that is used in the derivation of the upper cross-section limits is studied. Further details are given in Section 7.2.5.

Systematic Uncertainties	Resolved selection yield impact [%] total bkg.	Z'	Boosted selection yield impact [%] total bkg.	Z'
Luminosity	2.5	2.8	2.6	2.8
PDF	2.4	3.6	4.7	2.3
$t\bar{t}$ ISR/FSR	3.7	–	1.2	–
$t\bar{t}$ PS + fragmentation	4.8	–	1.5	–
$t\bar{t}$ normalisation	5.3	–	5.5	–
$t\bar{t}$ EW virtual correction	0.2	–	0.5	–
$t\bar{t}$ generator	0.3	–	2.6	–
$t\bar{t}$ top-quark mass	0.6	–	1.4	–
W+jets shape, "iqopt3"	0.3	–	0.1	–
W+jets shape, "ptjmin10"	0.1	–	0.1	–
Multi-jets norm., e+jets	0.5	–	0.2	–
Multi-jets norm., μ+jets	0.1	–	< 0.1	–
AKT4 JES3 (Modelling1)	3.0	1.4	< 0.1	0.5
AKT4 JES7 (Detector1)	0.4	0.4	0.2	0.5
AKT4 JES12 (EtaInter)	0.9	0.8	0.3	0.7
AKT4 JES18 (PU Rho)	2.2	1.1	0.1	0.1
AKT4 JES20 (FlavourComp)	3.1	1.4	0.1	0.7
AKT4 JES21 (FlavourResp)	1.7	0.7	0.1	0.5
AKT4 JES22 (bJES)	0.4	0.1	< 0.1	0.1
AKT4 JES (Others)	2.1	0.7	< 0.1	0.5
AKT4 jet energy res.	1.8	1.4	< 0.1	0.2
AKT10 JES1 (dataMC)	0.1	0.6	4.0	0.3
AKT10 JES13 (Topology)	0.1	1.3	7.7	0.5
AKT10 JES (Others)	< 0.1	0.5	2.7	0.2
AKT10 jet m/d12 scale	< 0.1	1.5	3.5	2.7
AKT10 jet energy res.	< 0.1	0.2	1.0	< 0.1
AKT10 jet mass res.	< 0.1	0.2	0.2	0.2
b-tag EV6	0.1	0.4	0.2	> 0.1
b-tag EV7	0.2	0.2	0.7	1.3
b-tag EV8	0.7	0.6	1.4	1.8
b-tag EV9	0.8	0.7	0.5	0.8
b-tag high-p_T	0.1	1.7	2.4	16.9
c-tag	0.1	0.7	0.1	2.1
Mistag	< 0.1	< 0.1	0.5	0.2
Electron SF	0.3	0.6	0.6	1.3
Muon SF	0.9	1.0	1.0	1.1
MC stat. uncertainty	0.4	6.0	1.3	1.8
Total Uncertainty	10.8	8.8	13.4	18.0

Table 6.2.: Average impact of the dominant systematic uncertainties on the estimated total background yield and on the estimated yield for a hypothetical Z' signal with $m_{Z'} = 1.75$ TeV for the resolved- and boosted-topology selection. The spectra of the e+jets and μ+jets channels are added. The relative variation of the yields are given in percent of the nominal value. Certain systematic uncertainties are not applicable to the Z' samples, which is indicated with a bar (−) in the table. Reduced version published in [1].

7. Statistical Interpretation

The statistical interpretation of the analysis results presented in Section 6.1.3 focuses exclusively on the distributions of the invariant mass of the reconstructed $t\bar{t}$ system, $m_{t\bar{t}}^{\text{reco}}$, for the selected events in the twelve mutually exclusive categories defined in Section 5.4.5. It consists of two consecutive stages: first, the compatibility of the observed data with the SM-only hypothesis is tested; second, as no significant deviation of the data from the nominal background expectation is found, upper limits on the production cross-section times branching ratio, $\sigma_X \times BR(X \to t\bar{t})$, are derived for the four benchmark models described in Section 2.5.

7.1. Compatibility of Observed Data with the Null Hypothesis

Many BSM searches, including the one presented in this thesis, are **model independent** searches which aim at detecting *any* significant deviation from the SM-only prediction without making a priori assumptions about the type of BSM physics that may be causing it. Therefore, the **null hypothesis** $H^{(B)}$ under scrutiny is chosen to be the SM-only (or background-only) assumption. The expected $m_{t\bar{t}}^{\text{reco}}$ distribution under $H^{(B)}$ is given by the sum of the distributions for all SM background processes estimated from MC simulations and data-driven techniques, as described in Section 5.5.

The compatibility of the observed data with $H^{(B)}$ is tested using `BumpHunter` [280], a hypothesis testing tool that systematically searches for excesses or deficits of the observed data with respect to the expected background. While such deviations are expected in the presence of BSM physics, they may also be caused by statistical fluctuations due to the finite number of background events in the search region.

The task of `BumpHunter` is to identify the most significant deviation of the observed data in a given distribution, quantify it using a **test statistic** (defined below) and derive its p-value, which is a measure of the probability that a given deviation may be caused merely by a statistical fluctuation of the expected background under $H^{(B)}$.

When considering a distribution with multiple bins, as is the case for the $m_{t\bar{t}}^{\text{reco}}$ spectra under consideration, the probability that a significant deviation of the observed data (as defined in the following paragraphs) is found in a single bin naturally increases with the number of bins that are tested. This is known as the **trials factor** or **look-elsewhere effect**. In `BumpHunter`, this is taken into account by defining test windows of varying sizes and positions, and comparing the deviations in different windows with each other, instead of considering each bin separately: For a given $m_{t\bar{t}}^{\text{reco}}$ distribution with N bins, windows with sizes from 2 to N bins are formed and for each size all possible window positions are tested by moving the window position by one bin.

In each window i, the (integer) number of data events d_i is compared to the number of background events b_i, a real number representing the expectation value under $H^{(B)}$. If searching for a data excess, the Poisson probability distribution function

$$P(d_i, b_i) = \begin{cases} \Gamma(d_i, b_i) = \sum_{n=d_i}^{\infty} \frac{b_i^n}{n!} e^{-b_i} & \text{if } d_i \geq b_i \\ 1 - \Gamma(d_i + 1, b_i) & \text{if } d_i < b_i \end{cases} \tag{7.1}$$

is calculated. The Γ function in the first line quantifies the probability that a data count equal to or greater than d_i is observed given the background expectation value b_i under $H^{(B)}$. The inequality signs in Equation 7.1 are reversed when searching for a data deficit.

`BumpHunter` also includes the effects of systematic variations, which affect the expected number of background events in a given bin through changes of the overall normalisation and/or the shape of the $m_{t\bar{t}}^{\text{reco}}$ distribution for the total SM background. This is taken into account by extending the function in Equation 7.1 as follows:

$$P(d_i, b_i) \longrightarrow \max_{\lambda_i} \{P(d_i, b_i + \lambda_i \theta_i) \exp(-\lambda_i^2/2)\}, \tag{7.2}$$

where θ_i is the total systematic uncertainty in bin i and the real number $\lambda_i \in [-8, 8]$ is varied in steps of 1 in an initial scan and then in steps of 0.1 around the value from the initial scan that maximises the function in Equation 7.2. The final value of λ_i that maximises the extended probability density function is denoted as $\tilde{\lambda}$. The factor $\exp(-\lambda^2/2)$ in Equation 7.2 reflects the assumption that the systematic uncertainties follow a Gaussian distribution.

The most interesting bump corresponds to the window i_0 with minimal Poisson probability: $P_{i_0}^{\min}(\tilde{\lambda}) \equiv \min_i P_i(\tilde{\lambda})$. The procedure is repeated to identify the most signficant deviation in each of the twelve search channels.

Once the most interesting deviation in a given channel is identified, its size is quantified in two steps. First, a test statistic t is defined. When looking for a data excess, it takes the form

$$t = \begin{cases} 0 & \text{if } d_i \leq b_i \\ -\log P_{i_0}^{\min}(\tilde{\lambda}) & \text{otherwise.} \end{cases} \tag{7.3}$$

The inequality sign is reversed in the case of a data deficit. The value of the test statistic calculated for the observed data deviation in the window of interest is denoted as t_{obs}. The larger the value of t_{obs}, the bigger the discrepancy between data and background expectation.

Next, a measure is derived for the probability that the observed deviation, quantified by t_{obs}, is caused by a background fluctuation alone, assuming $H^{(B)}$ is true. This measure is called the **p-value** of the deviation. To this end, a set of at least $N = 10,000$ pseudo-experiments is conducted by taking the background count b_{i_0} in the chosen bin as the mean (and variance) of a Poisson distribution and using this distribution to generate samples of pseudo-data. For each of these pseudo-experiments, the test statistic is evaluated and the results are used to calculate the **local** p-value for the given window, which is defined as

$$p = \frac{\int_{t_{obs}}^{\infty} f(t)\mathrm{d}t}{\int_{0}^{\infty} f(t)\mathrm{d}t}, \tag{7.4}$$

where $f(t)$ is the distribution of the test statistic t derived numerically from the pseudo-experiments.

The p-value quantifies the probability that, under the assumption of $H^{(B)}$, a measurement returns a test statistic greater than or equal to the one observed in the data for the actual measurement. The smaller the p-value the smaller the probability that an observed data excess or deficit is caused by a fluctuation of the expected background under $H^{(B)}$ alone.

It is customary in high-energy physics to convert the p-value into a **significance** Z, where Z is the number of standard deviations in an upward fluctuation of a Gaussian-distributed random variable such that the tail of the Gaussian distribution integrated from this point to infinity corresponds to the given p-value. More precisely:

$$Z = \Phi^{-1}(1 - p), \tag{7.5}$$

where Φ^{-1} is the inverse function of the cumulative Gaussian distribution Φ [52]. It has become

standard practice to only declare a *discovery* if a deviation from the null hypothesis (typically the SM-only hypothesis) has a significance of at least 5σ which corresponds to a p-value of 2.87×10^{-7} or less. A 3σ deviation is often referred to as *evidence* for an unknown effect. This is somewhat mis-leading since the p-value quoted in a hypothesis test merely reflects the degree of belief that an observed deviation can be explained under the assumption of $H^{(B)}$ and no assumptions are made about a possible alternative hypothesis $H^{(S+B)}$.

The results of the hypothesis tests conducted by `BumpHunter` are summarised in Tables 7.1 and 7.2 for the pre- and post-fit m_{tt}^{reco} distributions, respectively. For each of the twelve search channels, the p-value and significance Z in units of standard deviations σ are listed for the most significant excess (upper part) and deficit (lower part), together with the mass range corresponding to the window in which it was observed.

The errors on the significance are derived by first calculating the errors δp on the p-value and then using them to calculate high and low significance values corresponding to the high and low p-values ($p \pm \delta p$). The error δp is defined as [281]

$$\delta p = \sqrt{\frac{p(1-p)}{N}}, \tag{7.6}$$

where N is the number of pseudo-experiment used in the numerical calculation of the p-value.[1]

The last column of each table contains the value of $\tilde{\lambda}$ for the given deviation. It is a measure for the fraction of the total systematic uncertainty θ_i in the given window by which the background count would have to be scaled to minimise the discrepancy with the observed data. A value of 0 corresponds to no scaling, while a value of ± 1 means that the background count was corrected up/down by one standard deviation of the Gaussian-distributed total systematic uncertainty.

In addition to the results from the twelve individual channels, Tables 7.1 and 7.2 also list the size and position for the most significant excesses and deficits in the four search channels ("resolved, e, cat 1,2,3", "resolved, μ, cat 1,2,3", "boosted, e, cat 1,2,3", "boosted, μ, cat 1,2,3") that one obtains by dropping the classification of the events into b-tagging categories. The results of a further combination of these four channels into a single resolved ("resolved, $e+\mu$, cat 1,2,3") and a single boosted ("boosted, $e + \mu$, cat 1,2,3") channel as well as into a single combined channel ("combined, $e + \mu$, cat 1,2,3") are also quoted.

[1] This uncertainty is derived by the same logic as the uncertainty on the efficiency of a selection cut: Numerically, the p-value is calculated by counting the number of pseudo-experiments with a test statistic t greater or equal to the "cut value" t_{obs} [281].

This combination of different search channels is another way of taking into account the look-elsewhere effect: The more channels that are considered for hypothesis testing, the more likely it is that at least one will exhibit a significant data deviation if $H^{(B)}$ is true. If a deviation was caused by a BSM signal, it would be expected to be seen in other channels at roughly the same position. In particular, none of the BSM signals under consideration is expected to bias the subsequent leptonic decay of a top quark towards either the e or μ flavour. These considerations are used to improve the reliability of the `BumpHunter` results: The positions of the most significant excesses (deficits) are compared between the individual channels. If they do not overlap, the combination of these channels is classified as having "no excess" ("no deficit"). If an overlap is found, the **combined (global) p-value** is calculated as follows: The Poisson probability density functions of the individual deviations are multiplied and the resulting value is used to derive the combined test statistic $t_{\text{obs}}^{\text{comb}}$. Next, a new set of pseudo-data samples is generated from the sum of the background distributions for the two channels and the p-value is calculated as before.

The biggest excess among all of the individual channels in the pre-fit distributions is found in b-tagging category 2 of the resolved e+jets channel for $m_{t\bar{t}}^{\text{reco}}$ values between 1600 and 2000 GeV, see Table 7.1. It has a p-value of 0.038 and a significance of 1.774σ. The comparison with the excesses observed for the other two b-tagging categories in the resolved e+jets channel (adjoining table rows) shows no overlap between the respective mass ranges of interest and hence "no excess" is reported for the combination of these channels, "resolved, e, cat 1,2,3". The same holds for the combination of the other channels and overall no excess is reported.

The biggest deficit in the pre-fit distributions is reported in b-tagging category 2 of the boosted μ+jets channel for $m_{t\bar{t}}^{\text{reco}}$ values between 1600 and 2000 GeV. It has a p-value of 0.024 and a significance of 1.975σ but again there is no overlap with other channels.

For the post-fit spectra, the largest deviation is found to be an excess in b-tagging category 1 of the boosted e+jets channel in the mass window between 2000 and 3600 GeV. Its significance of 2.201σ is slightly larger than that of the biggest deviation in the pre-fit spectra. This is expected given the constraints on the systematic uncertainties compared to the pre-fit spectra. However, a comparison with the most significant excess in the other search channels shows no overlap. As with the pre-fit spectra, no overall excess or deficit is found in the post-fit spectra.

Excesses				
Channel	p-value	$Z[\sigma]$ (low, high)	mass range [GeV]	$\tilde{\lambda}$
resolved, μ, cat. 1	0.043	1.709 (1.704,1.714)	1600 – 2000	1.20
resolved, μ, cat. 2	0.394	0.267 (0.264,0.270)	1400 – 1800	0.50
resolved, μ, cat. 3	0.273	0.602 (0.599,0.605)	1280 – 1800	0.80
resolved, μ, cat. 1,2,3	0.049	1.647 (1.640,1.654)	1280 – 1800	0.80
resolved, e, cat. 1	0.229	0.740 (0.737,0.744)	2000 – 3600	0.40
resolved, e, cat. 2	0.038	1.774 (1.768,1.779)	1600 – 2000	1.10
resolved, e, cat. 3	0.352	0.378 (0.375,0.381)	920 – 1160	0.70
resolved, e, cat. 1,2,3	1.000	No Excess	–	0.70
resolved, e+μ, cat. 1,2,3	1.000	No Excess	–	0.80
boosted, μ, cat. 1	0.388	0.283 (0.280,0.286)	920 – 1160	0.50
boosted, μ, cat. 2	0.414	0.217 (0.214,0.220)	2000 – 3600	0.50
boosted, μ, cat. 3	0.235	0.721 (0.718,0.724)	1280 – 1600	0.80
boosted, μ, cat. 1,2,3	1.000	No Excess	–	0.80
boosted, e, cat. 1	0.393	0.270 (0.267,0.273)	560 – 720	0.50
boosted, e, cat. 2	0.311	0.490 (0.487,0.493)	400 – 560	0.80
boosted, e, cat. 3	0.214	0.792 (0.788,0.795)	400 – 560	0.80
boosted, e, cat. 1,2,3	1.000	No Excess	–	0.80
boosted, e+μ, cat. 1,2,3	1.000	No Excess	–	1.10
combined, e+μ, cat. 1,2,3	1.000	No Excess	–	1.10
Deficits				
Channel	p-value	$Z[\sigma]$ (low, high)	mass range [GeV]	$\tilde{\lambda}$
resolved, μ, cat. 1	0.450	0.124 (0.121,0.127)	1040 – 1280	-0.30
resolved, μ, cat. 2	0.286	0.564 (0.561,0.567)	2000 – 3600	-0.30
resolved, μ, cat. 3	0.466	0.084 (0.081,0.087)	400 – 560	-0.30
resolved, μ, cat. 1,2,3	1.000	No Deficit	–	-0.30
resolved, e, cat. 1	0.309	0.496 (0.492,0.499)	1280 – 2000	-0.70
resolved, e, cat. 2	0.445	0.136 (0.133,0.139)	1040 – 1280	-0.30
resolved, e, cat. 3	0.321	0.463 (0.460,0.467)	1400 – 1800	-0.90
resolved, e, cat. 1,2,3	1.000	No Deficit	–	-0.90
resolved, e+μ, cat. 1,2,3	1.000	No Deficit	–	-0.00
boosted, μ, cat. 1	0.107	1.241 (1.237,1.245)	400 – 560	-1.00
boosted, μ, cat. 2	0.024	1.975 (1.968,1.981)	1600 – 2000	-1.50
boosted, μ, cat. 3	0.434	0.163 (0.160,0.166)	2000 – 3600	-0.60
boosted, μ, cat. 1,2,3	1.000	No Deficit	–	-0.60
boosted, e, cat. 1	0.405	0.238 (0.235,0.241)	1800 – 2500	-0.70
boosted, e, cat. 2	0.464	0.088 (0.085,0.091)	560 – 720	-0.40
boosted, e, cat. 3	0.375	0.316 (0.313,0.319)	1160 – 1400	-0.60
boosted, e, cat. 1,2,3	1.000	No Deficit	–	-0.60
boosted, e+μ, cat. 1,2,3	1.000	No Deficit	–	-0.00
combined, e+μ, cat. 1,2,3	1.000	No Deficit	–	-0.00

Table 7.1.: The most significant excesses and deficits of observed data with respect to the nominal background expectation in the twelve independent search channels and their various combinations. Numbers are derived with `BumpHunter` using the **pre-fit** $m_{t\bar{t}}$ distributions shown in Figures 6.5 and 6.6 as input. Taken from [2].

Excesses				
Channel	p-value	$Z[\sigma]$ (low, high)	mass range [GeV]	$\tilde{\lambda}$
resolved, μ, cat. 1	0.202	0.833 (0.829,0.836)	1040 – 1280	1.10
resolved, μ, cat. 2	0.451	0.121 (0.118,0.124)	1400 – 1800	0.70
resolved, μ, cat. 3	0.344	0.400 (0.397,0.403)	640 – 800	1.10
resolved, μ, cat. 1,2,3	1.000	No Excess	–	1.10
resolved, e, cat. 1	0.139	1.082 (1.079,1.086)	2000 – 3600	0.30
resolved, e, cat. 2	0.044	1.705 (1.700,1.710)	1600 – 2500	1.00
resolved, e, cat. 3	0.285	0.566 (0.563,0.569)	800 – 1040	1.20
resolved, e, cat. 1,2,3	1.000	No Excess	–	1.20
resolved, e+μ, cat. 1,2,3	1.000	No Excess	–	1.10
boosted, μ, cat. 1	0.046	1.678 (1.673,1.683)	480 – 640	1.20
boosted, μ, cat. 2	0.203	0.828 (0.825,0.832)	480 – 640	1.00
boosted, μ, cat. 3	0.343	0.402 (0.399,0.405)	1400 – 1800	0.90
boosted, μ, cat. 1,2,3	1.000	No Excess	–	0.90
boosted, e, cat. 1	0.013	2.201 (2.194,2.209)	2000 – 3600	0.80
boosted, e, cat. 2	0.063	1.526 (1.521,1.531)	400 – 560	1.30
boosted, e, cat. 3	0.126	1.141 (1.137,1.145)	480 – 640	1.10
boosted, e, cat. 1,2,3	1.000	No Excess	–	1.10
boosted, e+μ, cat. 1,2,3	1.000	No Excess	–	0.70
combined, e+μ, cat. 1,2,3	1.000	No Excess	–	0.70
Deficits				
Channel	p-value	$Z[\sigma]$ (low, high)	mass range [GeV]	$\tilde{\lambda}$
resolved, μ, cat. 1	0.031	1.863 (1.857,1.869)	1800 – 3600	-0.70
resolved, μ, cat. 2	0.354	0.373 (0.370,0.376)	2000 – 3600	-0.20
resolved, μ, cat. 3	0.398	0.256 (0.253,0.259)	800 – 1160	-0.90
resolved, μ, cat. 1,2,3	1.000	No Deficit	–	-0.90
resolved, e, cat. 1	0.172	0.943 (0.939,0.946)	1600 – 2000	-1.10
resolved, e, cat. 2	0.448	0.130 (0.127,0.133)	400 – 560	-0.60
resolved, e, cat. 3	0.097	1.297 (1.293,1.301)	1400 – 1800	-1.10
resolved, e, cat. 1,2,3	1.000	No Deficit	–	-1.10
resolved, e+μ, cat. 1,2,3	1.000	No Deficit	–	-0.00
boosted, μ, cat. 1	0.209	0.807 (0.804,0.811)	2000 – 3600	-0.80
boosted, μ, cat. 2	0.465	0.085 (0.083,0.088)	1600 – 2000	-0.70
boosted, μ, cat. 3	0.345	0.396 (0.393,0.399)	920 – 1280	-1.20
boosted, μ, cat. 1,2,3	1.000	No Deficit	–	-1.20
boosted, e, cat. 1	0.460	0.098 (0.095,0.101)	1040 – 1280	-0.70
boosted, e, cat. 2	0.223	0.758 (0.755,0.762)	640 – 800	-1.30
boosted, e, cat. 3	0.484	0.037 (0.034,0.040)	1160 – 1400	-0.50
boosted, e, cat. 1,2,3	1.000	No Deficit	–	-0.50
boosted, e+μ, cat. 1,2,3	1.000	No Deficit	–	-1.20
combined, e+μ, cat. 1,2,3	1.000	No Deficit	–	-1.20

Table 7.2.: The most significant excesses and deficits of observed data with respect to the nominal background expectation in the twelve independent search channels and their various combinations. Numbers are derived with `BumpHunter` using the **post-fit** $m_{t\bar{t}}$ distributions, derived as described in Section 7.2.4, as input. Taken from [2].

7.2. Upper Cross-section Limits on Benchmark Models

No significant deviation of the observed data from the expected distributions under $H^{(B)}$ is found in the $m_{t\bar{t}}^{\text{reco}}$ spectra, as shown in Section 7.1. Therefore, upper limits on $\sigma_X \times BR(X \to t\bar{t})$ are derived for the four benchmark models in Section 2.5.

Two fundamentally different approaches to hypothesis testing and, consequently, to limit setting exist: The **Frequentist** approach builds on the assumption that the parameter of interest, for example the cross-section of a signal process, has some fixed but unknown value. A measurement yields a value for an estimator of this parameter, which may differ from its true value due to statistical and systematic uncertainties. If the measurement was repeated any number of times, the measured values of the parameter estimator would follow a probability distribution determined by the true value of the parameter and the uncertainties of the measurement. It is then possible to define an interval (or one-sided bound in the case of upper cross-section limits) such that it covers the true value of the parameter of interest with a given probability. This probability is referred to as the **confidence level (CL)** of the test and an observed parameter value that lies outside this interval would be rejected at the chosen CL. The **Bayesian** approach differs from the Frequentist approach in that it considers neither a true parameter value nor the possibility of repeating a measurement a given number of times. Instead, it relies on a *prior* assumption about the form of the probability distribution of the parameter of interest and relies on *Bayes' theorem* to update this assumption in the light of a given, single measurement. The resulting *posterior* probability distribution is then integrated to obtain a confidence interval or upper limit for the desired CL. A more extensive, pedagogical introduction into the concepts of Frequentist and Bayesian limit setting can be found in [282].

The approach to limit setting has undergone major changes since the last iterations of this analysis [174, 39]. They are the result of the decision to replace the previous Bayesian limit setting procedure, developed by the DØ collaboration [283] and implemented in an analysis tool called `top_statistics` [284], by a Frequentist approach implemented within the `HistFitter` [285] framework. `HistFitter`, which is based on `HistFactory` [286], `RooFit` [287] and `RooStats` [288], has been the standard statistics tool in the ATLAS SUSY group since 2012 and has come to be used within other ATLAS groups in recent years. In the search presented in this thesis, a major motivation for using `HistFitter` for the limit setting procedure is the fact that it provides an asymptotic approximation of the CL_s limits (see below), which is far less computationally

intense than the generation of thousands of pseudo-data samples required by alternative approaches. A significant reduction of computing time and resources has become mandatory in light of the significantly increased scope and complexity of the search compared to previous iterations: First, the introduction of exclusive b-tagging categories (Section 5.4.5) has increased the number of search channels from four to twelve. Second, the number of mass points for which upper cross-section limits are derived has grown from 23 to 73 due to the introduction of two new benchmark models, the addition of KK gluon samples with varying width, and the introduction of additional mass points for the existing benchmark models. Finally, the number of systematic uncertainties considered in the statistical analysis has increased from 22 in previous iterations of the search to 36 (Table 6.2).[2]

7.2.1. Statistical Method

Upper cross-section limits are derived by conducting a hypothesis test that relies on a test statistic to quantify the agreement between the observed data with the expectations under an alternative hypothesis $H^{(S+B)}$ that predicts a BSM signal S on top of the SM background B. Unlike the search stage discussed in the previous section, which is completely model-independent, the limit setting stage relies on the specific benchmark models introduced in Section 2.5 to formulate the expectation under the alternative hypothesis.

Definition of the Test Statistic

The test statistic used at the limit setting stage is defined based on the following considerations:[3] In the signal region, the expectation value $E[n_{i,j}]$ for the number of events $n_{i,j}$ in bin i of the $m_{t\bar{t}}^{\text{reco}}$ spectrum for a given channel j under an alternative hypothesis $H^{(S+B)}$ can be written as

$$E_\mu[n_{i,j}] = \mu s_{i,j} + b_{i,j}, \tag{7.7}$$

where $s_{i,j} = a_{i,j}^{(s)}\sigma^{(s)}$ and $b_{i,j}$ are the number of expected signal and background events, respectively, $a_{i,j}^{(s)}$ denotes the signal efficiency times acceptance (times integrated luminosity) for the given bin in the given channel and $\sigma^{(s)}$ is the predicted (nominal) signal cross-section times branching ratio for the chosen mass point of the benchmark model under consideration. The parameter μ is called the **signal strength** and is chosen such that the case $\mu = 0$ corresponds

[2] Note that this number is still significantly smaller than the full set of systematic uncertainties whose impact on the $m_{t\bar{t}}^{\text{reco}}$ spectrum has been studied in this search (Section 5.6).
[3] The structure of and naming conventions in this and the following sections are partly based on [289].

to the background-only hypothesis $H^{(B)}$ while the case $\mu = 1$ yields the signal+background hypothesis $H^{(S+B)}$ for the nominal signal cross-section $\sigma^{(s)}$. The signal-strength parameter thus allows for a smooth variation between the two hypotheses. In particular, it is possible to test the compatibility between the observed data and the predictions under a range of alternative hypotheses with different signal cross-sections by varying μ. This is key to deriving upper limits on the cross-section times branching ratio.

The expected yields $s_{i,j}$ and $b_{i,j}$ are affected by both systematic and statistical uncertainties. These are taken into account as **nuisance parameters** in the hypothesis test: $s_{i,j} = s_{i,j}(\boldsymbol{\theta})$ and $b_{i,j} = b_{i,j}(\boldsymbol{\theta})$, where $\boldsymbol{\theta}$ is the vector of the nuisance parameters that correspond to the uncertainties listed in Table 6.2. The exact parameterisation of $s_{i,j}$ and $b_{i,j}$ in terms of the nuisance parameters $\boldsymbol{\theta}$ is given in Section 7.2.2.

With this parameterisation of the expectation value per bin, the probability to observe $n_{i,j}$ data events in bin i for channel j is given by the Poisson distribution with mean and variance $\lambda(\mu, \boldsymbol{\theta}) \equiv E_\mu[n_{i,j}] \overset{\text{Eq.7.7}}{=} \mu s_{i,j}(\boldsymbol{\theta}) + b_{i,j}(\boldsymbol{\theta})$:

$$\text{Pois}(n_{i,j}|\mu, \boldsymbol{\theta}) = \frac{\lambda^{n_{i,j}}}{n_{i,j}!}\, e^{-\lambda}. \tag{7.8}$$

Then the overall agreement between the $m_{t\bar{t}}^{\text{reco}}$ distributions observed in data D with those expected based on a hypothesis $H_\mu^{(S+B)}$ can be quantified by the **likelihood function**, which is defined as the product of the Poisson probabilities of the N (independent) bins of the $m_{t\bar{t}}^{\text{reco}}$ histograms for the M (exclusive) search channels under consideration:

$$L(D|\mu, \boldsymbol{\theta}) = \underbrace{\prod_{j=1}^{M}\prod_{i=1}^{N} \text{Pois}(n_{i,j}|\mu, \boldsymbol{\theta})}_{\text{Poisson terms}} \cdot \underbrace{\prod_{\text{NP}} f(\theta^{(\text{NP})})}_{\text{Constraint terms}} \quad . \tag{7.9}$$

The second factor in this equation represents the product of constraint functions $f(\theta^{(\text{NP})})$, one for each nuisance parameter $\theta^{(\text{NP})}$. The choice of the constraint functions and the parameterisation of the signal and background yields $s_{i,j}(\boldsymbol{\theta})$ and $b_{i,j}(\boldsymbol{\theta})$ in terms of the nuisance parameters will be discussed in Section 7.2.2.

In the search presented in this thesis, there are twelve independent $m_{t\bar{t}}^{\text{reco}}$ spectra, one for each search channel, hence $M = 12$ in Equation 7.9. Only bins with non-negligible event yields are considered in the likelihood function to reduce the complexity of the input to the statistics tools

and thus the computing time: In the case of the spectra for the resolved-topology channels, bins below 0.24 TeV and above 2 TeV are excluded from the likelihood function. In the case of the spectra for the boosted-topology channels, only bins between 0.4 TeV and 3.0 TeV are considered. This yields $N = 15$ bins for each of the twelve $m_{t\bar{t}}^{\text{reco}}$ spectra under consideration.

The likelihood function in Equation 7.9 depends on both the signal strength μ, also referred to as the **parameter of interest**, and the vector of nuisance parameters $\boldsymbol{\theta}$. In the derivation of the upper cross-section limits, only the parameter of interest is relevant. The test statistic is therefore based on the **profile likelihood ratio**

$$\lambda(D|\mu) = \frac{L(D|\mu, \hat{\hat{\boldsymbol{\theta}}}(\mu))}{L(D|\hat{\mu}, \hat{\boldsymbol{\theta}})}, \tag{7.10}$$

for which the explicit dependence on the nuisance parameters has been eliminated. The numerator is the **profile likelihood function** that depends only on the signal strength μ and the *conditional* maximum likelihood estimator (MLE) $\hat{\hat{\boldsymbol{\theta}}}(\mu)$. The latter denotes the value $\boldsymbol{\theta}$ that maximises the likelihood function in Equation 7.9 for a given value of μ and is therefore a function of μ itself. The denominator, in contrast, is the *unconditional* maximum likelihood obtained by varying both μ and $\boldsymbol{\theta}$ to find the unconditional MLEs $\hat{\mu}$ and $\hat{\boldsymbol{\theta}}$. By construction, $0 < \lambda(D|\mu) \leq 1$ with smaller values of $\lambda(D|\mu)$ indicating larger incompatibility between the observed data and the expectation under $H_\mu^{(S+B)}$. The test statistic t_μ is then defined as the **(profile) log-likelihood ratio**

$$t_\mu = -2 \ln \lambda(D|\mu). \tag{7.11}$$

It quantifies the agreement between the data observed in a given measurement and the expectation under $H_\mu^{(S+B)}$ with smaller values of t_μ indicating better agreement. Larger values of this test statistic are obtained either if the observed yields are larger ($\hat{\mu} > \mu$) or smaller ($\hat{\mu} < \mu$) than those expected under $H_\mu^{(S+B)}$ for a given value of μ.

The test statistic defined in Equation 7.11 needs to be adapted for the derivation of one-sided (upper) limits on the cross-section times branching ratio and with regard to the type of signal that is studied in the search presented in this thesis: First, the signal processes under consideration can only increase the event yields with regard to the yields expected under the background-only hypothesis.[4] Hence only non-negative values of the signal strength are considered. Note that it

[4] A reduction of the event yields compared to those expected under the background-only hypothesis is possible in the case of negative interference between a BSM signal and SM processes. Interference effects, however, are not considered in the search presented in this thesis.

is still possible to find $\hat{\mu} < 0$ for a downward fluctuation of the data. In this case, the maximum likelihood under the condition that the signal strength μ takes only physically allowed values is obtained for $\mu = 0$ and a modified test statistic is defined accordingly as (Section 2.2 of [289]):

$$\tilde{t}_\mu = \begin{cases} t_\mu & \text{if } \hat{\mu} \geq 0 \\ -2 \ln \frac{L(D|\mu, \hat{\hat{\boldsymbol{\theta}}}(\mu))}{L(D|0, \hat{\hat{\boldsymbol{\theta}}}(0))} & \text{if } \hat{\mu} < 0. \end{cases} \tag{7.12}$$

This test statistic is further modified for the calculation of *upper* limits on the cross-section times branching ratio, which requires the derivation of a one-sided (upper) bound on μ. In this case, an upward fluctuation of the data ($\hat{\mu} > \mu$) should not lead to the rejection of the hypothesised value of μ. This is achieved by setting the test statistic to zero, its smallest possible value, which is obtained for $\mu = \hat{\mu}$, thus artificially indicating good agreement between the data and the prediction under $H_\mu^{(S+B)}$ for $\hat{\mu} > \mu$. Hence the following **one-sided log-likelihood ratio** is used as a test statistic in the derivation of the upper cross-section limits (Section 2.5 of [289]):

$$\tilde{q}_\mu = \begin{cases} \tilde{t}_\mu & \text{if } \hat{\mu} \leq \mu \\ 0 & \text{if } \hat{\mu} > \mu \end{cases} = \begin{cases} -2 \ln \frac{L(D|\mu, \hat{\hat{\boldsymbol{\theta}}}(\mu))}{L(D|0, \hat{\hat{\boldsymbol{\theta}}}(0))} & \text{if } \hat{\mu} < 0 \\ -2 \ln \frac{L(D|\mu, \hat{\hat{\boldsymbol{\theta}}}(\mu))}{L(D|\hat{\mu}, \hat{\boldsymbol{\theta}})} & \text{if } 0 \leq \hat{\mu} \leq \mu \\ 0 & \text{if } \hat{\mu} > \mu. \end{cases} \tag{7.13}$$

Definition of Exclusion Limits

In the Frequentist approach to hypothesis testing, the decision whether to accept or reject the hypothesis $H_\mu^{(S+B)}$ for a given value of μ is based on the p-value

$$p_\mu^{(\mathrm{CL}_{s+b})} = P(\tilde{q}_\mu > \tilde{q}_{\mu,obs} | H_\mu^{(S+B)}) = \int_{\tilde{q}_{\mu,obs}}^{\infty} f(\tilde{q}_\mu | H_\mu^{(S+B)}) \mathrm{d}\tilde{q}_\mu, \tag{7.14}$$

which quantifies the probability that, assuming $H_\mu^{(S+B)}$ is true, a measurement yields a value of the test statistic that is less compatible with the expectation under $H_\mu^{(S+B)}$ than the observed value $\tilde{q}_{\mu,obs}$. The so-called **sampling distribution** $f(\tilde{q}_\mu | H_\mu^{(S+B)})$ is the probability density distribution of the test statistic $\tilde{q}_\mu$. The determination of the sampling distribution is discussed in the next section.

An exclusion criterion for the hypothesis $H_\mu^{(S+B)}$ can be imposed by requiring that the hypothesis be rejected if the p-value defined in Equation 7.14 is below some predefined threshold α. A

common choice is $\alpha = 0.05$. This hypothesis test, which is based purely on the p-value $p_\mu^{(\mathrm{CL}_{s+b})}$ for the alternative hypothesis $H_\mu^{(S+B)}$, is referred to as the **$\mathbf{CL}_{s+b}$ method**.

A weakness of this method lies in the fact that it may lead to the exclusion of alternative hypotheses to which the search has little or no sensitivity. This may, for example, be the case if the predicted number of signal events in the signal region(s) is significantly smaller than the expected number of background events in the same region(s). The degree to which an alternative hypothesis $H_\mu^{(S+B)}$ can be distinguished from the background-only hypothesis $H^{(B)}$ by means of the chosen test statistic $\tilde{q}_\mu$ can be quantified by the probability that, assuming $H^{(B)}$ is true, a measurement yields a value of $\tilde{q}_\mu$ that indicates greater compatibility with the alternative hypothesis than the data observed in the measurement under consideration:

$$p_\mu^{(\mathrm{CL}_b)} = 1 - P(\tilde{q}_\mu > \tilde{q}_{\mu,obs}|H^{(B)}) = 1 - \int_{\tilde{q}_{\mu,obs}}^{\infty} f(\tilde{q}_\mu|H^{(B)})\mathrm{d}\tilde{q}_\mu. \tag{7.15}$$

The two p-values $p_\mu^{(\mathrm{CL}_{s+b})}$ and $p_\mu^{(\mathrm{CL}_b)}$ are visualised in Figure 7.1. They are represented by the green (labelled p_{s+b}) and yellow (labelled p_b) areas under the sampling distributions $f(Q|s+b)$ and $f(Q|b)$ of an arbitrary test statistic Q under an (arbitrary) signal+background hypothesis "$s+b$" and a background-only hypothesis "b", respectively. On the left-hand side, the case in which the two distributions can be clearly distinguished from one another is shown. In this case, p_b and hence the probability to reject the signal+background hypothesis in favour of the background-only hypothesis is small. The case in which the sampling distributions are very similar is shown on the right-hand side. In the context of the resonance search presented in this thesis, such a case may occur if the nominal signal cross-section or the value of μ that is being tested is very small, resulting in a small hypothesized (relative) signal contribution in the signal region(s).

To avoid the exclusion of a hypothesis $H_\mu^{(S+B)}$ to which the search has little or no sensitivity, a modified exclusion criterion is defined based on the following ratio of p-values:

$$p_\mu^{(\mathrm{CL}_s)} = \frac{p_\mu^{(\mathrm{CL}_{s+b})}}{1 - p_\mu^{(\mathrm{CL}_b)}}. \tag{7.16}$$

The hypothesis $H_\mu^{(S+B)}$ is excluded if $p_\mu^{(\mathrm{CL}_s)} < 0.05$ for the observed dataset. This approach, which is widely used in high-energy physics, is referred to as the **$\mathbf{CL}_s$ method** [291]. If the two hypotheses can be clearly distinguished, $p_\mu^{(\mathrm{CL}_b)}$ will be small and hence $p_\mu^{(\mathrm{CL}_s)} \approx p_\mu^{(\mathrm{CL}_{s+b})}$. In this

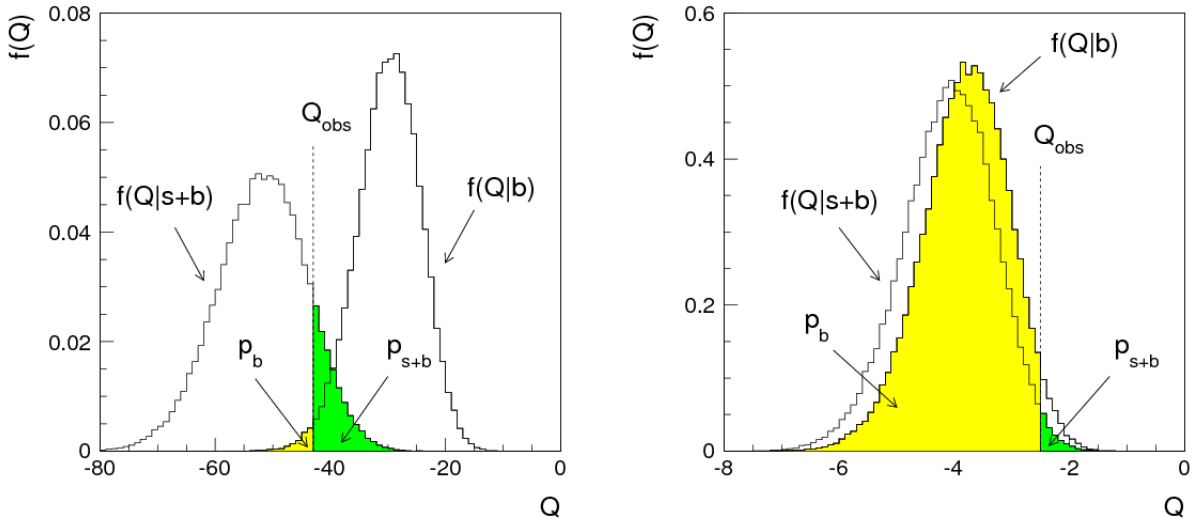

(a) **(b)**

Figure 7.1.: Sampling distributions $f(Q|s+b)$ and $f(Q|b)$ for an arbitrary test statistic Q under the signal+background and the background-only hypothesis, respectively, and the corresponding p-values $p_{\mathrm{s+b}}$ (green) and p_{b} (yellow) for the observed value of the test statistic, Q_{obs}. The plot on the left shows the case in which the two hypothesis can be clearly distinguished. A scenario in which the two hypotheses yield very similar sampling distributions is shown on the right. Note that the nomenclature in these plots, taken from [290], differs from that in the text.

case, the limits derived with the CL_s method are comparable to those derived using the simpler CL_{s+b} method. The "penalty term" $(1 - p_\mu^{(\mathrm{CL}_b)})^{-1}$ in Equation 7.16, however, becomes large if the two hypotheses are very similar. Note that by construction $p_\mu^{(\mathrm{CL}_s)} \geq p_\mu^{(\mathrm{CL}_{s+b})}$. The upper cross-section limits obtained with the CL_s method are therefore more conservative than those that would be obtained using the CL_{s+b} method.

In practice, the upper limit on the cross-section times branching ratio for a mass point m_X of a given signal model at 95% CL is obtained by calculating $p_\mu^{(\mathrm{CL}_s)}$ for a range of different values of the signal strength μ and determining the value of μ_{95} for which $p_{\mu_{95}}^{(\mathrm{CL}_s)} = 0.05$. The corresponding value of the cross-section (times branching ratio), calculated using Equation 7.7, is taken as the upper limit on $\sigma_X \times BR(X \to t\bar{t})$.

This procedure is illustrated in Figure 7.2, in which the observed values for $p_\mu^{(\mathrm{CL}_s)}$, $p_\mu^{(\mathrm{CL}_{s+b})}$ and $(1 - p_\mu^{(\mathrm{CL}_b)})$ are shown as a function of the signal strength μ. The point at which the curve for $p_\mu^{(\mathrm{CL}_s)}$ ($p_\mu^{(\mathrm{CL}_{s+b})}$) falls below the p-value of 0.05 marks the 95% upper limit on the signal strength for the CL_s (CL_{s+b}) method. Note that the curve for $p_\mu^{(\mathrm{CL}_s)}$ is consistently higher than that for $p_\mu^{(\mathrm{CL}_{s+b})}$), which results in a more conservative upper limit on μ for the CL_s compared to the CL_{s+b} method, as explained above.

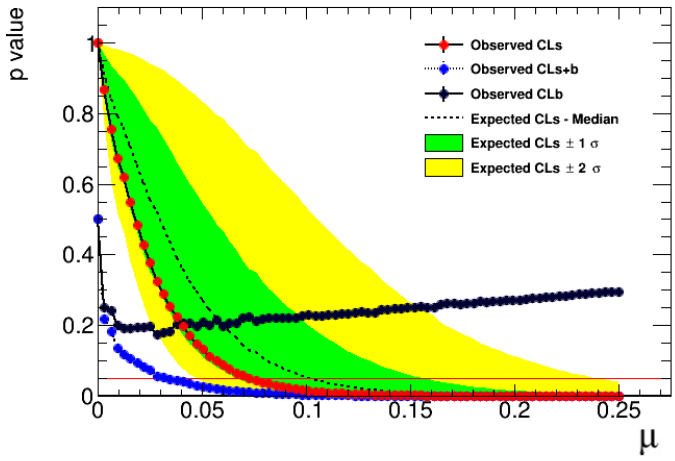

Figure 7.2.: Observed values for $p_\mu^{(\mathrm{CL}_s)}$ (`Observed CLs`), $p_\mu^{(\mathrm{CL}_{s+b})}$ (`Observed CLs+b`) and $(1 - p_\mu^{(\mathrm{CL}_b)})$ (`Observed CLb`) as a function of the signal strength μ. The expected values for $p_\mu^{(\mathrm{CL}_s)}$ and the corresponding $\pm 1\sigma$ and $\pm 2\sigma$ variations are also shown. The red horizontal line marks the p-value of 0.05, which is used to determine the 95% CL exclusion limit, μ_{95}, on the signal strength. The signal model used in this plot is a Z' resonance with $m_{Z'} = 1.5$ TeV and $\sigma_X \times BR(X \to t\bar{t}) = 1.0$ pb. Plot produced with `HistFitter`.

Distribution of the Test Statistic

The sampling distributions $f(\tilde{q}_\mu|H_\mu^{(S+B)})$ and $f(\tilde{q}_\mu|H^{(B)})$ needed to calculate $p_\mu^{(\mathrm{CL}_s)}$ can be determined numerically by conducting a sufficiently large number of pseudo-experiments, similar to the approach used by `BumpHunter` (Section 7.1). This approach, however, is computationally intensive as a new set of pseudo-data has to be generated for each value of μ that is tested for a given mass point and upper limits need to be derived on a total of 73 signal mass points in the search presented in this thesis.[5]

For this reason, an analytic approximation of the test statistic and its sampling distribution is used. It is based on results by S. Wilks [292] and A. Wald [293] according to which the test statistic $\tilde{q}_\mu$ for the single parameter of interest μ can be approximated by an analytic function with one parameter of freedom if the number of observed data events is sufficiently large. The analytic expressions for the test statistic $\tilde{q}_\mu$ and its sampling distribution are given in Section 3.7 of [289]. They have been found to be valid for data samples comprising as few as $\mathcal{O}(10)$ events [289] and are available as standard functions in the `HistFitter` framework.

[5] Typically, 80 scan points are used to determine the value of μ above which $\mathrm{CL}_s < 1 - \alpha$ for a single mass point/signal hypothesis.

7.2.2. Treatment of Nuisance Parameters

Before moving on to present the upper limits on the cross-section times branching ratio for the different benchmark models, the profiling procedure and the role of the nuisance parameters must be discussed in further detail.[6]

As mentioned in Section 7.2.1, both the expected signal and background yields in a bin i of the $m_{t\bar{t}}^{\text{reco}}$ spectrum for a given channel j, denoted as $s_{i,j}$ and $b_{i,j}$, respectively, are affected by systematic and statistical uncertainties. The systematic uncertainties, such as those related to the JES, the b-tagging efficiency or the background estimates, have been determined in *auxiliary measurements*. Their impact on both the shape and the normalisation of the $m_{t\bar{t}}^{\text{reco}}$ spectra is estimated *before* the profiling procedure as described in Section 5.6. The $m_{t\bar{t}}^{\text{reco}}$ spectra corresponding to the $\pm 1\sigma$ variations for a given systematic uncertainty, NP, are represented by pairs of histograms $h_{j,k}^{(\text{NP}+)}$ and $h_{j,k}^{(\text{NP}-)}$, where the indices j and k denote the channel and sample, respectively. The sample index k may refer either to the signal sample under consideration or any of the three background components "SM $t\bar{t}$", "SM W+jets" and "Other SM" (Section 6.1.2). The nominal and "$\pm 1\sigma$ variation" histograms, summarised schematically in Table 7.3 serve as input to the profiling procedure.

Systematic	Channel 1	...	Channel 12
Nominal	$h_{1,k}^{(0)}$	...	$h_{12,k}^{(0)}$
NP1	$h_{1,k}^{(\text{NP1}+)}$, $h_{1,k}^{(\text{NP1}-)}$	...	$h_{12,k}^{(\text{NP1}+)}$, $h_{12,k}^{(\text{NP1}-)}$
$\vdots$	$\vdots$	$\ddots$	$\vdots$
NP36	$h_{1,k}^{(\text{NP36}+)}$, $h_{1,k}^{(\text{NP36}-)}$	...	$h_{12,k}^{(\text{NP36}+)}$, $h_{12,k}^{(\text{NP36}-)}$

Table 7.3.: Schematic overview of the set of $m_{t\bar{t}}^{\text{reco}}$ histograms that serve as input to the profiling procedure. The set comprises the nominal and "$\pm 1\sigma$ variation" histograms for the systematic uncertainties NP (rows) in the twelve search channels j (columns) for the three background components "SM $t\bar{t}$", "SM W+jets" and "Other SM" and the signal sample under consideration (denoted by sample index k).

In the profiling procedure, a nuisance parameter $\theta^{(\text{NP})}$ is assigned to each source of systematic uncertainty NP. The combined effect of all systematic uncertainties on the $m_{t\bar{t}}^{\text{reco}}$ spectrum for a given channel j and sample k can then be parameterised as follows:

$$h_{j,k}(\boldsymbol{\theta}) = h_{j,k}^{(0)} + \sum_{\text{NP}} \theta^{(\text{NP})} \cdot I_{\text{lin}}(h_{j,k}^{(0)}, h_{j,k}^{(\text{NP}+)}, h_{j,k}^{(\text{NP}-)}), \tag{7.17}$$

[6] The structure of and naming conventions in this and the following sections are partly based on [286].

where

$$I_{\text{lin}}(I^{(0)}, I^{(+)}, I^{(-)}) = \begin{cases} I^{(+)} - I^{(0)} & \text{if } \theta \geq 0 \\ I^{(0)} - I^{(-)} & \text{if } \theta < 0. \end{cases} \tag{7.18}$$

The parameterisation is chosen such that $\boldsymbol{\theta} = \mathbf{0}$ yields the nominal spectrum, $h_{j,k}(\mathbf{0}) = h_{j,k}^{(0)}$, while the case $\theta^{(\text{NP})} = \pm 1$ corresponds to the $\pm 1\sigma$ variations of the systematic NP. The function $I_{\text{lin}}(\ I^{(0)}, I^{(+)}, I^{(-)})$ describes a linear interpolation between these cases.

The signal and background yields, $s_{i,j}(\boldsymbol{\theta})$ and $b_{i,j}(\boldsymbol{\theta})$, which are used to define the likelihood function in Equation 7.9, are given by the content of bin i of the parameterised $m_{t\bar{t}}^{\text{reco}}$ distribution in channel j in Equation 7.17:

$$s_{i,j}(\boldsymbol{\theta}) = h_{j,S}(\boldsymbol{\theta})[i], \tag{7.19}$$

where S denotes the signal sample under consideration, and

$$b_{i,j}(\boldsymbol{\theta}) = \sum_{k \in \{Bgr\}} h_{j,k}(\boldsymbol{\theta})[i], \tag{7.20}$$

where k runs over the three background components "SM $t\bar{t}$", "SM W+jets" and "Other SM". When the likelihood function is maximised during the profiling procedure, the nuisance parameters are varied in order to adjust the signal and background expectations to best fit the observed data. The variation of the nuisance parameters is controlled by the constraint terms in the likelihood function (Equation 7.9). In the case of the systematic uncertainties, these are conventionally chosen to be Gaussian probability density functions [286]:

$$\text{G}(\theta^{(\text{NP})} | \theta_0^{(\text{NP})}, \Delta\theta^{(\text{NP})}) = \frac{1}{\Delta\theta^{(\text{NP})}\sqrt{2\pi}} \exp\left[-\frac{(\theta^{(\text{NP})} - \theta_0^{(\text{NP})})^2}{2(\Delta\theta^{(\text{NP})})^2} \right], \tag{7.21}$$

where $\theta_0^{(\text{NP})} = 0$ and $\Delta\theta^{(\text{NP})} = 1$. It should be noted that, for each systematic uncertainty NP, there is only a single nuisance parameter, $\theta^{(\text{NP})}$. This means that the systematic variations are correlated between all bins, channels and samples - with the obvious exception of systematic uncertainties, such as the $t\bar{t}$ `normalisation` uncertainty, that only apply to a single background component. The impact of the systematic uncertainties on the shape of the $m_{t\bar{t}}^{\text{reco}}$ distributions is fully determined by the auxiliary measurements and set by the input histograms. The MC statistical uncertainty on the total background estimate, on the other hand, is treated as uncorrelated between different bins and channels. It is constrained by Poissonian probability

distribution functions, one for each bin in each channel [286].

7.2.3. Profile Likelihood Fit under the Background-only Hypothesis

The nuisance parameters discussed in the previous section are treated as free parameters that are adjusted to maximise the likelihood function in the calculation of the likelihood ratio (Equation 7.10), either for a fixed value of μ (numerator) or with μ as another free parameter (denominator). This procedure is referred to as **profiling**. The fitted value $\hat{\theta}^{(\mathrm{NP})}$ of a nuisance parameter $\theta^{(\mathrm{NP})}$ may deviate from its initial value $\theta_0^{(\mathrm{NP})}$. The difference relative to its initial uncertainty, $\Delta\theta^{(\mathrm{NP})}$, is referred to as its **pull**:

$$x^{(\mathrm{NP})} \equiv \frac{(\hat{\theta}^{(\mathrm{NP})} - \theta_0^{(\mathrm{NP})})}{\Delta\theta^{(\mathrm{NP})}}. \tag{7.22}$$

Note that $x^{(\mathrm{NP})} = \hat{\theta}^{(\mathrm{NP})}$ for the parameterisation chosen above, where $\theta_0^{(\mathrm{NP})} = 0$, $\Delta\theta^{(\mathrm{NP})} = 1$. The uncertainty on $\hat{\theta}^{(\mathrm{NP})}$ relative to the initial uncertainty $\Delta\theta^{(\mathrm{NP})}$ quantifies the **constraint** on the corresponding systematic uncertainty. `HistFitter` relies on the `Minuit` package, implemented in `RooFit`, to calculate symmetric `HESSE` (Section 7.2 of [294]) uncertainties on the nuisance parameters. An alternative determination of the uncertainties using `MINOS` (Section 7.2 of [294]), which produces asymmetric errors, has been tested. The differences between the two methods have been found to be negligible.

The pulls and constraints for the nuisance parameters considered in the limit setting procedure for the search presented in this thesis are studied in the context of a fit of the likelihood function for the background-only hypothesis, $L(D|0, \hat{\hat{\boldsymbol{\theta}}}(0))$. In this *background-only fit*, the shape and normalisation of the $m_{t\bar{t}}^{\mathrm{reco}}$ distributions for the SM background prediction are adjusted within the systematic uncertainties by varying the nuisance parameters to achieve a better agreement with the distributions observed in data. Studying the outcome of this fit serves a dual purpose: first, the pulls provide information on the agreement between the predicted and observed distributions while the constraints are related to the statistical power of the data in the signal regions, as will be discussed below; second, the results of the fit can be used to adjust the reconstructed $t\bar{t}$ invariant mass distributions for the estimated SM background in light of the information gained by comparison to the distributions observed in data. The derivation of these **post-fit** $m_{t\bar{t}}^{\mathrm{reco}}$ spectra is described in the following section. Note that this procedure relies on the assumption that *no BSM signal* is present in the signal regions and that any discrepancy between the observed and expected distributions can be attributed to systematic and statistical uncertainties.

This assumption has been tested using the procedure described in Section 7.1 which showed no significant data excess or deficit with regard to the SM prediction.

The background-only fit is performed twice. First, the predicted background distributions are fitted to those observed in data. A second, independent fit is carried out in which the real data distributions are replaced by those for the nominal background prediction. This generic dataset, which represents the combined contribution of all background components in the signal regions, is referred to as the **Asimov dataset**.[7] Using the Asimov dataset, the nuisance parameter constraints can be studied separately from the pulls, the latter being zero by construction while the statistical power of the Asimov dataset is equivalent to that of the observed dataset.

The pulls and constraints for all 36 nuisance parameters considered in the limit setting procedure after the background-only fit are summarised in Figure 7.3. The units on the x-axis are chosen such that the values ± 1 correspond to the $\pm 1\sigma$ variations for a given systematic uncertainty before the fit. Before the fit, the pull values are zero by construction and the pre-fit constraints would be represented by markers centred at zero with error bars of unit length. The pulls obtained for the fit to the Asimov dataset are zero, as expected. The nuisance parameters are constrained to varying degrees: Some nuisance parameters, for example $t\bar{t}$ `EW virtual correction`, show little or no constraint, while the uncertainty on others, like $t\bar{t}$ `ISR/FSR` and $t\bar{t}$ `PS + fragmentation`, is reduced to around 25% of its initial value. The fit to the real dataset yields similar constraints. In addition various nuisance parameters are pulled away from zero, a consequence of the expected background distributions deviating slightly from those observed in data, especially in the range $m_{t\bar{t}}^{\text{reco}} > 1.5$ TeV (Figures 6.5–6.7).

To gain a better understanding of the pulls and constraints on the individual nuisance parameters, the background-only fit is repeated twice, using only the six channels for the resolved-topology selection and only the six channels for the boosted-topology selection, respectively. The resulting pulls and constraints are summarised in Figure 7.4. In general, the pulls and constraints are stronger in the case of the resolved-topology selection for which the total number of data events in the six signal channels amounts to 223,000 events, compared to 8,200 events for the six channels of the boosted-topology selection. The constraint on a single nuisance parameter can be explained qualitatively by the shape and size of the $\pm 1\sigma$ variations of the $m_{t\bar{t}}^{\text{reco}}$ spectrum before the fit. In the following, only a few selected nuisance parameters and their constraints are discussed in detail. The full set of figures showing the impact of the systematic

[7] The term, which refers to the short story "Franchise" by I. Asimov [295], is used, for example, in [289].

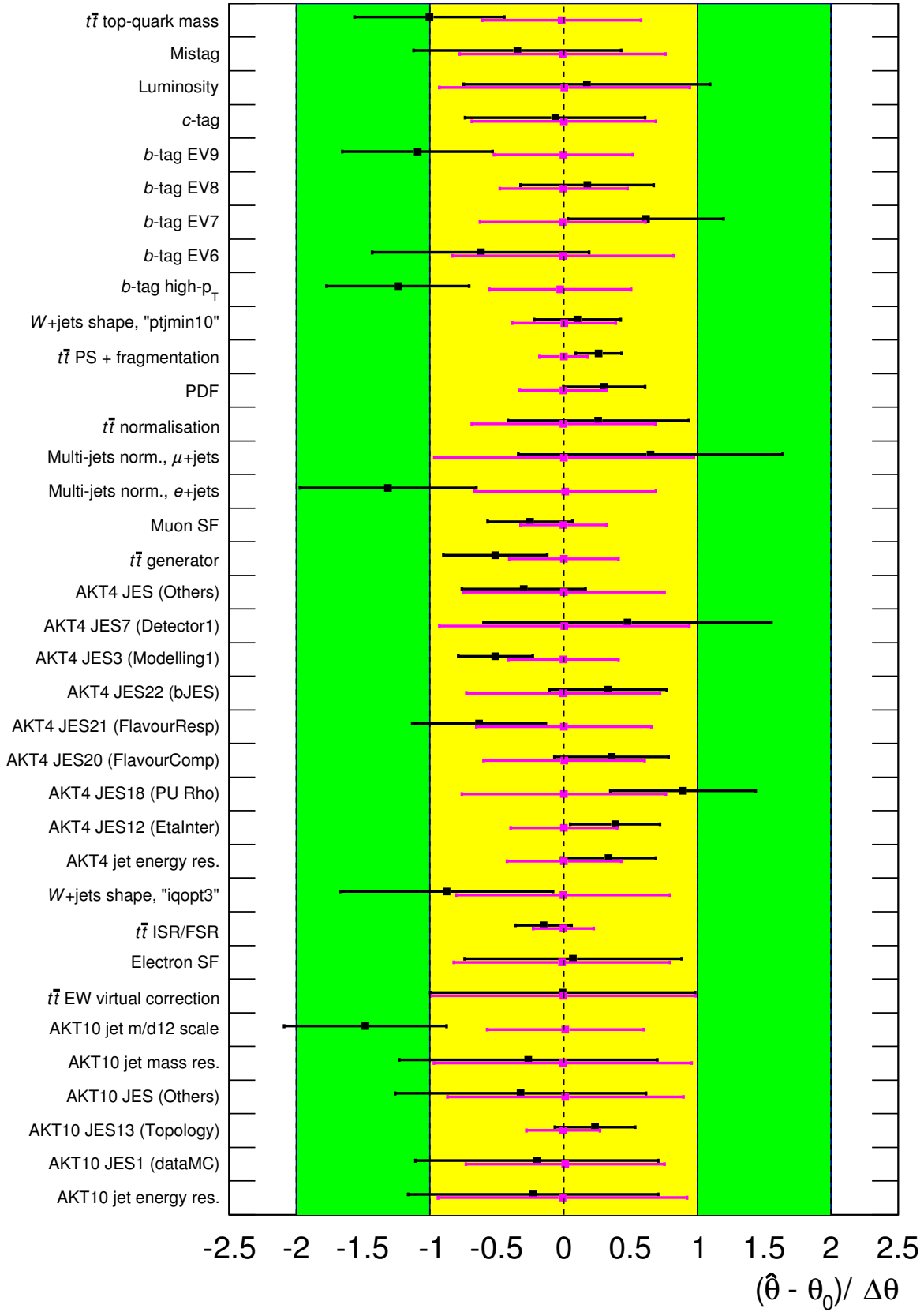

Figure 7.3.: Pulls and constraints for the 36 nuisance parameters considered in the statistical analysis after a profile likelihood fit to observed data (black) and Asimov data (magenta), respectively, under the background-only hypothesis. All twelve search channels are considered in the definition of the likelihood function. The central markers denote the pulls; the error bars represent the constraints. The units on the x-axis are chosen such that the values ± 1 correspond to the $\pm 1\sigma$ variations for a given systematic uncertainty before the fit. Documented in [2].

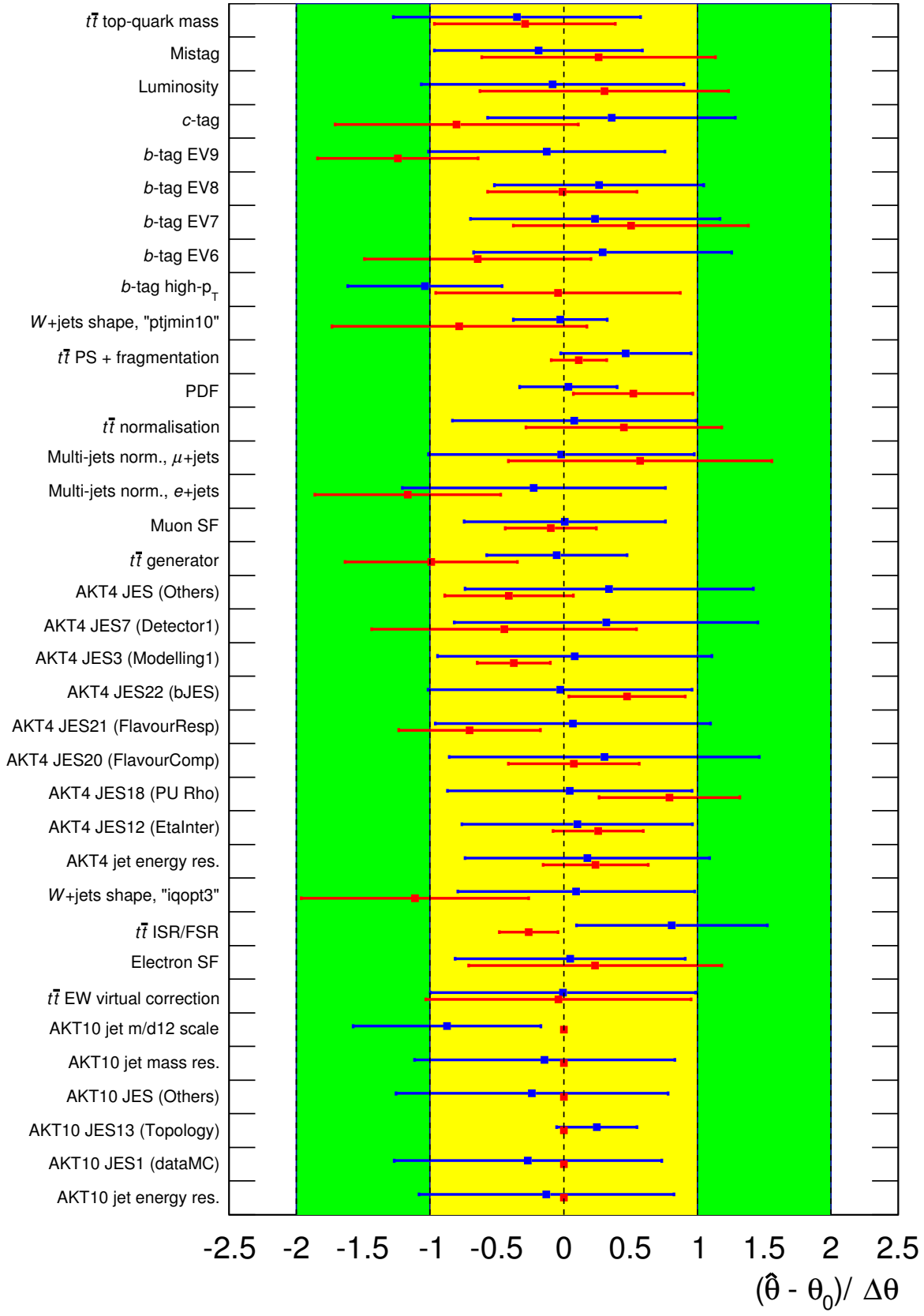

Figure 7.4.: Pulls and constraints for the 36 nuisance parameters considered in the statistical analysis after a profile likelihood fit to observed data under the background-only hypothesis. The red (blue) markers correspond to the case in which only the six channels of the resolved-topology (boosted-topology) selection are considered in the likelihood function. The central markers denote the pulls; the error bars represent the constraints. The units on the x-axis are chosen such that the values ± 1 correspond to the $\pm 1\sigma$ variations for a given systematic uncertainty before the fit. Documented in [2].

variations for all 36 nuisance parameters in the different channels is given in [2].

In the case of the resolved-topology selection, strong constraints are found for some of the nuisance parameters corresponding to systematic uncertainties of the SM $t\bar{t}$ background, the main background component. The impact of the systematic variations for the $t\bar{t}$ `ISR/FSR` and $t\bar{t}$ `PS + fragmentation` uncertainties in the e+jets and μ+jets channel is shown in Figures 7.5a–7.5b and Figures 7.5c–7.5d, respectively. The variations due to the $t\bar{t}$ `ISR/FSR` uncertainty are around 5% in the range $m_{t\bar{t}}^{\text{reco}} > 0.5$ TeV, and those due to the $t\bar{t}$ `PS + fragmentation` uncertainty amount to almost 10% for $m_{t\bar{t}}^{\text{reco}} < 0.5$ TeV. In both cases, the impact of the systematic variations in the respective mass ranges is significantly larger than the corresponding statistical uncertainty (indicated by the black error bars). Systematic uncertainties related to reconstructed objects can also be constrained considerably, as in the case of the `AKT4 JES3 (Modelling1)` uncertainty, which is reduced to around 25% of its initial value. Figures 7.5e–7.5f illustrate that the corresponding variations are of similar size and shape as in the case of the $t\bar{t}$ `ISR/FSR` uncertainty and thus considerably larger than the statistical precision.

The statistical power in the channels for the boosted-topology selection is smaller than in the case of the resolved topology, but still sufficient to constrain some of the more conservative systematic uncertainties such as the $t\bar{t}$ `generator` and the `AKT10 JES13 (Topology)` uncertainty. In the former case, the variations amount to only around 2% which is comparable to the statistical precision in the region of the maximum of the $m_{t\bar{t}}^{\text{reco}}$ distribution around 0.8 TeV (Figures 7.6a–7.6b). In the latter case, the variations are as large as 15% for $m_{t\bar{t}}^{\text{reco}} < 1.0$ TeV (Figures 7.6c–7.6d), a consequence of the conservative estimation of this systematic uncertainty, as described in the paragraph on the uncertainties related to large-R jets in Section 5.6.2. The effect of the variations for the b-`tag high-`p_T uncertainty is shown in Figures 7.6e–7.6f.

The impact of this conservative uncertainty, which is introduced due to the lack of reliable in-situ measurements of the b-tagging efficiency in the high-p_T regime (Section 5.6.2), increases steadily for $m_{t\bar{t}}^{\text{reco}} > 1.0$ TeV. The tension between observed data and the expected background increases over the same mass range, as illustrated in Section 6.1.3. This observation qualitatively explains the downward pull that is observed for the nuisance parameter of this uncertainty: Its shape matches that of the discrepancy between the observed and expected distributions. Hence a downward scaling of the expected background distribution, corresponding to a -1σ variation of the b-`tag high-`p_T uncertainty, improves the agreement with the observed data. This effect is discussed further in Sections 7.2.5 and 7.2.7.

It should be noted that, for the sake of simplicity, the effect of the systematic variations is only shown for the cases in which the three b-tagging categories for e+jets and μ+jets channels of the resolved- and boosted-topology selections are combined in the same plot. The separation into the individual b-tagging categories typically leads to tighter constraints than can be expected for an inclusive treatment of the three categories, as discussed in [2].

The profiling procedure not only leads to constraints on systematic variations; it also introduces **correlations** between them because the same dataset is used to constrain all 36 nuisance parameters in a single fit. The correlation matrix for the background-only fit to real data is shown in Figure 7.7. The diagonal elements are unity by construction and the correlations are small for the majority of nuisance parameter pairs. Anti-correlations are observed mostly for systematic uncertainties that have a similar impact on the shape of the $m_{t\bar{t}}^{\text{reco}}$ spectrum. To illustrate this effect, imagine two systematic variations that have identical effects on the mass spectrum, for example the `Luminosity` and $t\bar{t}$ `normalisation` uncertainties, which both correspond to a flat scaling of the mass distribution. An upward scaling of the overall spectrum can be achieved, for example, by a $+1\sigma$ variation of one nuisance parameter while keeping the other at its nominal value or by "up" variations of both nuisance parameters by an amount smaller than the $+1\sigma$ variation in each case. By the same logic, systematic uncertainties that have complementary effects on the mass spectrum, for example the `Electron SF` and `Muon SF` uncertainties, tend to be correlated.

7.2.4. Derivation of the Post-fit $t\bar{t}$ Invariant Mass Spectra

The results from the background-only fit described in the previous section are used to derive a set of **post-fit** $m_{t\bar{t}}^{\text{reco}}$ distributions, which reflect the improved knowledge of the shape and normalisation of the background estimate and its systematic uncertainties that is obtained from the fit to the observed data under the background-only hypothesis.

The nominal post-fit $m_{t\bar{t}}^{\text{reco}}$ histogram, $\tilde{h}_{j,k}^{(0)}$, for a given channel j and (signal or background) sample k is obtained from the corresponding **pre-fit** histogram $h_{j,k}^{(0)}$ as follows:

$$\tilde{h}_{j,k}^{(0)} = h_{j,k}^{(0)} + \sum_{(\text{NP})} x^{(\text{NP})} \cdot |I_{\text{lin}}(h_{j,k}^{(0)}, h_{j,k}^{(\text{NP}+)}, h_{j,k}^{(\text{NP}-)})|. \tag{7.23}$$

Here, $x^{(\text{NP})}$ is the pull (Equation 7.22) of the nuisance parameter $\theta^{(\text{NP})}$ after the background-only fit as given in Figure 7.3. The linear interpolation function I_{lin} is defined in Equation 7.18.

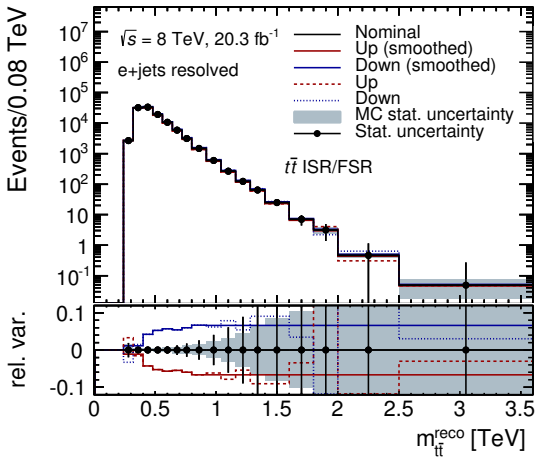

(a) $t\bar{t}$ `ISR/FSR`, e+jets channel, resolved topology

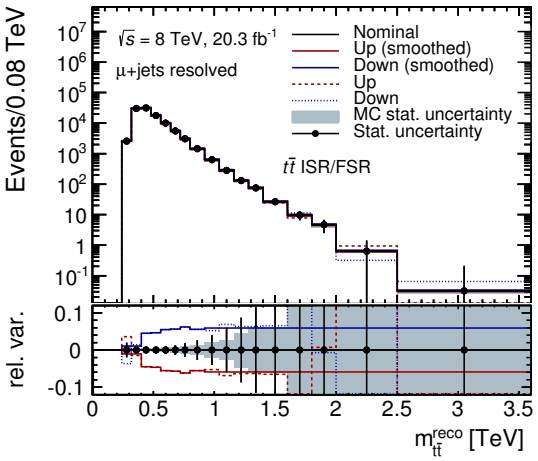

(b) $t\bar{t}$ `ISR/FSR`, μ+jets channel, resolved topology

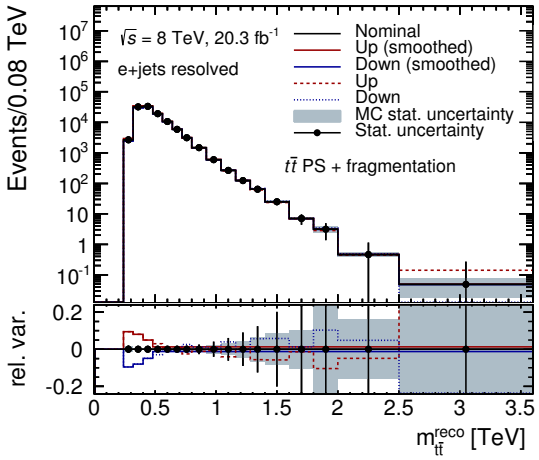

(c) $t\bar{t}$ `PS + fragmentation`, e+jets channel, resolved topology

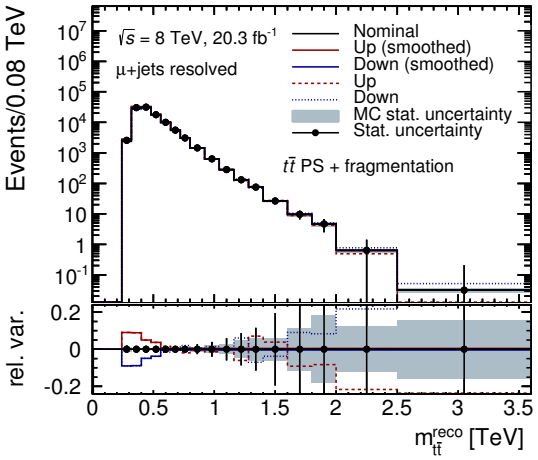

(d) $t\bar{t}$ `PS + fragmentation`, μ+jets channel, resolved topology

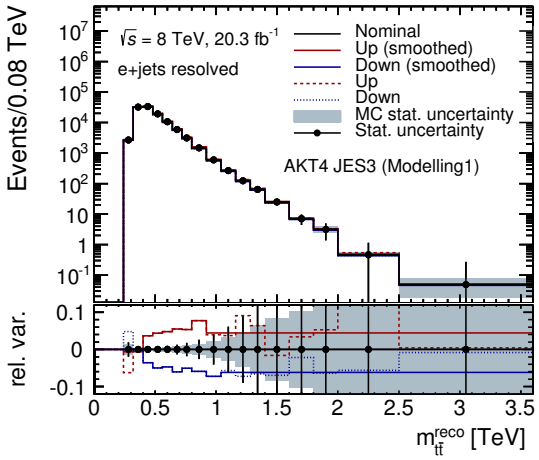

(e) `AKT4 JES3 (Modelling1)`, e+jets channel, resolved topology

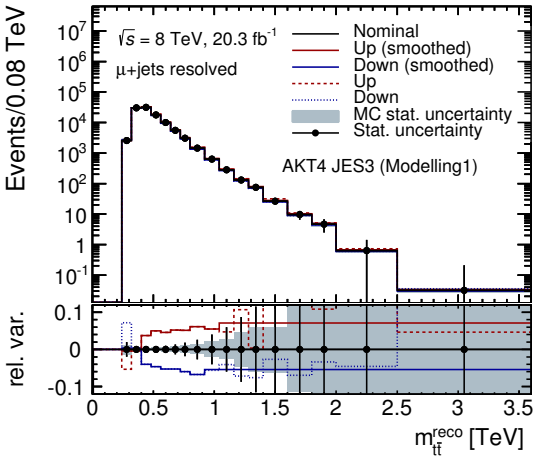

(f) `AKT4 JES3 (Modelling1)`, μ+jets channel, resolved topology

Figure 7.5.: Effect of selected systematic variations on the $m_{t\bar{t}}^{\text{reco}}$ spectrum for the e+jets (left) and μ+jets (right) channels of the resolved-topology selection with all b-tagging categories combined: (a)-(b) $t\bar{t}$ `ISR/FSR`, (c)-(d) $t\bar{t}$ `PS + fragmentation`, (e)-(f) `AKT4 JES3 (Modelling1)`.

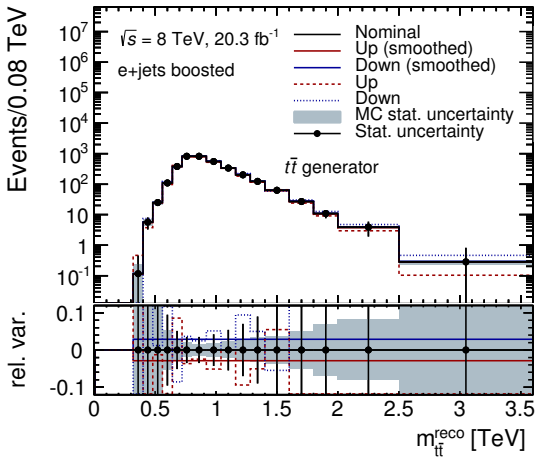

(a) $t\bar{t}$ `generator` , e+jets channel, boosted topology

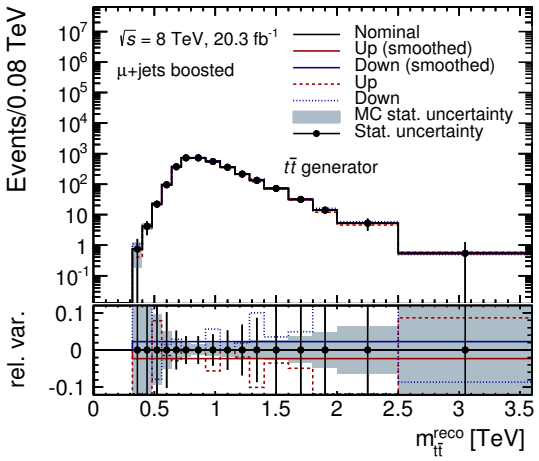

(b) $t\bar{t}$ `generator` , μ+jets channel, boosted topology

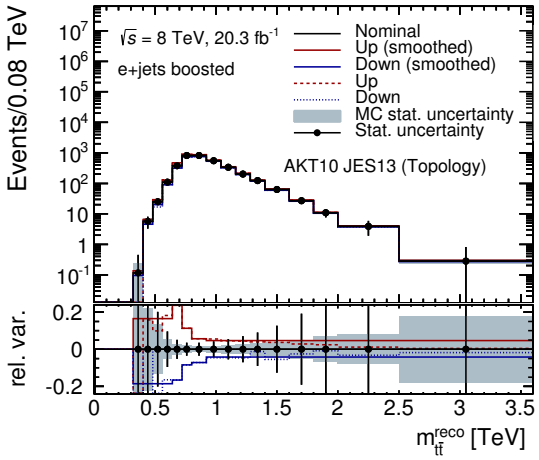

(c) `AKT10 JES13 (Topology)`, e+jets channel, boosted topology

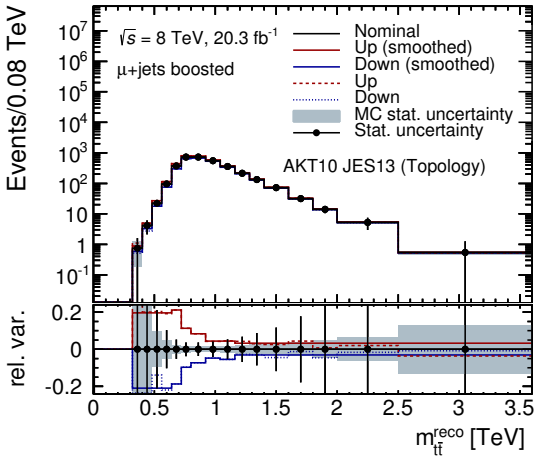

(d) `AKT10 JES13 (Topology)`, μ+jets channel, boosted topology

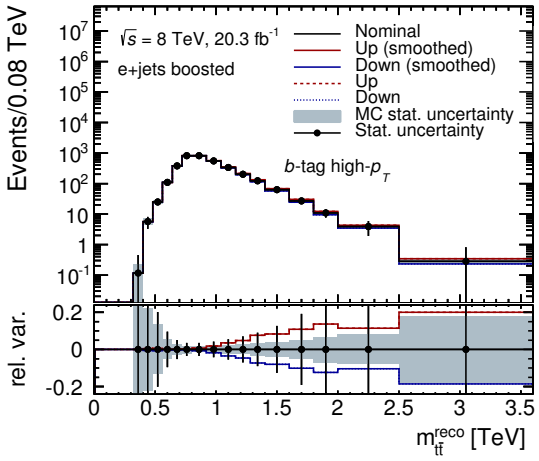

(e) b-`tag high-`p_T, e+jets channel, boosted topology

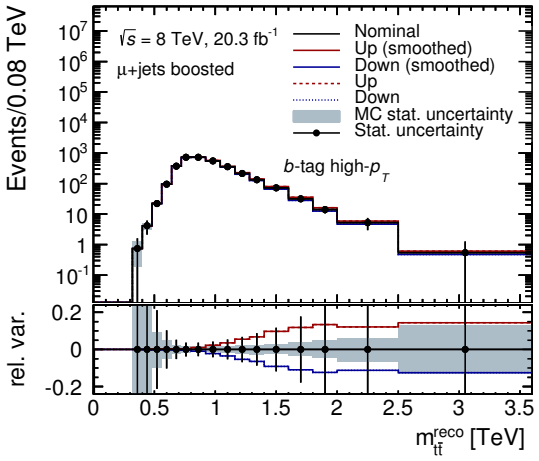

(f) b-`tag high-`p_T, μ+jets channel, boosted topology

Figure 7.6.: Effect of selected systematic variations on the $m_{t\bar{t}}^{\text{reco}}$ spectrum for the e+jets (left) and μ+jets (right) channels of the boosted-topology selection with all b-tagging categories combined: (a)-(b) $t\bar{t}$ `generator`, (c)-(d) `AKT10 JES13 (Topology)`, (e)-(f) b-`tag high-`p_T.

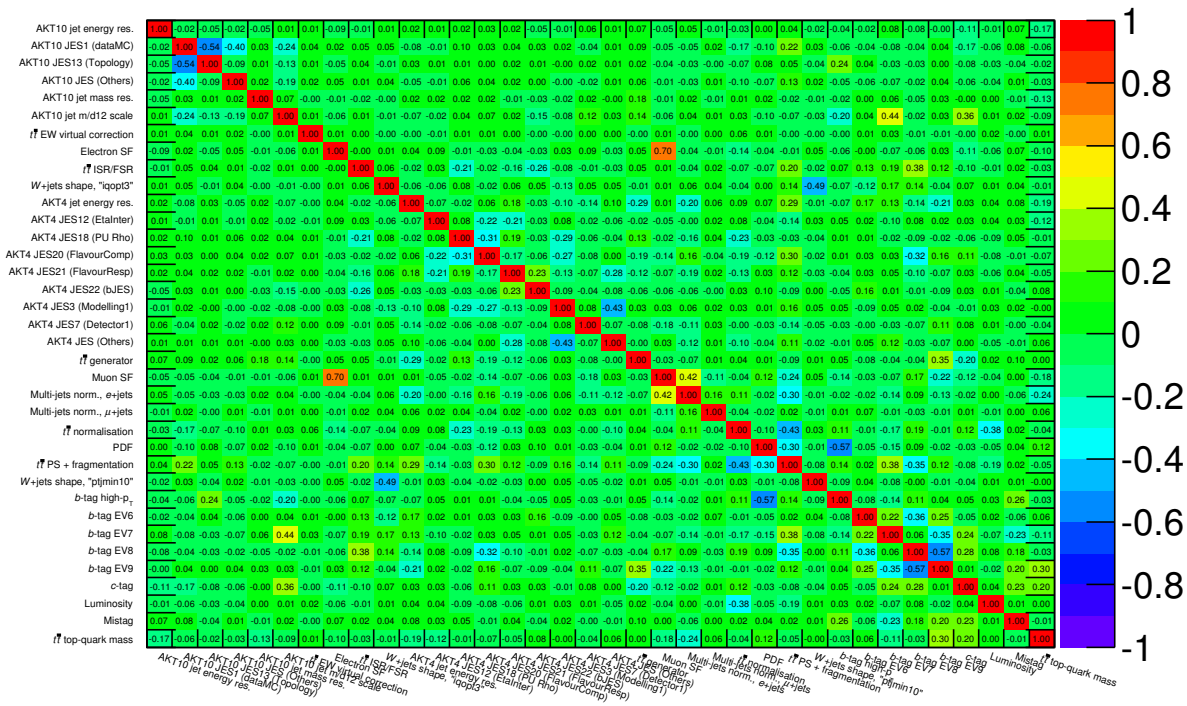

Figure 7.7.: Matrix showing the correlations of the constraints on the 36 nuisance parameters after the profile likelihood fit to observed data under the background-only hypothesis. The values on the colour scale range from -1.0 (100% anticorrelated) over 0.0 (uncorrelated) to 1.0 (100% correlated). Plot produced with `HistFitter`.

The second term in the equation is the sum of the relative (pre-fit) $\pm 1\sigma$ variations for the various systematic uncertainties, scaled by the respective post-fit pulls $x^{(\mathrm{NP})}$. If $x^{(\mathrm{NP})} = 0$ for some nuisance parameter, the corresponding systematic variation does not lead to a shift of the post-fit relative to the pre-fit distribution. Note that the pulls $x^{(\mathrm{NP})}$ may take negative values. Hence the systematic variations may lead to both upwards and downwards shifts of the post-fit compared to the pre-fit spectrum.

The total systematic uncertainty on the post-fit spectrum is derived from the uncertainties on the pulls, $\delta x^{(\mathrm{NP})}$, represented by the horizontal error bars in Figure 7.3, and the relative $\pm 1\sigma$ variations for the systematic uncertainties before the fit, which are defined as

$$\delta h_{j,k}^{(\mathrm{NP}+)} = h_{j,k}^{(\mathrm{NP}+)} - h_{j,k}^{(0)} \quad \text{and} \quad \delta h_{j,k}^{(\mathrm{NP}-)} = h_{j,k}^{(0)} - h_{j,k}^{(\mathrm{NP}-)}. \tag{7.24}$$

The uncertainties on the pulls quantify the constraints on these relative variations: If $\delta x^{(\mathrm{NP})} = 1$, the corresponding systematic uncertainty is not constrained. The case $\delta x^{(\mathrm{NP})} = 0.5$, for example, implies that the systematic variation is reduced by half.

The correlations between the uncertainties on the pulls are taken into account by the correlation matrix $\boldsymbol{\mathcal{C}}$ (Figure 7.7). The total systematic uncertainty after the background-only fit is then obtained from the expression

$$(\boldsymbol{v}^{\pm})^T \boldsymbol{\mathcal{C}} \boldsymbol{v}^{\pm}, \tag{7.25}$$

where the elements of the vector $\boldsymbol{v}^{\pm}$ are the histograms for the constrained relative systematic variations: $\delta x^{(\mathrm{NP})} \cdot \delta h_{j,k}^{(\mathrm{NP}\pm)}$. The two histograms described by Equation 7.25 represent the quadratic sum of the $\pm 1\sigma$ variations of all systematic uncertainties after the fit. The histograms for the $\pm 1\sigma$ variations of the total systematic uncertainty after the fit are straightforwardly obtained by taking the square-root of each bin.

The resulting post-fit $m_{t\bar{t}}^{\mathrm{reco}}$ spectra for the combination of the six channels for the boosted topology only, the six channels for the resolved topology only, and the combination of all twelve channels are shown in Figure 6.8 in Section 6.1.3 to allow for a direct comparison with the corresponding pre-fit spectra in Figure 6.7 in the same section. The overall uncertainty (grey bands) is visibly reduced in the post-fit compared to the pre-fit spectra. In addition, the background prediction in the post-fit spectra for $m_{t\bar{t}}^{\mathrm{reco}} \gtrsim 1.5$ TeV is slightly lower than in the pre-fit spectra. This is a consequence of the data yields being systematically lower than the expected background yields in this region. In the fit of the background prediction to the observed data, the

nuisance parameters are adjusted such that the predicted background yields in this region are scaled downwards to better match those observed in data. Overall, the observed data is found to agree with the post-fit background prediction within the *constrained* total uncertainty on the post-fit background estimate, although the tension between data and expected background distributions for $m_{t\bar{t}}^{\text{reco}} \gtrsim 1.5$ TeV is still visible in Figure 6.8c.

7.2.5. Impact of Systematic Uncertainties on the Signal Strength

The effect of the profiling procedure on the nuisance parameters has been discussed in the previous sections for a fit of the likelihood function *under the background-only hypothesis*. It has been shown that the number of observed data events in the signal regions is large enough to lead to considerable pulls and constraints on a number of nuisance parameters. In light of these results, it is reasonable to extend the studies on the effect of profiling to a fit of the likelihood function *under a signal+background hypothesis* $H_\mu^{(S+B)}$ in order to study the impact of the systematic uncertainties on the fitted value of the signal strength.

The impact is determined by the following procedure, which was first used in ATLAS in the measurement of the $t\bar{t}W$ and $t\bar{t}Z$ cross-section [296] and documented in [297]:[8] First, an unconditional maximum likelihood fit is performed in which both the signal strength μ and the nuisance parameters $\boldsymbol{\theta}$ are treated as fit parameters to obtain the unconditional MLEs $\hat{\mu}$ and $\hat{\boldsymbol{\theta}}$ (as used in the denominator of Equation 7.11). The likelihood fit is then repeated twice for each of the 36 nuisance parameters. In each case, the nuisance parameter in question is fixed to the value that corresponds to its $\pm 1\sigma$ variation with respect to the MLE, $\hat{\theta}^{(\text{NP})}$, from the initial, unconditional likelihood fit. The size of the $\pm 1\sigma$ variation is determined by the (constrained) uncertainty on the nuisance parameter from the unconditional likelihood fit. The difference $\Delta\hat{\mu} \equiv \hat{\mu}^{(\text{NP})\pm} - \hat{\mu}$ between the new fit value $\hat{\mu}^{(\text{NP})\pm}$ for the signal strength and its MLE $\hat{\mu}$ is defined as the **post-fit impact** of the systematic uncertainty described by the nuisance parameter under consideration. The **pre-fit impact** of the systematic uncertainties is determined in the same way by repeating the procedure with each of the nuisance parameters fixed to the (unconstrained) pre-fit $\pm 1\sigma$ variation with respect to the MLE $\hat{\theta}^{(\text{NP})}$.

The impact of the systematic uncertainties on the fitted signal strength is shown in Figure 7.8 for four representative signal mass points. Three Z' signal mass points, $m_{Z'} = 0.5$ TeV, $m_{Z'} = 1.0$ TeV and $m_{Z'} = 2.0$ TeV, are considered to compare the impact of the systematic uncertainties

[8] A number of minor, mostly technical, adjustments to the original algorithm were made to adapt it for use in the search presented in this thesis.

in different kinematic regions. A g_{KK} model with $m_{g_{KK}} = 2.0$ TeV and $\Gamma_{g_{KK}}/m_{g_{KK}} = 15.3\%$ is chosen for a comparison between a narrow and a broad resonance model. In all four cases, the input histograms for the signal distributions are normalised to a signal cross-section of 1 pb.

The systematic uncertainties that have the largest (post-fit) impact on the signal strength for the lowest signal mass point are those related to the JES of small-R jets (Figure 7.8a). This finding can be explained by the fact that the signal efficiency times acceptance in this kinematic regime is dominated by that for the resolved-topology selection (compare Figure 5.6) and is consistent with the results in Table 6.2, which also show a noticeable impact of these systematic uncertainties on the signal and background yields for the resolved-topology selection. In the case of the Z' signal with $m_{Z'} = 1.0$ TeV, both the boosted- and resolved-topology selection contribute to the overall signal efficiency times acceptance. The dominant systematic uncertainties in this case are those related to the JES and JMS of large-R jets as well as the b-`tag high-`p_T uncertainty (Figure 7.8b). The `AKT4 JES12 (EtaInter)` uncertainty, which was found to have the highest impact for $m_{Z'} = 0.5$ TeV, is ranked as the uncertainty with the sixth highest impact on the signal strength. The Z' and g_{KK} mass points with $m_X = 2.0$ TeV are of particular interest because this value of the resonance mass is close to the lower mass limits for these two resonance models (Section 7.2.6). The ranking of the systematic uncertainties are similar between both signal models (Figures 7.8c and 7.8d). For both signal models, the systematic uncertainty with the largest impact on the signal strength is the b-`tag high-`p_T uncertainty. Notably, the nuisance parameter for this uncertainty is found to have a significant downward pull of more than one (pre-fit) standard deviation and to be constrained to about half its initial variation. This effect is almost identical to that observed in the case of the background-only fit to data (Section 7.3).

7.2.6. Upper Limits on the Cross-section Times Branching Ratio

The observed and expected limits on the cross-section times branching ratio, $\sigma_X \times BR(X \to t\bar{t})$, for the four benchmark models considered in this thesis are shown in Figure 7.9, the corresponding numbers are listed in Table 7.5. All limits are upper exclusion limits at 95% CL and are derived using the CL_s method with the profile-likelihood based test statistic $\tilde{q}_\mu$ and its asymptotic approximation introduced in the previous sections. The expected limits are derived using Asimov data and thus represent the expected sensitivity of the search *before* the analysis of the observed data.

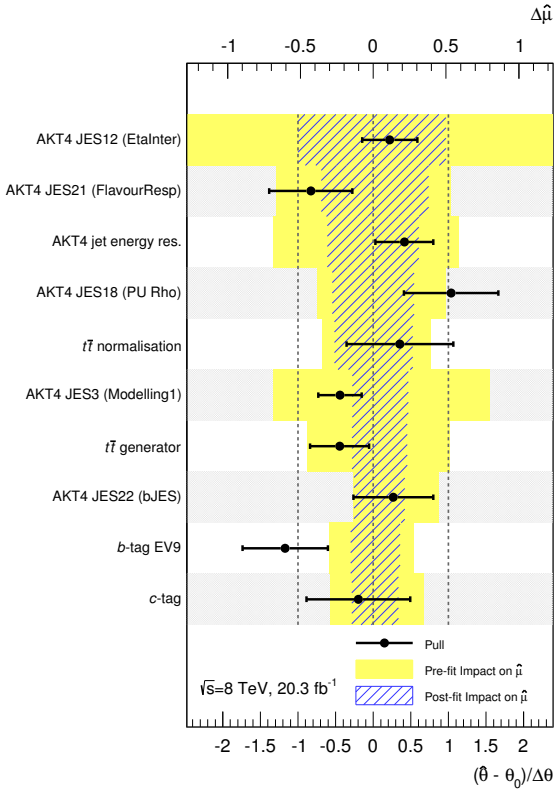

(a) Z' resonance, $m_{Z'} = 0.5$ TeV

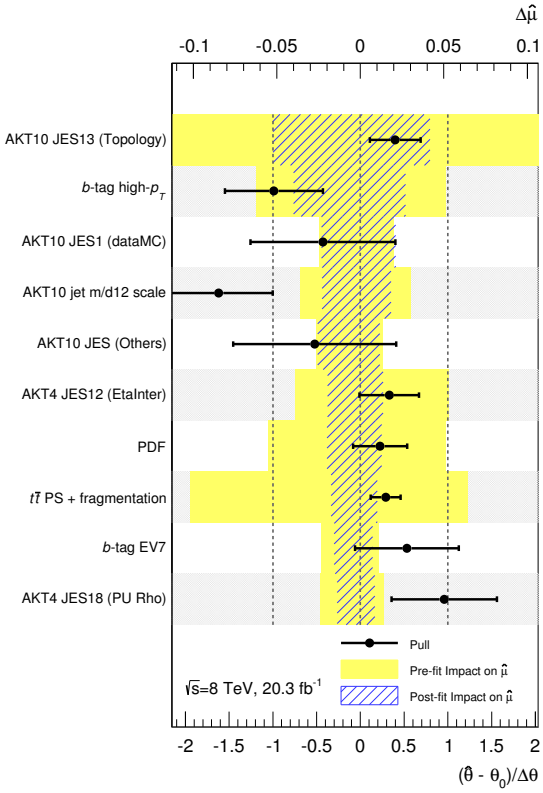

(b) Z' resonance, $m_{Z'} = 1.0$ TeV

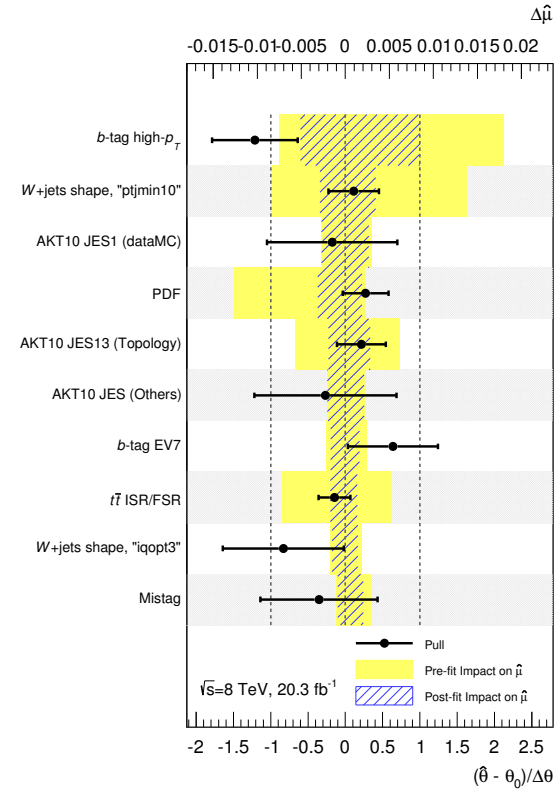

(c) Z' resonance, $m_{Z'} = 2.0$ TeV

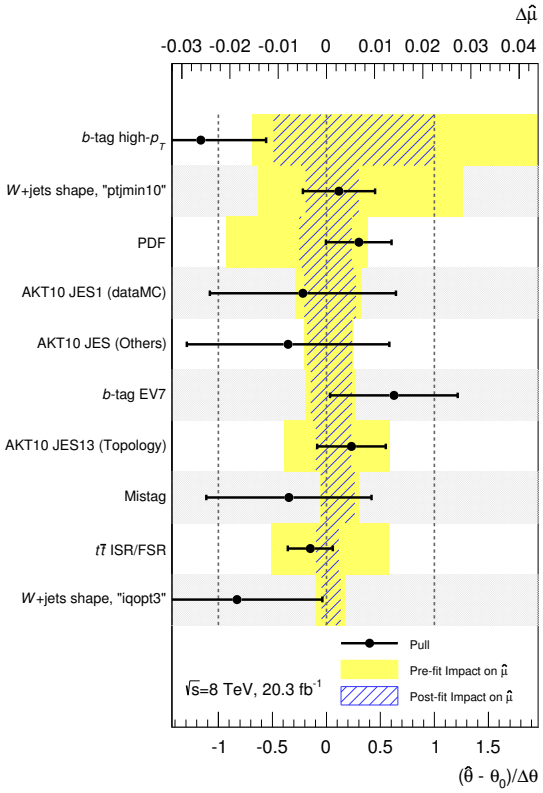

(d) g_{KK} resonance, $m_{g_{KK}} = 2.0$ TeV

Figure 7.8.: Ranking of the nuisance parameters based on their post-fit impact on the fitted value of the signal strength, $\hat{\mu}$, in a fit under the signal+background hypothesis for four representative signal mass points: (a) Z', $m_{Z'} = 0.5$ TeV, (b) Z', $m_{Z'} = 1.0$ TeV, (c) Z', $m_{Z'} = 2.0$ TeV, (d) g_{KK}, $m_{g_{KK}} = 2.0$ TeV. The grey (yellow) bands represent the post-fit (pre-fit) impact of the nuisance parameters (top axis). The pulls and constraints are also given (black markers, bottom axis). Only the ten nuisance parameters with the largest impact are shown. Documented in [2].

In the case of the topcolor-assisted technicolor Z'_{TC2} resonance, the observed upper limits range between 4.2 pb for $m_{Z'_{TC2}} = 0.4$ TeV and 0.03 pb for $m_{Z'_{TC2}} = 3.0$ TeV. The observed (expected) lower mass limit for a Z'_{TC2} resonance with a relative width of 1.2% is 1.8 TeV (2.0 TeV). Z'_{TC2} resonances with a relative width of 2.0% (3.0%), for which the predicted production cross-section is larger, are excluded for masses less than 2.0 TeV (2.3 TeV). For a Bulk RS Kaluza-Klein gluon g_{KK} with a relative width of 15.3%, the upper limits on $\sigma_X \times BR(X \to t\bar{t})$ lie between 4.8 pb for $m_{g_{KK}} = 0.4$ TeV and 0.09 pb for $m_{g_{KK}} = 3.0$ TeV. Mass values below 2.2 TeV (2.3 TeV) are observed (expected) to be excluded. The upper limits on $\sigma_X \times BR(X \to t\bar{t})$ for a Bulk RS Kaluza-Klein graviton G_{KK} are found to vary between 2.5 pb for $m_{G_{KK}} = 0.4$ TeV and 0.03 pb for $m_{G_{KK}} = 2.5$ TeV. No mass range has been excluded yet as the predicted cross-section times branching ratio for this model is roughly two orders of magnitude lower than in the case of the Z'_{TC2} and g_{KK} resonances. For a generic scalar resonance, upper cross-section limits of 3.0 pb for a mass of 0.4 TeV and of 0.03 pb for a mass of 3.0 TeV are obtained.

A comparison of the cross-section limits for the individual benchmark models shows that the limits are generally stronger for the scalar resonance and Bulk RS Kaluza-Klein graviton models. This is a result of the larger signal efficiency times acceptance for these resonances compared to the spin-1 Z'_{TC2} and g_{KK} resonances as discussed in Section 5.3.6.

Moreover, stronger limits on the cross-section times branching ratio are obtained for Z'_{TC2} compared to g_{KK} resonances as the larger width of the latter renders them harder to distinguish from the falling background distribution. The effect of the resonance width on the limits is illustrated in Figure 7.10 (with numbers listed in Table 7.6), where the observed and expected upper limits on $\sigma_X \times BR(X \to t\bar{t})$ are shown as a function of the relative width for three representative g_{KK} mass points. The limits weaken by roughly a factor of two for $m_{g_{KK}} = 1.0$ TeV as the width is increased from 10% to 40%. The effect is larger for the cases $m_{g_{KK}} = 2.0$ TeV and $m_{g_{KK}} = 3.0$ TeV for which the observed limits weaken by a factor of three as the width is increased. This mass dependence is a result of the fact that, for a fixed resonance width, the width of the reconstructed $t\bar{t}$ invariant mass distribution increases with the resonance mass due to FSR and the shape of the parton luminosity function, as discussed in Section 5.4.4. The impact of these effects increases with the resonance mass and width (see also Figure A.4 in the appendix).

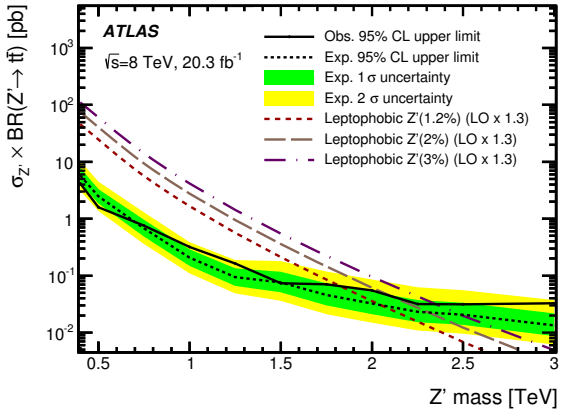

(a) Z', combination of boosted- and resolved-topology channels.

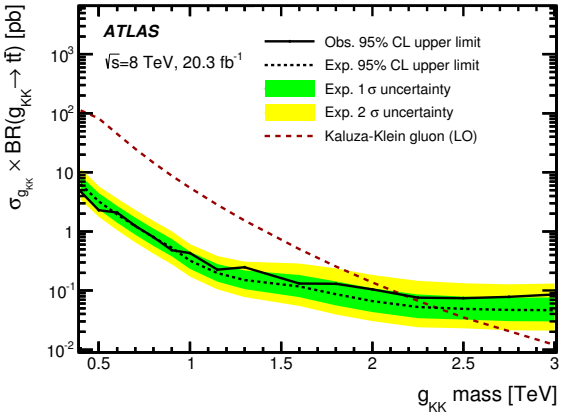

(b) g_{KK}, combination of boosted- and resolved-topology channels.

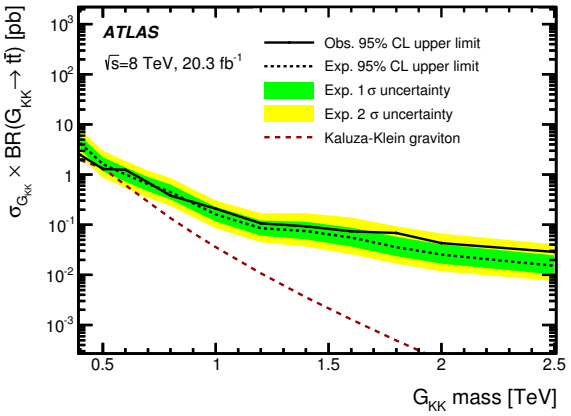

(c) G_{KK}, combination of boosted- and resolved-topology channels.

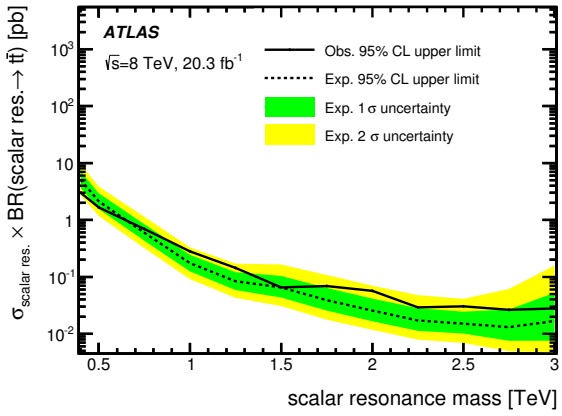

(d) Scalar resonance, combination of boosted- and resolved-topology channels.

Figure 7.9.: Observed and expected upper limits on the cross-section times branching ratio $\sigma_X \times BR(X \to t\bar{t})$ as a function of the resonance mass m_X for the four benchmark models: (a) Topcolor-assisted technicolor Z'_{TC2}, (b) Bulk RS Kaluza-Klein gluon g_{KK}, (c) Bulk RS Kaluza-Klein graviton G_{KK} and (d) scalar resonance. The expected limits are derived using the nominal background expectation in place of the observed data (*Asimov* expected limits). The predicted cross-sections for the respective signal processes are also shown. Published in [1].

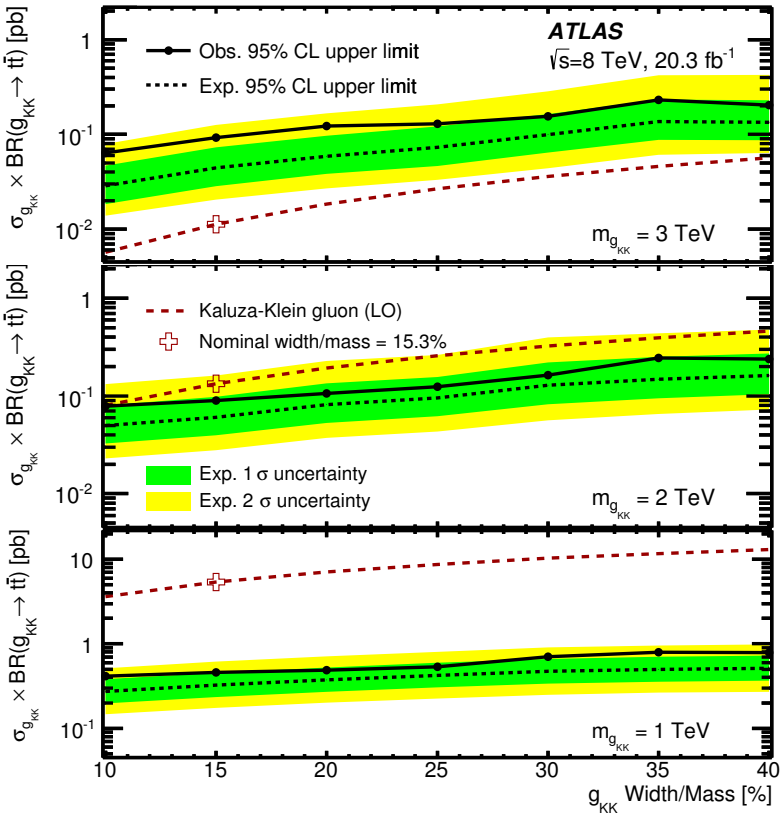

Figure 7.10.: Observed and expected upper limits on the cross-section times branching ratio $\sigma_{g_{KK}} \times BR(g_{KK} \rightarrow t\bar{t})$ as a function of the resonance width $\Gamma_{g_{KK}}/m_{g_{KK}}$ of the Bulk RS Kaluza-Klein gluon g_{KK} for three representative mass points: $m_{g_{KK}} = 1.0$ TeV, 2.0 TeV and 3.0 TeV. The expected limits are derived using the nominal background expectation in place of the observed data (*Asimov* expected limits). The predicted cross-sections for the respective signal processes are also shown. Published in [1].

Comparison of Upper Limits from the Boosted- and Resolved-Topology Channels

The upper cross-section limits discussed above have been derived by combining the search channels for two different event selection strategies, tailored towards the resolved and boosted event topologies, respectively, in order to maximise the sensitivity of the search across the whole $t\bar{t}$ invariant mass range between 0.4 TeV and 3.0 TeV. It is interesting to compare these limits with the expected limits that are obtained if only the six search channels for the boosted event topology or only the six channels for the resolved topology are considered in the likelihood function for the limit setting.

The resulting limit plot for a topcolor-assisted technicolor Z'_{TC2} model is shown in Figure 7.11. The corresponding numbers for the expected limits obtained from the combination of all twelve channels and those for the boosted- and resolved-topology selections[9] only are given in Table 7.4. In the region for $m_X < 0.9$ TeV, the sensitivity of the search is dominated by the channels for the resolved topology, although the combination with the channels for the boosted topology leads to a small improvement of the limits by around 4% even for the lowest mass point $m_{Z'} = 0.4$ TeV, compared to the case where only the resolved-topology channels are considered. For $m_X > 0.9$ TeV, the sensitivity is dominated by the channels for the boosted topology. The contribution of the channels for the resolved topology to the combined limits for the two highest mass points is negligible. Similar results are obtained for the other benchmark models.

The results demonstrate the importance of a search strategy tailored towards boosted top quarks for the resonance search in the high-mass regime. Without the boosted event selection, the expected upper limits on the production cross-section for the two highest mass points would be around two orders of magnitudes higher than the limits for the combination of all channels. The excluded mass range for the topcolor-assisted technicolor Z'_{TC2} model would also be significantly smaller, with mass values below 1.5 TeV excluded based on the resolved-topology channels only, compared to 2.0 TeV for the combination with the boosted-topology channels. This finding is particularly relevant with regard to the expected extension of the search range to higher resonance masses in Run 2 of the LHC, as it implies that sensitivity improvements in this high-mass regime depend almost exclusively on improvements of the selection and reconstruction techniques for boosted top quarks. Nevertheless, the traditional resolved-topology approach

[9] The limits for the resolved topology are obtained by applying the resolved-topology selection criteria with the exception of the veto on events that also pass the selection criteria for the boosted topology. The resolved-topology-only limits therefore reflect the limits that would be obtained in a search based purely on traditional resolved-topology selection and reconstruction criteria.

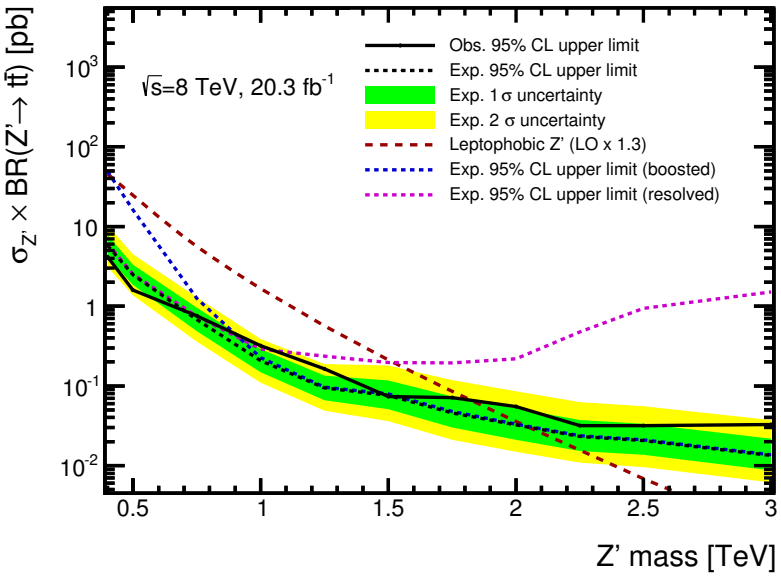

(a) Z'.

Figure 7.11.: Comparison of the combined upper limits on the cross-section times branching ratio for a topcolor-assisted technicolor Z'_{TC2} with the Asimov expected limits obtained by considering only the search channels for the boosted-topology selection (blue) and resolved-topology selection (magenta), respectively. The limits for the resolved topology are obtained without applying the veto on events passing the boosted-topology selection. Documented in [2].

remains relevant for future searches to be sensitive to potential BSM signals with resonance masses below 1 TeV.

Additional tests were carried out to quantify the improvements in the cross-section limits due to the introduction of the three exclusive b-tagging categories, defined in Section 5.4.5, which had not been used in previous iterations of the search. The (Asimov) expected limits for the nominal setup (*exclusive setup*) with twelve independent search channels have been compared to those obtained for the setup with only four independent channels, the e+jets and μ+jets channels for the resolved- and boosted-topologies without the additional b-tagging categorisation (*inclusive setup*). The cross-section limits for the boosted (resolved) topology with the exclusive setup are around 15% (10%) stronger than the corresponding limits for the inclusive setup [298].

7.2.7. Discussion

A comparison of the observed and expected cross-section limits, discussed in the previous section, shows that the former are systematically higher than the latter for large resonance masses. For $m_X \gtrsim 1.8$ TeV, the deviation is comparable to the $+1\sigma$ variation from the expected median. This result may seem counter-intuitive in light of the finding that the observed data yields in the

$m_{Z'}$ [TeV]	Exp. [pb]	Exp. (boosted only) [pb]	Exp. (resolved only) [pb]
0.40	5.897	43.109	6.157
0.50	2.453	14.581	2.531
0.75	0.675	1.281	0.752
1.00	0.215	0.238	0.290
1.25	0.106	0.111	0.236
1.50	0.101	0.109	0.196
1.75	0.071	0.076	0.194
2.00	0.056	0.057	0.219
2.25	0.044	0.044	0.476
2.50	0.042	0.041	0.942
3.00	0.028	0.028	1.512

Table 7.4.: Comparison of the combined upper limits on the cross-section times branching ratio for a topcolor-assisted technicolor Z'_{TC2} with the Asimov expected limits obtained by considering only the search channels for the boosted- and the resolved-topology selection, respectively. Included in [2].

$m_{t\bar{t}}^{\text{reco}}$ distributions are systematically lower than the background expectation for $m_{t\bar{t}}^{\text{reco}} \gtrsim 1.5$ TeV (Section 6.1.3), which would lead to the anticipation of the observed limits being stronger than the expected limits.

However, the profile likelihood fit in the derivation of the upper cross-section limits results in a downward scaling of the background expectation to better match the observed data in this kinematic region (Section 7.2.4). This is reflected in considerable negative pulls on a number of nuisance parameters, as observed in both the background-only fit (Section 7.2.3) and the fit under the signal+background hypothesis (Section 7.2.5). In the latter case, the nuisance parameter for the b-`tag high-`p_T uncertainty, which exhibits a downward pull of more than one (pre-fit) standard deviation, is found to play a key role as the nuisance parameter with the largest impact on the fitted signal strength for a resonance mass of $m_X = 2.0$ TeV.

The b-`tag high-`p_T uncertainty is related to reconstructed physics objects and must therefore be treated as fully correlated between any BSM signal and the SM background. This is reflected by the use of a single nuisance parameter for both signal and background in the profiling, as discussed in Section 7.2.2. Hence, a negative pull leads to a reduction of the efficiency for *both* BSM signal and SM background. The ratio of the post- and pre-fit signal efficiency in the boosted- and the resolved-topology selection for a Z' model as a function of $m_{Z'}$ is shown in Figure 7.12a. The signal efficiency for the boosted-topology selection after the profile likelihood fit is considerably lower than that before the fit, amounting to only around 75%

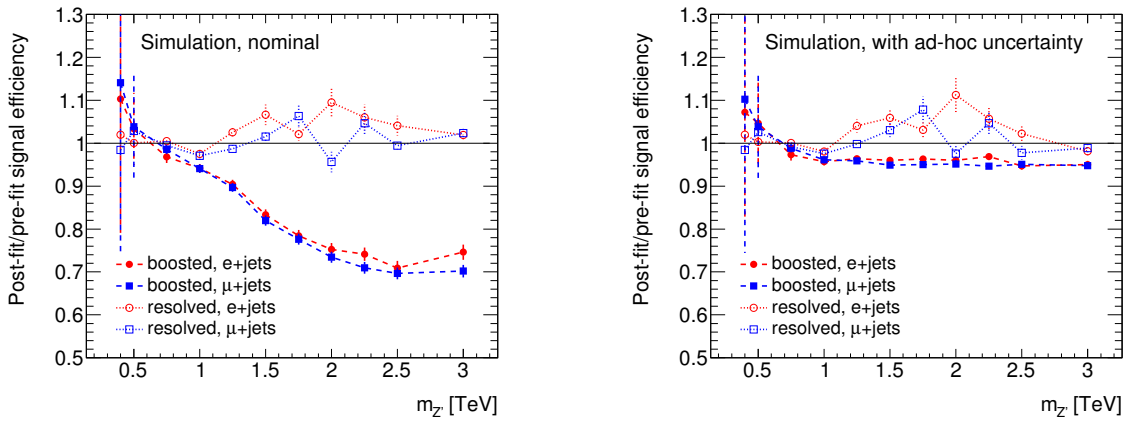

(a) **(b)**

Figure 7.12.: Ratio of the values for the signal efficiency after and before the likelihood fit under the signal+background hypothesis for a Z' model as a function of $m_{Z'}$ (a) for a profile likelihood fit with the nominal set of systematic uncertainties and (b) for a profile likelihood fit with an additional ad-hoc uncertainty on the SM $t\bar{t}$ background that has the same impact on the shape of the $m_{t\bar{t}}^{\text{reco}}$ distribution for this background as the b-`tag high-`p_T uncertainty. The error bars represent the statistical uncertainty on the efficiency ratio. Plots produced by the author. An equivalent plot to the one on the left can be found in [2].

for $m_{Z'} = 2.0$ TeV and around 70% for $m_{Z'} = 3.0$ TeV. The ratio of the post- and pre-fit signal efficiency for the resolved-topology selection, on the other hand, is close to unity. This is expected since the distributions observed in data agree well with those for the background expectation in the corresponding kinematic regime (Section 6.1.3) and significant negative pull values are found neither for the background-only fit of the resolved channels (Section 7.2.3) nor the signal+background fit for small resonance masses (Section 7.2.5).

The *ad-hoc* introduction of an additional, generic systematic uncertainty that applies to the SM $t\bar{t}$ background only and has the same impact on the shape of the $m_{t\bar{t}}^{\text{reco}}$ distribution for this background as the b-`tag high-`p_T uncertainty would allow for a downward scaling of the expected background without reducing the signal efficiency. This case is illustrated in Figure 7.12b.

However, there is no physical justification for the introduction of such a generic uncertainty. Nevertheless, the above considerations motivate further investigations regarding the introduction of an additional uncertainty on the SM $t\bar{t}$ background estimation that may account for the observed tension between data and the background prediction. As discussed in Section 3.4.2, the `hdamp` parameter of the POWHEG MC generator affects the shape of the p_T spectrum of the top quarks, which is harder in the simulation than in data for high p_T^{top}, as well as other kinematic distributions. The difference between the $m_{t\bar{t}}^{\text{reco}}$ spectra with the default value `hdamp` $= m_{top}$ and those with the previous default setting `hdamp` $= \infty$ can be taken as an additional uncertainty

on the SM $t\bar{t}$ background.

Alternatively, it is possible to reweight the simulated events such that the p_T spectrum of the top quarks for the MC sample matches that in data. Such a reweighting procedure has been applied in various analyses by both the ATLAS and CMS collaborations, as discussed in further detail in Chapter 8. In the analysis presented in this thesis, no p_T^{top} reweighting is used due to the fact that the weights that were available at the time the analysis was completed had been derived from a measurement of the $t\bar{t}$ differential cross-section at $\sqrt{s} = 7$ TeV. This raised concerns about both the applicability of these weights at $\sqrt{s} = 8$ TeV and similarities in the definition of the signal regions of both analyses. While no reweighting is applied in the case of the nominal $m_{t\bar{t}}^{\text{reco}}$ spectra, the difference between the nominal spectra and those obtained with a p_T^{top} reweighting applied can be taken as an additional uncertainty on the SM $t\bar{t}$ background.

The profile likelihood fit and limit setting procedure were repeated for each of the two cases, taking into account the additional uncertainty on the SM $t\bar{t}$ background as an extra nuisance parameter. In both cases, the effect of the additional nuisance parameter on the exclusion limits was found to be negligible and the negative pull on the nuisance parameter for the b-`tag high-`p_T uncertainty remained almost unchanged.

Eventually, no approach that would have allowed for the mitigation of the effects of the negative pull for the b-`tag high-`p_T uncertainty on the signal efficiency and the observed upper cross-section limit was found.

Additional tests were carried out, in collaboration with the ATLAS Flavour Tagging Group, to study the reliability of the extrapolation of the flavour tagging scale factors, derived through in-situ measurements on jets with $p_T^{\text{jet}} < 300$ GeV, to jets with larger transverse momenta (Section 5.6.2). The aim was to test the possibility of the pull on the b-`tag high-`p_T uncertainty being a result of a mis-modelling of the extrapolated scale factors. Such a mis-modelling would not only lead to a non-unity ratio of the observed and expected $m_{t\bar{t}}^{\text{reco}}$ distributions, it would also affect this ratio differently in the three b-tagging categories. The double ratios constructed from the data/MC ratio distributions for all pairs of b-tagging categories were found to be consistent with unity in all channels [299]. The scale factor extrapolation is therefore deemed reliable, indicating that the large pull on the nuisance parameter for the b-`tag high-`p_T uncertainty is not caused by a mismodelling of the b-tagging scale factors for high-p_T jets or their uncertainties.

It should also be noted that there are on-going efforts within the ATLAS Flavour Tagging

Group that are aimed at reducing the uncertainty on the scale factor extrapolation as well as the need for extrapolation scale factors by extending the kinematic range of the in-situ measurements [259]. In particular, a new calibration method, which relies on $t\bar{t}$ events and is tailored especially towards high-p_T b-jets in dense decay topologies is currently being tested within ATLAS [236]. A reduction of the scale factor extrapolation uncertainty is expected to reduce both the constraints on and the impact of the corresponding nuisance parameter in the profile likelihood fit.

The expected upper limits on the cross-section times branching ratio shown in the previous section have been derived from the background expectation after a profile likelihood fit to the *Asimov dataset*. An alternative set of expected limits, which has been derived from the background expectation after a profile likelihood fit to the *observed dataset* and reflects the effects of the non-zero nuisance parameter pulls, has been derived for comparison. In Figure 7.13, the expected limit from the profile likelihood fit to the observed dataset (dashed blue line) is overlaid on the expected and observed limits for a topcolor-assisted technicolor Z'_{TC2} boson, which have been shown in Figure 7.9a in the previous section. It is in good agreement with the observed limit, reflecting the improved agreement between the observed data and the background expectation after the profile likelihood fit.

7.3. Summary

The distributions of the invariant mass of the reconstructed $t\bar{t}$ pair that are observed in data have been compared to those predicted by the SM in twelve mutually exclusive signal regions. Different reconstruction approaches are used for the resolved and boosted $t\bar{t}$ decay topologies to achieve optimal sensitivity over a large $t\bar{t}$ invariant mass range between 0.4 TeV and 3.0 TeV. The full dataset collected by the ATLAS detector at $\sqrt{s} = 8$ TeV in 2012, which corresponds to an integrated luminosity of 20.3 fb^{-1}, has been analysed. No significant deviation from the SM prediction and hence no evidence for resonant $t\bar{t}$ production through BSM processes is found. Upper limits on the cross-section times branching ratio to $t\bar{t}$ final states have been derived for BSM resonances of different spin, mass and width that are predicted by four different benchmark models: a topcolor-assisted technicolor Z' boson, a Bulk RS Kaluza-Klein gluon, a Bulk RS Kaluza-Klein graviton, and a generic scalar resonance. Based on these limits, the existence of a topcolor-assisted technicolor Z'_{TC2} resonance with a width of 1.2% is excluded at 95% CL for resonance masses in the range between 0.4 TeV and 1.8 TeV. The existence of a

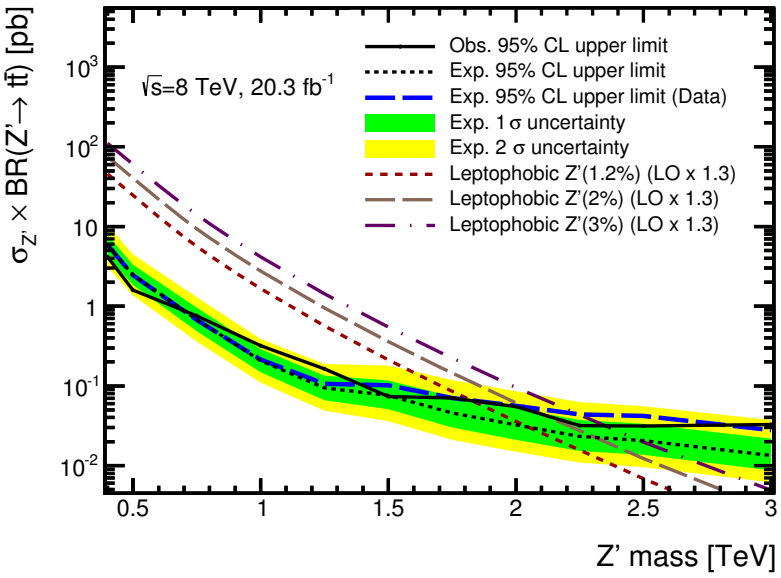

(a) Z'.

Figure 7.13.: Observed and expected upper limits on the cross-section times branching ratio $\sigma_X \times BR(X \to t\bar{t})$ as a function of the resonance mass m_X for a topcolor-assisted technicolor Z'_{TC2} boson. The expected limits obtained from the predicted background after a profile likelihood fit to observed data are shown (dashed blue line) in addition those obtained from a fit to the Asimov dataset. Included in [2].

Bulk RS Kaluza-Klein gluon g_{KK} with a relative width of 15.3% is excluded at 95% CL over the resonance mass range 0.4 TeV $< m_{g_{KK}} <$ 2.2 TeV.

Mass [TeV]	Obs. [pb]	Exp. [pb]	Exp.-1σ [pb]	Exp.+1σ [pb]
0.40	4.169	5.750	4.194	7.863
0.50	1.594	2.486	1.849	3.307
0.75	0.756	0.682	0.487	0.956
1.00	0.320	0.206	0.148	0.288
1.25	0.163	0.094	0.066	0.135
1.50	0.074	0.076	0.051	0.118
1.75	0.071	0.046	0.030	0.073
2.00	0.055	0.032	0.021	0.052
2.25	0.032	0.023	0.015	0.037
2.50	0.031	0.021	0.014	0.033
3.00	0.033	0.013	0.009	0.022

(a) Z'

Mass [TeV]	Obs. [pb]	Exp. [pb]	Exp.-1σ [pb]	Exp.+1σ [pb]
0.40	4.755	6.341	4.595	8.750
0.50	2.283	3.242	2.361	4.446
0.60	2.079	1.946	1.400	2.720
0.70	1.237	1.223	0.880	1.716
0.80	0.805	0.796	0.570	1.119
0.90	0.484	0.531	0.381	0.746
1.00	0.431	0.322	0.233	0.454
1.15	0.226	0.198	0.142	0.280
1.30	0.249	0.150	0.105	0.218
1.60	0.131	0.117	0.077	0.184
1.80	0.130	0.086	0.056	0.142
2.00	0.105	0.066	0.043	0.109
2.25	0.076	0.052	0.034	0.086
2.50	0.074	0.049	0.032	0.079
2.75	0.079	0.047	0.030	0.076
3.00	0.086	0.047	0.030	0.077

(b) g_{KK}

Mass [TeV]	Obs. [pb]	Exp. [pb]	Exp.-1σ [pb]	Exp.+1σ [pb]
0.40	2.476	4.252	3.101	5.913
0.50	1.303	1.614	1.168	2.219
0.60	1.243	1.009	0.728	1.395
0.70	0.670	0.649	0.466	0.902
0.80	0.382	0.450	0.321	0.634
0.90	0.284	0.267	0.192	0.375
1.00	0.209	0.161	0.116	0.227
1.20	0.107	0.085	0.060	0.123
1.40	0.093	0.075	0.051	0.114
1.50	0.074	0.055	0.036	0.088
1.80	0.069	0.036	0.024	0.057
2.00	0.043	0.025	0.017	0.041
2.50	0.029	0.015	0.010	0.025

(c) G_{KK}

Mass [TeV]	Obs. [pb]	Exp. [pb]	Exp.-1σ [pb]	Exp.+1σ [pb]
0.40	3.011	5.118	3.688	7.105
0.50	1.666	2.141	1.562	2.933
0.75	0.697	0.599	0.430	0.839
1.00	0.281	0.174	0.125	0.243
1.25	0.144	0.084	0.059	0.121
1.50	0.065	0.066	0.044	0.104
1.75	0.069	0.039	0.025	0.064
2.00	0.057	0.025	0.017	0.042
2.25	0.029	0.017	0.011	0.028
2.50	0.030	0.015	0.010	0.024
2.75	0.026	0.013	0.008	0.027
3.00	0.028	0.017	0.008	0.053

(d) Scalar

Table 7.5.: Observed and expected upper limits on the cross-section times branching ratio $\sigma_X \times BR(X \to t\bar{t})$ as a function of the resonance mass m_X for the four benchmark models: (a) Topcolor-assisted technicolor Z'_{TC2}, (b) Bulk RS Kaluza-Klein gluon g_{KK}, (c) Bulk RS Kaluza-Klein graviton G_{KK} and (d) scalar resonance. The expected limits are derived using the nominal background expectation in place of the observed data (*Asimov* expected limits). Numbers have been documented in [2].

Width/Mass [%]	Obs. [pb]	Exp. [pb]	Exp.-1σ [pb]	Exp.+1σ [pb]
10	0.416	0.273	0.196	0.382
15	0.458	0.326	0.234	0.455
20	0.489	0.375	0.270	0.524
25	0.533	0.424	0.304	0.595
30	0.702	0.471	0.337	0.665
35	0.799	0.499	0.356	0.702
40	0.789	0.515	0.368	0.725

(a) g_{KK} 1 TeV

Width/Mass [%]	Obs. [pb]	Exp. [pb]	Exp.-1σ [pb]	Exp.+1σ [pb]
10	0.078	0.050	0.033	0.080
15	0.090	0.061	0.040	0.098
20	0.107	0.082	0.053	0.134
25	0.124	0.095	0.062	0.156
30	0.164	0.129	0.082	0.221
35	0.245	0.148	0.094	0.251
40	0.239	0.162	0.104	0.272

(b) g_{KK} 2 TeV

Width/Mass [%]	Obs. [pb]	Exp. [pb]	Exp.-1σ [pb]	Exp.+1σ [pb]
10	0.064	0.029	0.018	0.047
15	0.093	0.044	0.028	0.073
20	0.123	0.059	0.038	0.097
25	0.129	0.073	0.047	0.122
30	0.156	0.100	0.065	0.165
35	0.232	0.137	0.088	0.233
40	0.205	0.135	0.087	0.229

(c) g_{KK} 3 TeV

Table 7.6.: Observed and expected upper limits on the cross-section times branching ratio $\sigma_{g_{KK}} \times BR(g_{KK} \rightarrow t\bar{t})$ as a function of the resonance width $\Gamma_{g_{KK}}/m_{g_{KK}}$ of the Bulk RS Kaluza-Klein gluon g_{KK} for three representative mass points: $m_{g_{KK}}$ = 1.0 TeV, 2.0 TeV and 3.0 TeV. The expected limits are derived using the nominal background expectation in place of the observed data (*Asimov* expected limits). Numbers have been documented in [2].

8. Conclusion

In this thesis, a search for new, massive resonances decaying to a top-antitop ($t\bar{t}$) pair in the ℓ+jets channel has been presented. The search has been carried out on the full dataset collected by the ATLAS experiment in 2012 in pp collisions at the LHC at a centre-of-mass energy of $\sqrt{s} = 8$ TeV. The dataset corresponds to an integrated luminosity of 20.3 fb^{-1}. The search focuses on the distributions of the invariant mass of the reconstructed $t\bar{t}$ pair in the range 0.4–3.0 TeV, which are analysed for deviations between observed data and the SM expectation.

Two different strategies for the selection and reconstruction of $t\bar{t}$ events in the ℓ+jets channel in different kinematic regimes are combined to optimise the sensitivity of the search over the whole $t\bar{t}$ invariant mass range under consideration (Section 5.1). The resolved-topology selection and reconstruction is tailored towards events in which the hadronic showers initiated by the decay products of the hadronically decaying top quark are well separated in the detector and can be reconstructed as three individual jets with small R parameter. The boosted-topology selection and reconstruction, in contrast, are optimised for events in which these showers are merged into a single, large-R jet with a characteristic substructure.

The combination of these two strategies is motivated by the fact that the angular separation between the decay products of the top quark in the detector frame decreases with increasing transverse momentum of the top quark, such that the decay products appear collimated in the direction of the top quark and are likely to overlap or merge at large transverse momenta.

The collimation of the decay products is also reflected in the selection and reconstruction criteria for the semileptonically decaying top quark: Leptons are required to be isolated based on the transverse momentum sum of all tracks in an isolation cone around the lepton with a radius that decreases proportionally to the inverse of the lepton transverse momentum. This mini-isolation definition has already been used in previous iterations of this search [174, 39]. Furthermore, the treatment of overlap between leptons and jets has been optimised with regard to the increasing collimation of the decay products from the semileptonically decaying top quark: The lower

bound on the allowed separation between a muon and a jet, which was set to a fixed value in previous iterations of the search, has been replaced by a threshold that depends on the muon transverse momentum, allowing the minimum separation between the muon and the jet to shrink with increasing transverse momentum of the muon. Moreover, the search presented in this thesis is the first ATLAS analysis that uses electrons reconstructed within small-R jets to increase the efficiency of the event selection in the boosted regime (Section 5.2.3).

Further improvements to the analysis strategy, compared to previous iterations of this search, include the use of scale factors for simulated SM $t\bar{t}$ events to take into account higher-order electroweak corrections to the $t\bar{t}$ kinematics (Section 3.4.2), the use of a large-R jet trigger in the delayed data stream to enhance the overall signal efficiency times acceptance in the μ+jets channel (Section 5.3.2), and the introduction of an additional selection requirement for the resolved topology, which relies on the outcome of the χ^2 fit for the reconstruction of the $t\bar{t}$ system (Section 5.4.3) to improve the purity of events with a $t\bar{t}$ pair in the final state by rejecting non-$t\bar{t}$ background events. The introduction of three exclusive b-tagging categories in the definition of the signal regions yields an improvement in the expected cross-section limits of 10-15% (Section 7.2.6), but it also significantly increases the complexity of the statistical analysis (Section 7.2). A re-evaluation of the benefits of this additional b-tagging categorisation is recommended with regard to future searches.

Finally, two new benchmark models, a Bulk RS Kaluza-Klein graviton (spin 2) and a scalar resonance, have been introduced in addition to the spin-1 models, a Z' boson and a Bulk RS Kaluza-Klein gluon, that were already used in previous iterations of the search. While the same scalar resonance model has also been considered by the CMS collaboration in a search for resonant $t\bar{t}$ production in the fully hadronic and ℓ+jets final states at $\sqrt{s} = 8$ TeV [130], the search presented in this thesis is the first search at the LHC to consider a Bulk RS Kaluza-Klein graviton decaying to $t\bar{t}$ (Section 2.5.3). The new benchmark models allow for the search results to be interpreted in the context of a wider range of BSM models with resonances decaying to $t\bar{t}$, as they allow for a comparison of the signal efficiency times acceptance and sensitivity of the search to resonances with different spins. In addition, this search includes the first systematic study of the dependence of the upper cross-section limits on the resonance width (Section 7.2.6).

No significant deviation between observed data and the SM prediction has been found in the reconstructed $t\bar{t}$ invariant mass distributions for the twelve channels considered in the search. Upper limits on the cross-section times branching ratio to $t\bar{t}$ have been derived for all benchmark

models. In total, upper limits have been derived for 73 mass and width points. 36 sources of systematic uncertainties have been taken into account in the search and limit setting stages.

The limits are found to be comparable to those obtained in the previous iteration of this analysis, a search using 14 fb^{-1} of $\sqrt{s} = 8$ TeV collision data, with a topcolor-assisted technicolor Z'_{TC2} boson excluded below 1.8 TeV at 95% CL in both cases [174]. A Bulk RS Kaluza-Klein gluon with a relative width of 15.3% is excluded below 2.2 TeV in the search presented in this thesis compared to 2.0 TeV in the previous search. The exclusion limits for the topcolor-assisted technicolor Z'_{TC2} boson are weaker than the most stringent limits available to date, set by the CMS collaboration in a search using 19.7 fb^{-1} of $\sqrt{s} = 8$ TeV and relying on all three $t\bar{t}$ decay channels [45]. In this case, a Z'_{TC2} resonance is excluded at 95% CL in the mass range below 2.4 TeV. A previous, preliminary search conducted by the CMS collaboration on the same dataset, relying on the ℓ+jets channel alone, lead to the exclusion of masses below 2.1 TeV [300]. This is comparable to the *expected* mass limits obtained in the search presented in this thesis, with a topcolor-assisted technicolor Z'_{TC2} boson *expected* to be excluded at 95% CL in the mass range below 2.0 TeV.

The reason for the discrepancy between observed and expected limits has been traced to a pull on the nuisance parameter for the b-`tag high-`p_T extrapolation uncertainty, which is shifted downwards by around one standard deviation and constrained to around half the size of the original uncertainty during the likelihood fit, causing a reduction of the signal efficiency by more than 25% for resonances masses greater than 2.0 TeV (Section 7.2.7). This pull is related to a shape difference between the $t\bar{t}$ invariant mass distributions observed in data and those expected based on SM predictions in the kinematic region with $m_{t\bar{t}}^{\text{reco}} \gtrsim 1.5$ TeV, where the expected event yields per bin are systematically larger than the observed ones (Section 6.1.3), an effect that is also visible in measurements of the $t\bar{t}$ differential cross-section as a function of $m_{t\bar{t}}$ [301, 302]. A similar tension between data and simulated distributions has been observed in measurements of the differential $t\bar{t}$ production cross-section as a function of the transverse momentum of the top quarks, which have been conducted by the ATLAS and CMS collaborations at $\sqrt{s} =$ 7 TeV [301, 303] and $\sqrt{s} = 8$ TeV [172, 302]. Both collaborations have relied on reweighting procedures for simulated SM $t\bar{t}$ events in various searches and measurements [304, 305, 306, 307] to correct the simulated samples for this discrepancy in the transverse momentum distribution.

While such a reweighting procedure may also reduce the tension in the $m_{t\bar{t}}^{\text{reco}}$ distributions, it is not a satisfactory solution: It is important to understand the cause for the observed discrepancies

in the measured and simulated $m_{t\bar{t}}^{\text{reco}}$ and p_T^{top} distributions. First systematic comparisons of different MC generators, parameter settings and PDF sets have already been conducted, as discussed in Section 3.4.2. Further investigations into the cause of the discrepancy between data and simulated distributions, involving both theorists and experimentalists, are strongly recommended.

9. Outlook

In 2015, the LHC started operating at a higher centre-of-mass energy, $\sqrt{s} = 13$ TeV. This is the largest energy increase in hadron collisions since the LHC reached $\sqrt{s} = 7$ TeV, surpassing the energy $\sqrt{s} = 1.96$ TeV at which the Tevatron had last been operating. This increase of collision energy significantly extends the kinematic regime accessible to BSM physics searches, including the search for resonant $t\bar{t}$ production, which will now be able to probe the $t\bar{t}$ invariant mass regime above 3 TeV. Moreover, with a projected integrated luminosity of up to 100 fb^{-1} [308], the sensitivity of the search to potential signal processes with smaller cross-sections will increase.

While these technical upgrades of the LHC hold considerable potential with regard to the reach and sensitivity of searches for BSM resonances in Run 2, both the increased collision energy and the expected higher instantaneous luminosity, $\mathcal{L} = 10^{34}$ cm^{-2} s^{-1}, present a number of challenges that will need to be addressed in future searches.

Firstly, the increased rates of both in-time and out-of-time pile-up require the adaptation of particle reconstruction and identification strategies to make them more robust against pile-up. This affects all physics objects used in the search presented in this thesis. Many changes and improvements have already been or are being implemented centrally within ATLAS. For example, a more aggressive trimming strategy for large-R jets that uses subjets with $R = 0.2$ instead of $R = 0.3$ has been adopted [309] to preserve the discriminating power of jet selection variables, such as the jet mass and substructure variables, in events with high levels of pile-up.

Another significant challenge in Run 2 is the preservation and improvement of the sensitivity of the search to potential BSM resonances with masses below 1 TeV. While BSM resonances in this mass regime have been excluded at 95% CL for certain benchmark models, the objective for a model-independent search must be to maximise its sensitivity over a large mass range. The sensitivity in the low-mass regime depends crucially on the trigger efficiency for potential signal events: The higher event rates as well as the higher levels of pile-up, which lead to an increase of the average event size, require an optimisation of the trigger selection to keep the trigger

rates, in particular those at L1, within the limits set by the computing, read-out and storage infrastructure. An increase of the momentum thresholds on trigger objects, such as leptons and jets, is unavoidable for many trigger signatures. However, the increase can be kept at a minimum if other object and selection criteria, such as b-tagging or topological requirements, are introduced early in the trigger chain to suppress unwanted background events, ideally already at L1. A more sophisticated trigger selection will also benefit from a number of upgrades to the ATLAS trigger system [144], most notably the introduction of a topological processor at L1 (**L1Topo**), which will allow for the calculation of quantities such as the angular separation between two L1 objects and their combined invariant mass, and a new, fast hardware-based track-finder, the **Fast TracKer (FTK)** [310]. The FTK will provide track and vertex information at the beginning of the HLT selection without the CPU the constraints of the HLT software, thus allowing, for example, for a more efficient selection of b-jets at the HLT at the same output rate as equivalent b-jet triggers that do not rely on the FTK. Different trigger strategies, tailored towards the signature of the ℓ+jets final state of $t\bar{t}$ events, have been investigated with regard to future searches [311].

The third major challenge in Run 2 lies in the **increasing collimation of the top-quark decay products** at high transverse momenta. For top quarks with transverse momenta above 1 TeV, the angular separation between the decay products approaches the calorimeter granularity and the substructure of large-R jets can no longer be efficiently resolved [312]. This instrumental limitation may be overcome through the additional use of **tracking information** from the ID, which has a spatial resolution that is between one and two orders of magnitude higher than that of the calorimeter. A strategy for tracking-based top tagging has been presented in [312]. Further investigations in this direction are recommended.

The collimation of the top-quark decay products also affects the b-tagging efficiency, especially for b-jets from hadronically-decaying top quarks, since the b-hadron decay products can no longer be separated from the constituents of other, close-by jets. **Track-based b-taggers** that rely on jets with small R parameters, such as $R = 0.3$ or $R = 0.2$ instead of $R = 0.4$, have been shown to yield considerable improvements of the b-tagging efficiency, and consequently the signal selection efficiency for heavy resonances decaying to four b-quarks via a pair of Higgs bosons, $pp \to hh \to (b\bar{b})(b\bar{b})$, with resonance masses above 1 TeV [246]. The smaller jet sizes allow the b-hadron decay products to be separated from close-by jets even if the Higgs decay products are strongly collimated. The use of track instead of calorimeter jets allows for smaller jet sizes

as well as a better suppression of pile-up effects through appropriate track- and vertex-quality requirements. This new b-tagging strategy is also expected to increase the selection efficiency for $t\bar{t}$ final states with boosted top quarks.

The new track-based analysis strategies mentioned above will also benefit from a recent upgrade of the ATLAS pixel detector, which was extended through the installation of a fourth pixel layer, the **insertable B-layer (IBL)** [313], at a distance of only 25.7 mm from the beam line. The IBL exploits new sensor and read-out technologies, specifically optimised for radiation hardness, and is expected to improve the vertexing and flavour tagging performance of the ATLAS detector, especially with regard to the increased number of interactions per bunch crossing and consequently higher track densities of Run 2.

The performance improvements in boosted event topologies achieved through the use of b-tagging algorithms operating on jets with smaller than standard R parameters indicate that the optimal jet size depends on the kinematic regime. It is therefore reasonable to consider a modified jet clustering algorithm with variable R parameter, which automatically adapts to the transverse momentum scale of the jet. In this so-called **Variable-R algorithm** [5], the fixed R_0 parameter (Equation 4.2 in Section 4.3.1), which controls the effective jet size, becomes a function of the transverse momentum $p_{T,i}$ of input object i in a given clustering step:

$$R_{\text{eff,i}}(p_T) = \frac{\rho}{p_{T,i}}, \tag{9.1}$$

where the parameter ρ is set by the user, along with a minimum and a maximum value of $R_{\text{eff,i}}$, denoted R_{max} and R_{min}, respectively. This algorithm returns jets with a size in the η-ϕ plane that scales roughly like the inverse of the jet transverse momentum. Hence these jets are ideally suited for the reconstruction of boosted objects, like top quarks or Higgs bosons, for which the angular separation between the decay products is proportional to the inverse of the transverse momentum of the mother particle (Equation 5.1 in Section 5.1), a functional dependence that is already used in the mini-isolation and overlap removal criteria for leptons.

Variable-R jets can be used in the reconstruction of boosted objects in two different ways: Firstly, they can replace small-R jets for the reconstruction of the individual (hadronic) decay products. The shrinking of the jets with increasing collimation of the decay products reduces the probability of overlap between close-by jets, compared to traditional algorithms, thus allowing for an extension of the kinematic regime over which the resolved topology can be maintained.

The use of Variable-R jets in the resolved topology of $t\bar{t}$ decays was first studied in the context of the Ph.D. project of S. Livermore [279]. These studies were extended to the $hh \to (b\bar{b})(b\bar{b})$ final state (Figure 9.1a) by the author of this thesis to investigate the potential of Variable-R jets for track-based b-tagging.

The potential of Variable-R jets with regard to **b-tagging in dense environments** is illustrated in Figure 9.1b, where the fraction of $hh \to (b\bar{b})(b\bar{b})$ events in which all four b-hadrons can be matched to a different (track) jet is shown as a function of the true di-Higgs invariant mass m_{hh}^{true}. A b-hadron ($p_T > 5$ GeV, $|\eta| < 2.2$) is considered matched to a jet ($p_T > 7$ GeV, $|\eta| < 2.2$) if $\Delta R(\text{hadron}, \text{jet}) < 0.75 \cdot R$. The study relies on the same simulated samples of a Bulk RS Kaluza-Klein graviton decaying to hh as the ATLAS study of track-based b-tagging in dense environments [246]. The comparison between traditional anti-k_T jets with different R parameters indicates that larger jets ($R = 0.4$) fail to resolve the b-hadrons at higher invariant masses, where the Higgs boson decay products are more collimated. Smaller jets ($R = 0.3$ or 0.2) improve the resolution in this mass regime but fail to capture all b-hadron decay products at lower values of m_{hh}^{true}, where the b-hadrons tend to be less energetic, resulting in a lower matching efficiency between b-hadrons and jets. Variable-R jets combine the advantages of the different jet collections with fixed R parameters, yielding a more stable performance across the whole invariant mass regime. Further investigations into the development of Variable-R based b-tagging algorithms for ATLAS analyses in Run 2 are currently in progress.

The second application of Variable-R jets is the **reconstruction of boosted particle jets**, where they can be used to replace traditional large-R jets, such as the trimmed anti-k_T $R = 1.0$ jets that are used to reconstruct the hadronically decaying top quark in the search presented in this thesis. This application is motivated by the fact that the hadron showers not only merge into a single jet if the top quark is sufficiently energetic, but they become increasingly collimated as the transverse momentum of the top quark increases. This is illustrated in Figure 9.2a, in which the radial transverse momentum distribution of the constituents within trimmed anti-k_T $R = 1.0$ jets is plotted as a function of the jet transverse momentum. For $p_T^{\text{jet}} = 1$ TeV, more than 95% of the total transverse momentum of the jet stems from constituents that are within $\Delta R(\text{constit,jet}) < 0.4$ from the jet axis [6]. Variable-R jets reflect this increasing collimation of the hadron showers from the top-quark decay products, thus providing a more natural description of top-quark jets. Moreover, their on average smaller areas make them less susceptible to contaminations from pile-up. This is reflected in the discriminating power of the jet mass

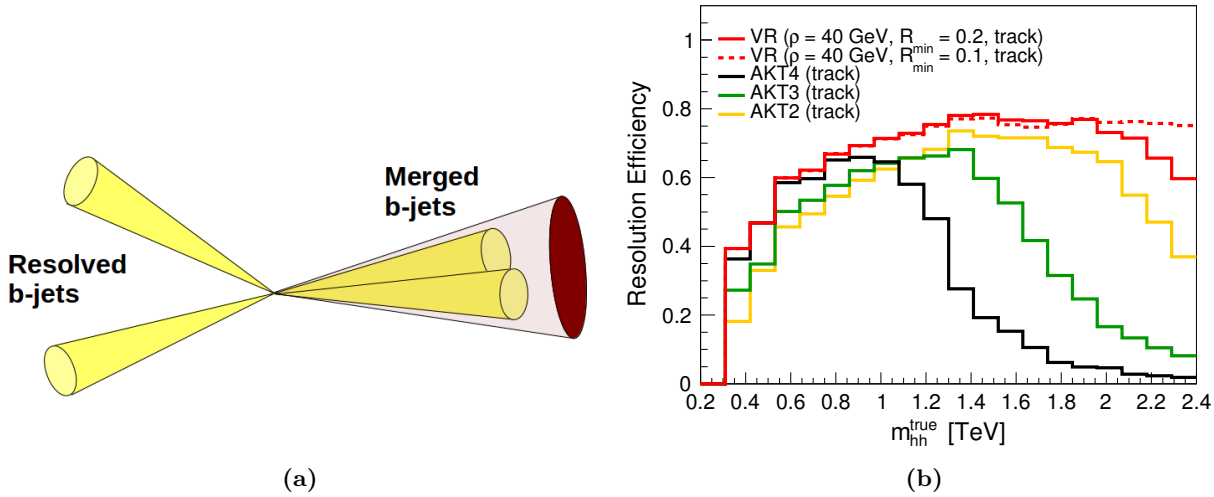

(a) **(b)**

Figure 9.1.: (a) Schematic representation of a $hh \to (b\bar{b})(b\bar{b})$ final state in which the b-jets from one Higgs boson decay are merged while those from the other Higgs boson decay are well separated. (b) Fraction of $hh \to (b\bar{b})(b\bar{b})$ events in which all four b-hadrons are matched to a different (track) jet for a given jet algorithm. The efficiency, which is given as a function of the true di-Higgs invariant mass m_{hh}^{true}, is compared for anti-k_T jets with $R = 0.4$, $R = 0.3$ and $R = 0.2$ and Variable-R jets with $\rho = 40$ GeV, $R_{\text{max}} = 0.4$ and $R_{\text{min}} = 0.2$ ($R_{\text{min}} = 0.1$).

distributions for Variable-R jets: In Figure 9.2b (equivalent to Figure 4.1a in Section 4.3.3), the jet mass distributions in a $Z' \to t\bar{t}$ signal and a QCD multi-jet MC sample are compared for Variable-R jets ($\rho = 600$ GeV, $R_{\text{max}} = 1.0$, $R_{\text{min}} = 0.2$) and both trimmed and ungroomed anti-k_T $R = 1.0$ jets. In the chosen kinematic regime, $1000 < p_T^{\text{jet}} < 1500$ GeV, the effective size of the Variable-R jets varies between $R_{\text{eff,jet}} = 0.6$ for $p_T^{\text{jet}} = 1000$ GeV and $R_{\text{eff,jet}} = 0.4$ for $p_T^{\text{jet}} = 1500$ GeV. Remarkably, Variable-R jets, to which *no grooming* has been applied, yield distributions similar to those obtained for trimmed anti-k_T $R = 1.0$ jets. The signal significance $S/\sqrt{B}$ obtained from these distributions if a lower threshold is imposed on the jet mass, as used in the event selection for the boosted decay topology (Section 5.2), is found to be 14% higher for Variable-R jets compared to trimmed anti-k_T $R = 1.0$ jets [6]. Further performance improvements are possible if trimming is also applied to Variable-R jets. Studies into the use of Variable-R jets for the tagging of boosted top quarks are currently in progress [6].

In summary, the recent increase of the centre-of-mass energy of the LHC provides the unique opportunity to significantly extend the kinematic regime accessible to model-independent searches for BSM resonances decaying to $t\bar{t}$ pairs. The increasing collimation of the top-quark decay products as well as the higher levels of pile-up require the development of novel analysis techniques to increase the search sensitivity to resonance masses ranging from around 400 GeV to a few TeV. These include novel trigger and b-tagging strategies, and the possibility for a more

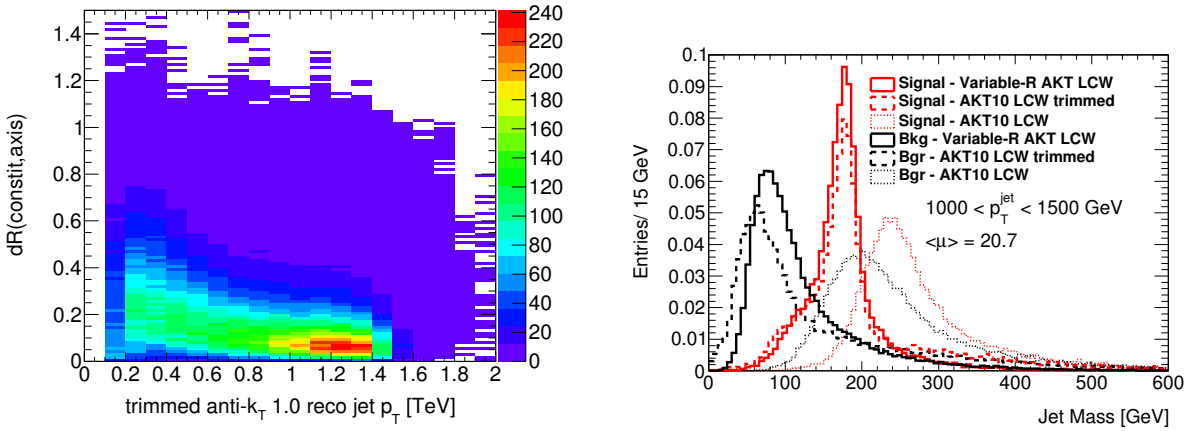

(a) **(b)**

Figure 9.2.: (a) Radial transverse momentum profile of trimmed anti-k_T $R = 1.0$ top-quark jets in simulated $Z' \to t\bar{t}$ signal events as a function of the jet transverse momentum. For each jet, the angular separation ΔR(constit,jet) between each constituent topological cluster and the jet axis is plotted, with each entry weighted by the transverse momentum of the constituent. (b) Comparison of the mass distributions for Variable-R (solid lines), trimmed (dashed lines) and ungroomed (dotted lines) anti-k_T $R = 1.0$ LCW jets with $1000 < p_T^{\text{jet}} < 1500$ GeV on simulated $Z' \to t\bar{t}$ signal and QCD multi-jet background events. All distributions are normalised to unity.

flexible approach to jet reconstruction in different kinematic regimes. Track-based techniques are expected to gain in importance, in particular in the highly boosted regime. These techniques benefit from recent and on-going hardware upgrades, such as the installation of the IBL and the FTK in the ATLAS detector. These techniques are not only targeted at final states with boosted top quarks but are also developed for and applied in the reconstruction of boosted Higgs bosons. These developments underline the key importance of both top quarks and Higgs bosons, the youngest and heaviest particles in the SM, as probes in the search for phenomena beyond the SM at the high-energy frontier.

Appendix

A. Kinematic Properties of the Resonances in the Four Benchmark Models

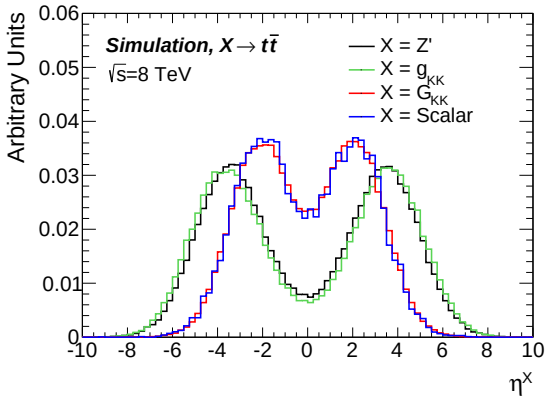

(a) η^X ($m_X = 1.0$ TeV)

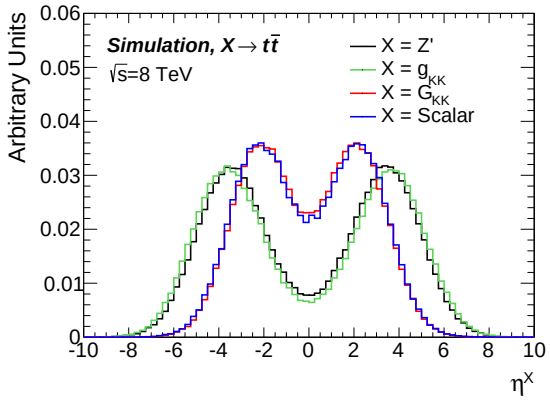

(b) η^X ($m_X = 2.0$ TeV)

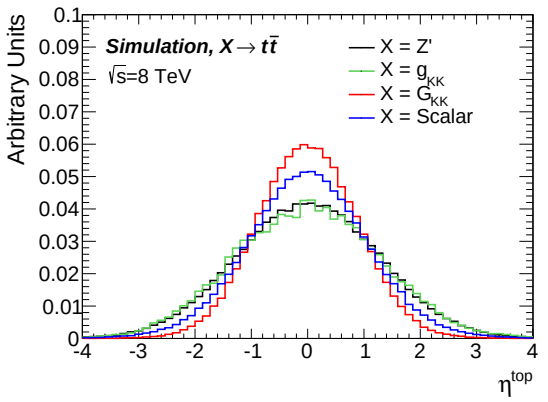

(c) η^{tops} ($m_X = 1.0$ TeV)

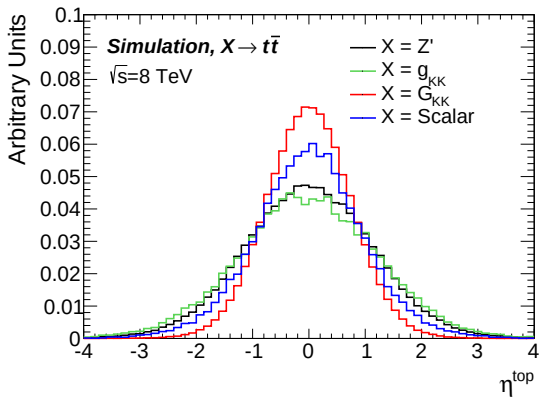

(d) η^{tops} ($m_X = 2.0$ TeV)

Figure A.1.: Pseudorapidity distributions for (a)-(b) the resonances and (c)-(d) the (anti)top quarks from the resonance decays (before FSR) for $m_X = 1.0$ TeV (left column) and $m_X = 2.0$ TeV (right column).

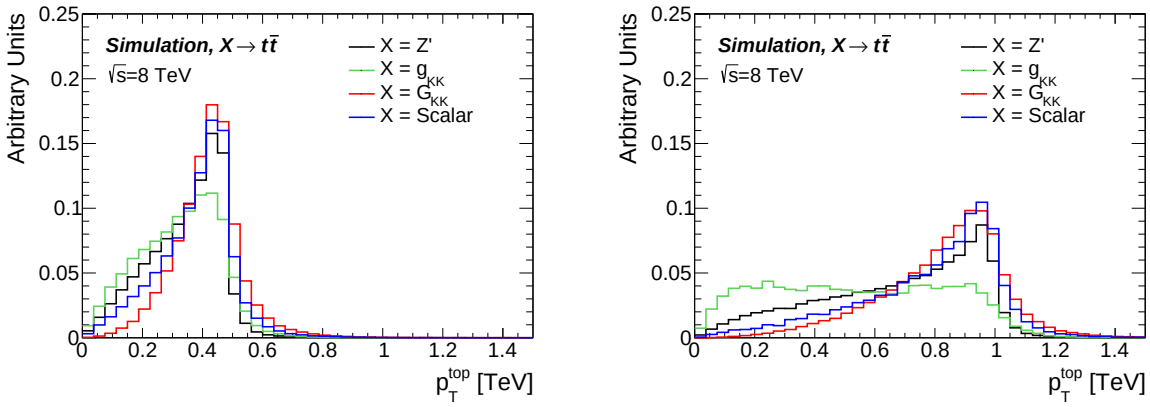

(a) p_T^{top} ($m_X = 1.0$ TeV) **(b)** p_T^{top} ($m_X = 2.0$ TeV)

Figure A.2.: Transverse momentum distributions for the (anti)top quarks from the resonance decays (before FSR) for (a) $m_X = 1.0$ TeV and (b) $m_X = 2.0$ TeV.

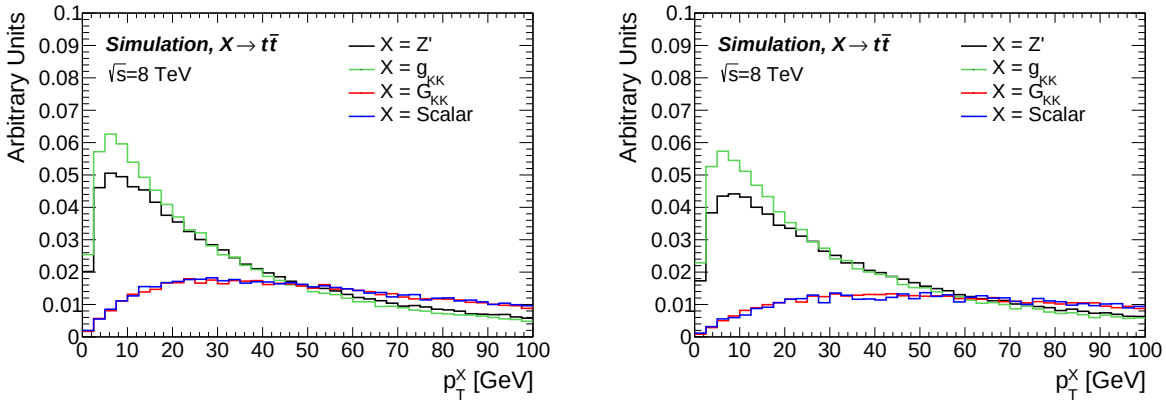

(a) $p_T^{t\bar{t}}$ ($m_X = 1.0$ TeV) **(b)** $p_T^{t\bar{t}}$ ($m_X = 2.0$ TeV)

Figure A.3.: Transverse momentum distributions for the $t\bar{t}$ pair from the resonance decays (before FSR) for (a) $m_X = 1.0$ TeV and (b) $m_X = 2.0$ TeV.

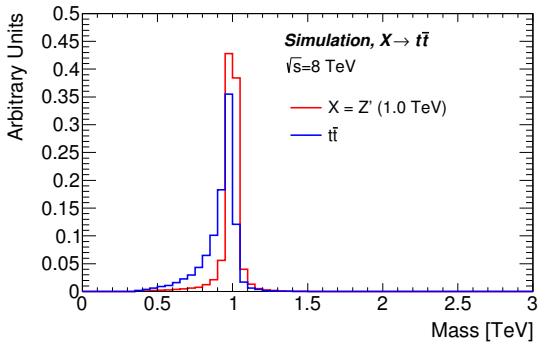

(a) $m_{Z'} = 1.0$ TeV

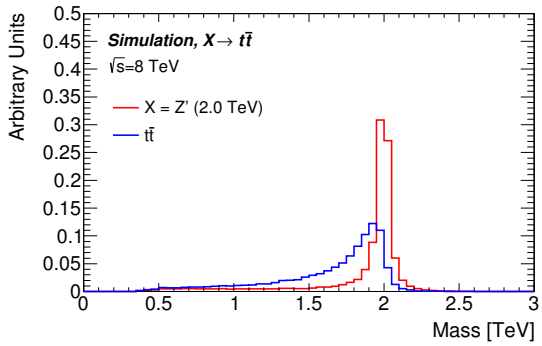

(b) $m_{Z'} = 2.0$ TeV

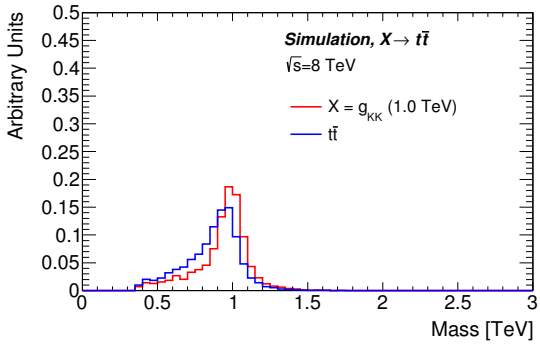

(c) $m_{g_{KK}} = 1.0$ TeV

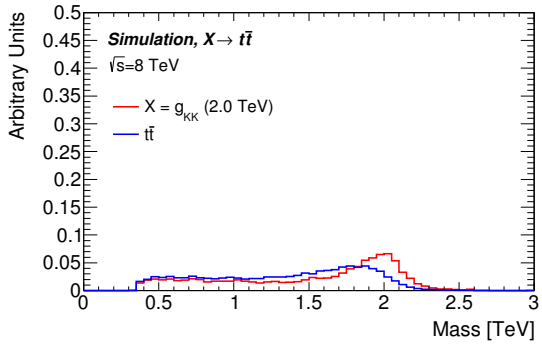

(d) $m_{g_{KK}} = 2.0$ TeV

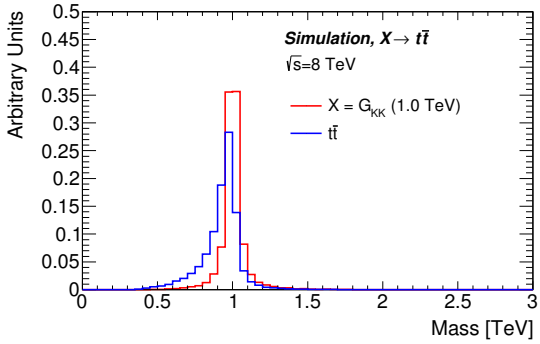

(e) $m_{G_{KK}} = 1.0$ TeV

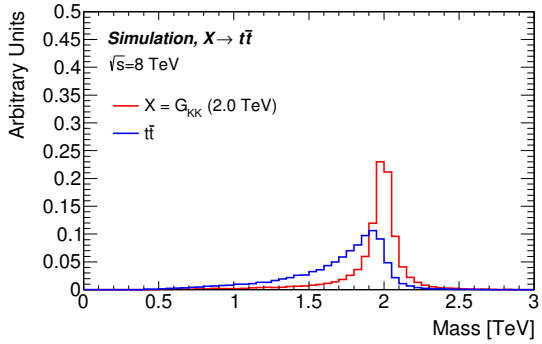

(f) $m_{G_{KK}} = 2.0$ TeV

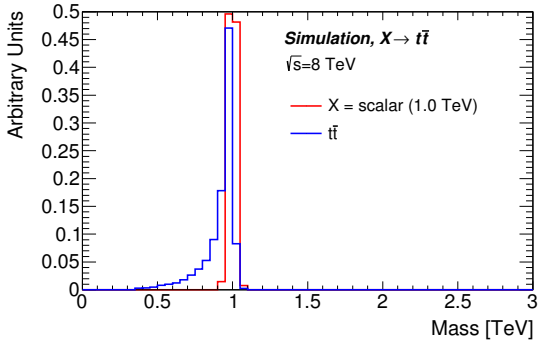

(g) $m_{\text{scalar}} = 1.0$ TeV

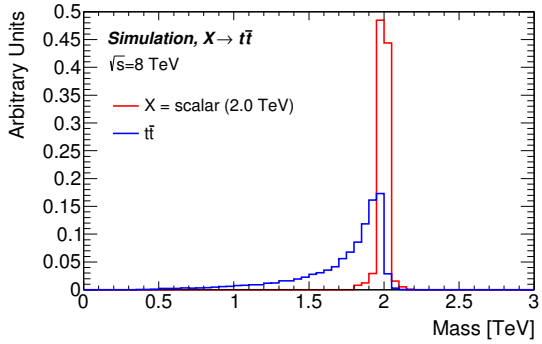

(h) $m_{\text{scalar}} = 2.0$ TeV

Figure A.4.: Generated resonance mass (red) and invariant mass of the $t\bar{t}$ pair, reconstructed from the six top-quark decay products $bq'\bar{q}\bar{b}\ell\nu_\ell$ at generator level after the emission of FSR (blue) for (a)-(b) Z', (c)-(d) g_{KK}, (e)-(f) G_{KK}, and (g)-(h) scalar resonance, each for the 1.0 TeV (left column) and 2.0 TeV mass points (right column).

Glossary and List of Acronyms

Acceptance	Efficiency related to the geometric coverage of the detector. See also "efficiency".
BSM	Beyond Standard Model
Efficiency	Fraction of events passing a given number of selection criteria. The total efficiency for a process, for example a signal of interest, depends on the details of the detector and analysis design. It is the product of the detector acceptance, the efficiencies for the reconstruction and identification of the physics objects involved in the selection, and the efficiencies for the event selection criteria. It is commonly referred to as efficiency times acceptance or simply efficiency of a process.[1]
EW	Electroweak
EWSB	Electroweak Symmetry Breaking
FSR	Final-state radiation
ISR	Inital-state radiation
JER	Jet energy resolution
JES	Jet energy scale. Defined in Section 4.3.4.
JMR	Jet mass resolution
JMS	Jet mass scale. Defined in Section 4.3.4.
JVF	Jet vertex fraction. Defined in Section 4.3.3.

[1] Note that the terms "efficiency" and "acceptance" are often used interchangeably. The use and definition of these terms may differ between different experiments or even analyses in the same experiment.

k-factor	Multiplicative correction factor applied to Monte Carlo events simulated at a given order in a perturbative expansion to correct the simulated (total) cross-section to that at the next higher order. Obtained as the ratio of the calculated higher-order and lower-order cross-sections.
LCW	Local Cluster Weighting. Defined in Section 4.3.4.
LHC	Large Hadron Collider
MC	Monte Carlo
MLE	Maximum Likelihood Estimator
QED	Quantum Electrodynamics
QCD	Quantum Chromodynamics
SF	Scale factor
SM	Standard Model

Bibliography

[1] **ATLAS** Collaboration, *A search for $t\bar{t}$ resonances using lepton-plus-jets events in proton-proton collisions at $\sqrt{s} = 8$ TeV with the ATLAS detector*, *JHEP* **1508** (2015) 148, [arXiv:1505.07018].

[2] **ATLAS** Collaboration, *A search for $t\bar{t}$ resonances in the lepton plus jets final state with ATLAS using 20 fb^{-1} of pp collisions at $\sqrt{s} = 8$ TeV*, 2015. ATL-COM-PHYS-2014-003 [internal], https://cds.cern.ch/record/1640960/.

[3] **ATLAS** Collaboration, *Performance of the ATLAS Electron and Photon Triggers in p-p at Collisions at $\sqrt{s}$=7 TeV and $\sqrt{s}$=8 TeV in Run-1*, . ATL-COM-DAQ-2014-107, https://cds.cern.ch/record/1755819/. Paper draft under ATLAS-internal review.

[4] J. K. Behr, N. Bin Norjoharuddeen, D. Bortoletto, J. Frost, N. P. Hartland, C. Issever, and J. Rojo, *Boosting Higgs Pair Production in the $b\bar{b}b\bar{b}$ Channel at the LHC with Multivariate Techniques*, 2015. Publication in preparation for submission to JHEP.

[5] D. Krohn, J. Thaler, and L.-T. Wang, *Jets with Variable R*, *JHEP* **0906** (2009) 059, [arXiv:0903.0392].

[6] J. K. Behr, C. Issever, L. A. Kogan, and J. Zhong, *The Performance of Variable-R Jets in the Reconstruction and Identification of Highly-energetic Top-Quarks at the ATLAS Detector*, Tech. Rep. ATL-COM-PHYS-2014-1152, CERN, Geneva, Sep, 2014. ATLAS internal, https://cds.cern.ch/record/1755181. Prepared for release as an ATLAS Public Note.

[7] J. K. Behr, *High-p_T b-tagging and Top-Tagging with Variable-R Jets in ATLAS*, DPG-Frühjahrstagung. Wuppertal, 9. - 13. März 2015. http://www.dpg-verhandlungen.de/year/2015/conference/wuppertal/part/t/session/46/contribution/2.

[8] **ATLAS** Collaboration, *Search for Higgs boson pair production in the $b\bar{b}b\bar{b}$ final state from pp collisions at $\sqrt{s} = 8$ TeV with the ATLAS detector*, arXiv:1506.00285. Accepted for publication in the European Journal of Physics C.

[9] S. L. Glashow, *Partial-symmetries of weak interactions*, *Nuclear Physics* **22** (1961), no. 4 579 – 588.

[10] S. Weinberg, *A model of leptons*, *Phys. Rev. Lett.* **19** (Nov, 1967) 1264–1266.

[11] G. 't Hooft and M. Veltman, *Regularization and renormalization of gauge fields*, *Nuclear Physics B* **44** (1972), no. 1 189 – 213.

[12] A. Salam, *Weak and electromagnetic interactions*, p. 367. Almqvist & Wiksell, 1968.

[13] G. Arnison et al., *Experimental Observation of Isolated Large Transverse Energy Electrons with Associated Missing Energy at $\sqrt{s}$ = 540 GeV*, *Physics Letters B* **122B** (1983) 103.

[14] G. Arnison, *Experimental Observation of Lepton Pairs of Invariant Mass around 95 GeV at the CERN SPS Collider*, *Physics Letters B* **126B** (1983) 398.

[15] **CDF** Collaboration, F. Abe et al., *Observation of Top Quark Production in $\bar{p}p$ Collisions with the Collider Detector at Fermilab*, *Phys. Rev. Lett.* **74** (1995) 2626.

[16] **D0** Collaboration, S. Abachi et al., *Observation of the Top Quark*, *Phys. Rev. Lett.* **74** (1995) 2632.

[17] **ATLAS** Collaboration, *Observation of a new particle in the search for the Standard Model Higgs boson with the ATLAS detector at the LHC*, *Phys. Lett.* **B716** (2012) 1–29, [arXiv:1207.7214].

[18] **CMS** Collaboration, *Observation of a new boson at a mass of 125 GeV with the CMS experiment at the LHC*, *Phys. Lett.* **B716** (2012) 30–61, [arXiv:1207.7235].

[19] **ATLAS** Collaboration, *Measurements of the Higgs boson production and decay rates and coupling strengths using pp collision data at $\sqrt{s} = 7$ and 8 TeV in the ATLAS experiment*, arXiv:1507.04548.

[20] **CMS** Collaboration, *Precise determination of the mass of the Higgs boson and tests of compatibility of its couplings with the standard model predictions using proton collisions at 7 and 8 TeV*, *Eur. Phys. J.* **C75** (2015), no. 5 212, [arXiv:1412.8662].

[21] F. Englert and R. Brout, *Broken symmetry and the mass of gauge vector mesons*, *Phys. Rev. Lett.* **13** (Aug, 1964) 321–323.

[22] P. W. Higgs, *Broken Symmetries and the Masses of Gauge Bosons*, *Phys. Rev. Lett.* **13** (1964) 508–509.

[23] P. W. Higgs, *Broken symmetries, massless particles and gauge fields*, *Phys. Lett.* **12** (1964) 132–133.

[24] P. W. Higgs, *Spontaneous Symmetry Breakdown without Massless Bosons*, *Phys. Rev.* **145** (1966) 1156–1163.

[25] G. S. Guralnik, C. R. Hagen, and T. W. B. Kibble, *Global Conservation Laws and Massless Particles*, *Phys. Rev. Lett.* **13** (1964) 585–587.

[26] T. W. B. Kibble, *Symmetry breaking in nonAbelian gauge theories*, *Phys. Rev.* **155** (1967) 1554–1561.

[27] **ALEPH, DELPHI, L3, OPAL** Collaboration, The LEP WG for Higgs Boson Searches, *Search for the standard model higgs boson at {LEP}*, *Physics Letters B* **565** (2003) 61 – 75.

[28] **CDF** Collaboration, T. Aaltonen et al., *Combined search for the standard model Higgs boson decaying to a bb pair using the full CDF data set*, *Phys. Rev. Lett.* **109** (2012) 111802, [arXiv:1207.1707].

[29] **D0** Collaboration, V. M. Abazov et al., *Combined search for the standard model Higgs boson decaying to $b\bar{b}$ using the D0 Run II data set*, *Phys. Rev. Lett.* **109** (2012) 121802, [arXiv:1207.6631].

[30] **CDF, D0** Collaboration, T. Aaltonen et al., *Evidence for a particle produced in association with weak bosons and decaying to a bottom-antibottom quark pair in Higgs boson searches at the Tevatron*, *Phys. Rev. Lett.* **109** (2012) 071804, [arXiv:1207.6436].

[31] S. H. Neddermeyer and C. D. Anderson, *Note on the Nature of Cosmic Ray Particles*, *Phys. Rev.* **51** (1937) 884–886.

[32] H. Yukawa, *On the interaction of elementary particles*, in *Proc. Physico-Math. Soc. Jpn. 17, 48*, 1935.

[33] D. Griffiths, *Introduction to Elementary Particles*. WILEY-VCH, second (revised) ed., 2008.

[34] **ATLAS, CDF, CMS, D0** Collaboration, *First combination of Tevatron and LHC measurements of the top-quark mass*, arXiv:1403.4427.

[35] **ATLAS, CMS** Collaboration, G. Aad et al., *Combined Measurement of the Higgs Boson Mass in pp Collisions at $\sqrt{s} = 7$ and 8 TeV with the ATLAS and CMS Experiments*, *Phys. Rev. Lett.* **114** (2015) 191803, [arXiv:1503.07589].

[36] **CDF** Collaboration, T. Aaltonen et al., *Search for resonant production of $t\bar{t}$ decaying to jets in $p\bar{p}$ collisions at $\sqrt{s} = 1.96$ TeV*, *Phys.Rev.* **D84** (2011) 072003, [arXiv:1108.4755].

[37] **CDF** Collaboration, T. Aaltonen et al., *Search for Resonant Top-Antitop Production in the Lepton Plus Jets Decay Mode Using the Full CDF Data Set*, *Phys.Rev.Lett.* **110** (2013), no. 12 121802, [arXiv:1211.5363].

[38] **D0** Collaboration, V. M. Abazov et al., *Search for a Narrow $t\bar{t}$ Resonance in $p\bar{p}$ Collisions at $\sqrt{s} = 1.96$ TeV*, *Phys.Rev.* **D85** (2012) 051101, [arXiv:1111.1271].

[39] **ATLAS** Collaboration, *Search for $t\bar{t}$ resonances in the lepton plus jets final state with ATLAS using 4.7 fb^{-1} of pp collisions at $\sqrt{s} = 7$ TeV*, *Phys.Rev.* **D88** (2013), no. 1 012004, [arXiv:1305.2756].

[40] **ATLAS** Collaboration, *Search for resonances decaying into top-quark pairs using fully hadronic decays in pp collisions with ATLAS at $\sqrt{s} = 7$ TeV*, *JHEP* **1301** (2013) 116, [arXiv:1211.2202].

[41] **ATLAS** Collaboration, *A Search for ttbar Resonances in the Dilepton Channel in 1.04/fb of pp Collisions at sqrt(s) = 7 TeV*, Tech. Rep. ATLAS-CONF-2011-123, CERN, Geneva, Aug, 2011.

https://cds.cern.ch/record/1376423.

[42] **CMS** Collaboration, *Search for resonant $t\bar{t}$ production in lepton+jets events in pp collisions at $\sqrt{s} = 7$ TeV*, *JHEP* **1212** (2012) 015, [arXiv:1209.4397].

[43] **CMS** Collaboration, *Search for Anomalous $t\bar{t}$ Production in the Highly-Boosted All-Hadronic Final State*, *JHEP* **1209** (2012) 029, [arXiv:1204.2488].

[44] **CMS** Collaboration, *Search for Z ' resonances decaying to $t\bar{t}$ in dilepton+jets final states in pp collisions at $\sqrt{s} = 7$ TeV*, *Phys.Rev.* **D87** (2013), no. 7 072002, [arXiv:1211.3338].

[45] **CMS** Collaboration, *Search for Resonant $\mathrm{t\bar{t}}$ Production in Proton-Proton Collisions at $\sqrt{s} = 8$ TeV*, arXiv:1506.03062. Submitted to Phys. Rev. D.

[46] J. K. Behr, *Searches with Boosted Objects*, in *34th International Symposium on Physics in Collision (PIC 2014) Bloomington, Indiana, United States, September 16-20, 2014*, 2014. arXiv:1411.3521.

[47] M. E. Peskin and D. V. Schroeder, *An Introduction to Quantum Field Theory*. Westview Press, 1995.

[48] T.-P. Cheng and L. F. Li, *Gauge Theory of Elementary Particle Physics*. Oxford University Press, 1984.

[49] R. K. Ellis, W. J. Stirling, and B. R. Webber, *QCD and collider physics*, *Camb. Monogr. Part. Phys. Nucl. Phys. Cosmol.* **8** (1996) 1–435.

[50] N. Cabibbo, *Unitary Symmetry and Leptonic Decays*, *Phys. Rev. Lett.* **10** (1963) 531–533.

[51] M. Kobayashi and T. Maskawa, *CP Violation in the Renormalizable Theory of Weak Interaction*, *Prog. Theor. Phys.* **49** (1973) 652–657.

[52] K. A. Olive and others (Particle Data Group), *Review of Particle Physics*, *Chin. Phys. C* **38** (2014), no. 090001. http://pdg.lbl.gov/.

[53] B. Pontecorvo, *Inverse beta processes and nonconservation of lepton charge*, *Sov. Phys. JETP* **7** (1958) 172–173. [Zh. Eksp. Teor. Fiz.34,247(1957)].

[54] Z. Maki, M. Nakagawa, and S. Sakata, *Remarks on the unified model of elementary particles*, *Prog. Theor. Phys.* **28** (1962) 870–880.

[55] **LHCb** Collaboration, R. Aaij et al., *Observation of $J/\Psi p$ Resonances Consistent with Pentaquark States in $\Lambda_b^0 \to J/\Psi K^- p$ Decays*, *Phys. Rev. Lett.* **115** (2015) 072001, [arXiv:1507.03414].

[56] J. C. Collins, D. E. Soper, and G. F. Sterman, *Factorization of Hard Processes in QCD*, *Adv. Ser. Direct. High Energy Phys.* **5** (1989) 1–91, [hep-ph/0409313].

[57] M. Aliev, H. Lacker, U. Langenfeld, S. Moch, P. Uwer, et al., *HATHOR: HAdronic Top and Heavy quarks crOss section calculatoR*, *Comput.Phys.Commun.* **182** (2011) 1034–1046, [arXiv:1007.1327].

[58] M. C. Smith and S. S. Willenbrock, *Top quark pole mass*, *Phys. Rev. Lett.* **79** (1997) 3825–3828, [hep-ph/9612329].

[59] **ATLAS** Collaboration, *Reference $t\bar{t}$ production cross sections for use in ATLAS analyses*, 2015. ATL-COM-PHYS-2014-112 [internal], https://cds.cern.ch/record/1662536/files/ATL-COM-PHYS-2014-112.pdf.

[60] J. K. Behr, *Measurement of the Top-Quark Mass in the Semileptonic Decay Channel at the ATLAS Experiment*, Diplomarbeit, Ludwig-Maximilians Universität München, 2012.

[61] Y. L. Dokshitzer, *Calculation of the Structure Functions for Deep Inelastic Scattering and e+ e- Annihilation by Perturbation Theory in Quantum Chromodynamics.*, *Sov. Phys. JETP* **46** (1977) 641–653. [Zh. Eksp. Teor. Fiz.73,1216(1977)].

[62] V. N. Gribov and L. N. Lipatov, *Deep inelastic e p scattering in perturbation theory*, *Sov. J. Nucl. Phys.* **15** (1972) 438–450. [Yad. Fiz.15,781(1972)].

[63] G. Altarelli and G. Parisi, *Asymptotic Freedom in Parton Language*, *Nucl. Phys.* **B126** (1977) 298.

[64] Devenish, Roban and Cooper-Sarkar, Amanda, *Deep Inelastic Scattering*. Oxford University Press, 2004.

[65] J. Rojo et al., *The PDF4LHC report on PDFs and LHC data: Results from Run I and preparation for Run II*, arXiv:1507.00556.

[66] S. Alekhin et al., *The PDF4LHC Working Group Interim Report*, arXiv:1101.0536.

[67] A. Martin, W. Stirling, R. Thorne, and G. Watt, *Parton distributions for the LHC*, *Eur.Phys.J.* **C63** (2009) 189–285, [arXiv:0901.0002].

[68] *The Durham HepData Project*, Sep, 2015. http://hepdata.cedar.ac.uk/pdf/pdf3.html.

[69] W. J. Stirling, *Private communication*, Jul, 2015. http://www.hep.ph.ic.ac.uk/~wstirlin/plots/plots.html/.

[70] M. Czakon and A. Mitov, *Top++: A Program for the Calculation of the Top-Pair Cross-Section at Hadron Colliders*, *Comput.Phys.Commun.* **185** (2014) 2930, [arXiv:1112.5675].

[71] Y. Delenda, *Soft gluons and non-perturbative effects in QCD observables*. PhD thesis, University of Manchester, 2007. http://www.hep.manchester.ac.uk/theses/Yazid_Delenda.pdf.

[72] M. Czakon and A. Mitov, *NNLO corrections to top pair production at hadron colliders: the quark-gluon reaction*, *JHEP* **1301** (2013) 080, [arXiv:1210.6832].

[73] M. Czakon, P. Fiedler, and A. Mitov, *Total Top-Quark Pair-Production Cross Section at Hadron Colliders Through $O(\alpha\frac{4}{S})$*, *Phys.Rev.Lett.* **110** (2013) 252004, [arXiv:1303.6254].

[74] **ATLAS** Collaboration, *Measurement of the $t\bar{t}$ production cross-section using $e\mu$ events with b -tagged jets in pp collisions at $\sqrt{s} = 7$ and 8 TeV with the ATLAS detector*, *Eur. Phys. J.* **C74** (2014), no. 10 3109, [arXiv:1406.5375].

[75] **ATLAS** Collaboration, *Measurement of the top pair production cross section in 8 TeV proton-proton collisions using kinematic information in the lepton+jets final state with ATLAS*, *Phys. Rev.* **D91** (2015), no. 11 112013, [arXiv:1504.04251].

[76] **CMS** Collaboration, *Measurement of the $t\bar{t}$ production cross section in the dilepton channel in pp collisions at $\sqrt{s}$ = 8 TeV*, *JHEP* **02** (2014) 024, [arXiv:1312.7582]. [Erratum: JHEP02,102(2014)].

[77] **CMS** Collaboration, *Measurement of the $t\bar{t}$ production cross section in pp collisions at $\sqrt{s} = 8$ TeV in dilepton final states containing one τ lepton*, *Phys. Lett.* **B739** (2014) 23–43, [arXiv:1407.6643].

[78] S. Bethke, *World Summary of α_s (2012)*, arXiv:1210.0325. [Nucl. Phys. Proc. Suppl.234,229(2013)].

[79] **ATLAS** Collaboration, *Measurement of Spin Correlation in Top-Antitop Quark Events and Search for Top Squark Pair Production in pp Collisions at $\sqrt{s} = 8$ TeV Using the ATLAS Detector*, *Phys. Rev. Lett.* **114** (2015), no. 14 142001, [arXiv:1412.4742].

[80] **CMS** Collaboration, *Measurement of spin correlations in top pair events in the lepton + jets channel with the matrix element method at 8 TeV*, Tech. Rep. CMS-PAS-TOP-13-015, CERN, Geneva, 2015.

[81] **ATLAS** Collaboration, *Measurement of top quark polarisation in $t\bar{t}$ events with the ATLAS detector in proton-proton collisions at $\sqrt{s} = 7$ TeV*, Tech. Rep. ATLAS-CONF-2012-133, CERN, Geneva, Sep, 2012. http://cds.cern.ch/record/1478373.

[82] **CMS** Collaboration, *Measurement of the W boson helicity using $t\bar{t}$ events in the dilepton final state at sqrt(s) = 8 TeV*, Tech. Rep. CMS-PAS-TOP-14-017, CERN, Geneva, 2015. http://cds.cern.ch/record/2035390.

[83] M. Baumgart and B. Tweedie, *Discriminating Top-Antitop Resonances using Azimuthal Decay Correlations*, *JHEP* **09** (2011) 049, [arXiv:1104.2043].

[84] **LHCb** Collaboration, *Measurement of the ratio of branching fractions $\mathcal{B}(\bar{b}^0 \to D^{*+}\tau^-\bar{\nu}_\tau)/\mathcal{B}(\bar{b}^0 \to D^{*+}\mu^-\bar{\nu}_\mu)$*, *Phys. Rev. Lett.* **115** (2015), no. 11 111803, [arXiv:1506.08614]. [Addendum: Phys. Rev. Lett.115,no.15,159901(2015)].

[85] A. D. Sakharov, *SPECIAL ISSUE: Violation of CP in variance, C asymmetry, and baryon asymmetry of the universe*, *Soviet Physics Uspekhi* **34** (May, 1991) 392–393.

[86] P. Huet, *Electroweak baryogenesis and the standard model*, in *Phenomenology of Unification from*

Present to Future: Proceedings of the 1st International Conference, March 23-26, 1994, Rome, pp. 77–91, 1994. hep-ph/9406301.

[87] V. C. Rubin and W. K. Ford, Jr., *Rotation of the Andromeda Nebula from a Spectroscopic Survey of Emission Regions*, *Astrophys. J.* **159** (1970) 379–403.

[88] R. Massey, T. Kitching, and J. Richard, *The dark matter of gravitational lensing*, *Reports on Progress in Physics* **73** (Aug., 2010) 086901, [arXiv:1001.1739].

[89] **Planck** Collaboration, P. A. R. Ade et al., *Planck 2015 results. XIII. Cosmological parameters*, arXiv:1502.01589.

[90] G. Bertone, D. Hooper, and J. Silk, *Particle dark matter: Evidence, candidates and constraints*, *Phys. Rept.* **405** (2005) 279–390, [hep-ph/0404175].

[91] C. Quigg, *Unanswered Questions in the Electroweak Theory*, *Ann. Rev. Nucl. Part. Sci.* **59** (2009) 505–555, [arXiv:0905.3187].

[92] **CDF** Collaboration, *CDF Top Quark Physics Public Results: Tevatron W Mass vs Top Mass (March 2012 Combination)*, 2012. http://www-cdf.fnal.gov/physics/new/top/public_mass.html. Accessed on 22 September 2015.

[93] **CDF, D0** Collaboration, T. E. W. Group, *2012 Update of the Combination of CDF and D0 Results for the Mass of the W Boson*, arXiv:1204.0042.

[94] **CDF** Collaboration, T. Aaltonen et al., *Measurement of the top quark forward-backward production asymmetry and its dependence on event kinematic properties*, *Phys. Rev.* **D87** (2013), no. 9 092002, [arXiv:1211.1003].

[95] **D0** Collaboration, V. M. Abazov et al., *Forward-backward asymmetry in top quark-antiquark production*, *Phys. Rev.* **D84** (2011) 112005, [arXiv:1107.4995].

[96] J. A. Aguilar-Saavedra, D. Amidei, A. Juste, and M. Perez-Victoria, *Asymmetries in top quark pair production at hadron colliders*, *Rev. Mod. Phys.* **87** (2015) 421–455, [arXiv:1406.1798].

[97] M. Czakon, P. Fiedler, and A. Mitov, *Resolving the Tevatron Top Quark Forward-Backward Asymmetry Puzzle: Fully Differential Next-to-Next-to-Leading-Order Calculation*, *Phys. Rev. Lett.* **115** (2015), no. 5 052001, [arXiv:1411.3007].

[98] **D0** Collaboration, V. M. Abazov et al., *Measurement of the forward-backward asymmetry in top quark-antiquark production in ppbar collisions using the lepton+jets channel*, *Phys. Rev.* **D90** (2014) 072011, [arXiv:1405.0421].

[99] C. T. Hill, *Topcolor assisted technicolor*, *Phys.Lett.* **B345** (1995) 483–489, [hep-ph/9411426].

[100] R. M. Harris, C. T. Hill, and S. J. Parke, *Cross-section for topcolor Z-prime(t) decaying to t anti-t: Version 2.6*, hep-ph/9911288.

[101] R. M. Harris and S. Jain, *Cross Sections for Leptophobic Topcolor Z' Decaying to Top-Antitop*, *Eur.Phys.J.* **C72** (2012) 2072, [arXiv:1112.4928].

[102] S. Weinberg, *Implications of dynamical symmetry breaking: An addendum*, *Phys. Rev. D* **19** (Feb, 1979) 1277–1280.

[103] L. Susskind, *Dynamics of spontaneous symmetry breaking in the weinberg-salam theory*, *Phys. Rev. D* **20** (Nov, 1979) 2619–2625.

[104] J. Bardeen, L. N. Cooper, and J. R. Schrieffer, *Microscopic Theory of Superconductivity*, *Physical Review* **106** (Apr., 1957) 162–164.

[105] W. A. Bardeen, C. T. Hill, and M. Lindner, *Minimal dynamical symmetry breaking of the standard model*, *Phys. Rev. D* **41** (Mar, 1990) 1647–1660.

[106] M. Piai, *Lectures on walking technicolor, holography and gauge/gravity dualities*, *Adv.High Energy Phys.* **2010** (2010) 464302, [arXiv:1004.0176].

[107] R. Foadi, M. T. Frandsen, and F. Sannino, *125 GeV Higgs boson from a not so light technicolor scalar*, *Phys.Rev.* **D87** (2013), no. 9 095001, [arXiv:1211.1083].

[108] A. Doff and A. Natale, *Light composite scalar boson from a see-saw mechanism in two-scale TC*

models, arXiv:1506.07711.

[109] B. Lillie, L. Randall, and L.-T. Wang, *The Bulk RS KK-gluon at the LHC*, *JHEP* **0709** (2007) 074, [hep-ph/0701166].

[110] N. Arkani-Hamed, S. Dimopoulos, and G. Dvali, *The Hierarchy problem and new dimensions at a millimeter*, *Phys.Lett.* **B429** (1998) 263–272, [hep-ph/9803315].

[111] I. Antoniadis, N. Arkani-Hamed, S. Dimopoulos, and G. Dvali, *New dimensions at a millimeter to a Fermi and superstrings at a TeV*, *Phys.Lett.* **B436** (1998) 257–263, [hep-ph/9804398].

[112] L. Randall and R. Sundrum, *A Large mass hierarchy from a small extra dimension*, *Phys.Rev.Lett.* **83** (1999) 3370–3373, [hep-ph/9905221].

[113] L. Randall and R. Sundrum, *An Alternative to compactification*, *Phys.Rev.Lett.* **83** (1999) 4690–4693, [hep-th/9906064].

[114] H. Davoudiasl, J. Hewett, and T. Rizzo, *Bulk gauge fields in the Randall-Sundrum model*, *Phys.Lett.* **B473** (2000) 43–49, [hep-ph/9911262].

[115] A. Pomarol, *Gauge bosons in a five-dimensional theory with localized gravity*, *Phys.Lett.* **B486** (2000) 153–157, [hep-ph/9911294].

[116] Y. Grossman and M. Neubert, *Neutrino masses and mixings in nonfactorizable geometry*, *Phys.Lett.* **B474** (2000) 361–371, [hep-ph/9912408].

[117] T. Gherghetta and A. Pomarol, *Bulk fields and supersymmetry in a slice of AdS*, *Nucl.Phys.* **B586** (2000) 141–162, [hep-ph/0003129].

[118] K. Agashe, A. Delgado, M. J. May, and R. Sundrum, *RS1, custodial isospin and precision tests*, *JHEP* **0308** (2003) 050, [hep-ph/0308036].

[119] L. Randall and M. D. Schwartz, *Quantum field theory and unification in AdS5*, *JHEP* **0111** (2001) 003, [hep-th/0108114].

[120] T. Kaluza, *On the Problem of Unity in Physics*, *Sitzungsber.Preuss.Akad.Wiss.Berlin (Math.Phys.)* **1921** (1921) 966–972.

[121] O. Klein, *Quantentheorie und fünfdimensionale Relativitätstheorie*, *Zeitschrift für Physik* **37** (1926), no. 12 895–906.

[122] O. Klein, *The Atomicity of Electricity as a Quantum Theory Law*, *Nature* **118** (1926) 516.

[123] K. Agashe, A. Belyaev, T. Krupovnickas, G. Perez, and J. Virzi, *LHC Signals from Warped Extra Dimensions*, *Phys.Rev.* **D77** (2008) 015003, [hep-ph/0612015].

[124] K. Agashe, H. Davoudiasl, G. Perez, and A. Soni, *Warped Gravitons at the LHC and Beyond*, *Phys.Rev.* **D76** (2007) 036006, [hep-ph/0701186].

[125] A. L. Fitzpatrick, J. Kaplan, L. Randall, and L.-T. Wang, *Searching for the Kaluza-Klein Graviton in Bulk RS Models*, *JHEP* **0709** (2007) 013, [hep-ph/0701150].

[126] **ATLAS** Collaboration, *Search for resonant diboson production in the $\ell\ell q\bar{q}$ final state in pp collisions at $\sqrt{s} = 8$ TeV with the ATLAS detector*, *Eur.Phys.J.* **C75** (2015), no. 2 69, [arXiv:1409.6190].

[127] **ATLAS** Collaboration, *Search for production of WW/WZ resonances decaying to a lepton, neutrino and jets in pp collisions at $\sqrt{s} = 8$ TeV with the ATLAS detector*, *Eur.Phys.J.* **C75** (2015), no. 5 209, [arXiv:1503.04677].

[128] **ATLAS** Collaboration, *Search for high-mass diboson resonances with boson-tagged jets in proton-proton collisions at $\sqrt{s} = 8$ TeV with the ATLAS detector*, arXiv:1506.00962.

[129] **CMS** Collaboration, *Search for massive resonances decaying into pairs of boosted bosons in semi-leptonic final states at $\sqrt{s} = 8$ TeV*, *JHEP* **1408** (2014) 174, [arXiv:1405.3447].

[130] **CMS** Collaboration, *Searches for new physics using the $t\bar{t}$ invariant mass distribution in pp collisions at $\sqrt{s} = 8$ TeV*, *Phys.Rev.Lett.* **111** (2013), no. 21 211804, [arXiv:1309.2030].

[131] L. R. Evans and P. Bryant, *LHC Machine*, *J. Instrum.* **3** (2008) S08001. 164 p. This report is an abridged version of the LHC Design Report (CERN-2004-003).

[132] O. S. Brüning, P. Collier, P. Lebrun, S. Myers, R. Ostojic, J. Poole, and P. Proudlock, *LHC*

Design Report. CERN, Geneva, 2004.

[133] *Luminosity Public Results*, Mar, 2015. ATLAS Twiki [internal], https://twiki.cern.ch/twiki/bin/view/AtlasPublic/LuminosityPublicResults.

[134] **ALICE** Collaboration, *The ALICE experiment at the CERN LHC*, *JINST* **3** (2008) S08002.

[135] **ATLAS** Collaboration, *The ATLAS Experiment at the CERN Large Hadron Collider*, *JINST* **3** (2008) S08003.

[136] **CMS** Collaboration, *The CMS experiment at the CERN LHC*, *JINST* **3** (2008) S08004.

[137] **LHCb** Collaboration, *The LHCb Detector at the LHC*, *JINST* **3** (2008) S08005.

[138] *CERN Document Server: Photos (public)*, Mar, 2015. https://cds.cern.ch/collection/Photos.

[139] **ATLAS** Collaboration, *ATLAS: Detector and physics performance technical design report. Volume 1*, .

[140] **ATLAS** Collaboration, *ATLAS liquid argon calorimeter: Technical design report*. CERN, Geneva, 1996.

[141] **ATLAS** Collaboration, *ATLAS tile calorimeter: Technical Design Report*. CERN, Geneva, 1996.

[142] **ATLAS** Collaboration, *ATLAS muon spectrometer: Technical Design Report*. CERN, Geneva, 1997.

[143] **ATLAS** Collaboration, *Performance of the ATLAS muon trigger in pp collisions at* $\sqrt{s} = 8$ *TeV*, *Eur.Phys.J.* **C75** (2015), no. 3 120, [arXiv:1408.3179].

[144] **ATLAS** Collaboration, *Recommendations of the Panel of the 2012 Atlas Trigger Workshop*, 2013. ATL-COM-DAQ-2013-007 [internal], https://cds.cern.ch/record/1514136/.

[145] *Website of the Worldwide LHC Computing Grid (WLCG)*, Apr, 2015. http://wlcg.web.cern.ch/.

[146] **ATLAS** Collaboration, *ATLAS Computing: technical design report*. Technical Design Report ATLAS. CERN, Geneva, 2005.

[147] G. Barrand, I. Belyaev, P. Binko, M. Cattaneo, R. Chytracek, et al., *GAUDI - A software architecture and framework for building HEP data processing applications*, *Comput.Phys.Commun.* **140** (2001) 45–55.

[148] R. Brun and F. Rademakers, *ROOT: An object oriented data analysis framework*, *Nucl.Instrum.Meth.* **A389** (1997) 81–86.

[149] A. Buckley, J. Butterworth, S. Gieseke, D. Grellscheid, S. Hoche, et al., *General-purpose event generators for LHC physics*, *Phys.Rept.* **504** (2011) 145–233, [arXiv:1101.2599].

[150] T. Sjostrand, S. Mrenna, and P. Z. Skands, *PYTHIA 6.4 Physics and Manual*, *JHEP* **0605** (2006) 026, [hep-ph/0603175].

[151] T. Sjostrand, S. Mrenna, and P. Z. Skands, *A Brief Introduction to PYTHIA 8.1*, *Comput.Phys.Commun.* **178** (2008) 852–867, [arXiv:0710.3820].

[152] G. Corcella, I. Knowles, G. Marchesini, S. Moretti, K. Odagiri, et al., *HERWIG 6: An Event generator for hadron emission reactions with interfering gluons (including supersymmetric processes)*, *JHEP* **0101** (2001) 010, [hep-ph/0011363].

[153] G. Corcella, I. Knowles, G. Marchesini, S. Moretti, K. Odagiri, et al., *HERWIG 6.5 release note*, hep-ph/0210213.

[154] **ATLAS** Collaboration, *The simulation principle and performance of the ATLAS fast calorimeter simulation FastCaloSim*, tech. rep., Oct, 2010. ATL-PHYS-PUB-2010-013, https://cds.cern.ch/record/1300517/.

[155] **ATLAS** Collaboration, *The ATLAS Simulation Infrastructure*, *Eur.Phys.J.* **C70** (2010) 823–874, [arXiv:1005.4568].

[156] **GEANT4** Collaboration, S. Agostinelli et al., *GEANT4: A Simulation toolkit*, *Nucl.Instrum.Meth.* **A506** (2003) 250–303.

[157] J. Gao, C. S. Li, B. H. Li, C.-P. Yuan, and H. X. Zhu, *Next-to-leading order QCD corrections to the heavy resonance production and decay into top quark pair at the LHC*, *Phys.Rev.* **D82** (2010) 014020, [arXiv:1004.0876].

[158] F. Caola, K. Melnikov, and M. Schulze, *Complete next-to-leading order QCD description of resonant Z' production and decay into $t\bar{t}$ final states*, *Phys.Rev.* **D87** (2013), no. 3 034015, [arXiv:1211.6387].

[159] *Top group's MC12 Samples For 2012 Data Analyses*, Aug, 2015. ATLAS Twiki [internal], https://twiki.cern.ch/twiki/bin/view/AtlasProtected/TopMC12.

[160] J. Alwall, M. Herquet, F. Maltoni, O. Mattelaer, and T. Stelzer, *MadGraph 5 : Going Beyond*, *JHEP* **1106** (2011) 128, [arXiv:1106.0522].

[161] J. Pumplin, D. Stump, J. Huston, H. Lai, P. M. Nadolsky, et al., *New generation of parton distributions with uncertainties from global QCD analysis*, *JHEP* **0207** (2002) 012, [hep-ph/0201195].

[162] J. Alwall, R. Frederix, S. Frixione, V. Hirschi, F. Maltoni, et al., *The automated computation of tree-level and next-to-leading order differential cross sections, and their matching to parton shower simulations*, *JHEP* **1407** (2014) 079, [arXiv:1405.0301].

[163] P. Nason, *A New method for combining NLO QCD with shower Monte Carlo algorithms*, *JHEP* **0411** (2004) 040, [hep-ph/0409146].

[164] S. Frixione, P. Nason, and C. Oleari, *Matching NLO QCD computations with Parton Shower simulations: the POWHEG method*, *JHEP* **0711** (2007) 070, [arXiv:0709.2092].

[165] S. Alioli, P. Nason, C. Oleari, and E. Re, *A general framework for implementing NLO calculations in shower Monte Carlo programs: the POWHEG BOX*, *JHEP* **1006** (2010) 043, [arXiv:1002.2581].

[166] J. M. Campbell, R. K. Ellis, P. Nason, and E. Re, *Top-pair production and decay at NLO matched with parton showers*, arXiv:1412.1828.

[167] P. Z. Skands, *Tuning Monte Carlo Generators: The Perugia Tunes*, *Phys.Rev.* **D82** (2010) 074018, [arXiv:1005.3457].

[168] H.-L. Lai, M. Guzzi, J. Huston, Z. Li, P. M. Nadolsky, et al., *New parton distributions for collider physics*, *Phys.Rev.* **D82** (2010) 074024, [arXiv:1007.2241].

[169] J. K. Behr, *Top Results for Powheg/Pythia6+CT10+Hdamp*, Oct, 2014. Talk in the ATLAS Physics Modelling Group Plenary Meeting. On behalf of the Top Group analysis teams [internal], https://indico.cern.ch/event/345106/contribution/4.

[170] **ATLAS** Collaboration, *Comparison of Monte Carlo generator predictions to ATLAS measurements of top pair production at 7 TeV*, Tech. Rep. ATL-PHYS-PUB-2015-002, Jan, 2015. https://cds.cern.ch/record/1981319.

[171] **ATLAS** Collaboration, *Comparison of Monte Carlo generator predictions for gap fraction and jet multiplicity observables in top-antitop events*, Tech. Rep. ATL-PHYS-PUB-2014-005, May, 2014. https://cds.cern.ch/record/1703034.

[172] **ATLAS** Collaboration, *Measurement of the differential cross-section of highly boosted top quarks as a function of their transverse momentum using the ATLAS detector in $\sqrt{s}$ = 8 TeV proton-proton collisions*, Tech. Rep. ATLAS-CONF-2014-057, CERN, Geneva, Sep, 2014. https://cds.cern.ch/record/1951328.

[173] A. V. Manohar and M. Trott, *Electroweak Sudakov Corrections and the Top Quark Forward-Backward Asymmetry*, *Phys.Lett.* **B711** (2012) 313–316, [arXiv:1201.3926].

[174] **ATLAS** Collaboration, *A search for $t\bar{t}$ resonances in the lepton plus jets final state with ATLAS using 14 fb^{-1} of pp collisions at $\sqrt{s} = 8$ TeV*, 2013. ATLAS-CONF-2013-052, http://cds.cern.ch/record/1547568.

[175] J. Kühn, A. Scharf, and P. Uwer, *Weak Interactions in Top-Quark Pair Production at Hadron Colliders: An Update*, *Phys.Rev.* **D91** (2015), no. 1 014020, [arXiv:1305.5773].

[176] S. Frixione, E. Laenen, P. Motylinski, B. R. Webber, and C. D. White, *Single-top hadroproduction in association with a W boson*, *JHEP* **0807** (2008) 029, [arXiv:0805.3067].

[177] N. Kidonakis, *NNLL resummation for s-channel single top quark production*, *Phys. Rev.* **D81** (2010) 054028, [arXiv:1001.5034].

[178] N. Kidonakis, *Next-to-next-to-leading-order collinear and soft gluon corrections for t-channel single top quark production*, *Phys. Rev.* **D83** (2011) 091503, [arXiv:1103.2792].

[179] N. Kidonakis, *Two-loop soft anomalous dimensions for single top quark associated production with a W- or H-*, *Phys.Rev.* **D82** (2010) 054018, [arXiv:1005.4451].

[180] M. Garzelli, A. Kardos, C. Papadopoulos, and Z. Trocsanyi, *$t\bar{t}\,W^{+-}$ and $t\bar{t}\,Z$ Hadroproduction at NLO accuracy in QCD with Parton Shower and Hadronization effects*, *JHEP* **1211** (2012) 056, [arXiv:1208.2665].

[181] M. L. Mangano, M. Moretti, F. Piccinini, R. Pittau, and A. D. Polosa, *ALPGEN, a generator for hard multiparton processes in hadronic collisions*, *JHEP* **0307** (2003) 001, [hep-ph/0206293].

[182] J. Alwall, S. Hoche, F. Krauss, N. Lavesson, L. Lonnblad, et al., *Comparative study of various algorithms for the merging of parton showers and matrix elements in hadronic collisions*, *Eur.Phys.J.* **C53** (2008) 473–500, [arXiv:0706.2569].

[183] **ATLAS** Collaboration, *Monte Carlo samples used for top physics*, Dec, 2010. ATL-PHYS-INT-2010-132 [internal], https://cds.cern.ch/record/1312945/.

[184] R. Gavin, Y. Li, F. Petriello, and S. Quackenbush, *W Physics at the LHC with FEWZ 2.1*, *Comput.Phys.Commun.* **184** (2013) 208–214, [arXiv:1201.5896].

[185] **ATLAS** Collaboration, *Single Boson and Diboson Production Cross Sections in pp Collisions at sqrts=7 TeV*, Aug, 2010. ATL-COM-PHYS-2010-695 [internal], https://cds.cern.ch/record/1287902.

[186] T. Gleisberg, S. Hoeche, F. Krauss, M. Schonherr, S. Schumann, et al., *Event generation with SHERPA 1.1*, *JHEP* **0902** (2009) 007, [arXiv:0811.4622].

[187] J. M. Campbell and R. Ellis, *MCFM for the Tevatron and the LHC*, *Nucl.Phys.Proc.Suppl.* **205-206** (2010) 10–15, [arXiv:1007.3492].

[188] W. Lampl et al., *Calorimeter Clustering Algorithms: Description and Performance*, Tech. Rep. ATL-LARG-PUB-2008-002, CERN, Geneva, Apr, 2008. https://cds.cern.ch/record/1099735.

[189] **ATLAS** Collaboration, *Improved electron reconstruction in ATLAS using the Gaussian Sum Filter-based model for bremsstrahlung*, Tech. Rep. ATLAS-CONF-2012-047, CERN, Geneva, May, 2012. https://cds.cern.ch/record/1449796.

[190] T. G. Cornelissen et al., *The global chi**2 track fitter in ATLAS*, *J.Phys.Conf.Ser.* **119** (2008) 032013.

[191] **ATLAS** Collaboration, *Electron efficiency measurements with the ATLAS detector using the 2012 LHC proton-proton collision data*, Tech. Rep. ATLAS-CONF-2014-032, CERN, Geneva, Jun, 2014. http://cds.cern.ch/record/1706245.

[192] K. Rehermann and B. Tweedie, *Efficient Identification of Boosted Semileptonic Top Quarks at the LHC*, *JHEP* **1103** (2011) 059, [arXiv:1007.2221].

[193] **ATLAS** Collaboration, *Electron and photon energy calibration with the ATLAS detector using LHC Run 1 data*, *Eur.Phys.J.* **C74** (2014), no. 10 3071, [arXiv:1407.5063].

[194] A. Hocker et al., *TMVA - Toolkit for Multivariate Data Analysis*, *PoS* **ACAT** (2007) 040, [physics/0703039].

[195] S. Calvet, C. Pollard, and J. Zhong, *Electron-Jet Overlap Removal for the l + jets $t\bar{t}$ Resonances Search*, Tech. Rep. ATL-COM-PHYS-2014-343, CERN, Geneva, Apr, 2014. ATLAS internal, https://cds.cern.ch/record/1696833.

[196] **ATLAS** Collaboration, *Object selection and calibration, background estimations and MC samples for the Winter 2013 Top Quark analyses with 2012 data*, 2013. ATL-COM-PHYS-2013-088 [internal], https://cds.cern.ch/record/1509562.

[197] **ATLAS** Collaboration, *Performance of the ATLAS Electron and Photon Triggers in p-p Collisions at $\sqrt{s} = 8$ TeV in 2012*, Tech. Rep. ATL-COM-DAQ-2013-121, CERN, Geneva, Oct, 2013. Paper in preparation [internal], https://cds.cern.ch/record/1609629.

[198] **ATLAS** Collaboration, *Identification of muon candidates in pp collisions at sqrt(s)=900 GeV with the ATLAS detector*, Tech. Rep. ATLAS-CONF-2010-015, CERN, Geneva, Jul, 2010. https://cds.cern.ch/record/1276549.

[199] **ATLAS** Collaboration, *Measurement of the muon reconstruction performance of the ATLAS detector using 2011 and 2012 LHC proton-proton collision data*, *Eur.Phys.J.* **C74** (2014), no. 11 3130, [arXiv:1407.3935].

[200] *ATLAS Muon Combined Performance - Preliminary Guidelines for Analyses of 2012 Data*, Apr, 2015. ATLAS Twiki [internal], https://twiki.cern.ch/twiki/bin/viewauth/AtlasProtected/MCPAnalysisGuidelinesData2012.

[201] **ATLAS** Collaboration, *Jet energy measurement with the ATLAS detector in proton-proton collisions at $\sqrt{s} = 7$ TeV*, *Eur.Phys.J.* **C73** (2013), no. 3 2304, [arXiv:1112.6426].

[202] Y. Dokshitzer, G. Leder, S. Moretti, and B. Webber, *Better jet clustering algorithms*, *JHEP* **9708** (1997) 001, [9707323].

[203] M. Wobisch and T. Wengler, *Hadronization corrections to jet cross-sections in deep inelastic scattering*, hep-ph/9907280.

[204] S. D. Ellis and D. E. Soper, *Successive combination jet algorithm for hadron collisions*, *Phys.Rev.* **D48** (1993) 3160–3166, [hep-ph/9305266].

[205] S. Catani, Y. L. Dokshitzer, M. Seymour, and B. Webber, *Longitudinally invariant K_t clustering algorithms for hadron hadron collisions*, *Nucl.Phys.* **B406** (1993) 187–224.

[206] M. Cacciari, G. P. Salam, and G. Soyez, *The Anti-k(t) jet clustering algorithm*, *JHEP* **0804** (2008) 063, [arXiv:0802.1189].

[207] S. D. Ellis, Z. Kunszt, and D. E. Soper, *The One Jet Inclusive Cross-Section at Order alpha-s**3. 1. Gluons Only*, *Phys.Rev.* **D40** (1989) 2188.

[208] M. Cacciari, G. P. Salam, and G. Soyez, *FastJet User Manual*, *Eur.Phys.J.* **C72** (2012) 1896, [arXiv:1111.6097].

[209] M. Cacciari and G. P. Salam, *Dispelling the N^3 myth for the k_t jet-finder*, *Phys.Lett.* **B641** (2006) 57–61, [hep-ph/0512210].

[210] **ATLAS** Collaboration, *Performance of boosted top quark identification in 2012 ATLAS data*, Tech. Rep. ATLAS-CONF-2013-084, CERN, Geneva, Aug, 2013. https://cds.cern.ch/record/1571040.

[211] *Identification of high transverse momentum top quarks in pp collisions at $\sqrt{s} = 8$ TeV with the ATLAS detector*, Tech. Rep. ATLAS-CONF-2015-036, CERN, Geneva, Aug, 2015. https://cds.cern.ch/record/2043862.

[212] **CMS** Collaboration, *Boosted Top Jet Tagging at CMS*, Tech. Rep. CMS-PAS-JME-13-007, CERN, Geneva, 2014. https://cds.cern.ch/record/1647419.

[213] **ATLAS** Collaboration, *Performance of Boosted W Boson Identification with the ATLAS Detector*, Tech. Rep. ATL-PHYS-PUB-2014-004, CERN, Geneva, Mar, 2014. https://cds.cern.ch/record/1690048.

[214] **CMS** Collaboration, *Identification techniques for highly boosted W bosons that decay into hadrons*, *JHEP* **12** (2014) 017, [arXiv:1410.4227].

[215] **ATLAS** Collaboration, *Performance of jet substructure techniques for large-R jets in proton-proton collisions at $\sqrt{s} = 7$ TeV using the ATLAS detector*, *JHEP* **1309** (2013) 076, [arXiv:1306.4945].

[216] D. Krohn, J. Thaler, and L.-T. Wang, *Jet Trimming*, *JHEP* **1002** (2010) 084, [arXiv:0912.1342].

[217] S. D. Ellis, C. K. Vermilion, and J. R. Walsh, *Techniques for improved heavy particle searches with jet substructure*, *Phys.Rev.* **D80** (2009) 051501, [arXiv:0903.5081].

[218] J. M. Butterworth, A. R. Davison, M. Rubin, and G. P. Salam, *Jet substructure as a new Higgs search channel at the LHC*, *Phys.Rev.Lett.* **100** (2008) 242001, [arXiv:0802.2470].

[219] **ATLAS** Collaboration, *Pile-up subtraction and suppression for jets in ATLAS*, Tech. Rep. ATLAS-CONF-2013-083, CERN, Geneva, Aug, 2013.

[220] C. Issever, K. Borras, and D. Wegener, *An Improved weighting algorithm to achieve software compensation in a fine grained LAr calorimeter*, *Nucl.Instrum.Meth.* **A545** (2005) 803–812, [physics/0408129].

[221] **ATLAS** Collaboration Tech. Rep. ATL-LARG-PUB-2009-001-2, CERN, Geneva, June, 2008. https://cds.cern.ch/record/1112035.

[222] **ATLAS** Collaboration, *Monte Carlo Calibration and Combination of In-situ Measurements of Jet Energy Scale, Jet Energy Resolution and Jet Mass in ATLAS*, Tech. Rep. ATLAS-CONF-2015-037, CERN, Geneva, Aug, 2015. http://cds.cern.ch/record/2044941.

[223] *Beam Spot Public Results*, May, 2015. ATLAS Twiki [internal], https://twiki.cern.ch/twiki/bin/view/AtlasPublic/BeamSpotPublicResults.

[224] **ATLAS** Collaboration, *Jet global sequential corrections with the ATLAS detector in proton-proton collisions at sqrt(s) = 8 TeV*, Tech. Rep. ATLAS-CONF-2015-002, CERN, Geneva, Mar, 2015. https://cds.cern.ch/record/2001682.

[225] **ATLAS** Collaboration, *Data-driven determination of the energy scale and resolution of jets reconstructed in the ATLAS calorimeters using dijet and multijet events at* $\sqrt{s} = 8\ TeV$, Tech. Rep. ATLAS-CONF-2015-017, CERN, Geneva, Apr, 2015. https://cds.cern.ch/record/2008678.

[226] **ATLAS** Collaboration, *Determination of the jet energy scale and resolution at ATLAS using* Z/γ*-jet events in data at* $\sqrt{s} = 8\ TeV$, Tech. Rep. ATL-COM-PHYS-2014-791, CERN, Geneva, Jul, 2014. https://cds.cern.ch/record/1741697.

[227] **ATLAS** Collaboration, *Jet energy measurement and its systematic uncertainty in proton-proton collisions at* $\sqrt{s} = 7\ TeV$ *with the ATLAS detector*, *Eur.Phys.J.* **C75** (2015), no. 1 17, [arXiv:1406.0076].

[228] *JetEtmiss Group Public Results*, May, 2015. ATLAS Twiki [internal], https://twiki.cern.ch/twiki/bin/view/AtlasPublic/JetEtmissApproved2013JESUncertainty.

[229] L. A. Kogan, *The Jet Energy Scale Uncertainty Derived from* γ*-jet Events for Small and Large Radius Jets and the Calibration and Performance of Variable R Jets with the ATLAS Detector.* PhD thesis, University of Oxford, 2014. Presented 24 Nov 2014. https://cds.cern.ch/record/2125290.

[230] *Software and data package for the* $t\bar{t}$ *resonance search in the* 1ℓ*+jets channel at* $\sqrt{s} = 8\ TeV$, Jun, 2015. ATLAS SVN Repository [internal], https://svnweb.cern.ch/trac/atlasphys/browser/Physics/Top/PhysAnalysis/ttResoSingleLepton.

[231] **ATLAS** Collaboration, *Expected performance of the ATLAS experiment: detector, trigger and physics*. CERN, Geneva, 2009. https://cds.cern.ch/record/1125884.

[232] **ATLAS** Collaboration, *Commissioning of the ATLAS high-performance b-tagging algorithms in the 7 TeV collision data*, Tech. Rep. ATLAS-CONF-2011-102, CERN, Geneva, Jul, 2011. https://cds.cern.ch/record/1369219.

[233] **ATLAS** Collaboration, *b-tagging in dense environments*, Tech. Rep. ATL-PHYS-PUB-2014-014, CERN, Geneva, Aug, 2014. https://cds.cern.ch/record/1750682.

[234] R. E. Kalman, *A New Approach to Linear Filtering and Prediction Problems*, *Transactions of the ASME–Journal of Basic Engineering* **82** (1960), no. Series D 35–45.

[235] **ATLAS** Collaboration, *Measurement of the b-tagging performance in the 2012 ATLAS data*, Tech. Rep. ATL-COM-PHYS-2013-456, CERN, Geneva, Apr, 2013. Publication in preparation [internal], https://cds.cern.ch/record/1542409.

[236] **ATLAS** Collaboration, *Calibration of ATLAS b-tagging algorithms in dense jet environments*, Tech. Rep. ATL-COM-PHYS-2015-010, CERN, Geneva, Jan, 2015. Publication in preparation [internal], https://cds.cern.ch/record/1981534.

[237] **ATLAS** Collaboration, *Calibration of the performance of b-tagging for c and light-flavour jets in the 2012 ATLAS data*, Tech. Rep. ATLAS-CONF-2014-046, CERN, Geneva, Jul, 2014. https://cds.cern.ch/record/1741020.

[238] **ATLAS** Collaboration, *Performance of Missing Transverse Momentum Reconstruction in*

Proton-Proton Collisions at 7 TeV with ATLAS, *Eur.Phys.J.* **C72** (2012) 1844, [arXiv:1108.5602].

[239] W. J. Stirling, *private communication*, Mar, 2015. Imperial College HEP Research Group Web Server: http://www.hep.ph.ic.ac.uk/~wstirlin/plots/crosssections2012_v5.pdf.

[240] J. Zhong, *Variable $\Delta R(\mu, j)$ cut*, Mar, 2013. Talk in the ATLAS Boosted Top Quark Reconstruction Performance Workshop [internal], https://indico.cern.ch/event/230294/session/4/contribution/51/material/slides/0.pdf.

[241] T. Koi et al., *Monte Carlo calculations for the ATLAS cavern background*, *Progress in Nuclear Science and Technology* **4** (2014) 507–510.

[242] **ATLAS** Collaboration, G. Aad et al., *Search for vectorlike B quarks in events with one isolated lepton, missing transverse momentum and jets at $\sqrt{s} = 8$ TeV with the ATLAS detector*, *Phys. Rev.* **D91** (2015), no. 11 112011, [arXiv:1503.05425].

[243] A. Altheimer et al., *MET Cut Optimization*, Oct, 2013. Talk in the ATLAS Meeting "Ttbar resonance searches in one lepton channel"[internal], https://indico.cern.ch/event/260790/contribution/2/attachments/460655/638349/METCutOptimization.pdf.

[244] L. Valery and S. Calvet, *CHI2 CUT OPTIMISATION*, Oct, 2013. Talk in the ATLAS Meeting "Ttbar resonance searches in one lepton channel"[internal], https://indico.cern.ch/event/260787/contribution/1/attachments/460635/638328/Chi2_v2.pdf.

[245] J. Zhong, *Analysis status of $t\bar{t}$ resonance search*, Mar, 2013. Talk in the ATLAS Joint Top Property/4GT Meeting [internal], https://indico.cern.ch/event/240988/session/0/contribution/2/material/slides/0.pdf.

[246] **ATLAS** Collaboration, *Flavor Tagging with Track Jets in Boosted Topologies with the ATLAS Detector*, Tech. Rep. ATL-PHYS-PUB-2014-013, CERN, Geneva, Aug, 2014. https://cds.cern.ch/record/1750681.

[247] C.-H. Kom and W. J. Stirling, *Charge asymmetry in W + jets production at the LHC*, *Eur.Phys.J.* **C69** (2010) 67–73, [arXiv:1004.3404].

[248] J. Zhong, *Re: Questions on W+jets background estimation*, E-mail to Katharina Behr, 2 March 2015.

[249] J. Ferrando, *Re: Questions on W+jets background estimation*, E-mail to Katharina Behr, 2 March 2015.

[250] **D0** Collaboration, *Extraction of the width of the W boson from measurements of $\sigma(p\bar{p} \to W + X) \times B(W \to e\nu)$ and $\sigma(p\bar{p} \to Z + X) \times B(Z \to ee)$ and their ratio*, *Phys.Rev.* **D61** (2000) 072001, [hep-ex/9906025].

[251] **ATLAS** Collaboration, *Measurement of the top quark pair production cross-section with ATLAS in the single lepton channel*, *Phys.Lett.* **B711** (2012) 244–263, [arXiv:1201.1889].

[252] **CMS** Collaboration, *Measurement of the $t\bar{t}$ production cross section in the dilepton channel in pp collisions at $\sqrt{s} = 7$ TeV*, *JHEP* **1211** (2012) 067, [arXiv:1208.2671].

[253] **ATLAS** Collaboration, *Estimation of non-prompt and fake leptons background in final states with top quarks produced in proton-proton collision at $\sqrt{s} = 8$ TeV with the ATLAS detector*, 2014. ATL-COM-PHYS-2013-1100 [internal], https://cds.cern.ch/record/1571043.

[254] D. E. Ferreira de Lima, *Re: Questions on estimation of multi-jet background*, E-mail to Katharina Behr, 7 March 2015.

[255] **ATLAS** Collaboration, *Improved luminosity determination in pp collisions at $\sqrt{s} = 7$ TeV using the ATLAS detector at the LHC*, *Eur.Phys.J.* **C73** (2013), no. 8 2518, [arXiv:1302.4393].

[256] *Twiki page of the ATLAS Luminosity Group*, Feb, 2015. ATLAS Twiki [internal], https://twiki.cern.ch/twiki/bin/view/Atlas/LuminosityForPhysics#2012_8_TeV_Moriond_2013.

[257] *b-tagging Calibration Data Interface*, May, 2015. ATLAS Twiki [internal], https://twiki.cern.ch/twiki/bin/viewauth/AtlasProtected/BTaggingCalibrationDataInterface.

[258] *Flavour Tagging calibration results in 2014*, May, 2015. ATLAS Twiki [internal], https://twiki.cern.ch/twiki/bin/viewauth/AtlasProtected/BTagCalib2014.

[259] T. Scanlon and G. Piacquadio, *Re: Derivation of high-pt b-tagging uncertainty (8 TeV)*, E-mail to Katharina Behr, 14 September 2015.

[260] S. Schramm, *Searching for Dark Matter with the ATLAS Detector in Events with an Energetic Jet and Large Missing Transverse Momentum*. PhD thesis, Toronto U., 2015. Presented 26 Feb 2015. https://cds.cern.ch/record/2014029.

[261] **ATLAS** Collaboration, *Jet energy measurement and systematic uncertainties using tracks for jets and for b-quark jets produced in proton-proton collisions at $\sqrt{s} = 7$ TeV in the ATLAS detector*, Tech. Rep. ATLAS-CONF-2013-002, CERN, Geneva, Jan, 2013. https://cds.cern.ch/record/1504739.

[262] *JetEnergyResolutionProvider2012*, May, 2015. ATLAS Twiki [internal], https://twiki.cern.ch/twiki/bin/view/AtlasProtected/JetEnergyResolutionProvider2012.

[263] *JVFUncertaintyTool*, May, 2015. ATLAS Twiki [internal], https://twiki.cern.ch/twiki/bin/view/AtlasProtected/JVFUncertaintyTool.

[264] *Jet Substructure Recommendations* , Jun, 2015. ATLAS Twiki [internal], https://twiki.cern.ch/twiki/bin/viewauth/AtlasProtected/JetSubstructureRecommendations.

[265] M. Botje, J. Butterworth, A. Cooper-Sarkar, A. de Roeck, J. Feltesse, et al., *The PDF4LHC Working Group Interim Recommendations*, arXiv:1101.0538.

[266] S. Frixione and B. R. Webber, *Matching NLO QCD computations and parton shower simulations*, *JHEP* **0206** (2002) 029, [hep-ph/0204244].

[267] S. Frixione, P. Nason, and B. R. Webber, *Matching NLO QCD and parton showers in heavy flavor production*, *JHEP* **0308** (2003) 007, [hep-ph/0305252].

[268] S. Frixione, F. Stoeckli, P. Torrielli, B. R. Webber, and C. D. White, *The MCaNLO 4.0 Event Generator*, arXiv:1010.0819.

[269] J. Butterworth, J. R. Forshaw, and M. Seymour, *Multiparton interactions in photoproduction at HERA*, *Z.Phys.* **C72** (1996) 637–646, [hep-ph/9601371].

[270] B. P. Kersevan and E. Richter-Was, *The Monte Carlo event generator AcerMC versions 2.0 to 3.8 with interfaces to PYTHIA 6.4, HERWIG 6.5 and ARIADNE 4.1*, *Comput.Phys.Commun.* **184** (2013) 919–985, [hep-ph/0405247].

[271] **ATLAS** Collaboration, *Monte Carlo samples used for top physics*, 2010. ATL-COM-PHYS-2010-836 [internal], https://cds.cern.ch/record/1298803/files/ATL-COM-PHYS-2010-836.pdf.

[272] *ATLAS Twiki: W+jets re-weighting tool* , Feb, 2015. ATLAS Twiki [internal], https://twiki.cern.ch/twiki/bin/view/AtlasProtected/WjetsReweighting.

[273] *ATLAS Twiki: TTplusV*, Feb, 2015. ATLAS Twiki [internal], https://twiki.cern.ch/twiki/bin/view/AtlasProtected/TTplusV.

[274] **ATLAS** Collaboration, *Measurement of the top quark-pair production cross section with ATLAS in pp collisions at $\sqrt{s} = 7$ TeV*, *Eur.Phys.J.* **C71** (2011) 1577, [arXiv:1012.1792].

[275] *ATLAS Twiki: Top Systematic Uncertainties*, Feb, 2015. ATLAS Twiki [internal], https://twiki.cern.ch/twiki/bin/viewauth/AtlasProtected/TopSystematicUncertainties.

[276] R. D. Ball, V. Bertone, S. Carrazza, C. S. Deans, L. Del Debbio, et al., *Parton distributions with LHC data*, *Nucl.Phys.* **B867** (2013) 244–289, [arXiv:1207.1303].

[277] *LHAPDF Project Webpage*, Feb, 2015. https://lhapdf.hepforge.org/.

[278] *ATLAS Twiki: TopPdfUncertainty*, Feb, 2015. ATLAS Twiki [internal], https://twiki.cern.ch/twiki/bin/viewauth/AtlasProtected/TopPdfUncertainty.

[279] S. Livermore, *A search for massive top quark resonances with the ATLAS detector at the Large Hadron Collider*. PhD thesis, University of Oxford, 2013. Presented 01 Mar 2013. https://cds.cern.ch/record/1551556.

[280] G. Choudalakis, *On hypothesis testing, trials factor, hypertests and the BumpHunter*, arXiv:1101.0390.

[281] S. Calvet, *Re: Question on Sliding Windows in BumpHunter*, E-mail to Katharina Behr, 13 January 2015.

[282] G. Cowan, *Statistical Methods for Discovery and Limits in HEP Experiments. Day 3: Exclusion Limits.* , Lecture at the Graduiertenkolleg "Physik an Hadron-Beschleunigern", 2011. http://www.pp.rhul.ac.uk/~cowan/stat/freiburg/cowan_freiburg_2011_3.pdf. Accessed on 4 Sep 2015.

[283] **D0** Collaboration, I. Bertram et al., *A Recipe for the construction of confidence limits*, *FERMILAB-TM-2104* (2000). http://lss.fnal.gov/archive/test-tm/2000/fermilab-tm-2104.pdf.

[284] **D0** Collaboration, S. Jain et al., *Statistical methods implemented in the Package top statistics*, *D0 Note 5817* (2009).

[285] M. Baak, G. Besjes, D. Cote, A. Koutsman, J. Lorenz, et al., *HistFitter software framework for statistical data analysis*, arXiv:1410.1280.

[286] K. Cranmer et al., *HistFactory: A tool for creating statistical models for use with RooFit and RooStats*, tech. rep., CERN, Geneva, Jul, 2012. http://cds.cern.ch/record/1456844.

[287] *RooFit Webpage*, Feb, 2015. https://root.cern.ch/drupal/content/roofit.

[288] *RooStats CERN Twiki*, Feb, 2015. https://twiki.cern.ch/twiki/bin/view/RooStats/WebHome.

[289] G. Cowan, K. Cranmer, E. Gross, and O. Vitells, *Asymptotic formulae for likelihood-based tests of new physics*, *Eur.Phys.J.* **C71** (2011) 1554, [arXiv:1007.1727].

[290] G. Cowan, *Statistics for Searches at the LHC*, in *Proceedings, 69th Scottish Universities Summer School in Physics : LHC Phenomenology (SUSSP69)*, pp. 321–355, 2013. arXiv:1307.2487.

[291] A. L. Read, *Presentation of search results: The CL(s) technique*, *J. Phys.* **G28** (2002) 2693–2704. [,11(2002)].

[292] S. Wilks, *The Large-Sample Distribution of the Likelihood Ratio for Testing Composite Hypotheses*, *Annals Math.Statist.* **9** (1938), no. 1 60–62.

[293] A. Wald, *Tests of Statistical Hypotheses Concerning Several Parameters When the Number of Observations is Large*, *Transactions of the Americ. Math. Soc.* **54** (1943), no. 3 426–482.

[294] F. James, *MINUIT Function Minimization and Error Analysis: Reference Manual Version 94.1*, .

[295] I. Asimov, *The Complete Stories*, vol. 1. Doubleday Books, 1 ed., 1990.

[296] *Measurement of the $t\bar{t}W$ and $t\bar{t}Z$ production cross sections in pp collisions at $\sqrt{s} = 8$ TeV with the ATLAS detector.*, Tech. Rep. ATLAS-CONF-2015-032, CERN, Geneva, Jul, 2015. https://cds.cern.ch/record/2038143.

[297] V. Dao, S. Guindon, E. Shabalina, and T. Vazquez Schroeder, *Measurement of the associated production of a vector boson (W, Z) and top quark pair in the opposite sign dilepton channel with $\boldsymbol{pp}$ collisions at $\boldsymbol{\sqrt{s} = 8}$ TeV with the ATLAS detector at the LHC*, Tech. Rep. ATL-COM-PHYS-2015-068, CERN, Geneva, Feb, 2015. https://cds.cern.ch/record/1987086.

[298] D. Duda, *Identification of bottom-quarks in searches for new heavy resonances decaying into boosted top-quarks with the ATLAS detector and a development of an improved b-tagging algorithm.* PhD thesis, Bergische Universität Wuppertal, 2015. Presented 08 Sep 2015. https://cds.cern.ch/record/2069170.

[299] J. K. Behr and J. Zhong, *Run1 search: systematics profiling*, Feb, 2015. Talk in the ATLAS Meeting "Ttbar resonance searches in one lepton channel"[internal], https://indico.cern.ch/event/365060/contribution/1/attachments/726072/996412/TR_2015Feb03_Btag10Pulls.pdf.

[300] **CMS** Collaboration, *Search for ttbar resonances in semileptonic final state*, Tech. Rep. CMS-PAS-B2G-12-006, CERN, Geneva, 2013. https://cds.cern.ch/record/1543467.

[301] **ATLAS** Collaboration, G. Aad et al., *Measurements of normalized differential cross sections for $t\bar{t}$ production in pp collisions at $\sqrt{s} = 7$ TeV using the ATLAS detector*, *Phys. Rev.* **D90** (2014), no. 7 072004, [arXiv:1407.0371].

[302] **CMS** Collaboration, *Measurement of the differential cross section for top quark pair production in pp collisions at $\sqrt{s}$ = 8 TeV*, arXiv:1505.04480.

[303] **CMS** Collaboration, S. Chatrchyan et al., *Measurement of differential top-quark pair production cross sections in pp colisions at $\sqrt{s} = 7$ TeV*, *Eur. Phys. J.* **C73** (2013), no. 3 2339, [arXiv:1211.2220].

[304] B. Lemmer, *Measurement of Spin Correlations in $t\bar{t}$ Events from pp Collisions at $\sqrt{s}$ = 7 TeV in the Lepton + Jets Final State with the ATLAS Detector*, arXiv:1410.1791.

[305] **ATLAS** Collaboration, *Search for the Standard Model Higgs boson produced in association with top quarks and decaying into $b\bar{b}$ in pp collisions at $\sqrt{s}$ = 8 TeV with the ATLAS detector*, *Eur. Phys. J.* **C75** (2015), no. 7 349, [arXiv:1503.05066].

[306] **CMS** Collaboration, *Measurements of ttbar Spin Correlations and Top-Quark Polarization Using Dilepton Final States in pp Collisions at sqrt(s) = 8 TeV*, Tech. Rep. CMS-PAS-TOP-14-023, CERN, Geneva, 2015. https://cds.cern.ch/record/2052636.

[307] **CMS** Collaboration, *Search for W' $\to$ tb decays in the lepton + jets final state in pp collisions at $\sqrt{s}$ = 8 TeV*, *JHEP* **05** (2014) 108, [arXiv:1402.2176].

[308] P. L. Rocca and F. Riggi, *The upgrade programme of the major experiments at the large hadron collider*, *Journal of Physics: Conference Series* **515** (2014), no. 1 012012.

[309] *Performance of jet substructure techniques in early $\sqrt{s} = 13$ TeV pp collisions with the ATLAS detector*, Tech. Rep. ATLAS-CONF-2015-035, CERN, Geneva, Aug, 2015. https://cds.cern.ch/record/2041462.

[310] M. Shochet, L. Tompkins, V. Cavaliere, P. Giannetti, A. Annovi, and G. Volpi, *Fast TracKer (FTK) Technical Design Report*, Tech. Rep. CERN-LHCC-2013-007. ATLAS-TDR-021, CERN, Geneva, Jun, 2013. ATLAS Fast Tracker Technical Design Report.

[311] J. K. Behr, C. Issever, and J. Zhong, *Trigger Strategies for Boosted Top Analyses*, Dec, 2012. Talk at the ATLAS Trigger Workshop [internal]. https://indico.cern.ch/event/202564/session/4/contribution/33.

[312] S. Schaetzel and M. Spannowsky, *Tagging highly boosted top quarks*, *Phys. Rev.* **D89** (2014), no. 1 014007, [arXiv:1308.0540].

[313] M. Capeans et al., *ATLAS Insertable B-Layer Technical Design Report*, Tech. Rep. CERN-LHCC-2010-013. ATLAS-TDR-19, CERN, Geneva, Sep, 2010.